

**FABRICATION OF NOBLE METAL MODIFIED  
TITANIA PHOTOANODE FOR HIGHER EFFICIENCY  
DYE-SENSITIZED SOLAR CELLS**

**LIM SU PEI**

**THESIS SUBMITTED IN FULFILLMENT OF THE  
REQUIREMENTS FOR THE DEGREE OF  
DOCTOR OF PHILOSOPHY**

**DEPARTMENT OF PHYSICS  
FACULTY OF SCIENCE  
UNIVERSITY OF MALAYA  
KUALA LUMPUR**

**2015**

UNIVERSITI MALAYA

**ORIGINAL LITERARY WORK DECLARATION**

Name of Candidate: **LIM SU PEI**

(I.C/Passport No: **870529-02-5726**)

Registration/Matric No: **SHC130075**

Name of Degree: **DOCTOR OF PHILOSOPHY**

Title of ~~Project Paper/Research Report/Dissertation~~/Thesis ("this Work"):

**FABRICATION OF NOBLE METAL MODIFIED TITANIA PHOTOANODE  
FOR HIGHER EFFICIENCY DYE-SENSITIZED SOLAR CELLS**

Field of Study: **ADVANCED MATERIALS**

I do solemnly and sincerely declare that:

- (1) I am the sole author/writer of this Work;
- (2) This Work is original;
- (3) Any use of any work in which copyright exists was done by way of fair dealing and for permitted purposes and any excerpt or extract from, or reference to or reproduction of any copyright work has been disclosed expressly and sufficiently and the title of the Work and its authorship have been acknowledged in this Work;
- (4) I do not have any actual knowledge nor do I ought reasonably to know that the making of this work constitutes an infringement of any copyright work;
- (5) I hereby assign all and every rights in the copyright to this Work to the University of Malaya ("UM"), who henceforth shall be owner of the copyright in this Work and that any reproduction or use in any form or by any means whatsoever is prohibited without the written consent of UM having been first had and obtained;
- (6) I am fully aware that if in the course of making this Work I have infringed any copyright whether intentionally or otherwise, I may be subject to legal action or any other action as may be determined by UM.

Candidate's Signature:

Date:

Subscribed and solemnly declared before,

Witness's Signature:

Date:

Name: **Dr. Huang Nay Ming**

Designation: **Senior Lecturer**

## ABSTRACT

The dye-sensitized solar cells (DSSCs), taken as a new generation or potential alternative for the traditional silicon and thin films solar panels, is an efficient and economical way to directly convert solar energy to electricity. The significant development of the DSSC technology has demonstrated its capability for future renewable solar electricity generation. One of the major challenges of this technology is that the efficiency is still less than half that of a single-crystal silicon cell. If the efficiency of DSSCs can be improved, these devices could significantly reduce the cost compared to the first and second generation photovoltaic devices. To address this problem, designing a novel photoanode with an efficient transport pathway from the photoinjected carriers to the current collector seems to be an attractive alternative to enhance the performance of DSSCs. Herein, the thesis reported on the synthesis of noble metal nanoparticles modified photoanode and investigation of the relationship between the photoanode and the device performance. This research work was divided into four stages. The initial study focused on the synthesis of silver-titanium dioxide ( $\text{Ag@TiO}_2$ ) nanocomposite materials. A single-step chemical reduction has been employed to synthesize binary nanocomposite films of  $\text{Ag@TiO}_2$ . An ultra-small Ag nanoparticle with a particle size range of 2-4 nm was uniformly distributed on the  $\text{TiO}_2$  surface. The incorporation of Ag on the  $\text{TiO}_2$  surface significantly influenced the optical properties in the region of 400–500 nm because of the surface plasmon resonance effect. The DSSC assembled with the  $\text{Ag@TiO}_2$ -modified photoanode demonstrated a better solar-to-electrical energy conversion efficiency,  $\eta$  (4.86 %) than that of bare  $\text{TiO}_2$  (2.57 %) due to the surface plasmon resonance effect. The SPR effect not only increase the number of excited electron being transferred to the current collector but also assist in trapping the light and near-field coupled with the dye molecules, hence improve the efficiency. The second part of the work was to improve the absorption to the visible

region on the  $\text{TiO}_2$  material by the integration of non-metal into  $\text{TiO}_2$ , specifically nitrogen (N), to improve the light absorption. Nitrogen has received attention due to the narrowing of band gap and shift to the visible region. Increase  $\eta$  (up to 8.15 %) was observed through the integration of Ag and N into  $\text{TiO}_2$ . The third stage of the work was to investigate the effect of co-deposition of sulphur (S) and N on  $\text{TiO}_2$  for the photovoltaic properties enhancement. The DSSC fabricated with N,S- $\text{TiO}_2$ -Ag showed an enhanced  $\eta$  of 8.22 % when compared to that of the unmodified  $\text{TiO}_2$ . The approximate 3-fold enhancement was contributed by the synergetic effects among the elements that modified the  $\text{TiO}_2$ , resulting in surface plasmon effect, reduction of band gap and effective charge transfer. The final studies sought to focus on bimetal gold (Au) and Ag modified  $\text{TiO}_2$ , which aimed to further enhance the overall efficiency by utilizing the plasmon resonance effect of Ag and Au. Finally, the greatly improved overall efficiency of 9.54% was attributed to the optimum Ag/Au ratio and uniformly dispersed Ag/Au nanoparticles on the  $\text{TiO}_2$  surface.

## ABSTRAK

Teknologi sel suria pewarna-sensitif (DSSCs) sebagai sel suria generasi yang baru atau pengganti yang berpotensi bagi sel suria konvensional sumber silikon dan filem nipis, merupakan sel suria yang cekap dan ekonomi untuk menukarkan tenaga suria kepada tenaga elektrik. Perkembangan penting teknologi bagi DSSC sejak kebelakangan ini telah menunjukkan keupayaan DSSC sebagai penjana elektrik suria yang boleh diperbaharui pada masa depan. Salah satu cabaran bagi teknologi ini adalah kecekapan sel suria yang masih jauh kurang berbanding dengan sel suria silikon. Jika kecekapan DSSC boleh diperbaiki, harga alat-alat DSSCs boleh dikurangkan dengan ketara berbanding alat-alat fotovoltai generasi pertama dan kedua. Untuk menangani masalah ini, reka-bentuk fotoanod dengan laluan pemindahan cas yang cekap dari tempat penghasilan cas ke pengumpul arus mungkin boleh menjadi salah satu cara yang berpotensi dalam meningkatkan kecekapan DSSCs. Dalam kerja penyelidikan ini, perhatian akan diberikan dalam sintesis fotoanod yang diubahsuai dengan logam kumpulan kuprum dan hubungan antara fotoanod dan kecekapan sel telah dikaji. Kerja penyelidikan akan dibahagikan kepada empat peringkat. Peringkat awal, perhatian akan diberikan kepada cara sintesis bahan hybrid Argentinum@ Titanium dioksida ( $\text{Ag@TiO}_2$ ). Proses penurunan tunggal dengan bahan kimia telah digunakan untuk mensintesis filem binari nanokomposit  $\text{Ag@TiO}_2$ . Zarah Ag yang bersize kecil, berukuran 2-4 nm telah bertaburan dengan seragam di atas permukaan  $\text{TiO}_2$ . Penambahan Ag di atas permukaan  $\text{TiO}_2$  telah mempengaruhi ciri-ciri bahagian spektrum optik dalam lingkungan 400–500 nm atas sebab resonans plasmon permukaan. DSSC yang berdasarkan  $\text{Ag@TiO}_2$  fotoanod menunjukkan kecekapan yang lebih baik dalam menukarkan tenaga suria kepada tenaga elektrik,  $\eta$  (4.86 %) berbanding dengan  $\text{TiO}_2$  (2.57 %) yang disebabkan oleh resonans plasmon permukaan. Kesan resonans

plasmon permukaan bukan hanya boleh menambahkan bilangan electron yang boleh dihantarkan ke pengumpul arus tetapi juga boleh memperangkap cahaya dan pewarna, seterusnya meningkatkan kecekapan sels. Bahagian kedua dalam penyelidikan ini adalah untuk mempertingkatkan bahagian spektrum optik bagi bahan  $\text{TiO}_2$  dengan menambahkan unsur bukan logam, khususnya Nitrogen (N). Nitrogen telah menjadi tumpuan sebagai bahan tambahan disebabkan ia dapat merapatkan jurang struktur tenaga dan anjakan ke bahagian spektrum optik. Peningkatan kecekapan  $\eta$  (8.15%) telah dicapai dengan mengintegrasikan Ag dan N ke dalam  $\text{TiO}_2$ . Pada peringkat ketiga, tumpuan akan diberikan untuk menyiasat kesan-kesan pemendapan serentak sulphur (S) dan N ke  $\text{TiO}_2$  untuk meningkatkan kemajuan ciri-ciri sel suria. DSSC yang dihasilkan daripada N,S- $\text{TiO}_2$ -Ag menunjukkan kemajuan dari segi kecekapan sel,  $\eta$  sebanyak 8.22 % berbanding dengan DSSC yang dihasilkan daripada  $\text{TiO}_2$ . Peningkatan yang hampir tiga kali ganda berbanding dengan  $\text{TiO}_2$  adalah disebabkan oleh kesan sinergis Ag, kesan resonans plasmon permukaan, pengurangan jurang struktur tenaga dan pemindahan cas yang cekap, seterusnya menambahkan hasilan arus-foto and kecekapan DSSC. Kajian pada peringkat akhir akan menumpukan kepada pengubahsuaian  $\text{TiO}_2$  dengan menggunakan dwilogam iaitu emas (Au) and Ag , dengan matlamat memanipulasikan kesan resonans plasmon permukaan daripada Au dan Ag untuk mempertingkatkan  $\eta\%$  secara keseluruhan. Akhirnya, pencapaian  $\eta$  (9.54%) yang ketara sudah dicapai atas sebab kesesuaian nisbah Ag/Au yang sesuai dan penghiasan yang bagus di atas permukaan  $\text{TiO}_2$ .

## ACKNOWLEDGEMENT

This PhD journey was indeed a truly life-changing experience for me and it would not be possible to endure it alone without the support and guidance that I have received from many people. First of all, I would like to express my unlimited appreciation and gratitude to my supervisor, Dr. Huang Nay Ming for his trust and full confidence in me throughout the whole duration of this research. Without your advice and constant feedback, I believe my PhD journey would not be so smooth. It was a great experience to be working with you.

I also would like to express my deepest thanks to Dr. Janet Lim Hong Ngee. I am most grateful for your precious time in guiding and helping me especially during the time when I was yet a PhD student. Many thanks to Dr. Alagasamy Pandikumar for the valuable advice given to me especially during the end of my research.

To my friends in the laboratory, I am grateful for having you. Without having all of you, the working atmosphere would definitely not be an enjoyable and cheerful one for me. Thanks for all the help, support and jokes from you to relief my stress especially when the road was bumpy.

Last but not least, I would like to thank my beloved parents whose have given me full support in my life. Thank you for in believing your daughter since I was young. Without your encouragement and understanding, it would not be possible for me to achieve this far in my life. Finally, special thanks to Dr. Lim Yee Seng who is always there for me anytime all this while.

## TABLE OF CONTENTS

DECLARATION.....	ii
ABSTRACT.....	iii
ABSTRAK .....	v
ACKNOWLEDGMENTS .....	vii
TABLE OF CONTENTS .....	viii
LIST OF FIGURES .....	xii
LIST OF TABLES .....	xvii
LIST OF ABBREVIATIONS .....	xviii
LIST OF SYMBOLS.....	xx
<b>CHAPTER 1 .....</b>	<b>1</b>
1.1 Types of Photovoltaic Solar Cells.....	2
<b>CHAPTER 2 .....</b>	<b>10</b>
2.1 Historical Overview .....	10
2.2 Operation Principle of DSSC .....	12
2.3 Principle and Methods of Experimental Evaluation .....	14
2.3.1 Current–Voltage (J-V) measurement .....	14
2.3.2 Electrochemical impedance spectroscopy (EIS).....	17
2.4 Materials of DSSC .....	19
2.4.1 Transparent Conducting Glass .....	20
2.4.2 Photoanode.....	22
2.4.3 Dyes .....	36
2.4.4 Electrolyte .....	41
2.4.5 Counter Electrode.....	43
2.5 Application of DSSC .....	47
2.6 Optimization of DSSC Parameters .....	49
2.6.1 Low Efficiency.....	49
2.6.2 Low Stability .....	52
<b>CHAPTER 3 .....</b>	<b>54</b>

3.1	Materials.....	54
3.2	Synthesis method .....	54
3.2.1	Preparation of N-TiO <sub>2</sub> .....	54
3.2.2	Preparation of N, S-TiO <sub>2</sub> .....	55
3.2.3	Synthesis of Ag@TiO <sub>2</sub> Nanocomposite.....	55
3.2.4	Synthesis of N-TiO <sub>2</sub> -Ag Nanocomposite .....	55
3.2.5	Synthesis of N,S- TiO <sub>2</sub> -Ag Nanocomposite .....	56
3.2.6	Synthesis of Au-Ag@TiO <sub>2</sub> Nanocomposite .....	56
3.2.7	Fabrication of TiO <sub>2</sub> based Nanocomposite Modified Photoanode.....	57
3.2.8	Fabrication of DSSCs and Evaluation of Their Performance .....	57
3.3	Characterization Techniques .....	58
3.3.1	X-ray Diffraction (XRD).....	58
3.3.2	X-ray Photoelectron Spectroscopy (XPS).....	59
3.3.3	Raman Spectroscopy .....	59
3.3.4	Ultraviolet-Visible Absorption Spectroscopy .....	59
3.3.5	Photoluminescence Spectroscopy .....	60
3.3.6	Electron Microscopy .....	60
3.4	Electrochemical Characterization .....	60
3.4.1	Photocurrent–Photovoltage (J-V) Measurement.....	61
3.4.2	Electrochemical Impedance Spectroscopy (EIS) .....	61
<b>CHAPTER 4 .....</b>		<b>62</b>
4.1	Introduction .....	62
4.2	Results and Discussion.....	64
4.2.1	Optical Properties of Ag@TiO <sub>2</sub> Nanocomposite Materials .....	64
4.2.2	Crystalline Properties of Ag@TiO <sub>2</sub> Nanocomposite Materials .....	67
4.2.3	XPS Analysis of Ag@TiO <sub>2</sub> Nanocomposite Materials .....	69
4.2.4	Morphological Studies of Ag@TiO <sub>2</sub> Nanocomposite Materials .....	70
4.2.5	Photovoltaic Performances of Ag@TiO <sub>2</sub> Plasmonic Nanocomposite-Modified Photoanode-Based DSSCs .....	72
4.2.6	Electrochemical Behaviour of Ag@TiO <sub>2</sub> Plasmonic Photoanode-Based DSSCs .....	76
4.2.7	Operation Principle of Ag@TiO <sub>2</sub> Plasmonic Photoanode-Based DSSC ..	79
4.3	Conclusion .....	80
<b>CHAPTER 5 .....</b>		<b>82</b>
5.1	Introduction .....	82
5.2	Results and Discussion.....	84
5.2.1	Morphological Studies of N-TiO <sub>2</sub> -Ag Nanocomposite.....	84

5.2.2	XPS Analysis of N-TiO <sub>2</sub> -Ag Nanocomposite.....	86
5.2.3	Crystalline Nature of N-TiO <sub>2</sub> -Ag Nanocomposite.....	87
5.2.4	Optical Properties of N-TiO <sub>2</sub> -Ag Nanocomposite .....	89
5.2.5	Photovoltaic Performance of N-TiO <sub>2</sub> -Ag-Modified Photoanode-Based DSSCs .....	92
5.2.6	Electrochemical Behavior of N-TiO <sub>2</sub> -Ag-Modified Photoanode .....	97
5.2.7	Operation Principle of N-TiO <sub>2</sub> -Ag-Modified Photoanode-Based DSSC	100
5.3	Conclusion .....	102
<b>CHAPTER 6 .....</b>		<b>103</b>
6.1	Introduction .....	103
6.2	Results and Discussion.....	105
6.2.1	Morphological Studies of N,S-TiO <sub>2</sub> @Ag Nanocomposite .....	105
6.2.2	Crystalline Studies of N,S-TiO <sub>2</sub> @Ag Nanocomposite .....	108
6.2.3	XPS Analysis of N,S-TiO <sub>2</sub> @Ag Nanocomposite .....	110
6.2.4	Optical properties of N,S-TiO <sub>2</sub> @Ag nanocomposite.....	112
6.2.5	Photovoltaic performance of N,S-TiO <sub>2</sub> @Ag photoanode-modified DSSCs .....	115
6.2.6	Influence of Ag content on photovoltaic performance of N,S-TiO <sub>2</sub> @Ag photoanode-modified DSSCs.....	118
6.2.7	Electrochemical Behavior of N,S-TiO <sub>2</sub> @Ag Photoanode-Modified DSSCs .....	121
6.2.8	Operation Principle of N,S-TiO <sub>2</sub> @Ag Photoanode-Modified DSSCs ...	124
6.3	Conclusion .....	127
<b>CHAPTER 7 .....</b>		<b>128</b>
7.1	Introduction .....	128
7.2	Results and Discussion.....	130
7.2.1	Formation of Au-Ag@TiO <sub>2</sub> Nanocomposite .....	130
7.2.2	Morphological Characterization of Au-Ag@TiO <sub>2</sub> Nanocomposite .....	131
7.2.3	Crystalline Studies of Au-Ag@TiO <sub>2</sub> Nanocomposite.....	133
7.2.4	XPS Analysis of Au-Ag@TiO <sub>2</sub> Nanocomposite.....	136
7.2.5	Optical Properties of Au-Ag@TiO <sub>2</sub> Nanocomposite .....	137
7.2.6	Photovoltaic Performance of Au-Ag@TiO <sub>2</sub> Nanocomposite Photoanode Based DSSCs .....	140
7.2.7	Electrochemical Properties of Au-Ag@TiO <sub>2</sub> Photoanode-Based DSSCs .... .....	144
7.2.8	Operation Principle of Au-Ag@TiO <sub>2</sub> Modified Photoanode-Based DSSCs .....	146
7.2.9	Conclusion .....	147

<b>CHAPTER 8 .....</b>	<b>149</b>
8.1 Summary .....	149
8.2 Recommendations for Future Works .....	152
<b>REFERENCES.....</b>	<b>155</b>
<b>LIST OF PUBLICATIONS AND PAPERS PRESENTED .....</b>	<b>169</b>

## LIST OF FIGURES

<b>Figure 2.1</b> Schematic diagram of DSSC .....	12
<b>Figure 2.2</b> Schematic diagramme of regenerative working cycle of the DSSC.....	13
<b>Figure 2.3</b> Current–voltage ( <i>J</i> - <i>V</i> ) curve of DSSC .....	15
<b>Figure 2.4</b> Power curve of DSSC .....	16
<b>Figure 2.5</b> Bode plot of DSSC .....	18
<b>Figure 2.6</b> Nyquist plot of DSSC .....	19
<b>Figure 2.7</b> Typical configuration of DSSC .....	20
<b>Figure 2.8</b> Energy level position of feasible charge transition in dye-sensitized solar cells .....	37
<b>Figure 2.9</b> Energy level position of non-feasible charge transition in dye-sensitized solar cell. ....	38
<b>Figure 2.10</b> Molecular structure of several ruthenium complexes dye (Kong et al., 2007) .....	40
<b>Figure 2.11</b> Wireless products based on DSSC.....	47
<b>Figure 2.12</b> Outdoor products based on DSSC .....	48
<b>Figure 2.13</b> DSSC fabrication for power-generating windows, room lights and solar mobile device charger .....	48
<b>Figure 2.14</b> Schematic of kinetic in DSSC (Hagfeldt et al., 2000).....	50
<b>Figure 2.15</b> Energy level, approximate redox potentials and band energies of the N719, I <sup>-</sup> /I <sub>3</sub> <sup>-</sup> and Fc/Fc <sup>+</sup> versus normal hydrogen electrode (NHE).....	51
<b>Figure 4.1</b> Schematic representation of formation of Ag on TiO <sub>2</sub> surface and (b) physical appearance of as-prepared Ag@TiO <sub>2</sub> nanocomposites with different Ag content.....	65
<b>Figure 4.2</b> (A) Absorption spectra of (a) TiO <sub>2</sub> and (b) Ag@TiO <sub>2</sub> . Plots of $(\alpha h\nu)^2$ versus $h\nu$ obtained for (B) TiO <sub>2</sub> and (C) Ag@TiO <sub>2</sub> .....	66
<b>Figure 4.3</b> (A) Photoluminescence spectra of (a) TiO <sub>2</sub> and (b) Ag@TiO <sub>2</sub> nanocomposites under 325-nm laser excitation. (B) Photoluminescence spectra of Ag@TiO <sub>2</sub> nanocomposites with different Ag contents under 325-nm laser excitation..	67
<b>Figure 4.4</b> X-ray diffraction patterns of (a) TiO <sub>2</sub> and (b) Ag@TiO <sub>2</sub> nanocomposites...	68
<b>Figure 4.5</b> Raman spectra of (a) TiO <sub>2</sub> and (b) Ag@TiO <sub>2</sub> nanocomposites with inset showing the anatase and rutile features of TiO <sub>2</sub> .....	69

<b>Figure 4.6</b> XPS spectra of TiO <sub>2</sub> and Ag@TiO <sub>2</sub> and their corresponding (a) Ti 2p (b) O 1s, and (c) Ag 3d core-level spectra.....	70
<b>Figure 4.7</b> FESEM images of (a) TiO <sub>2</sub> , (b) Ag@TiO <sub>2</sub> and (c) EDX analysis of Ag@TiO <sub>2</sub> nanocomposite.....	71
<b>Figure 4.8</b> TEM image of (a) TiO <sub>2</sub> and (b) Ag@TiO <sub>2</sub> nanocomposites, (c) SAED pattern, (d) lattice-resolved TEM image, and (e) elemental mapping of Ag@TiO <sub>2</sub> nanocomposite.....	72
<b>Figure 4.9</b> Photocurrent density–photovoltage (J–V) curves obtained for Ag@TiO <sub>2</sub> nanocomposite thin films with (a) 0, (b) 1, (c) 2.5, (d) 10, and (e) 20 wt% of Ag content under 100 mW cm <sup>–2</sup> simulated AM 1.5G solar light irradiation.....	74
<b>Figure 4.10</b> Plots of (a) Fill factor (FF) and power conversion efficiency ( $\eta$ ), (b) short-circuit current density ( $J_{sc}$ ) and open-circuit voltage ( $V_{oc}$ ) and (c) maximum photocurrent density ( $J_{max}$ ) and maximum photovoltage ( $V_{max}$ ) with different Ag content for the Ag@TiO <sub>2</sub> nanocomposites based DSSCs. ....	75
<b>Figure 4.11</b> (A) Nyquist plots and (B) Bode angle phase plots for (a) TiO <sub>2</sub> and.....	77
<b>Figure 4.12</b> Electron lifetime, electron transport time and charge collection efficiency of the TiO <sub>2</sub> and Ag@TiO <sub>2</sub> nanocomposite modified photoanode based DSSCs.....	78
<b>Figure 4.13</b> Schematic functions of Ag@TiO <sub>2</sub> nanocomposite-modified photoanode-based dye-sensitized solar cells.....	80
<b>Figure 5.1</b> FESEM images of (a) N-TiO <sub>2</sub> and (b) N-TiO <sub>2</sub> -Ag. (c) EDAX element mapping, (d and e) TEM images, (f) SAED pattern, and (h) lattice resolved TEM image of N-TiO <sub>2</sub> -Ag. ....	85
<b>Figure 5.2</b> XPS spectra of TiO <sub>2</sub> , N-TiO <sub>2</sub> , and N-TiO <sub>2</sub> -Ag and their corresponding (a).86	
<b>Figure 5.3</b> X-ray diffraction patterns of (a) ITO, (b) TiO <sub>2</sub> , (c) N-TiO <sub>2</sub> , and (d) N-TiO <sub>2</sub> -Ag.....	87
<b>Figure 5.4</b> Raman spectra of (a) TiO <sub>2</sub> , (b) N-TiO <sub>2</sub> , and (c) N-TiO <sub>2</sub> -Ag in different frequency regions: (A) 100–900 cm <sup>–1</sup> , (B) 100–200 cm <sup>–1</sup> , and (C) 180–900 cm <sup>–1</sup> , which are provided separately for better clarity of the anatase and rutile phase TiO <sub>2</sub> . ....	89
<b>Figure 5.5</b> (a) UV–visible absorption spectra of TiO <sub>2</sub> , N-TiO <sub>2</sub> , and N-TiO <sub>2</sub> -Ag. Plots of $(\alpha h\nu)^2$ versus $h\nu$ obtained for (b) TiO <sub>2</sub> , (c) N-TiO <sub>2</sub> , and (d) N-TiO <sub>2</sub> -Ag.....	91
<b>Figure 5.6</b> (A) Photoluminescence spectra of (A) TiO <sub>2</sub> , (b) N-TiO <sub>2</sub> , and (c) N-TiO <sub>2</sub> -Ag. (B) N-TiO <sub>2</sub> -Ag nanocomposite thin films with (a) 2.5, (b) 5, (c) 10, and (d) 20 wt% of Ag content. ....	92
<b>Figure 5.7</b> (A) Photocurrent density–photovoltage curves obtained for (a) TiO <sub>2</sub> ,.....	93

<b>Figure 5.8</b> Photocurrent density–photovoltage (J–V) curves obtained for N-TiO <sub>2</sub> -Ag nanocomposite photoanode-modified DSSCs with different Ag content. ....	95
<b>Figure 5.9</b> Plots of (a) fill factor (FF) and power conversion efficiency ( $\eta$ ), (b) short-circuit current density ( $J_{sc}$ ) and open-circuit voltage ( $V_{oc}$ ), and (c) maximum photocurrent density ( $J_{max}$ ) and maximum photovoltage ( $V_{max}$ ) obtained for N-TiO <sub>2</sub> -Ag-based DSSC with different Ag contents.....	96
<b>Figure 5.10</b> (A) Nyquist plot and (C) Bode phase plots obtained for N-TiO <sub>2</sub> -Ag nanocomposite-modified photoanodes with (a) 2.5, (b) 5, (c) 10, and (d) 20 wt% of Ag content. (B) Nyquist plot and (D) Bode phase plots of (a) TiO <sub>2</sub> , (b) N-TiO <sub>2</sub> , and (c) N-TiO <sub>2</sub> -Ag (10 wt% Ag).....	99
<b>Figure 5.11</b> (a) Schematic diagram and (b) charge transfer mechanism for N-TiO <sub>2</sub> -Ag photoanode-modified DSSC. ....	101
<b>Figure 6.1</b> FESEM images of (a) N,S-TiO <sub>2</sub> , (b) N,S-TiO <sub>2</sub> @Ag and (c) element mapping of N,S-TiO <sub>2</sub> @Ag nanocomposite. ....	106
<b>Figure 6.2</b> TEM images of (a) N,S-TiO <sub>2</sub> , (b) N,S-TiO <sub>2</sub> @Ag, (c) SAED pattern and (d) HRTEM image of N,S-TiO <sub>2</sub> @Ag.....	107
<b>Figure 6.3</b> XRD patterns of (a) TiO <sub>2</sub> , (b) N,S-TiO <sub>2</sub> and (c) N,S-Ti@Ag .....	108
<b>Figure 6.4</b> Raman spectra of (a) TiO <sub>2</sub> , (b) N,S-TiO <sub>2</sub> and (c) N,S-TiO <sub>2</sub> @Ag in different frequency regions. A: 100-900 cm <sup>-1</sup> , B: 100-200 cm <sup>-1</sup> and C: 180-900 cm <sup>-1</sup> separately given for better clarity of the anatase and rutile phase TiO <sub>2</sub> .....	110
<b>Figure 6.5</b> XPS spectra of TiO <sub>2</sub> , N,S-TiO <sub>2</sub> and N,S-TiO <sub>2</sub> @Ag and their corresponding (a) Ti 2p (b) O 1s (c) N 1s (d) S 2p and (e) Ag 3d core-level spectra. ....	112
<b>Figure 6.6</b> (A) UV-Visible absorption spectra of the (a) TiO <sub>2</sub> , (b) N,S-TiO <sub>2</sub> and (c) N,S-TiO <sub>2</sub> @Ag. Plots of $(ah\nu)^2$ versus $h\nu$ obtained for (B) TiO <sub>2</sub> , (C) N,S-TiO <sub>2</sub> and (D) N,S-TiO <sub>2</sub> @Ag. ....	114
<b>Figure 6.7</b> Photoluminescence spectra of (a) TiO <sub>2</sub> , (b) N,S-TiO <sub>2</sub> and (c) N,S-TiO <sub>2</sub> @Ag. ....	115
<b>Figure 6.8</b> Photocurrent density-photovoltage (J-V) curves obtained for the (a) TiO <sub>2</sub> , (b) N,S-TiO <sub>2</sub> and (c) N,S-TiO <sub>2</sub> @Ag photoanode modified DSSCs. ....	117
<b>Figure 6.9</b> Photocurrent density-photovoltage (J-V) curves obtained for the N,S-TiO <sub>2</sub> @Ag nanocomposite modified photoanodes with different Ag content. ....	119
<b>Figure 6.10</b> Plots of (a) Fill factor (FF) and power conversion efficiency ( $\eta$ ), (b) short-circuit current density ( $J_{sc}$ ) and open-circuit voltage ( $V_{oc}$ ) and (c) maximum photocurrent density ( $J_{max}$ ) and maximum photovoltage ( $V_{max}$ ) with different Ag content.....	120

<b>Figure 6.11(A)</b> Nyquist plot and <b>(C)</b> Bode phase plots obtained for N,S-TiO <sub>2</sub> @Ag nanocomposite modified photoanodes with (a) 5, (b) 10, (c) 20, and (d) 40 % of Ag content. <b>(B)</b> Nyquist plot and <b>(D)</b> Bode phase plots of (a) TiO <sub>2</sub> , (b) N/S-TiO <sub>2</sub> and (c) N,S-TiO <sub>2</sub> @Ag. ....	122
<b>Figure 6.12</b> Electron lifetime, electron transport time and charge collection efficiency of TiO <sub>2</sub> , N,S-TiO <sub>2</sub> and N,S-TiO <sub>2</sub> @Ag photoanode based DSSCs. ....	124
<b>Figure 6.13</b> Schematic on the (a) operation principles of DSSC containing N,S-TiO <sub>2</sub> @Ag photoanode and (b) photoinduced charge transfer process at the N,S-TiO <sub>2</sub> @Ag photoanode modified DSSC. ....	126
<b>Figure 7.1</b> Physical appearance of as-prepared Au@Ag/TiO <sub>2</sub> nanocomposites with different composition of Au:Ag ratio. ....	130
<b>Figure 7.2</b> FESEM image of TiO <sub>2</sub> , <b>(b)</b> Back-scattered electron image of Au@Ag/TiO <sub>2</sub> and <b>(c)</b> element mapping of Au@Ag/TiO <sub>2</sub> nanocomposite. ....	132
<b>Figure 7.3</b> TEM images of (a) Ag@TiO <sub>2</sub> , (b) Au@TiO <sub>2</sub> , (c) Au@Ag/TiO <sub>2</sub> (Au <sub>75</sub> :Ag <sub>25</sub> ) and (d) SAED pattern of Au@Ag/TiO <sub>2</sub> . ....	133
<b>Figure 7.4</b> XRD patterns of Au-Ag@TiO <sub>2</sub> nanocomposite with different composition of Au-Ag. ....	134
<b>Figure 7.5</b> Raman spectra of Au-Ag@TiO <sub>2</sub> nanocomposite with different composition of Au-Ag. ....	135
<b>Figure 7.6</b> XPS spectra of Au-Ag@TiO <sub>2</sub> nanocomposite with Au <sub>75</sub> -Ag <sub>25</sub> and their corresponding core-level spectra of (a) Ti 2p (b) O 1s (c) Au 4s and (d) Ag 3d. ....	137
<b>Figure 7.7</b> (a) UV-Visible absorption spectra of the Au-Ag@TiO <sub>2</sub> nanocomposite with different composition of Au-Ag and (b) the corresponding plot of SPR band ( $\lambda_{\max}$ ) vs. Au-Ag composition present in the nanocomposite. (c) Plots of $(\alpha h\nu)^2$ vs. $h\nu$ obtained for Au-Ag@TiO <sub>2</sub> nanocomposite with different composition of Au-Ag. ....	140
<b>Figure 7.8</b> Photoluminescence spectra of Au-Ag@TiO <sub>2</sub> nanocomposite with different composition of Au-Ag. ....	141
<b>Figure 7.9</b> Photocurrent density-photovoltage (J-V) curves obtained for the Au-Ag@TiO <sub>2</sub> nanocomposite modified photoanode contains different composition of Au-Ag based DSSCs sensitized with N719 dye under simulated AM 1.5 G solar irradiation of 100 mW/cm <sup>2</sup> . ....	143
<b>Figure 7.10</b> Plots of (a) Fill factor (FF) and power conversion efficiency ( $\eta$ ), (b) short-circuit current density ( $J_{sc}$ ) and open-circuit voltage ( $V_{oc}$ ) and (c) maximum photocurrent density ( $J_{max}$ ) and maximum photovoltage ( $V_{max}$ ) obtained for the Au-Ag/TiO <sub>2</sub> nanocomposite modified photoanode with different composition of Au-Ag. ....	144

<b>Figure 7.11</b> Nyquist plot and (b) Bode phase plots obtained for Au-Ag/TiO <sub>2</sub> nanocomposite modified photoanodes with different composition of Au-Ag.....	147
<b>Figure 7.12</b> Schematic functions of Au-Ag/TiO <sub>2</sub> nanocomposite-modified photoanode-based dye-sensitized solar cells.....	148

## LIST OF TABLES

<b>Table 2.1</b> Summary of noble metal modified TiO <sub>2</sub> photoanode for DSSC.....	24
<b>Table 3.1</b> Chemical and materials used in this thesis.....	54
<b>Table 4.1</b> Photovoltaic parameters of Ag@TiO <sub>2</sub> nanocomposite-modified photoanode-based DSSCs with different Ag contents. ....	74
<b>Table 4.2</b> Electrochemical parameters of TiO <sub>2</sub> and Ag@TiO <sub>2</sub> nanocomposite-based DSSCs. ....	78
<b>Table 5.1</b> Photovoltaic parameters of fabricated DSSCs with controlled configurations. ....	93
<b>Table 5.2</b> Photovoltaic parameters of N-TiO <sub>2</sub> -Ag nanocomposite photoanode-modified DSSCs with different Ag content.....	95
<b>Table 5.3</b> EIS analysis results for fabricated DSSC with controlled configurations.....	99
<b>Table 6.1</b> Photovoltaic parameters of the fabricated DSSCs with controlled configurations.....	117
<b>Table 6.2</b> Photovoltaic parameters of the N,S-TiO <sub>2</sub> @Ag photoanode with various Ag content.....	119
<b>Table 6.3</b> EIS analysis results of the fabricated DSSC. ....	123
<b>Table 7.1</b> Photovoltaic parameters of the fabricated DSSCs with Au-Ag@TiO <sub>2</sub> nanocomposite modified photoanodes.....	144
<b>Table 8.1</b> Summary of the DSSC performance and the optimization techniques carried in this research work. ....	152

## LIST OF ABBREVIATIONS

Al <sub>2</sub> O <sub>3</sub>	Aluminium oxide
Ag	Silver
Au	Gold
AgNO <sub>3</sub>	Silver Nitrate
AZO	Aluminium-doped zinc oxide
CaO	Calcium oxide
DSSC	Dye-sensitized solar cell
EIS	Electrical impedance spectroscopy
Eqn	Equation
FESEM	Field emission scanning electron microscopy
FTO	Flourine-doped tin oxide
Ge	Germanium
HAuCl <sub>4</sub> .3H <sub>2</sub> O	Hydrogen tetrachloroaurate trihydrate
HOMO	Highest occupied molecular orbital
hr	Hour
I <sup>-</sup>	Iodide
I <sub>3</sub> <sup>-</sup>	Triiodide
ITO	Indium-doped tin oxide
LUMO	Lowest unoccupied molecular orbital
MgO	Magnesium oxide
N	Nitrogen
NaBH <sub>4</sub>	Sodium borohydride
N719	Di-tetrabutylammonium cis-bis(isothiocyanato)bis(2,2'-bipyridyl-4,4'-dicarboxylato)ruthenium(II)
Nb <sub>2</sub> O <sub>5</sub>	Niobium pentoxide
P25	Commercial TiO <sub>2</sub>
PEN	Polyethylene naphtalate
PES	Polyether sulfone
PET	Polyethylene terephthalate
PL	Photoluminescence
Pt	Platinum
SAED	Selected area electron diffraction

S	Sulfur
Si	Silicon
SnO <sub>2</sub>	Tin oxide
SPR	Surface plasmonic resonance
TCO	Transparent conducting layer
TEM	Transmission electron microscopy
TTIP	Titanium isopropoxide
TiO <sub>2</sub>	Titanium dioxide
UV-vis	UV-vis spectrophotometer
XRD	X-ray diffraction
XPS	X-ray photoelectron spectroscopy
ZnO	Zinc oxide

## LIST OF SYMBOLS

$E_{bg}$	band-gap energy
$FF$	Fill Factor
$h$	Planck's constant
Hz	Hertz
$J_m$	Current density at maximum power output
$J_{sc}$	Short circuit photocurrent
J-V	Current density-voltage
$^{\circ}\text{C}$	degree celcius
$P_m$	Maximum power output
$\eta$	Energy conversion efficiency
$R_s$	Internal transfer resistance
$R_{ct}$	Charge transfer resistance
$V_{oc}$	Open circuit photovoltage
$V_m$	Voltage at maximum power output
$\nu$	Photon frequency
wt. %	Weight percentage
$Z'$	Real impedance
$Z''$	Imaginary impedance

## **CHAPTER 1**

### **INTRODUCTION**

Energy plays the most essential role in our lives, making it impossible to sustain without it. Modern technologies have developed to such an extent that everything we use nowadays requires energy for operation. Based on the recent energy demand trends and the current consumption rate, global energy depletion will become more inevitable. Moreover, the steady growth of human population, as well as the significant improvement in the living quality, leads to an increase energy consumption that will soon exceed the production capacity; the world energy is facing unprecedented uncertainty.

The World International Energy reported that the world primary energy is expected to increase 40% from the year 2007-2030 (Biro1, 2013); one driving factor for such growth is due to the developing Asian countries. Malaysia is a fast developing country and, is expected to consume energy exponentially to meet the growing demand of the nation. The excessive use of fossil fuel and coal diminishes the natural reserves of energy and brings upon massive global warming.

Fortunately, renewable energy resources, such as wind, hydro and solar energies are capable in meeting the growing energy demand and avoiding resource exhaustion, and can help alleviate the global warming issue while providing other important benefits. The solar energy, with its unlimited quantity, free availability and direct supply to our homes, is therefore very attractive and promising alternative energy sources. Devices with low manufacturing cost and high efficiency are therefore a necessity for the light to energy conversion. Recently, solar is a steadily growing energy

technology and solar cells have found markets in a variety of applications ranging from consumer electronics and small scale distributed power systems to centralized megawatt scale power plants.

As a solution, solar energy serves as a key ingredient for the development of a globally sustainable society. While silicon-based technologies have been developed to harness solar energy, regrettably, they are not yet competitive with the fossil fuels due to the high production costs. Hence, it is an urgent task to develop much cheaper photovoltaic technology. In this context, dye sensitized solar cells (DSSCs) have emerged as promising candidates for harnessing solar power, owing to its low cost, flexibility, ease of production, relatively high energy conversion efficiency, and low toxicity to the environment (O'Regan et al., 1991). After its introduction by Gratzel and co-workers in 1991, many strategies have been employed to achieve high-performance DSSCs, including novel counter electrodes, electrolytes, dyes, and semiconductor photoanode materials. Apparently, a further improvement on DSSC is key factor to accelerating the industrialization of DSSC.

## **1.1 Types of Photovoltaic Solar Cells**

Based on the nature of the material, maximum conversion efficiency obtainable, and the associated cost of the photovoltaic power, Martin Green has grouped various photovoltaic solar cells into three main categories (Kalyanasundaram, 2010). First generation photovoltaic uses the highest purity materials with the least structural defects. The most popular approach is based on silicon (Si) or germanium (Ge) that are doped with phosphorus and boron in pn-junction and it is first demonstrated at Bells Labs in 1954 by Chaplin, Fuller and Pearson (Chapin et al., 1954). Silicon based solar cells is dominating the commercial market and are breaking down into four categories;

single crystal, polycrystalline, amorphous and hybrid silicon cells. Due to the high-energy requirements involved in purifying silicon, the cost of high purity silicon is significantly more than the power output. There are, however, niches for each type of structure. For instance, low-power cheap consumer electronic devices employ amorphous silicon cells while the space industry uses high-grade single crystal cells. The less efficient polycrystalline silicon cells are also used because of its cheaper manufacturing costs. The highest power conversion efficiencies obtained to date are in the first generation photovoltaics. In addition to the single component Si and layered semiconductors, binary semiconductors of II-IV and III-IV have been examined.

Second generation photovoltaic devices appeared in the 1970's (Birkmire et al., 1997) and are based on low-energy, intensive preparation techniques such as vapour deposition and electroplating. Second-generation solar cells are usually called thin film solar cells because when compared to crystalline silicon based cells they are made from layers of semiconductor materials with few micrometres thickness. There are basically three types of solar cells such as amorphous Si, copper indium gallium diselenide (CIGS) (Kazmerski et al., 1976) and cadmium telluride (CdTe) (Cusano, 1963) both coupled with n-type cadmium selenide (CdS) to create pn-heterojunction. Due to the large bandgap of CdS (2.4eV), it is utilized as a window to the pn-junction. As direct band-gap semiconductor, a thin film ( $\sim 10\mu\text{m}$ ) is required for complete light absorption, unlike the first generation of silicon cells ( $\sim 100\mu\text{m}$ ). Since the second generation solar cells avoid the use of silicon wafers and have a lower material consumption, the production cost have been reduced compared to the first generation solar cells. However, as the production of second generation solar cells still includes vacuum processes and high temperature treatments, there is still a large energy consumption

associated during the production of these solar cells. Furthermore, the second generation solar cells are based on scarce elements and this is a limiting factor in terms of cost.

Generally, all photovoltaic systems that can potentially give power conversion efficiency above the 31% Shockley and Queisser limit are classified as third generation photovoltaic devices. This can be achieved by concentrating the light source (King et al., 2007), use of tandem cells with multiple bandgaps (Lantratov et al., 2007) or conversion of photons (Luque et al., 2007), where more than one electron hole pair is generated per photon. However, these system involve complicated preparation and high cost. Low cost solar cells have been the subject of intensive research work for the last three decades. Therefore, there are also third generation cheaper alternatives. They can be divided into categories following the organic heterojunctions (Benanti et al., 2006) and dye-sensitized solar cells(DSSCs) (O'Regan et al., 1991). However, DSSCs emerged as a new class of low cost energy conversion devices, which can be fabricated using simple manufacturing procedures.

The DSSCs based on titanium dioxide ( $\text{TiO}_2$ ) was first developed by Professor O'Regan and Gratzel in 1991 (O'Regan et al., 1991). A fundamental difference of DSSCs compared with conventional silicon systems is that light absorption (the photosensitizer dye) is separated from the charge carrier transport (the semiconductor). This type of solar cells is featured by their relatively high efficiency (exceeding 11% at full sunlight), which is comparable to that of amorphous Si, making it an attractive solution for low cost manufacturing (1/10-1/5 of silicon solar cells) (Tepavcevic et al., 2009). Since the invention of DSSCs, great efforts have been devoted to making these devices more efficient and stable. Extensive researches have been conducted and plenty of reviews have been reported concerning the operation and improvement of the

efficiency of these particular cells (Asim et al., 2012; Lenzmann et al., 2007; Rokesh et al., 2014; Smestad et al., 1994). Currently, the maximum reported efficiency is 13 % using novel proquinoidal benzothiadiazole incorporation porphyrin based dye and cobalt(II/III) redox electrolyte (Mathew et al., 2014). However, the typical efficiency is still less than half that of a single-crystal silicon cell. If the efficiency of DSSCs can be improved, the cost of these devices could significantly be reduced compared to first and second photovoltaic devices.

The unique characteristic of DSSC is that the photogeneration and electron transport happen in different materials. The photons from the light will generate the electron and hole in the dye, in which the injected electron will be transported through the conduction band of  $\text{TiO}_2$  and transparent conducting oxide layer of the glass substrate, and finally through an external load to the counter-electrode to provide the electricity output. Therefore, holes are not produced in the  $\text{TiO}_2$ 's valence band, dismissing direct charge-recombination within the semiconductor. However, the DSSC suffers from possible recombination at the  $\text{TiO}_2$ /dye/electrolyte interface. Therefore, studies aimed to improve the conversion efficiency of DSSC are highly desirable.

To date, modifications of  $\text{TiO}_2$  for improvement of efficiency have been mainly reported on the following few aspects:

1. To prevent the back electron transfer reaction of the photoinjected electrons from transparent conducting oxide (TCO) layer to the electrolyte. Other than the charge recombination, back reaction in DSSC is also another major problem for the low efficiency (Bach et al., 1998; Cameron et al., 2004). This will cause the percolation of redox electrolyte on the TCO surface that permits direct electrochemical reduction of  $\text{I}_3^-$

( $I_3^- + 2e^- \rightarrow 3I^-$ ), leading to the consumption of the photogenerated electron. Hence, attempts also have been made by introduction of a blocking layer (compact layer between TCO and photoanode) to prevent electron leakage, and increase the overall efficiency of the device. The use of a blocking layer has been shown to increase the solar cell's efficiency (Haque et al., 2005; Li et al., 2013).

2. Suppression of the recombination process at the  $TiO_2$ / dye/ electrolyte interfaces. The most common approach is to prevent the excited electron from recombining with the hole in the oxidized dye and iodine by addition of another metal oxide with a different band structure between the dye and  $TiO_2$  film. These semiconductors including  $SnO_2$  (Desai et al., 2013; Pang et al., 2014),  $Al_2O_3$  (Kim et al., 2009; Xuhui et al., 2014),  $ZnO$  (Chandiran et al., 2014; Xu et al., 2012),  $CaO$  (Xuhui et al., 2014; Zheng et al., 2012) and  $MgO$  (Li et al., 2010; Xuhui et al., 2014) are reported to effectively prevent the electrons from recombining with the holes, hence the dark current is hampered.

3. Improvement of light absorption in the visible region. Dyes have been used so far. Another promising alternative is the modification of semiconductor with noble metal. In the present decade,  $TiO_2$  has been modified with noble metal nanoparticles such as gold (Au) (Du et al., 2012; Jang et al., 2014; Muduli et al., 2012), silver (Ag) and platinum (Pt), with the aim of improving the efficiency of a DSSC. Modification of  $TiO_2$  with noble metal nanoparticles possesses two prominent features in the DSSC performance including a Schottky junction and localized surface plasmonic resonance (LSPR). The former is beneficial for charge separation and transfer (Lee et al., 2008; Mock et al., 2002; Schaadt et al., 2005; Wen et al., 2000; Zhao et al., 1997) whereas the latter contributes to the strong absorption of the visible light (Mock et al., 2002; Schaadt et al., 2005; Zhao et al., 1997).

## **1.2 Scope of Research**

The focus of the research reported in this present thesis is based on the above mentioned techniques to improve the efficiency of DSSC by enhancing the photon to electron conversion in the visible region with the incorporation of noble-metal nanoparticles into  $\text{TiO}_2$ . The driving question behind this doctoral work is to prepare  $\text{TiO}_2$  based materials for photoanode through simple and cost-effective methodologies. As energy conversion efficiency of devices is the key parameter to evaluate the performance of these newly prepared materials, efforts have been placed on the optimization of metal amount such as Ag and Au on  $\text{TiO}_2$  to enhance the device performance. There is also an effort to understand the relationship between as-prepared materials and corresponding device performance, which could provide guidelines for DSSC design in the future.

## **1.3 Research Objectives**

- (1) To develop a facile and cost-effective method for the preparation of  $\text{TiO}_2$  based nanocomposite as a photoanode for DSSC. The structure and basic properties of the synthesized nanocomposites were characterized using X-ray diffraction (XRD), field emission scanning electron microscopy (FESEM), transmission electron microscopy (TEM), selected area electron diffraction (SAED), X-ray photoelectron spectroscopy (XPS), UV-vis spectrophotometer, photoluminescence spectra and Raman spectra.
- (2) To investigate and evaluate the photovoltaic properties of the as-prepared  $\text{TiO}_2$  based nanocomposite materials for DSSC.

(3) To optimize the parameter that affects the device performance such as amount of metal loading. It should be carefully controlled to achieve the best conversion efficiency.

(4) Understanding the relationship between new materials and the device performance. This is achieved by correlation of the device performance with the charge transport and recombination process through electrical impedance spectroscopy (EIS).

#### **1.4 Outline of Thesis**

Chapter 1 begins with the history of the solar cell followed by a brief discussion on types of solar cells. Then the scopes of the research are highlighted and ended with the objectives of this thesis.

Chapter 2 serves to provide a comprehensive literature review on the background and working principles of DSSC. This chapter also discussed a thorough literature review on components, remaining challenges for DSSC and possible application for DSSC.

Chapter 3 presents the research strategy of synthesizing  $\text{TiO}_2$  based nanocomposite via chemical reduction method and its characterization techniques. Instrumental analysis, including x-ray photoelectron spectroscopy (XPS), x-ray diffraction (XRD), UV-vis absorption spectroscopy, field-emission scanning electron microscopy (FESEM), transmission electron microscopy (TEM), Raman and photoluminescence spectroscopy.

Chapter 4 discusses the preparation, characterization and DSSC performance based on silver@titania ( $\text{Ag@TiO}_2$ ) nanocomposite with an emphasis on the relationship of the

Ag content on the DSSC performance. The addition of Ag for the improvement of DSSC was discussed.

Chapter 5 demonstrates the preparation, characterization and photovoltaic performance of nitrogen-titania-silver (N-TiO<sub>2</sub>-Ag) nanocomposite as a promising photoanode for DSSC. The presence of N successfully reduced the band gap and helped to shift the optical absorbance toward the visible region. Furthermore, the synergetic effects of the Ag nanoparticles, surface plasmon resonance effect, reduction in the band gap, and effective charge transfer improved the photocurrent generation and conversion efficiency of DSSCs.

Chapter 6 reports the experimental setup of preparation and characterization of nitrogen,sulfur–titania@silver (N,S-TiO<sub>2</sub>@Ag). The relationship of the Ag content on N,S-TiO<sub>2</sub> with respect to the DSSC performance was investigated. The addition of the N and S successfully reduced the band gap and helped to shift the optical absorbance towards the visible region and also suppressed the charge recombination.

Chapter 7 focuses on the development of high efficiency DSSC. The efficiency of the DSSC is improved through the incorporation of Au and Ag by controlling the Au:Ag wt.% ratio. It presented gold@silver/titania (Au@Ag/TiO<sub>2</sub>) as an efficient photoanode for DSSC.

Chapter 8 summarizes the whole doctoral works that have been presented in this thesis. Possible future works in DSSC efficiency enhancement are proposed at the end of this chapter.

## CHAPTER 2

### LITERATURE REVIEW

#### 2.1 Historical Overview

The discovery of the dye-sensitization dated back to the 19<sup>th</sup> century; arose when photography was invented. Becquerel laid the foundations of the field of photoelectrochemistry way back in 1839 with his observation of measurable current passing between two platinum electrodes in the presence of sunlight when the electrodes are immersed in an electrolyte containing metal halide salts (Becquerel, 1839). The work of Vogel in Berlin after 1873 can be considered the first significant study of dye-sensitization of semiconductor, where the silver halide emulsions were sensitized by dyes to produce black and white photographic films (McEvoy et al., 1994). In 1887, Dr. Moser in Vienna University reported that the dye sensitized photoelectric effect using a similar chemistry (Grätzel et al., 2001). In the 1960s, the first experiment was carried out using single crystal semiconductor electrodes immersed into dye solution (Gerischer, 1969). In subsequent years, the idea developed that dye could function most efficiently if chemisorbed on the surface of the semiconductor (Hamnett et al., 1979; Tsubomura et al., 1976). Tsubomura *et.al* reported ZnO material that used iodide/triiodide redox system manifested high conversion efficiency (Tsubomura et al., 1976). The concept of using dispersed particles to provide sufficient interface for interaction had also emerged (Duonghond et al., 1984), followed by the use of phototelectode (Desilvestro et al., 1985). The main reason for the low conversion efficiency at that stage was due to a limited amount of dye that could be absorbed on the surface of semiconductor with the narrow spectral absorption range.

The use of dye-sensitization in photovoltaics remained, however, rather unsuccessful until a breakthrough at the early 1990's by Gratzel group. Professor

Gratzel and his co-worker developed a combination of nanostructured electrodes and efficient charge injection dyes with the energy conversion efficiency exceeding 7% in 1991 (O'Regan et al., 1991) and 10% in 1993 (Nazeeruddin et al., 1993). Improvement to this was achieved, thanks to nanotechnology and development of better dyes. This solar cell is called the dye-sensitized nanostructured solar cell or Gratzel cell after its inventor.

In contrast to the all-solid conventional semiconductor solar cells, the dye-sensitized solar cell is a photoelectrochemical solar cell. It uses a liquid electrolyte, polymer electrolyte and ion-conducting phase as a charge transport medium. Electricity is generated on the photoelectrode, which is a nanoporous  $\text{TiO}_2$  or  $\text{ZnO}$  film sensitized with a monolayer of visible light absorbing dye and penetrated with a redox electrolyte. The opposite substrate will be counter electrode and will sandwich together with the photoelectrode to complete the circuit. Thus, the DSSC resembles more electrochemical cell than a conventional semiconductor solar cell. Due to the high efficiencies obtained for dye-sensitized solar cells, the research interest in this technology grew rapidly since the 1990's.

## 2.2 Operation Principle of DSSC

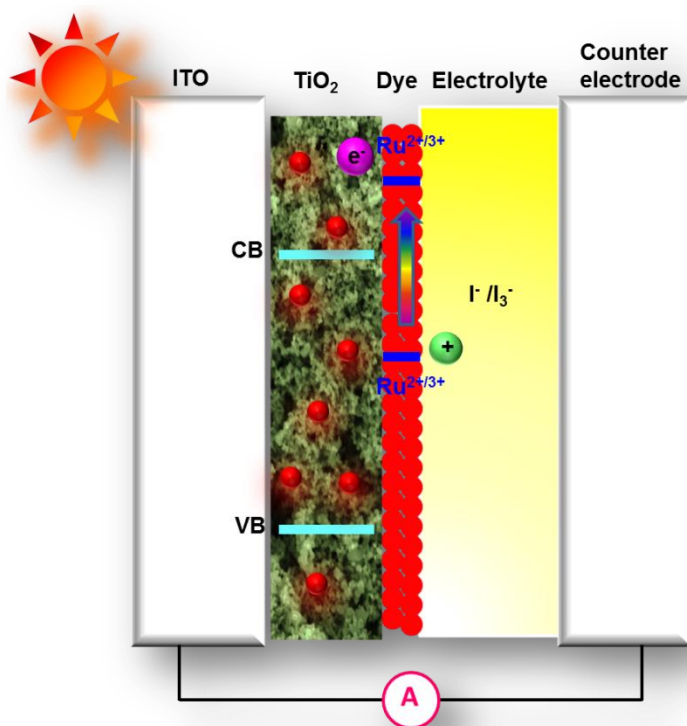


**Figure 2.1** Schematic diagram of DSSC

The simplest and typical dye-sensitized solar cell has a sandwich configuration. It includes a working electrode, dye, redox mediator and a counter electrode. The typical structure of a DSSC with liquid electrolyte is shown in **Figure 2.1**. Light will pass through the transparent conducting glass electrode, which acts as current collector and then to the working electrode, which is coated on the transparent conducting glass, to allow electronic conduction. The nanoparticle material including  $\text{TiO}_2$ ,  $\text{ZnO}$  and  $\text{Nb}_2\text{O}_5$  have been investigated as working electrode. Dye molecules attached to the surface of the working electrode whereas, an electrolyte comprises a reduction-oxidation couple such as  $\text{I}^-/\text{I}_3^-$ . At the opposite side, there is a counter electrode, consisting of a thin layer of catalyst and another piece of conducting glass to complete the circuit. During the illumination, the cell produces voltage and current through an external load to the electrodes.

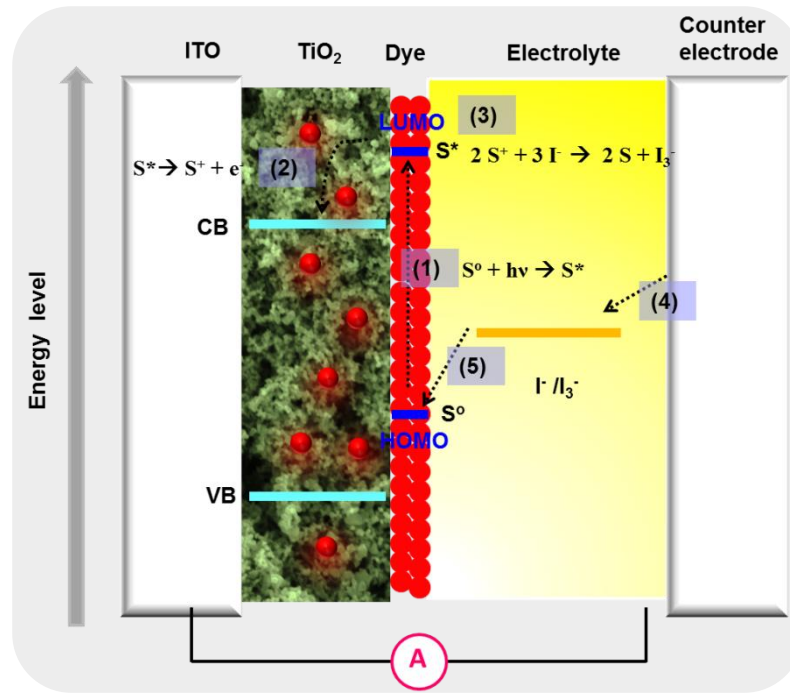
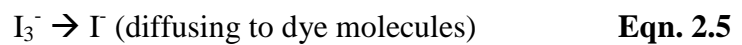
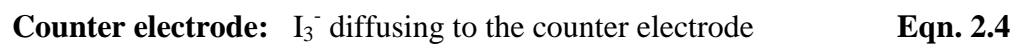


**Figure 2.2** Schematic diagramme of regenerative working cycle of the DSSC

The operating cycle can be summarized in five steps of chemical reaction below (Matthews et al., 1996) :



The regenerative working cycle of DSSC is shown in **Figure 2.2**. Under the irradiation of sunlight, the incoming photon is absorbed by the dye molecule adsorbed on the surface on the  $TiO_2$  particles and an electron from a molecular ground state ( $S^0$ ) is excited to a higher excited state ( $S^*$ ) (Eqn. 2.1). The excited electron ( $e^-$ ) is injected to the conduction band of  $TiO_2$  particle, leaving the dye molecule to an oxidized state ( $S^+$ ) (Eqn. 2.2). The injected electron transports through the  $TiO_2$  then to the transparent conducting oxide layer of the glass substrate (negative electrode/anode) and finally

through an external load to the counter-electrode (positive electrode/cathode) to contribute the electricity output. The cycle is complete when the oxidized dye ( $S^+$ ) is reduced to the ground state ( $S^0$ ) by accepting the electrons from iodide in the electrolyte (Eqn. 2.3). After reducing the oxidized dye, iodide ( $I^-$ ) will oxidize to triiodide ( $I_3^-$ ) and diffuse to the counter electrode, caused by the concentration gradient (Eqn. 2.4). Finally, the electron is transferred to triiodide ( $I_3^-$ ) to be reduced to iodide ( $I^-$ ). Iodide ( $I^-$ ) will diffuse back to the solid-liquid interface, and thus forms a continuous loop between the working electrode and counter electrode (Eqn. 2.5).

## 2.3 Principle and Methods of Experimental Evaluation

During the course of development, design of DSSC and measurement of photovoltaic properties of device are essential to evaluate the performance and applicability of the material. Generally, a few basic characterization techniques of DSSCs include using (1) photocurrent-photovoltage (J-V) measurement and (2) electrochemical impedance spectroscopy (EIS).

### 2.3.1 Current–Voltage (J-V) measurement

Current-voltage curve measurements are the most fundamental way to characterize the photovoltaic performance of DSSC. The photocurrent-photovoltage measurement of a DSSC is performed using an electrochemical workstation under the illumination of solar light. A typical J-V curve is shown in **Figure 2.3**. J-V curve is a useful technique as a quick screening procedure to identify potential working electrode material. In these measurements, the device is placed under a reserve bias voltage scan and the generated photocurrent is recorded.

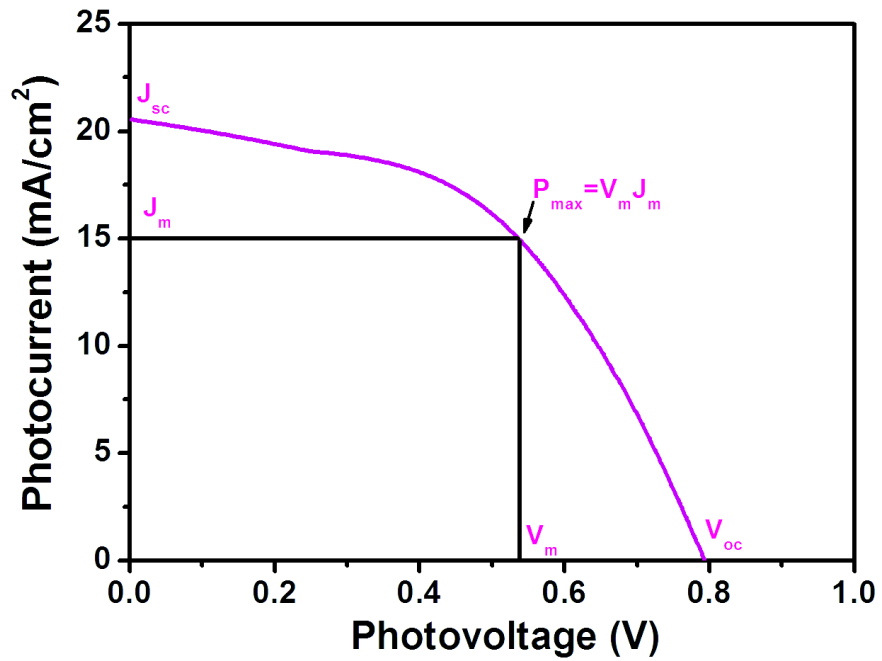


**Figure 2.3** Current–voltage ( $J$ - $V$ ) curve of DSSC

The overall conversion efficiency of the dye-sensitized solar cell is determined by the photocurrent density measured at the following four parameters:

**(1) Short circuit photocurrent ( $J_{sc}$ )**

The short circuit photocurrent ( $J_{sc}$ ) is the cell photocurrent measured at the point where the external bias voltage is zero, when there is no opposing force to the current flow from the cell and the maximum current the cell is able to generate. Generally, it is presented in the form of the short circuit current density ( $J_{sc}$ ) defined as the ratio of the short circuit photocurrent to the active cell area.

**(2) Open circuit photovoltage ( $V_{oc}$ )**

The open circuit photovoltage ( $V_{oc}$ ) is the cell voltage measured when the current within the cell is equal to zero.

### (3) Fill Factor ( $FF$ )

The fill factor measures the “squareness” of the curve. For instance, a resistive loss in the cell is shown directly from the shape of the  $J$ - $V$  curve, making it “flatter” and decreasing the fill factor.  $FF$  is defined as the ratio of maximum power output ( $P_m$ ) to the product of short circuit current and open circuit voltage:

$$FF = \frac{V_m \times J_m}{V_{oc} \times J_{oc}} \quad \text{Eqn. 2.6}$$

where  $V_m$  and  $J_m$  are the voltage and current density, respectively, at maximum power output, respectively.

#### Maximum Power Output ( $P_m$ ) Curve

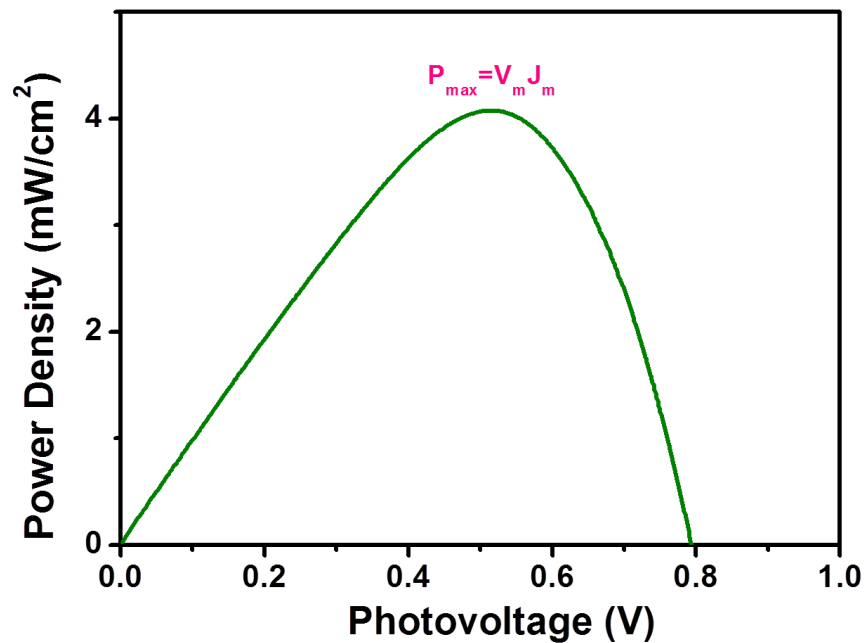


Figure 2.4 Power curve of DSSC

Maximum power output ( $P_m$ ) is the product of the short circuit photocurrent and open circuit photovoltage. The resultant values are then plotted vs the original photovoltage

and will give a curve in **Figure 2.4** and the maximum power is extracted. From the maximum power value,  $V_m$  and  $J_m$  can be obtained.

#### (4) Energy conversion efficiency ( $\eta$ )

The cell's overall energy conversion efficiency ( $\eta$ ) is estimated as follows:

$$\eta = \frac{V_{oc} \times J_{sc} \times FF}{I_s} \quad \text{Eqn. 2.7}$$

where  $I_s$  is the intensity of the incident light.

### 2.3.2 Electrochemical impedance spectroscopy (EIS)

The J-V is a useful tool to characterize and measure the photovoltaic behaviour of the working electrode material. In addition to this technique, the response function of alternating current (AC) generated in response to alternating voltage (AV), is a great technique in characterizing the interfacial charge transfer process of an electrode. In EIS, a small amplitude AC voltage signal which frequency is varied over a certain range is set over the cell and the resulting AC current signal recorded. The resultant current is monitored over a pre-determined frequency range and the impedance at each of the frequencies is calculated.

EIS technique has been widely employed to study the electrochemical system occurring in DSSC. It can accurately measure error-free kinetic and mechanistic information using a variety of techniques and output formats. The method is especially valuable because it enables the internal transfer resistance ( $R_s$ ) of the electrode materials, and charge transfer resistance ( $R_{ct}$ ) of the system to be separately evaluated.

Generally, EIS is conducted by applying small amplitude of alternative potential (5 ~ 10 mV) in a range of frequency (generally 100 kHz to 10 mHz). The small amplitude used is to ensure minimal perturbation of the electrochemical test system, reducing errors caused by the measurement technique. The evaluation of the phase relation between  $Z'$  and  $Z''$  impedances can be achieved by plotting the Nyquist (complex-plane or Cole-Cole) plot. From this plot, important circuit elements of the electrode structure, including  $R_s$  and  $R_{ct}$  can be determined. The impedance data can also be presented as a Bode plot. In the Bode plot, the real and imaginary parts of the impedance are shown as a function of frequency (**Figure 2.5**).

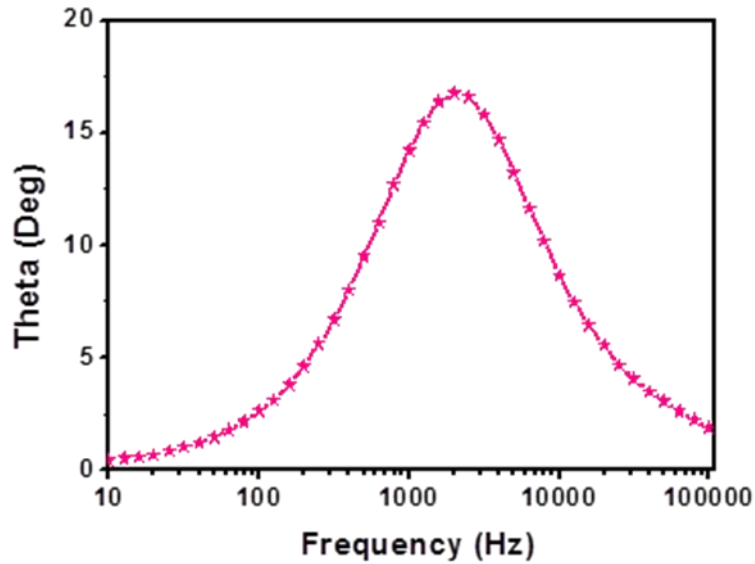


**Figure 2.5** Bode plot of DSSC

**Figure 2.6** shows the Nyquist plot for DSSC. In general, the EIS spectrum of the DSSC containing liquid electrolyte shows three semicircles in the measured frequency range of 0.01 Hz-100 kHz (Hoshikawa et al., 2006; Hoshikawa et al., 2005). The first semicircle from the left represents the charge transfer resistance at the counter electrode/electrolyte interface, usually in the  $10^3$ - $10^5$  region and the second large semicircle in the medium frequency region ( $1$ - $10^3$ ) represents the charge transfer

resistances throughout the semiconductor and at the semiconductor/dye/electrolyte interfaces. The third semicircle (0.1-1 Hz), which is the finite-warburg impedance represent the triiodide mass transport (Kern et al., 2002; Wang et al., 2005). The electron lifetimes in the semiconductor can be calculated from the Bode plot by extracting the peak frequency of the 2<sup>nd</sup> semicircle. However, in some of the cases, only one or two semicircle is presence. For example, sometimes the first semicircle is not clearly observed but overlapped with the second semicircle, which implies that the counter electrode exhibited a good redox ability in the devices (Chen et al., 2013; Longo et al., 2002). In the phenomenon where only one semicircle is present, it indicates that single phase of electrolyte is used and there is diffusion ability of the  $I_3^-/I^-$  in the electrolyte (Longo et al., 2002).

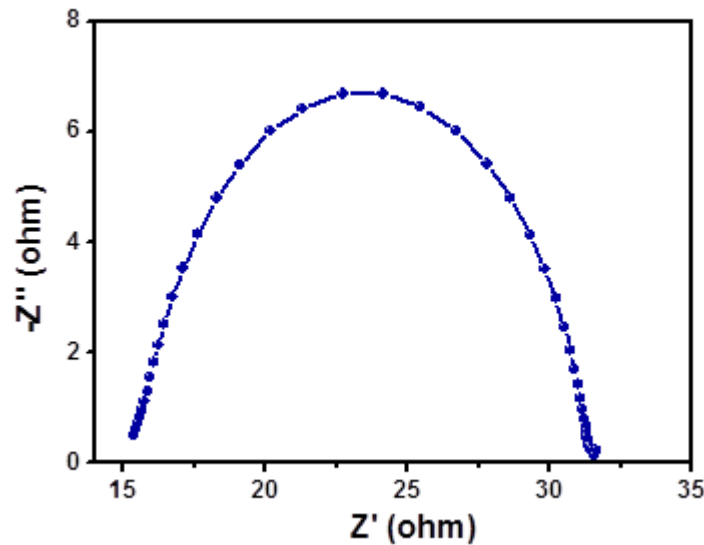


**Figure 2.6** Nyquist plot of DSSC

## 2.4 Materials of DSSC

In general, the DSSC design involves a set of different layers of components stacked in serial; transparent conducting layer, photoanode, dyes, electrolyte and counter electrode and the final assembly. The typical configuration is shown in **Figure. 2.7**.

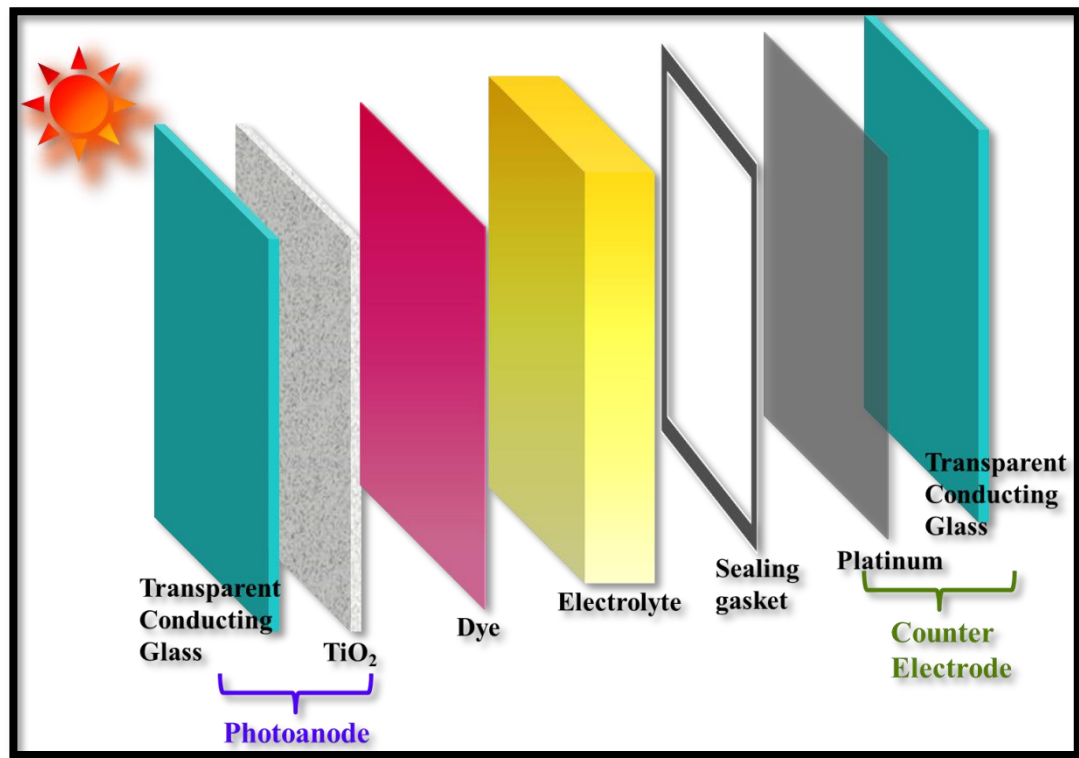


**Figure 2.7** Typical configuration of DSSC

#### 2.4.1 Transparent Conducting Glass

Requirements for a good transparent conducting layer (TCO) for DSSC are high transparency, ability to prevent impurities such as water and oxygen from entering into the cell, low resistance and high concentration of free electrons in the conduction band. This layer is crucial since it allows sunlight penetrating into the cell to excite the conducting electron carriers to the outer circuit. The traditional approach is to build the DSSC on the TCO coated glass sheets. The most often used TCOs include F-doped or In-doped tin oxide (FTO or ITO) (Grätzel, 2009; Yoshimura et al., 1999) and aluminium-doped zinc oxide (AZO). ITO performs the best among all the TCO substrates. Whilst ITO is an effective barrier towards water and oxygen penetration into cell, the drawback of ITO is that it contains rare, toxic and expansive metal

materials, resulting in some research groups replacing ITO with FTO. AZO thin films are also widely studied because the materials are cheap, non-toxic and easy obtainable.

The commercialization of DSSCs need improvement in engineering aspects, such as flexibility, roll to roll ease of fabrication, and utilization of cost effective substrates, which must be an alternatives to the expensive TCO based rigid glass materials. With this aim, flexible DSSCs fabricated using TCO-coated polymer substrates have been introduced by many researchers. Conductive polymer such as polyethylene terephthalate (PET) (Su et al., 2014; Yamaguchi et al., 2010), polyethylene naphtalate (PEN) (Lee et al., 2011; Liu et al., 2011) , and polyether sulfone (PES) (Chen et al., 2010) are flexible, light and cheap. However, the working electrode of DSSCs that based on  $\text{TiO}_2$  need high calcination temperature at around  $450^\circ\text{C}$ . Generally, these conducting polymer are unstable at high temperature. Therefore, the disadvantage of polymer substrates is the low temperature tolerance, which limits the calcination of the working electrode to below  $200^\circ\text{C}$ . In contrast to the flexible plastics substrate, thin metal foil based substrate (W, Ti, Co, Ni, Pt, Al and Zn) (Balasingam et al., 2013) could withstand the high temperature calcination process, which favours better internal resistance of the cell. For metals, the major problem is the iodine-containing electrolyte because triiodide ions are corrosive. Therefore, only metal that shows enough chemical stability in the iodine electrolyte can be successfully employed as a DSSC substrate. Long term stability and corrosion stability of the metal based DSSCs is still unknown, therefore further studies are required before transferring this type of device to large scale manufacturing.

## 2.4.2 Photoanode

The photoanode functions as a bridge and charge separator (Kelly et al., 2001). It consists of metal oxide semiconductor nanoparticles layered on the conductive surface of a transparent conducting electrode. The semiconductor material that forms the core of the photoanode should be chemically stable for dye bonding and inert towards the electrolyte species. Moreover, it should have a lattice structure suitable for dye bonding, its conduction band should be located slightly below the LUMO level of the dye in order to facilitate efficient electron injection and it should have a large surface area for the maximum dye uptake. Semiconductor oxides used in DSSC include  $\text{TiO}_2$ ,  $\text{ZnO}$ ,  $\text{SnO}_2$ ,  $\text{Nb}_2\text{O}_5$  and the lists go on, which serve as the carrier for the monolayers of the sensitizer using their large surface and electron transfer to the conducting substrate. So far,  $\text{TiO}_2$  based material is one of the most promising materials for a DSSC due to its low cost, abundance, nontoxicity, safety, large surface area and matched energy and band structure (Chen et al., 2012). It exhibits high photo absorption cross section value among the available semiconductor material in which above band gap of 3.0 eV. Titania have three different structural morphologies, which are rutile (tetragonal,  $E_g \sim 3.05$  eV), anatase (tetragonal,  $E_g \sim 3.23$  eV) and brookite (orthorhombic,  $E_g \sim 3.26$  eV). The rutile phase is thermodynamically stable and favours to solar cell application, although it is not widely applied in DSSC. The anatase has high electric conductivity. Hence it has a high electron diffusion coefficient and large absorbing capacity than the rutile photoelectrode (Byun et al., 2004; Fujishima, 1972; Park et al., 1999).

There are two commonly used deposition processes, doctor-blade and screen-printing method, to prepare nanocrystalline  $\text{TiO}_2$  film by spreading a dispersion of colloidal  $\text{TiO}_2$  onto the TCO before sintering at high temperature. There are also two commonly methods to prepare the colloidal of  $\text{TiO}_2$  dispersion: (1) Sol gel procedure

for preparation of colloidal  $\text{TiO}_2$  dispersion with autoclaving at 200-250°C, and (2) Preparation of nanocrystalline  $\text{TiO}_2$  using commercial  $\text{TiO}_2$  (P25). To prevent the aggregation of the particles, the P25 powder is ground with mortar in water or solvent containing acetylacetone or other stabilizers such as acids, bases or  $\text{TiO}_2$  chelating agents to avoid the aggregation of the particles. Normally, a detergent, Triton X-100 or ethyl cellulose was added to ease the spreading of the colloid on the substrate.

Nanocrystalline semiconductor films adsorb a large amount of the dye molecules and increase the harvesting efficiency of the solar energy. However, the major drawback associated with the use of large surface area  $\text{TiO}_2$  is its random electron transport, which will cause the electron-hole recombination process and hence affect the overall device performance (Kopidakis et al., 2005; van de Lagemaat et al., 2000). To overcome this problem, designing a photoanode with an efficient transport pathway from the photoinjected carriers to the current collector seems to be a possible alternative to enhance the performance of DSSCs. With this aim, surface modification with metal, doping, semiconductor coupling and hybridizing with carbon material have been attempted (Lai et al., 2010; Macak et al., 2007; Yang et al., 2007; Zhao et al., 2007). Modification of  $\text{TiO}_2$  with noble metals such as gold (Au) (Du et al., 2012; Jang et al., 2014; Muduli et al., 2012), silver (Ag) (Gao et al., 2013; Jiang et al., 2013) and platinum (Pt) (Jiang et al., 2013) were reported actively in the DSSC application to prevent the recombination of the photogenerated electron-hole pairs and improve the charge transfer efficiency. In the present decade,  $\text{TiO}_2$  has been modified with noble metal nanoparticles such as Ag, with the aim of improving the efficiency of a DSSC. The Ag nanoparticles play dual roles in the DSSC performance, including the enhancement of the absorption coefficient of the dye and optical absorption due to surface plasmonic resonance (Eagen, 1981; Mock et al., 2002; Schaadt et al., 2005)

Moreover, they act as an electron sink for photoinduced charge carriers, improve the interfacial charge transfer process, and minimize the charge recombination, thereby enhancing the electron transfer process in a DSSC (Lee et al., 2008; Mock et al., 2002; Schaadt et al., 2005; Wen et al., 2000; Zhao et al., 1997). Hence, the performance of a DSSC with Ag-TiO<sub>2</sub> and Au-TiO<sub>2</sub> plasmonic nanocomposite material-modified photoanodes has been actively investigated (Lee et al., 2008; Wen et al., 2000; Zhao et al., 1997).

The works on incorporating of noble metal into TiO<sub>2</sub> for DSSC enhancement have been extensively studied since 2010 and are still progressing actively. There are various methods to introduce noble metals into TiO<sub>2</sub>. The detailed survey is given in **Table 2.1**.

**Table 2.1** Summary of noble metal modified TiO<sub>2</sub> photoanode for DSSC

Ag Modified TiO <sub>2</sub>		
Ref.	Description	Year
(Chou et al., 2009)	The TiO <sub>2</sub> /Au and TiO <sub>2</sub> /Ag composite was prepared using mechanofusion system. The prepared electrode was kept immersed in N719 dye for 12 hr. The effect of the mass ratio of TiO <sub>2</sub> to Au or Ag on the conversion efficiency was also studied. The study showed enhanced conversion efficiency with addition of Ag and increasing amount of Au or Ag. The highest efficiency for TiO <sub>2</sub> /Au and TiO <sub>2</sub> /Ag are 1.96 and 0.93%, respectively. The enhancement of DSSC performance was due to the fact that the Schottky barrier, established in the TiO <sub>2</sub> /Au and TiO <sub>2</sub> /Ag particle, prevented the recombination of charges in the dye or electrolyte. This	2009

	<p>studied also showed that the <math>V_{oc}</math> of the <math>\text{TiO}_2/\text{Au}</math> was lower and unstable compared to <math>\text{TiO}_2/\text{Ag}</math> and <math>\text{TiO}_2</math>. These differences were due to three following fact: (1) The <math>V_{oc}</math> is in proportion to the difference between the Fermi level and the Nernst potential of the redox (Zaban et al., 1998) ;</p> <p>(2) The corrosion property of the <math>\text{I}^-/\text{I}_3^-</math> towards metals, the Fermi level of the <math>\text{TiO}_2/\text{Au}</math> composite was interfered and the Schottky barrier was weakened (Tian et al., 2005) .</p> <p>(3) The portion of Au stripped from <math>\text{TiO}_2/\text{Au}</math> composite facilitated the conductivity of the electrolytes.</p>	
(Enomoto et al., 2010)	<p><math>\text{TiO}_2</math> porous films were fabricated using slurry coating method and immersed into a solution of Ag nanoparticles. The conversion efficiency on 2 <math>\mu\text{m}</math> of <math>\text{TiO}_2</math> was improved from 1.5 to 2.4% by adding 12.5 nm Ag nanoparticles using N3 dye. The increase in efficiency was mainly due to the increase of <math>J_{sc}</math>. The efficiency initially increased, and then decreased with the increasing amount of Ag.</p>	2010
(Li et al., 2011)	<p>Silver nanoparticle doped <math>\text{TiO}_2</math> nanofibers have been prepared by electrospinning process. The Ag doped solar cells showed 25% improvement of conversion efficiency. For the undoped DSSC sample, the <math>V_{oc}</math> , <math>J_{sc}</math> , <math>FF</math> and <math>\eta</math> are 0.8 V, 7.57mA/cm<sup>2</sup> , 0.55 and 3.3% ,respectively. While for Ag doped DSSC, the <math>V_{oc}</math> , <math>J_{sc}</math> , <math>FF</math> and <math>\eta</math> are 0.78 V, 9.51 mA/cm<sup>2</sup> , 0.56 and 4.13 % , respectively. The improved performance is attributed to (1) the increased light harvesting efficiency due to the plasmon enhanced optical absorption</p>	2011

	induced by Ag nanoparticles and (2) the improved electron collection efficiency as a result of faster electron transport in the Ag doped TiO <sub>2</sub> nanofibre photoanode.	
(Qi et al., 2011)	The effect of localized surface plasmon resonance (LSPR) on the performance of DSSC was investigated. The LSPR from Ag nanoparticles increased the absorption of the dye molecules which allowed to decrease the thickness of the photoanodes and eventually improved the electron collection and device performance. A small amount of Ag nanoparticles improves the efficiency from 7.8 to 9.0 % while the photoanode thickness was decreased by 25 % as compared TiO <sub>2</sub> based DSSC.	2011
(Lan et al., 2012)	The micro-sized Ag powder was prepared from AgNO <sub>3</sub> by chemical reduction method with o-phenylenediamine as reducing agent before mixing with TiO <sub>2</sub> sol. The resulted paste could be well cemented to the FTO glass and showed high conductivity after the addition of Ag. Furthermore, the protecting TiO <sub>2</sub> and TiO <sub>2</sub> sol treatment acted as a blocking layer and enhanced the photovoltaic performance. The obtained conversion efficiency was 6.30% with $V_{oc}$ , $J_{sc}$ , $FF$ of 0.75 V, 14.35 mA/cm <sup>2</sup> and 0.58, respectively.	2011
(Agarwala et al., 2012)	The tri-sodium citrate reduced Ag nanoparticles was spin coated onto an electrochemically anodized TiO <sub>2</sub> nanotube film as a photoanode for DSSC. The Ag particle size of 87 nm resulted in conversion efficiency of 5.5% which showed increment of 22% compared to TiO <sub>2</sub> .	2011

(Sun et al., 2011)	<p>Oriented coaxial Ag/TiO<sub>2</sub> nanowire arrays were directly prepared on FTO through a one-step solvothermal method. It was then followed by filling the interspaces between the nanowires with TiO<sub>2</sub> paste by doctor-blade method. The composite photoanode with TiO<sub>2</sub> shell thickness of 2.1 times greater than the silver core diameter exhibited an enhanced energy efficiency of 9.8% compared to 7.7% for the pure TiO<sub>2</sub>. The favourable result was attributed to the thin silver cores which effectively reduced the charge recombination, and the TiO<sub>2</sub> nanoparticles between the nanowires, which provided the high specific surface area for dye loading.</p>	2011
(Zhao et al., 1997)	<p>TiO<sub>2</sub>/Ag composite film was prepared by incorporating Ag in the mesoporous of TiO<sub>2</sub> films using a photoreduction method. The Ag nanoparticles were face-centered cubic and varied in size in the range of 4.36-38.65 nm. The Ag nanoparticle was controlled by varying the UV exposure times from 5 min to 240 min. The optimum size of Ag was 19.16 nm with UV exposed time of 120 min, giving the highest efficiency of 4.76%.</p>	2011
(Guo et al., 2013)	<p>The Ag@TiO<sub>2</sub> core-shell nanoparticles have been developed as a photoanode for DSSC with the aim that the TiO<sub>2</sub> shell would protect the Ag nanoparticle core from being eroded by the electrolyte. The influence of Ag nanoparticles on the structure and the DSSC performance was also investigated. The best performing DSSC contained 0.15 wt% of Ag, and gave <math>J_{sc}</math> of 10.19 mA/cm<sup>2</sup>, <math>V_{oc}</math> of 0.69 V and <math>\eta</math> of 5.33%.</p>	2012

	using N719 dye. The increase in $J_{sc}$ was attributed to the enhanced light absorption and broadened absorption spectral range of the photoanode due to the surface plasmon resonance of Ag. Meanwhile the $V_{oc}$ decrease could be related to the more negative quasi-Fermi level energy of the Ag-TiO <sub>2</sub> composite system due to the enhanced electron capture and storage capability resulting from Ag doping.	
(Jin et al., 2012)	TiO <sub>2</sub> nanofibre (TN) and Ag-doped TiO <sub>2</sub> nanofibre (ATN) were introduced to a TiO <sub>2</sub> film to increase the amount of the dye loading. The conversion efficiency of TiO <sub>2</sub> based DSSC was 4.74% and was increased to 6.13% after adding 5 wt.% ATN into the TiO <sub>2</sub> film. It was found that the electron lifetime of DSSC with ATN addition increased from 0.29 to 0.34 sec and that electron recombination was reduced.	2012
(Tian et al., 2013)	The biomass coated Ag-TiO <sub>2</sub> photoanode have been prepared using syzygium extracts as a reducing agent, complexing agent and stabilizer. The syzygium-Ag-TiO <sub>2</sub> based DSSC exhibits the best performance with the $J_{sc}$ of 11.8 mA/cm <sup>2</sup> and conversion efficiency of 5.12 %, which was higher than the glucose-Ag-TiO <sub>2</sub> , UV-Ag-TiO <sub>2</sub> and TiO <sub>2</sub> . The residue hydroxyl groups of the biomass on the photoanode improved dye absorption and electron injection efficiency.	2013
(Park et al., 2014)	A bi-functional Nb-doped TiO <sub>2</sub> /Ag ternary nanostructures showed improve electron transfer and plasmonic effect in DSSC. TiO <sub>2</sub> nanoparticles were surface-modified via atom	2013

	transfer radical polymerization with a hydrophilic poly(oxyethylene)methacrylate, which coordinated to the Ag precursor. After reduction of the Ag ions, a Nb <sub>2</sub> O <sub>5</sub> was used as dopant. The Nb-doped TiO <sub>2</sub> /Ag based DSSC with a polymerized ionic liquid electrolyte showed an overall conversion efficiency of 6.9 % which was much higher than the pure TiO <sub>2</sub> (4.7 %) and Nb-TiO <sub>2</sub> (5.4 %)	
(Luan et al., 2014)	Evenly distributed and uniformly sized Ag nanoparticles were deposited on a TiO <sub>2</sub> nanotube array by pulse current deposition and used as a photoanode for DSSC. The amount and size of Ag particles were controlled by the pulse deposition time. The Ag-modified TiO <sub>2</sub> nanotubes showed the conversion efficiency of 1.68 % compared to TiO <sub>2</sub> nanotubes. Furthermore, it was found that the TiCl <sub>4</sub> post treatment could further increase the conversion efficiency to 3.82 %.	2013
(Sebo et al., 2013)	The Ag nanoparticles protected by thin shells of TiO <sub>2</sub> were incorporated within the TiO <sub>2</sub> photoanode. The plasmonic effect of Ag nanoparticles improved the conversion efficiency by 18.3 %, which resulted in an enhanced efficiency of 6.23 % as compared to 5.29 % of TiO <sub>2</sub> photoanode.	2013
(Tripathi et al., 2013)	Localized surface resonance induced by Ag nanoparticles was experimentally observed in FTO glass which improved light transmission and reduced reflection. $J_{sc}$ increased from 11.7 to 12.34 mA/cm <sup>2</sup> and $V_{oc}$ increased from 704 to	2013

	709.5 mV. Overall efficiency enhancement of 6.67% was observed in TiO <sub>2</sub> nanorod-based DSSC due to plasmon-induced light trapping.	
(Xu et al., 2013)	The Au-Ag alloy popcorn-shaped nanoparticles were prepared using reduction method by sodium citrate and showed enhancement in conversion efficiency. It was found that the irregular popcorn-shaped alloy exhibit absorption enhancement over a broad wavelength range due to the excitation of localized surface plasmon at different wavelength. By introducing the popcorn nanoparticle at the optimised concentration of 2.38 wt%, the conversion efficiency was increased by 16 %, from 5.26 to 6.09 %.	2013
(Zhang et al., 2013)	The plasmid DNA was applied as scaffold to fabricate Ag@TiO <sub>2</sub> plasmonic nanocomposites under mild conditions and use as photoanode DSSC. The performance of DSSC depended on the amount of Ag. The best performance was 1.83% at 0.8 wt.% of Ag compared to 1.42 % of pure TiO <sub>2</sub> with N719 dye.	2013
(Jiang et al., 2013)	Photoreduction method was employed to incorporate Ag into the patterned TiO <sub>2</sub> network. The patterned TiO <sub>2</sub> /Ag photoanode showed an enhancement in conversion efficiency as compared to TiO <sub>2</sub> and TiO <sub>2</sub> /Ag. The conversion efficiency of patterned TiO <sub>2</sub> /Ag based DSSC was 5.69 %.	2013
(Guo et al., 2013)	TiO <sub>2</sub> nanocomposite photoanodes with different amounts of Ag nanowire coated with SiO <sub>2</sub> were prepared using ball	

	milling method. The optimal properties were obtained in a DDSC with content of 0.60 wt.% of Ag and conversion efficiency of 6.26 %,significantly superior to those of the pure TiO <sub>2</sub> based DSSC.	
(Wang et al., 2014)	The (Ag,S)- modified photoanodes were prepared using garlic as the sulphur o-phenylenediamine source. After modification of TiO <sub>2</sub> with S, the $J_{sc}$ was improved by 21% and further synergizing with Ag resulted in pronounced increase in the photocurrent from 10 mA/cm <sup>2</sup> to 12.3 mA/cm <sup>2</sup> . It was found that the internal resistance reduced after sulphur introduction, which may be due to the increased acceleration of the electron transfer process in S-TiO <sub>2</sub> photoanode, leading to the positive influence on the cell performance. An overall conversion efficiency of 4.73% with 0.5 wt.% of Ag in S-TiO <sub>2</sub> was achieved.	2014
(Berginc et al., 2014)	The solutions of AgNO <sub>3</sub> in different solvent such as isopropanol, ethylene glycol or in TiO <sub>2</sub> sol was investigated as a possible precursor for Ag nanoparticles formation. The solution was then dip coated on a porous TiO <sub>2</sub> layer. The study showed that the formation of Ag from isopropanol solution led to a uniform distribution of Ag particles, giving the highest enhancement in DSSC, which was 3.9 %.	2014
<b>Au Modified TiO<sub>2</sub></b>		
<b>Ref.</b>	<b>Description</b>	<b>Year</b>
(Nahm et al., 2011)	100 nm of Au nanoparticles were incorporated into TiO <sub>2</sub> nanoparticles via a reduction method in an aqueous solution	2011

	and was used as a photoanode in DSSC. The optimum Au/TiO <sub>2</sub> mass ratio was 0.05 and showed the enhanced conversion efficiency from 2.7% to 3.3%. The Au nanoparticles generated field enhancement by surface plasmon resonance rather than prolonged optical paths by light scattering. The Au-TiO <sub>2</sub> film strongly absorbed light due to the LSPR, and thereby promoted light absorption of the dye.	
(Sahu et al., 2012)	A two-step method was employed to synthesize Au-TiO <sub>2</sub> core-shell nanowires. Au nanowires were first synthesized using a galvanostatic constant current electrodeposition technique. A shell of anatase TiO <sub>2</sub> was subsequently grown on the Au nanowires using pulsed laser deposition. The introduction of Au nanowire showed improvement in conversion efficiency, which, further increased to after TiCl <sub>4</sub> post treatment.	2012
(Du et al., 2012)	Au@TiO <sub>2</sub> hollow submicrospheres was synthesized using hydrothermal method and used as photoanode in DSSC. A conversion of 8.13% was obtained, which showed a 30 % enhancement compared to P25 TiO <sub>2</sub> photoanode.	2012
(Sheehan et al., 2012)	A nanostructure using metal-insulator-semiconductor system had been developed to insulate and protect plasmonic nanoparticles while simultaneously incorporated a photoactive semiconductor as its outermost layer. The Au@SiO <sub>2</sub> @TiO <sub>2</sub> was synthesized and used as photoanode in DSSC, resulting in increasing conversion efficiency from	2012

	2.81% to 5.52%.	
(Ghaffari et al., 2012)	Au nanoparticles were deposited on a hydrothermal produced TiO <sub>2</sub> nanorod array using a photoreduction method. The results showed the presence of Au nanoparticles, which significantly improved $FF$ and $J_{sc}$ , resulting as much as triple the overall conversion efficiency. The overall conversion efficiency was increased from 0.31 to 0.94 % after silver deposition.	2012
(Sahu et al., 2012)	The core shell Au-TiO <sub>2</sub> nanowire was prepared by a two-step method and used as a photoanode. The TiO <sub>2</sub> nanowire was first prepared using a sol-gel method before the Au nanoparticle was deposited on it using an electrodeposition method. The addition of Au resulted in a two-fold improvement in efficiency, which was enhanced from 0.41 to 1.04%. The conversion efficiency was further improved after post-treatment with TiCl <sub>4</sub> and gave the overall efficiency of 5.40% using N719 dye.	2012
(Muduli et al., 2012)	The Au-TiO <sub>2</sub> nonofibre was prepared using electrospinning method with the Au particle size of 4-5 nm. The Au:TiO <sub>2</sub> nanofibre showed improvement in efficiency by 25 % compared to TiO <sub>2</sub> nanoparticle. While TiO <sub>2</sub> nanofibre showed 12 % improvement in efficiency compared to TiO <sub>2</sub> nanoparticle. The Au:TiO <sub>2</sub> nonofibre showed the overall efficiency of 7.77 %.	2013
(Pandikumar et al., 2013)	Aminosilicate sol-gel functionalized P25-Au was fabricated in DSSC device using the dual-photosensitizer consisting of	2013

	<p>cadmium sulphide quantum dots (CdS QDs)</p> <p>and basic blue-3 (BB-3) dye and TiO<sub>2</sub> (P25) nanoparticles incorporated poly(ethyleneoxide) polymer electrolyte. It showed the conversion efficiency of 0.37%. The conversion efficiency of standard N719 dye sensitized (1.19%) DSSC was found to be higher than the dual sensitizer</p>	
(Muduli et al., 2012)	<p>Hydrothermal prepared TiO<sub>2</sub>-Au was used as a photoanode in DSSC. The <math>J_{sc}</math>, <math>V_{oc}</math>, <math>FF</math> and <math>\eta</math> are 12.6 mA/cm<sup>2</sup>, 0.70 V , 0.56 and 5 % , respectively for TiO<sub>2</sub> based DSSC. While the <math>J_{sc}</math>, <math>V_{oc}</math>, <math>FF</math> and <math>\eta</math> for TiO<sub>2</sub>-Au are 13.2 mA/cm<sup>2</sup>, 0.74 V , 0.61 and 6 % , respectively. The higher <math>J_{sc}</math> in TiO<sub>2</sub>-Au composite could be attributed to plasmon induce charge transfer from Au nanoparticle to TiO<sub>2</sub>. The increase in <math>V_{oc}</math> and <math>FF</math> after the addition of Au could be correlated to the decreased electron-hole recombination at TiO<sub>2</sub>-Au-dye-electrolyte interface. The 20% enhancement in conversion efficiency was attributed to the reduction of electron recombination process and also the Au plasmon mode energetically overlapping with the dye absorption zone, possibly rendering charge into the TiO<sub>2</sub> nanoparticles.</p>	2013
(Song et al., 2014)	<p>Microwave-assisted hydrothermal method was used to synthesize Au@TiO<sub>2</sub> core-shell nanoparticle with the ~40nm Au core and ~60 nm TiO<sub>2</sub> shell. It was found that Au nanoparticles were unstable and could dissolve in iodide electrolyte. Hence , hollow TiO<sub>2</sub> nanoparticle were produced</p>	2013

	by selectively etching of as-prepared Au@TiO <sub>2</sub> core-shell NPs and applied as a scattering layer on top of a nano-crystalline TiO <sub>2</sub> , serving as the photoanode of DSCs. The efficiency of 7.40 % was obtained with the TiO <sub>2</sub> hollow spheres, compared with 5.21% for the electrode with commercial TiO <sub>2</sub> nanoparticle.	
(Liu et al., 2013)	Controllable morphology of core and shell thickness method had been developed to prepare the Au@TiO <sub>2</sub> . The Au nanoparticle was firstly prepared using chemical reduction with trisodium citrate under heat for 12 hr before mixing with commercial TiO <sub>2</sub> and fabricated into a photoanode. It was found that doping with a thinner TiO <sub>2</sub> shell enhanced the excitation rate of dye sensitizers and increased the cell temperature, leading to enhancement in the short-circuit current. On the other hand, doping PCSNPs with a thicker shell allowed for charge equilibrium between the semiconductor and the metal cores, resulting in an increased open-circuit voltage. The efficiency for Au@TiO <sub>2</sub> core-shell NPs was 7.38% as compared to TiO <sub>2</sub> based DSSC.	2013
(Ng et al., 2014)	A series of plasmonic enhanced DSSC with typical N719 sensitizer had been prepared using self-assembly gold TiO <sub>2</sub> core-shell nanoislands. It was the first report showing that the same approach could be adopted simultaneously for both the photoanode and the counter electrode of a DSSC but using different enhancement mechanism. The maximum power conversion efficiency increased from 5.31 % to 6.32	2013

	% with optimum Au size of 9 nm.	
--	---------------------------------	--

In order to improve the light absorption to the visible region on TiO<sub>2</sub> material, various non-metals such as nitrogen (N), carbon (C), sulfur (S) and phosphorus (P) doped TiO<sub>2</sub> have been widely studied (Zhang et al., 2010). Among them, nitrogen doped TiO<sub>2</sub> possesses good photovoltaic properties activity and hence it has received much attention due to the narrowing of band gap and shift to the visible region (Kang et al., 2010). Soon *et al.* reported an increment of 23 % after doping with nitrogen, which achieved an overall conversion efficiency of 4.86 % (Kang et al., 2010). Xiang *et al.* also reported that the mesoporous nitrogen-doped TiO<sub>2</sub> sphere showed a more excellent photovoltaic performance compared to undoped TiO<sub>2</sub> (Xiang et al., 2011). In addition, the co-deposition of noble metal on the N,S-doped TiO<sub>2</sub> also showed enhanced photovoltaic and photocatalytic properties due to the presence of the synergistic effect between the noble metal and N,S -doped TiO<sub>2</sub> (Pany et al., 2013; Zhang et al., 2011). The N,S-doped TiO<sub>2</sub> based photoanode have been developed and showed 56.8% improvement in conversion efficiency after co-sensitized with poly (3-decylthiophene) and N719.

### 2.4.3 Dyes

Dyes molecules are one of the key components of a DSSC, which serves as the solar energy absorber in DSSC and contributes significantly to the light harvesting efficiency and the overall photoelectric conversion efficiency. The ideal dyes for DSSC should exhibit the following essential properties:

- Dye should exhibit high absorption in whole visible region and near IR region with higher molar extinction coefficients.

- It should be firmly grafted to the semiconductor oxide surface and produces excited electrons to be injected to the wide band gap semiconductor (Jayaweera et al., 2008).
- Dye should have good energy level alignment; LUMO level of the dye should be higher than conduction band of the semiconductor and HOMO level of the dye should be lower than the potential of the electrolyte. Its redox potential should be sufficiently high and can be regenerated rapidly via electron donation from the electrolyte or a hole conductor. **Figure 2.8** and **2.9** show the feasible and non-feasible charge transition in dye-sensitized solar cells.
- It should also be stable enough to sustain at  $10^8$  redox turnovers under illumination corresponding to about 20 years of exposure to natural light (Hagfeldt et al., 2000).
- Dye has to be stable against aggregation from the irradiation of light and should be hydrophilic in nature.
- Dye should have a simple preparation procedure, less hazardous and economical to produce.

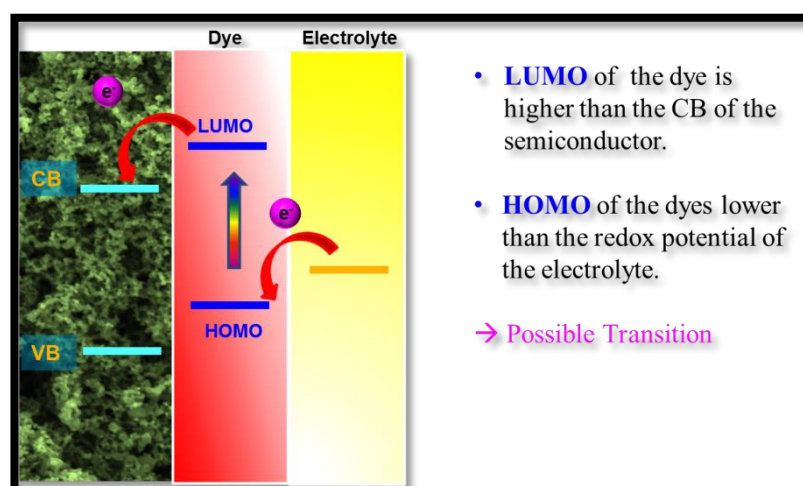


**Figure 2.8** Energy level position of feasible charge transition in dye-sensitized solar cells

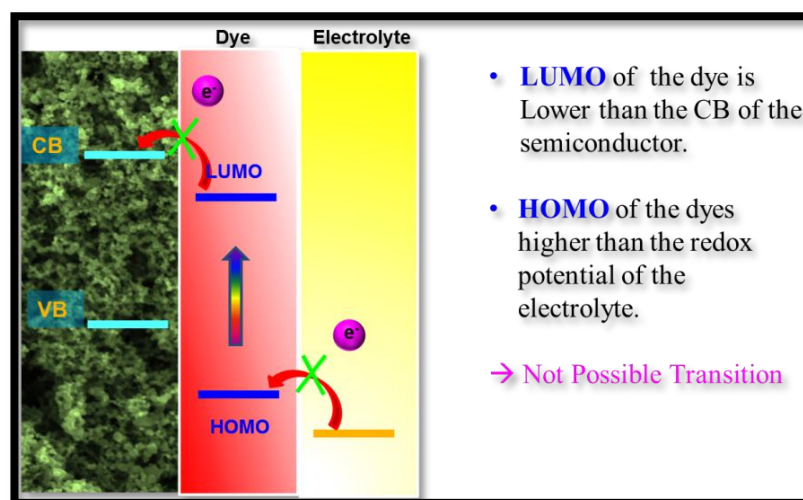


**Figure 2.9** Energy level position of non-feasible charge transition in dye-sensitized solar cell.

The dyes used in DSSC can be divided into two categories: organic dye and inorganic dye according to the structure. Inorganic dye includes metal complex, such as polypyridyl complexes of ruthenium and osmium, metal porphyrin, phthalocyanine and inorganic quantum dots, while organic dye includes natural organic dye and synthetic organic dye.

Early DSSC designs involved transition metal coordinated compounds as dye sensitizer because of their strong visible absorption; long excitation lifetime and efficient metal-to-ligand charge transfer (Grätzel, 2009; Ito et al., 2008; O'Regan et al., 1991). Compared to organic dye, inorganic complexes dye has high thermal stability and chemical stability, exhibits wide range of absorption in visible to near IR region and incorporated with different light absorbing groups in their structure which can tune a board absorption range to achieve high molar extinction coefficient value. Among these complexes, polypyridyl ruthenium sensitizers were widely used and investigated for their high stability, outstanding redox properties and good response to natural visible sunlight. Polypyridyl ruthenium sensitizers can be divided into carboxylate polypyridyl ruthenium, phosphonate ruthenium dye and polynuclear bipyridyl ruthenium dye. The difference between the first two types of sensitizers lies

in the adsorption group. The first two types of the sensitizers differ from the last type of the sensitizer in the number of metal center. The dyes grafted on the surface of the semiconductor photoanode with the carboxylate or phosphonate group enable the electron injection into the conduction band of semiconductor. The carboxylate polypyridyl ruthenium dye is in level structure, which enables the electron injection into the conduction band of the semiconductor quantitatively. Limitation of these inorganic dye are in ruthenium polypyridyl complexes because ruthenium are expensive, extra care is necessary during the synthesis, difficult steps purification step. Ruthenium based N945 dye anchored with  $\text{TiO}_2$  semiconductor achieved high photocurrent density of  $18.84 \text{ mA/cm}^2$  and efficiency 10.82 %, which exhibited efficient harvesting of visible light. Heteroleptic ruthenium complex based bipyridine with 2,2'-bis(3,4-ethylenedioxythiophene) (Nazeeruddin et al., 2007). TF1 dye which was Ruthenium (II) sensitizers incorporated with both 4, 4', 4''-tricarboxy-2,2':6,2''-terpyridine and 2,6-bis(5-pyrazolyl) pyridine ligands was used as dye for  $\text{TiO}_2$  photoanode (thickness of  $15 \mu\text{m}$ ) and achieved the efficiency of 10.7 % (Chou et al., 2011). Ruthenium based dye achieved maximum efficiency of 11.2% with iodine based redox couple (Park et al., 2005) but recently reported zinc porphyrin based dye achieved 12.3% efficiency by the Gratzel group (Yella et al., 2011). The Gratzel group reported that zinc porphyrin (YD2-0-C8) dye, co-sensitized with Y123 and YD2-0-C8, was capable with long chain alkoxy group and dye absorption covered with full visible region. Zinc complex integrated with alkoxy group will improve the photon-induced charge separation of DSSC using cobalt bipyridyl redox couple based electrolyte. Currently, the maximum reported efficiency is 13 % using novel proquinoidal benzothiadiazole incorporation porphyrin based dye (SM315) and cobalt(II/III) redox electrolyte (Mathew et al., 2014). This dye will maximize cobalt-electrolyte

compatibility and improve the light harvesting properties. Several examples of the ruthenium based dye are shown in **Figure 2.10**.

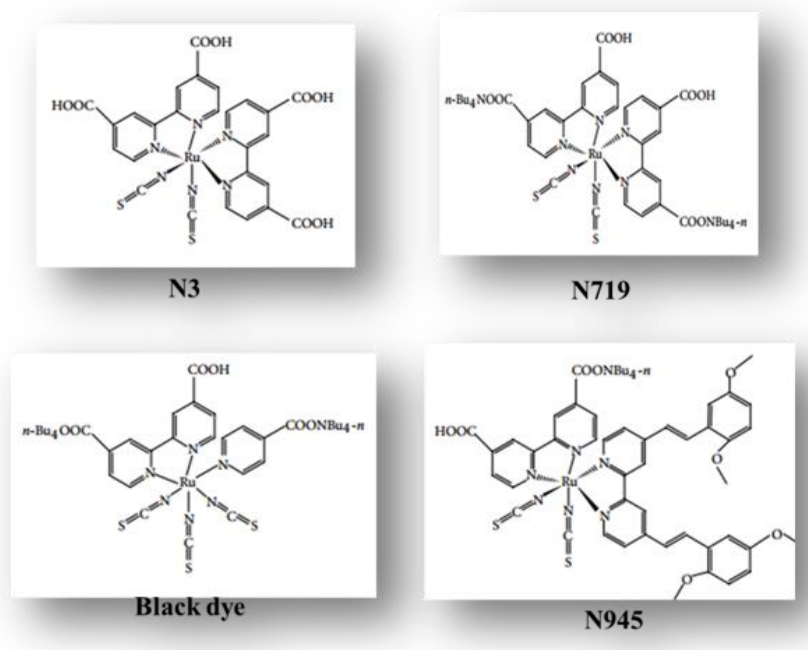


**Figure 2.10** Molecular structure of several ruthenium complexes dye (Kong et al., 2007)

Organic dyes, including natural pigments and synthetic organic dyes, have a donor-acceptor structure called as push-pull architecture, thus improving short circuit current density by improving the absorption in the red and infrared region. Natural pigments, like chlorophyll, carotene and anthocyanin, are freely available in plant leaves, flowers, and fruits. Natural dyes are easily available low cost dye, a substitute to the expensive inorganic dye. Limitations of natural dye are poor efficiency. Betalaine pigments in red turnip produced a highest efficiency of 1.70% (Calogero et al., 2010). Other natural dyes are shisonin, 1.01% (Kumara et al., 2006); mangosteen pericarp, 1.17% (Zhou et al., 2011); and Rhoeo spathacea, 1.49% (Lai et al., 2008). Synthetic organic dyes are more promising. Currently, metal free organic dyes have been attract more attention since they are quite inexpensive and suitable molecular structure can be designed to tune absorption and electrochemical properties. All organic donor-acceptor dyes attained high extinction coefficient from their structural properties relationship

known from basic dye chemistry (Langhals, 2004). Metal free organic dyes have achieved the maximum efficiency of 9.52% with indoline based dye D205 with CDCA (Ito et al., 2008). The chenodeoxycholic acid (CDCA) was used as an anti-aggregation reagent to prevent dye aggregation and enhanced the photovoltaic performance. Thiophene based cyclopentadithiophene-cyanoacrylic acid dyes with arylamine electron donors of dihexyloxy substituted triphenylamine dye (DHO-TPA, C218) with cobalt redox couple electrolyte attained an efficiency of 9.3% (Xu et al., 2011). It was reported that the organic dye TA-St-CA, containing p-conjugated oligo-phenylenevinylene unit with an electron donor–acceptor transfer and a carboxyl group anchoring unit showed photoconversion efficiency of 9.1 % (Ho & Lee., 2007) .

#### **2.4.4 Electrolyte**

An electrolyte is a crucial component in a DSSC, which transfers electron from a counter electrode to a photoanode. Therefore, an electrolyte should efficiently regenerate itself. Wolfbauer *et al.* have listed the ideal characteristics of the redox couple for a DSSC electrolyte (Wolfbauer et al., 2001) :

- Redox potential thermodynamically (energetically) favourable with respect to the redox potential of the dye to maximize cell voltage;
- High solubility to the solvent to ensure high concentration of charge carriers in the electrolyte;
- High diffusion coefficients in the used solvent to enable efficient mass transport;
- Absence of significant spectral characteristics in the visible region to prevent absorption of incident light in the electrolyte;

- High stability of both the reduced and oxidized forms of the couple to enable long operating life;
- Highly reversible couple to facilitate fast electron transfer kinetics;
- Chemically inert towards all other components in a DSSC.

The electrolyte used in a DSSC can be divided into three types: liquid electrolyte, solid-state electrolyte and quasi solid-state electrolyte.

### **(1) Liquid Electrolyte**

The most common electrolyte is based on  $I^-/I_3^-$  redox couple in organic solvents, such as acetonitrile has produced high photocurrent efficiency. Sometimes, additive such as lithium ions is added to facilitate the electron transport. This type of electrolyte is good for ionic diffusion and penetrates well with the  $TiO_2$  film, keeping the highest photocurrent efficiency. Liquid electrolyte exhibits dielectric constant organic solvent or uses low viscous ionic liquid as a solvent medium. The dielectric constant value, viscosity of the organic solvent and number of donor will greatly influence the performance of the electrolyte. However, liquid electrolyte suffers from long term stability due to volatilization and leaking of liquid, hence hinders its commercial use. The previously reported liquid electrolyte contains redox couple such as 2,2,6,6-Tetramethyl-1-piperidinyloxy (TEMP/TEMPO<sup>+</sup>) (Zhang et al., 2008), disulfide/thiolate (Wang et al., 2010), selenocyanate (SeCN<sup>-</sup>/(SeCN)<sub>3</sub><sup>-</sup>) (Wang et al., 2004) , Br<sup>-</sup>/Br<sub>3</sub><sup>-</sup> (Wang et al., 2005), hydroquinone/benzoquinone (Murakami et al., 2006), ferricyanide/ferrocyanide (Daeneke et al., 2012) and ferrocene/ferrocenium (Fc/Fc<sup>+</sup>) (Daeneke et al., 2011). Recently, Aswani et al reported liquid electrolyte with cobalt(II/III) tris bipyridyl redox couple co-sensitized with N719 dye, which showed a photocurrent efficiency of 12.3% (Yella et al., 2011).

## **(2) Solid-state electrolyte**

Researchers had worked on replacing the liquid electrolyte with solid-state electrolyte. Solid-state electrolytes overcome the disadvantages of the fluidity and volatility of the liquid electrolyte. Furthermore, many efforts have been done to design high efficiency solid-state DSSC. Solid-state DSSC utilizes hole transporting materials (HTMs) referred to as p-type semiconductor. Inorganic HTMs, organic HTMs and solid-state redox couple are widely used as charge carrier in solid-state DSSC. The first solid-state electrolyte based DSSC was reported to have photocurrent efficiency less than 1% (Bach et al., 1998). Last decades, organic HTMs achieved efficiency of 7.1% (Burschka et al., 2011). Recently, photocurrent efficiency of 10.2% is obtained based on the inorganic HTMs based  $\text{CsSnI}_{3-x}\text{F}_x$  compounds prepared from  $\text{CsSnI}_3$ , F and  $\text{SnF}_2$  (Chung et al., 2012).

## **(3) Quasi solid-state electrolyte**

The quasi solid electrolyte is prepared by composition of liquid electrolyte with low molecular weight gelator, nanoparticle or polymer matrix. The nanoparticles with either organic solvent based liquid electrolyte or ionic liquid based liquid electrolyte composite produces the quasi solid electrolyte. This composite of quasi solid electrolyte is exhibited by gel state. The polyacrylonitrile based composite gel was first introduced gel electrolyte which attained efficiency of 4.4 %. Thermo plastic gel electrolyte was reported to have better efficiency of 7.22% (Wu et al., 2007).

### **2.4.5 Counter Electrode**

Counter electrode plays an important role for catalytic triiodide reduction and reaction transfer. The main task of counter electrode acts as a catalyst by reducing the redox species, which are the mediators for regenerating the dye after the electron

injection (Thomas et al., 2014). A counter electrode material is chosen according to the particular application of a DSSC. A counter electrode should exhibit superior catalytic activity and high electrical conductivity for efficient electron transport (Murakami et al., 2008). In general, counter electrode will have catalytic material that is coated on the transparent conducting material and exhibit efficient reduction properties. In DSSC, counter electrode can be classified into two types: platinum counter electrode and platinum free counter electrode. Platinum counter electrode consists of platinum coated on transparent conducting material. Platinum free counter electrode is based on materials such as carbon material, polymer material, transition metal sulfides, transition metal nitrides, transition metal oxides, *etc.*

### **(1) Platinum**

As a standard choice of material for counter electrode in DSSC, platinum is always the best choice due to its attractive properties like high catalytic activity, high reflecting properties and excellent stability towards the iodide redox species (Calogero et al., 2008). Several efficient methods available to make platinum counter electrode are spin coating, screen printing and sputtering methods. Other than these techniques, there are several other deposition techniques such as pulse-current electrochemical deposition, thermal vapour depositions, spray pyrolysis, *etc.*, which use large quantity of expensive platinum. The main aspects to be considered for counter electrode in DSSC are optical transparency and cost. A highly transparent platinum counter electrode is important in DSSC for the back side illumination process and improves the light harvesting efficiency of the dye, thus improves the performance of the cell (Murakami et al., 2008; Papageorgiou, 2004). From the recent studies, it was reported that modifying the structural characteristics and facets of platinum can enhance its catalytic activity. Jeong *et al.* had prepared periodically aligned platinum nanocup and obtained the efficiency of

9.75%, compared to the planar platinum, which showed 7.87% efficiency (Jeong et al., 2012). The enhancement in efficiency was due to the large surface area of platinum with nanocup structure, in which the electrolyte can fully contact the inner and outer faces of the cup. The large surface area indicates a large number of active sites which are available for the reduction of  $I^-$ , thus increasing the current density (Calogero et al., 2008).

## **(2) Carbon**

While showing excellent catalytic action, platinum has the disadvantage of being too expensive. For a cost-effective DSSC, a cheap and abundant material in the Earth's crust should be utilized as the material for counter electrode. Carbon, which is the sixth most abundant material in the Earth's crust, is the best material to replace platinum (Pt). The main reason is due to its core features like cost-effectiveness, environment friendliness, availability, corrosion resistance and excellent catalytic activity towards redox species. All the carbon family including carbon black, activated carbon, mesoporous carbon, carbon nanotubes, graphene and fullerenes have been used as alternative materials for platinum in counter electrode. In 1996, Kay and Gratzel have developed a porous carbon counter electrode, made from a mixture of carbon black and graphite powder to replace the expensive platinum counter electrode. The cell showed the overall efficiency of 6.7 % (Kay et al., 1996). Murakami *et al.* worked on varying the thickness of the carbon black as the counter electrode material and reported an efficiency of 9.1% with the thin film's thickness of 14.47  $\mu\text{m}$  (Murakami et al., 2006). Bai *et al.* reported preparation of carbon black counter electrode with green approach, which showed an efficiency of 7.4% (Bai et al., 2011). Carbon aerogel (Zhao et al., 2011) and carbon nanoparticle (Ramasamy et al., 2007) modified counter electrodes showed a high power conversion efficiency of 9.06% and

6.73 %, respectively. Mesoporous carbon materials have received the greatest attention amongst all the carbon materials due to their large internal surface area, pore volume, tunable and narrow pore diameter. The most commonly used method for developing mesoporous carbon is a template mediated synthesis, which is also known as nonocasting. The large porous carbon helps in the penetration of the electrolyte, which resulted in giving an efficiency of around 7.1 % (Plonska-Brzezinska et al., 2011).

### **(3) Conducting Polymer**

Conducting polymers are promising materials that can be used to replace platinum as a counter electrode in DSSC because of their high electrochemical activity. Electrochemically developed flexible polyaniline nanofibres and graphitized polyimide carbon films have been used as a counter electrode and have high catalytic activity and low charge transfer (Chen et al., 2011). Lim *et al.* prepared polypyrrole nanoparticle incorporated reduced graphene oxide as a counter electrode and obtained the efficiency comparable with platinum (Lim et al., 2014). Polypyrrole/ functionalized MWCNT nanocomposite modified counter electrode achieved an efficiency of 7.02 % (Peng et al., 2011). Polystyrene sulfonate doped poly(3,4-ethylenedioxythiophene) with graphene composite electrode attained an efficiency of 4.5 % (Hong et al., 2008).

### **(4) Transition metal carbides/nitrides/oxides**

Transition metal carbides and nitrides are potential substitutes for a platinum counter electrode due to their low cost, high catalytic activity and good thermal stability. A high power conversion efficiency of 7.63 % was obtained when highly conducting mesoporous carbon was added to the vanadium carbide material (Hagfeldt et

al., 1995). The tungsten carbide showed excellent solar conversion efficiency of 7.01 % with TiO<sub>2</sub> based photoanode (Suk Jang et al., 2010).

## 2.5 Application of DSSC

Compared to other solar cells that utilize highly expensive polysilicon and vacuum equipment, the production cost of DSSC could save from 1/5 up to 1/2 of the production costs of other solar cells. DSSC gathers much attention recently as many international companies announce their plans of commercialization. DSSCs are being developed into consumer applications. G24i power group, founded in 2006, claimed the production of the first commercial grade dye sensitised thin films (<http://gcell.com/>). This group began manufacturing and production optimization in 2008-2009 and successfully manufactured indoor photovoltaic device. For instance, G24i power has produced indoor wireless product (**Figure 2.11**) and outdoor product (**Figure 2.12**).



**Figure 2.11** Wireless products based on DSSC



**Figure 2.12** Outdoor products based on DSSC

For indoor products, the indoor “energy harvesting” products create the ability to self-power under lowlight and brightly-lit condition. DSSCs are fabricated into the product range from remote control, alarm, smoke detector, keyboard, electronic shelf label and etc. While, for the outdoor products, the DSSCs have been integrated into bags, portable electronic devices, tents and serves as charging stations. Moreover, building integrated photovoltaics, which employs photovoltaic devices in building structures such as windows, skylights, roofs and walls to provide electric power for the building and save electric energy, can be benefited from dye-sensitized solar cells, because of their flexibility, easy installation and better performance in low and indirect illumination. **Figure 2.13** shows some example of DSSC possible fabrication for power-generating windows, room lights and solar mobile device charger by Sony (<http://www.sony.net/>).



**Figure 2.13** DSSC fabrication for power-generating windows, room lights and solar mobile device charger

## 2.6 Optimization of DSSC Parameters

Even though DSSC is having 10-11% of commercial efficiency and reduced cost by 1/5 with low cost manufacturing facility and process technology; the investors are still reluctant to bring it into commercialization due to the unsolved problems. Remaining problems or challenges for DSSC are listed as follows in brief:

### 2.6.1 Low Efficiency

Low efficiency in DSSC mostly comes from the low current density ( $J_{sc}$ ) and open circuit potential ( $V_{oc}$ ). The  $J_{sc}$  obtained from DSSC is still much lower than the silicon based solar cells. The basic concept of DSSC involves using highly porous  $TiO_2$  thin film as a photoanode, allowing a large amount of the sensitizing organic dye to be absorbed, absorbs light and improves the inter-penetration of liquid electrolyte. However, porous  $TiO_2$  layer, which essentially serves the purpose of collecting and transporting photoelectrons, could leave a portion of transparent conductive substrate (TCO) surface uncovered and creates a lot of trapping points, which quench the photoelectrons to photoanode and thus decreases the efficiency of the overall device (Peng et al., 2004). In DSSC with  $I^-/I_3^-$  redox couple, the interfacial recombination happens from microsecond to millisecond's time scale, which is slower than the electron transport within the nanoporous of  $TiO_2$  (Hagfeldt, 1995). However, the defects in the nanoporous layer will slow down the speed of the electron transport, which resulted in the internal losses. On the other hand, the reduction of oxidized dye also takes place from nanoseconds to microseconds, competing with the interfacial recombination, for example, between electrons in  $TiO_2$  and oxidised dye or between electrons in  $TiO_2$  and the redox electrolyte (Hagfeldt et al., 2000). Therefore, it is important to obtain dye with high cycle life for significantly fast regeneration than the

interfacial recombination process, to depress the internal loss in DSSC. **Figure 2.14** shows the simplified of schematic kinetics of DSSC.

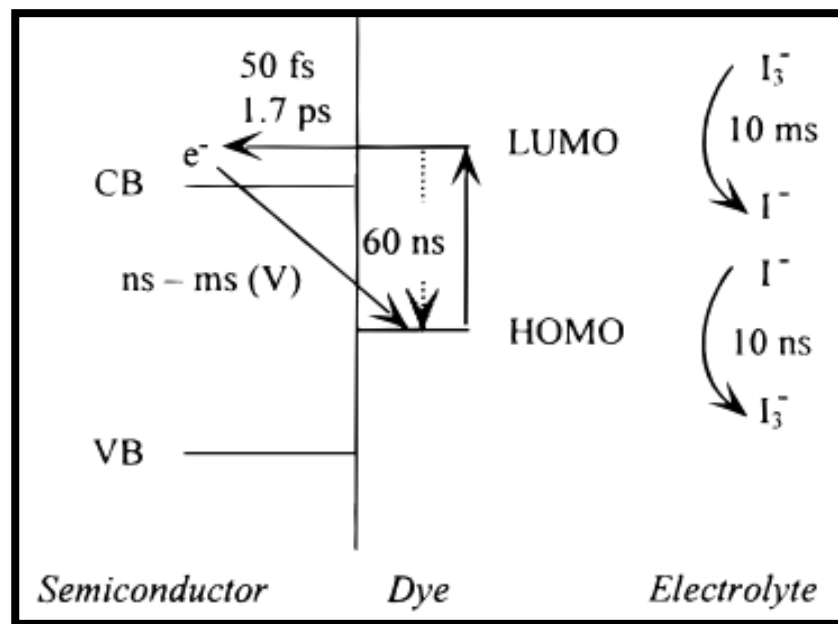


**Figure 2.14** Schematic of kinetic in DSSC (Hagfeldt et al., 2000)

Another factor leading to low  $J_{sc}$  is the limited light absorption. To improve the light absorption, dye should have good energy level alignment and higher photon absorption coefficient. The energy level alignment, LUMO and HOMO band gap cannot be too small, which would result in insufficient driving energy for electron excitation from the dye to the photoanode and dye regeneration by the redox mediator. The dye with the high photo absorption coefficient will have high capability of a chemical species to absorb light at specific wavelength (Wang et al., 2005). Hence, it is of paramount importance to find an appropriate dye that fulfil the above requirement, improving the  $J_{sc}$  and  $V_{oc}$  at the same time.

A more feasible way to improve the efficiency of DSSC is to improve the  $V_{oc}$ . Almost half of the initial photon energy is lost within the cell. In general, the  $V_{oc}$  depends on the difference between the conduction band and the redox potential of the electrolyte species. The most popular electrolyte in DSSC is  $I^-/I_3^-$ . However, its

relatively low redox potential limits the  $V_{oc}$  (Seo et al., 2012). An efficient charge injection requires a driving force of about 100-200 meV. However, the redox potential difference between dye N719 (1.12 V vs. NHE) and  $I/I_3^-$  (0.35 V vs. NHE) exceeded 800 mV. Subsequently, energy is lost during the regeneration of the oxidized dye due to an energy mismatch between the dye and electrolyte. Hence, to keep an improved  $V_{oc}$ , redox couples of more positive redox potentials should be used. Ferrocene/ferrocenium ( $Fc/Fc^+$ ) redox attracted attention as the replacement to  $I/I_3^-$  in DSSC application. The  $Fc/Fc^+$  redox potential (0.62 V) is more positive than the  $I/I_3^-$ , which seems to be a possible way to increase the  $V_{oc}$ . The major challenge, however, is that the recombination rate between the injected photoelectrons is very high (Daeneke et al., 2012). **Figure 2.15** illustrated that the redox potential difference between N719,  $I/I_3^-$  and  $Fc/Fc^+$ . To summarise, it still remains a challenge to find an alternative of electrolyte with reduced dye regeneration driving force and less electron recombination process, but compromising the efficiency of DSSC device.

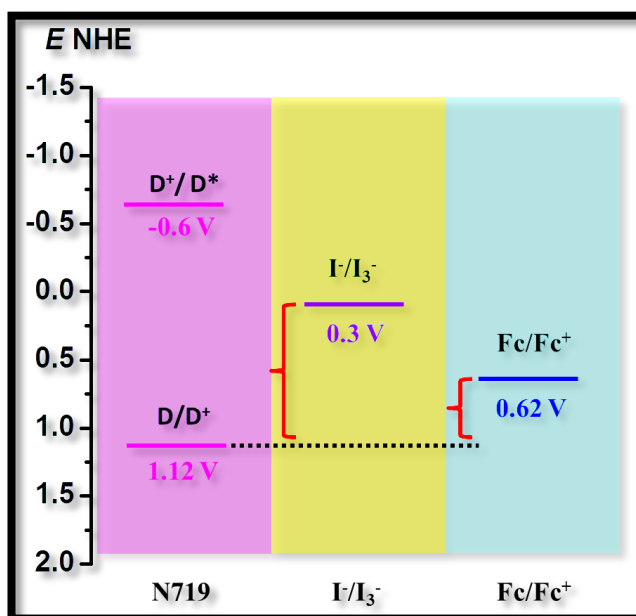


**Figure 2.15** Energy level, approximate redox potentials and band energies of the N719,  $I/I_3^-$  and  $Fc/Fc^+$  versus normal hydrogen electrode (NHE)

### 2.6.2 Low Stability

Long term stability is a key parameter for any type of solar cells. Introduction of DSSC on the market requires stable performance comparable to standard silicon cells. Most of the manufacturers will offer a warranty of 80-90 % of the initial performance after 20 years of cell operation. To fulfil this requirement, besides the power conversion efficiency, stability also serves as a key factor to commercialization. The cell must be extrinsically and intrinsically stable.

The intrinsic stability of a DSSC is usually tested with an accelerated aging experiment lasting for 1000 hr, which is based on the standard test condition requires for silicon cells (Xu et al., 2013). This test will elucidate the thermal stability sensitizer, the electrolyte and counter electrode at 80 °C. Thermal stress pointed out to be one of the most critical factors that determine the long term stability of DSSC. The life-time of the DSSC under thermal stress is strongly related to the chemical composition of the electrolyte solvents and additives.

Intrinsic stability are related to the solar cell under the condition of a perfectly closed/sealed system, while extrinsic factors are related to degradation process induced by the diffusion of molecule into or out from the cell. Penetration of water or escape of solvent is one of the examples for extrinsic factor. To improve the extrinsic stability, little effort has been undertaken to investigate the stability of the sealant in DSSC. Commonly, Surlyn and Bynel films are employed to seal the cells, which help to prevent the leakage or evaporation of the volatile electrolyte (O'Regan et al., 1991). This holment gasket is cheap and easy to process. For the standard acceleration ageing test for DSSC, a temperature of 85 °C is needed. However, due to the low melting point of Surlyn (60 °C), it seems impossible to operate DSSC at temperature more than 60 °C. Since 60 °C can be easily reached on a sunny day, the extrinsic stability based on Surlyn

is not sufficient. For improvement, a new sealant has been developed based on glass fit, which demonstrated are more stability demonstrated at 85 °C but not suitable for large scale production due to the decrease efficiency (Lenzmann et al., 2007). All these testings need to be confirmed under real outdoor condition. It is still questionable if this sealant will be stable for 20 years outdoor.

## CHAPTER 3

### EXPERIMENTAL SECTION

#### 3.1 Materials

The materials and chemicals used in this investigation are summarized in Table 3.1

**Table 3.1** Chemical and materials used in this thesis

Chemicals	Formula	Purity (%)	Supplier
Titanium dioxide	TiO <sub>2</sub>	98.0-100.5	Acros Orgnics
Silver nitrate	AgNO <sub>3</sub>	99.9	Merck
Hydrogen tetrachloroaurate trihydrate	HAuCl <sub>4</sub> .3H <sub>2</sub> O	99.9	Abcr
Urea	CO(NH <sub>2</sub> ) <sub>2</sub>	≥ 98	Merck
Thiourea	S=C(NH <sub>2</sub> ) <sub>2</sub>	≥ 97	Fluka
Sodium borohydride	NaBH <sub>4</sub>	≥ 98	R&M chemicals
Ruthenizer 535-bisTBA (N719)	C <sub>58</sub> H <sub>86</sub> O <sub>8</sub> N <sub>8</sub> S <sub>2</sub> Ru	-	Solaronix
Iodolyte Z-100	-	-	Solaronix
Titanium isopropoxide	Ti[OCH(CH <sub>3</sub> ) <sub>2</sub> ] <sub>4</sub>	98	Acros Orgnics
Indium tin oxide	ITO		Xin Yan Technology Limited

#### 3.2 Synthesis method

##### 3.2.1 Preparation of N-TiO<sub>2</sub>

N-TiO<sub>2</sub> was prepared by mixing P25 and urea (at a 1:1 weight ratio) and grounding it for at least 30 min with a mortar. It was then annealed in a furnace at 400 °C at a heating rate of 10 °C/min in air for 1 h. Subsequently, a pale yellow color N-TiO<sub>2</sub> was obtained.

### 3.2.2 Preparation of N, S-TiO<sub>2</sub>

Initially, 1:1 weight ratio of P25 and thiourea were mixed manually and ground for at least 30 min with a mortar. It was then annealed in furnace at 400 °C with a heating rate of 10 °C/min in air for 1 hr. Subsequently, the pale yellow colour of N, S-TiO<sub>2</sub> was obtained.

### 3.2.3 Synthesis of Ag@TiO<sub>2</sub> Nanocomposite

The Ag@TiO<sub>2</sub> nanocomposite materials were prepared using a simple one-step chemical reduction method. Briefly, 500 mg of TiO<sub>2</sub> were added to aqueous solution that contained different amounts of AgNO<sub>3</sub> (1, 2.5, 5, 10, and 20 wt %). Each mixture was vigorously stirred for 30 min at room temperature. The reduction of Ag<sup>+</sup> was carried out by the drop-wise addition of freshly prepared NaBH<sub>4</sub> until the color changed to greenish yellow. The appearance of this greenish yellow color indicated the formation of the Ag@TiO<sub>2</sub> nanocomposite, and the solution was continually stirred for another 30 min. The Ag@TiO<sub>2</sub> nanocomposite was collected and washed with distilled water and ethanol several times by centrifugation. Finally, the product was dried in an oven at 60 °C and stored under a dark condition.

### 3.2.4 Synthesis of N-TiO<sub>2</sub>-Ag Nanocomposite

The N-TiO<sub>2</sub>-Ag nanocomposite was prepared using a chemical reduction method. Initially, 500 mg of the preformed N-TiO<sub>2</sub> was added to an aqueous solution containing AgNO<sub>3</sub>. The amount of AgNO<sub>3</sub> used for the N-TiO<sub>2</sub> varied from 2.5 to 5, 10, and 20 wt%. The mixture was vigorously stirred for 30 min at room temperature. The reduction of Ag<sup>+</sup> was carried out by the drop-wise addition of freshly prepared NaBH<sub>4</sub> until a

change in the color of the solution was maintained. The yellowish-green appearance of the solution indicated the formation of the N-TiO<sub>2</sub>-Ag nanocomposite, and the solution was continually stirred for another 30 min. The nanocomposite was collected and washed with distilled water and ethanol several times using centrifugation. Finally, the product was dried in an oven at 60 °C and stored in the dark.

### **3.2.5 Synthesis of N,S- TiO<sub>2</sub>-Ag Nanocomposite**

The N,S-TiO<sub>2</sub>-Ag nanocomposite were prepared by a chemical reduction method. 500 mg of N,S-TiO<sub>2</sub> was added to the aqueous solution that containing AgNO<sub>3</sub>. The wt.% of AgNO<sub>3</sub> to N,S-TiO<sub>2</sub> varied from 0, 5, 10, 20 %, and 40%. The mixture was vigorously stirred for 30 min at room temperature. The reduction of Ag<sup>+</sup> was carried out the drop-wise addition of freshly prepared NaBH<sub>4</sub> until the changes of color for the solution maintain. The yellowish green of the solution formed indicated the formation of N,S-TiO<sub>2</sub>-Ag nanocomposite and the solution was continued stirred for another 30 min. The nanocomposite was collected and washed with distilled water and ethanol several times by centrifugation. Finally, the product was dried in an oven at 60 °C.

### **3.2.6 Synthesis of Au-Ag@TiO<sub>2</sub> Nanocomposite**

The Au-Ag@TiO<sub>2</sub> nanocomposite materials were prepared using a simple one-pot chemical reduction method. Briefly, 500 mg of TiO<sub>2</sub> were added to aqueous solutions that contained different composition of HAuCl: AgNO<sub>3</sub> (0:100, 25:75, 50:50, 75:25 and 100:0 wt.%). Each mixture was vigorously stirred for 30 min at room temperature. The reduction of Au(III) and Ag(I) were carried out by the drop-wise addition of NaBH<sub>4</sub> until the colour changed to greenish yellow or purple. The appearance of these greenish yellow or purple colours indicated the formation of the Ag@TiO<sub>2</sub> or Au-Ag@TiO<sub>2</sub> or

Au@TiO<sub>2</sub> nanocomposite, and the colloidal suspensions were continually stirred for another 30 min. The nanocomposite was collected and washed with distilled water and ethanol several times by centrifugation. Finally, the product was dried in an oven at 60 °C and stored under a dark condition.

### **3.2.7 Fabrication of TiO<sub>2</sub> based Nanocomposite Modified Photoanode**

TiO<sub>2</sub> based nanocomposite (including Ag@TiO<sub>2</sub>, N-TiO<sub>2</sub>-Ag, N, S- TiO<sub>2</sub>-Ag and Au/Ag@TiO<sub>2</sub>) modified photoanodes were fabricated using the following procedure. Initially, 300 mg of TiO<sub>2</sub> based nanocomposite was mixed in 1 mL of an ethanolic solution and stirred for 30 min. A 0.1 M of TTIP was slowly introduced into the above reaction mixture and stirred for at least 1 hr until homogenous solution is obtained. Finally, the TiO<sub>2</sub> based nanocomposite were coated on a conducting side of the ITO using the doctor-blade technique with the aid of scotch-3M tape and the thickness of the film was ~12 µm. In order to obtain a stable photoanode, the film was dried at room temperature, sintered at 150 °C for 30 min in a muffle furnace, and then allowed to cool naturally to room temperature.

### **3.2.8 Fabrication of DSSCs and Evaluation of Their Performance**

The prepared TiO<sub>2</sub> nanocomposite (including Ag@TiO<sub>2</sub>, N-TiO<sub>2</sub>-Ag, N, S- TiO<sub>2</sub>-Ag and Au/Ag@TiO<sub>2</sub>) photoanodes were immersed into the ethanolic solution of 0.3 mM N719 (Ruhenizer 535-bisTBA) dye for 24 h at room temperature. The dye-adsorbed photoanode was withdrawn from the solution and immediately cleaned with ethanol. A platinum sputtered ITO was placed on dye-absorbed photoanode and then clamped firmly together. An electrolyte (Iodolyte Z-100, Solaronix) solution was introduced into the cell assembly by capillary action. An active area of 0.5 cm<sup>2</sup> was used to measure the cell performance. A 150 W Xenon arc lamp (Newport, Model

69907) containing simulated AM 1.5G filter with a manual shutter was used as a light source for the throughout the experiments. Prior to test the photovoltaic parameter, Avaspec-2048 fibre optic spectrophotometer was used to measure the light illumination intensity. The photocurrent density-photovoltage measurements (J-V curves) were carried out with an active electrode area of  $0.5 \text{ cm}^2$  using a computer-controlled VersaSTAT 3 electrochemical workstation (Princeton Applied Research, USA).

### **3.3 Characterization Techniques**

After synthesis of plasmonic nanocomposite, the samples were characterized by various characterization techniques to study the crystal structures, optical properties, morphology and elemental compositions.

#### **3.3.1 X-ray Diffraction (XRD)**

X-ray diffraction (XRD) takes advantages of the coherent scattering of x-ray of crystalline materials to acquire a wide range of crystallographic information. The samples in this work were analysed using XRD (Siemens D5000) with monochromatic Cu K $\alpha$  radiation ( $\lambda = 1.5406 \text{ \AA}$ ) operated at 40 kV and 40 mA with a scanning speed of  $0.02 \text{ degrees s}^{-1}$ , scanning from  $5\text{-}80^\circ$ . The atomic structure was analysed using the PANanalytical X'pert Highscore software. The orientation of the planes in the crystal lattice also can be analysed by assigning three integers (h k l) known as Miller indices. From the (h k l) plane, we can determine the phase of TiO<sub>2</sub> such as rutile, anatase or bookite phase.

### **3.3.2 X-ray Photoelectron Spectroscopy (XPS)**

X-ray photoelectron spectroscopy (XPS) is used to measure the elemental composition, chemical stoichiometry, chemical state and electronic state on the element that presence in the samples. X-ray is used as the light source for the excitement of the electrons that bond in the inner core-level orbital. The bonding energy of the photoelectrons will provide the information of material where the electron is escaped. In this study, XPS measurements were performed using synchrotron radiation from beamline no. 3.2 at the Synchrotron Light Research Institute, Thailand.

### **3.3.3 Raman Spectroscopy**

Raman spectroscopy is a spectroscopic technique relies on inelastic scattering (Raman scattering) of monochromatic light (from laser source) interacts with a sample. Photons of the laser light are absorbed and then reemitted by a sample. The reemitted photons are shifted up or down (Raman shift) in comparison with original monochromatic frequency will provide information about vibrational, rotational and other low frequency transition in molecules. Raman is commonly employed in assessing molecular motion and fingerprint of species. In this thesis, Raman spectra were recorded using a Renashaw's inVia Raman microscope with a 514 nm laser. The measurements were scanned from in the range of 100-3000  $\text{cm}^{-1}$ . The peaks obtained from the spectrum will give the information about the molecular structure of the sample.

### **3.3.4 Ultraviolet-Visible Absorption Spectroscopy**

The chemical changed can also be confirmed by examining the shifting in the wavelength of the intensity. The optical absorption properties in the spectral region of 190–900 nm were assessed using a Avaspec UV–vis spectrometer. Furthermore, an

estimation band-gap energy can also be calculated using a well-known Tauc's plot method  $[(Ah\nu)^n \text{ vs. } h\nu]$  through the UV-vis spectra, where A is a constant, n is the power of the exponent (n=2 for a direct allowed transition and n=1/2 for an indirect allowed transition) and  $h\nu$  is the incident photon energy. The band gap energy can be obtained by extrapolation to the x-axis.

### **3.3.5 Photoluminescence Spectroscopy**

Understanding the charge recombination process for a semiconductor is crucial because it would significantly influence the photoelectrochemical properties and DSSC performance. The recombination of photoinduced electrons and holes releases energy in the form of photoluminescence. Photoluminescence spectra were collected using a Renishaw 2000 system with an argon ion laser emitting at 325 nm.

### **3.3.6 Electron Microscopy**

The morphology of the films was examined using field emission scanning electron microscopy (Hitachi, SU 8000) Transmission electron microscopy TEM (Hitachi, HT-7700) and high resolution TEM (JEOL JEM-2100 F). Element composition in the samples was identified using Energy dispersive X-ray Spectroscopy (EDX) measurement. Size of the metal particle can be measured using i-solution software.

## **3.4 Electrochemical Characterization**

Electrochemical measurements including cyclic voltammetry (CV) and electrochemical impedance spectroscopy (EIS) were used with computer-controlled VersaSTAT 3 electrochemical workstation (Princeton Applied Research, USA) to

understand the photovoltaic properties and characterizing the interfacial charge transfer process of photoanode.

### 3.4.1 Photocurrent–Photovoltage (J-V) Measurement

Current-voltage curve measurements are the most central way to characterize the photovoltaic performance of DSSC device. The photocurrent-photovoltage measurement of a DSSC is performed using Electrochemical Workstation under illumination of solar light. J-V curve is a useful technique as a quick screening procedure to identify potential working electrode material. In these measurements, the device is placed under a linear bias voltage scan and the generated photocurrent recorded. From the J-V curve, the conversion efficiency can be determined using **Eqn. 3.2** and **3.3**.

$$FF = \frac{V_m \times J_m}{V_{oc} \times J_{oc}} \quad \text{Eqn. 3.2}$$

$$\eta = \frac{V_{oc} \times J_{sc} \times FF}{I_s} \quad \text{Eqn. 3.3}$$

### 3.4.2 Electrochemical Impedance Spectroscopy (EIS)

Electrochemical impedance spectroscopy (EIS); the response function of alternating current (ac) generated in response to alternating voltage (av) provide a convenient way to characterize the interfacial charge transfer process of an electrode. The EIS was carried out in the frequency range between 0.01 Hz and 100 KHz with an AC amplitude of 10 mV.

## CHAPTER 4

### **Enhanced Photovoltaic Performance of Silver@Titania Plasmonic Nanocomposite Modified Photoanode in Dye-Sensitized Solar Cells**

#### **4.1 Introduction**

Renewable energy sources are the most important approaches and signify an important method for gaining independence from fossil fuels. Utilizing solar energy is certainly one of the most viable ways to solve the world's energy crisis. Dye-sensitized solar cells (DSSCs) have emerged as promising candidates for harnessing solar power because of their low cost, flexibility, ease of production, relatively high energy conversion efficiency, and low toxicity to the environment (O'Regan et al., 1991). Since first being introduced by Gratzel and co-workers in 1991, many strategies have been employed to achieve high-performance DSSCs, including novel counter electrodes, electrolytes, dyes, and semiconductor photoanode materials. Among these, the photoanode plays a crucial role in determining the cell performance. So far, titanium dioxide ( $\text{TiO}_2$ )-based material is one of the most promising materials for a DSSC due to its low cost, abundance, nontoxicity, safety, large surface area for maximum dye uptake and matched energy and band structure (Chen et al., 2012; Tao et al., 2013). However, the major drawback associated with the use of  $\text{TiO}_2$  is its random electron transport, which will cause the electron-hole recombination process and hence affect the overall performance (Kopidakis et al., 2005; van de Lagemaat et al., 2000).

There is an active search to overcome the deficiency of  $\text{TiO}_2$ -based DSSCs such as through surface modification with metal nanoparticles, doping of metals and non-metals, semiconductor coupling, and hybridizing with carbon materials (Lai et al., 2010; Macak et al., 2007; Yang et al., 2007; Zhao et al., 2007). In the present decade, surface of  $\text{TiO}_2$  has been modified with noble metal nanoparticles such as silver (Ag),

with the aim of improving the efficiency of a DSSC. The Ag nanoparticles play dual roles in the DSSC performance, including the enhancement of the absorption coefficient of the dye and optical absorption due to surface plasmonic resonance (Eagen, 1981; Mock et al., 2002; Schaadt et al., 2005). Moreover, they act as an electron sink for photoinduced charge carriers, improve the interfacial charge transfer process, and minimize the charge recombination, thereby enhancing the electron transfer process in a DSSC (Lee et al., 2008; Wen et al., 2000; Zhao et al., 1997). Hence, the performance of a DSSC with Ag@TiO<sub>2</sub> plasmonic nanocomposite material-modified photoanodes has been actively investigated (Lee et al., 2008; Wen et al., 2000; Zhao et al., 1997).

To make use of economically viable Ag to boost the DSSC performance, it is essential to control both the size and distribution of the nanoparticles on the TiO<sub>2</sub> surface. Two methods are commonly employed for Ag-TiO<sub>2</sub> nanocomposite preparation: (i) a two-step method involving the chemical and physical adsorption of preformed Ag nanoparticles on the TiO<sub>2</sub> surface (Binyu et al., 2011; Chou et al., 2009; Qi et al., 2011) and (ii) the photoreduction of Ag on the TiO<sub>2</sub> surface (Chen et al., 2010; Photiphitak et al., 2011). However, these synthetic methods are ineffective because of the aggregation of Ag nanoparticles in the first method and the difficulty controlling the size of the Ag nanoparticles in the later one.

In the present study, we successfully developed a facile synthesis method to prepare uniformly distributed Ag nanoparticles deposited on TiO<sub>2</sub> using a simple one-step chemical reduction method without adding any stabilizer or surfactant for DSSC application. The as-prepared Ag@TiO<sub>2</sub> plasmonic nanocomposites were characterized using various suitable analytical techniques and used as photoanodes in the DSSCs. The Ag@TiO<sub>2</sub> plasmonic nanocomposite-modified photoanode showed an enhanced solar

energy conversion efficiency compared to that of a bare  $\text{TiO}_2$ -based DSSC. The effect of the Ag content on the DSSC performance was also investigated. There are many positive aspects of the Ag-modified  $\text{TiO}_2$ , including the synergetic interaction of the Ag nanoparticles on the  $\text{TiO}_2$  surface, surface plasmon resonance effect, reduction of the band gap, and enhancement of the charge transfer process. These multifunctional properties of the prepared  $\text{Ag@TiO}_2$  plasmonic nanocomposite will lead to superior performance in a DSSC.

## **4.2 Results and Discussion**

### **4.2.1 Optical Properties of $\text{Ag@TiO}_2$ Nanocomposite Materials**

In the present synthetic method (Detailed synthetic method is given in Chapter: 3; Section: 3.2.3), the formation of the  $\text{Ag@TiO}_2$  nanocomposite takes place through the adsorption of  $\text{Ag}^+$  ions on the  $\text{TiO}_2$  surface, followed by the chemical reduction of  $\text{Ag}^+$  by  $\text{NaBH}_4$  at room temperature in the absence of any stabilizer and surfactant (**Figure 4.1(a)**). The physical appearances of the  $\text{Ag@TiO}_2$  with different quantities of Ag (wt %) are shown in **Figure 4.1(b)**, shows that the nanocomposite becomes darker in color with increasing Ag content.

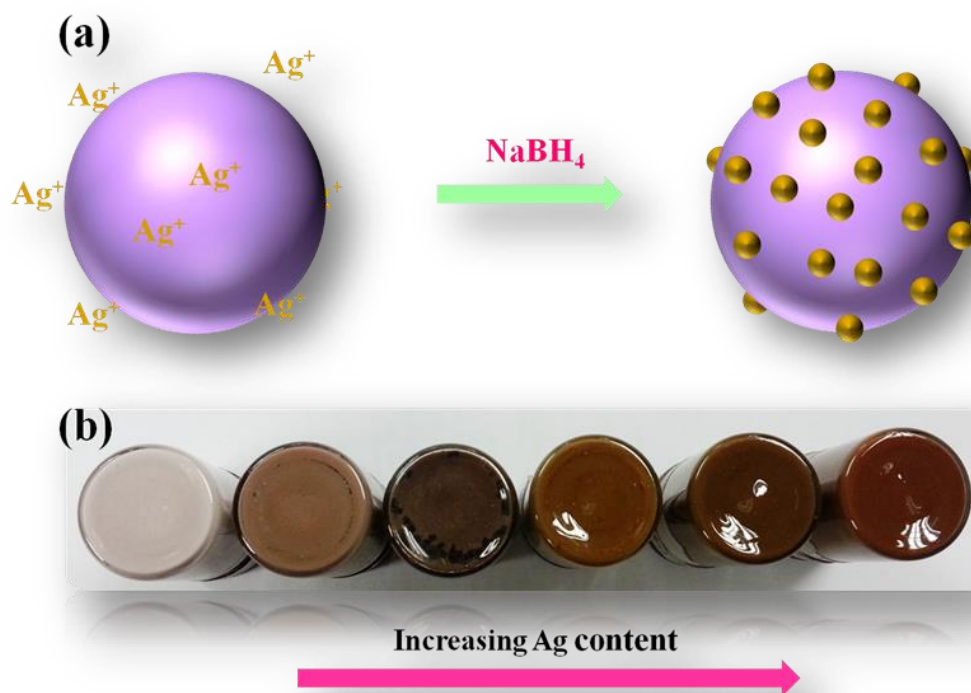


**Figure 4.1** Schematic representation of formation of Ag on  $\text{TiO}_2$  surface and (b) physical appearance of as-prepared  $\text{Ag@TiO}_2$  nanocomposites with different Ag content.

The UV-vis absorption spectra of the  $\text{TiO}_2$  and  $\text{Ag@TiO}_2$  were recorded and are shown in **Figure 4.2(A)**. The  $\text{TiO}_2$  did not show any absorbance in the visible region (**Figure 4.2(A)**) because of the wide band gap ( $\sim 3.2$  eV). The deposition of Ag on the  $\text{TiO}_2$  surface significantly influenced the absorption in the visible regions of 450 and 500 nm, which was due to the surface plasmon resonance (SPR) band of Ag nanoparticles (Photiphitak et al., 2011; Tian et al., 2013). A considerable shift in the adsorption edge toward the visible region was also observed for the  $\text{Ag@TiO}_2$  sample. The presence of Ag nanoparticles significantly influenced the visible light absorption properties of  $\text{TiO}_2$ . The band-gap energy ( $E_{\text{bg}}$ ) of the prepared  $\text{TiO}_2$  and  $\text{Ag@TiO}_2$  were calculated using a well-known Tauc's plot method (Lim et al., 2014b; Pandikumar et al., 2013). The relations of  $(\alpha h\nu)^2$  versus  $h\nu$  for the  $\text{TiO}_2$  and  $\text{Ag@TiO}_2$  are shown in **Figure 4.2(B and C)**. It can be observed that the band-gap energy values of  $\text{TiO}_2$  decreased from 3.36 eV to 3.22 eV with the addition of Ag nanoparticles. This has been

due to the presence of Ag, which decreased the absorbance band edge of TiO<sub>2</sub> close to the visible region.

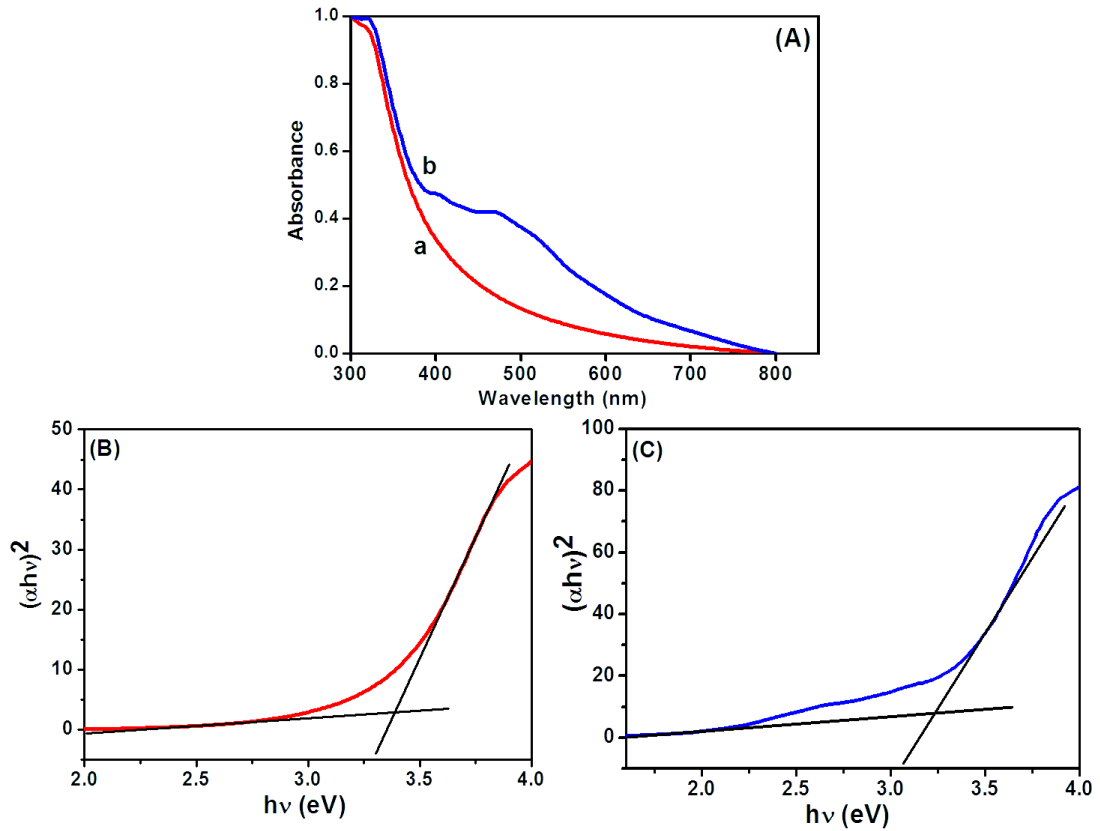


**Figure 4.2** (A) Absorption spectra of (a) TiO<sub>2</sub> and (b) Ag@TiO<sub>2</sub>. Plots of  $(\alpha h\nu)^2$  versus  $h\nu$  obtained for (B) TiO<sub>2</sub> and (C) Ag@TiO<sub>2</sub>.

Understanding the charge recombination process of a photoanode material is crucial because it can significantly influence the photovoltaic performance of a DSSC. The TiO<sub>2</sub> will absorb incident photons with sufficient energy equal to or higher than the band-gap energy. This will produce photoinduced charge carriers ( $h^+ \dots e^-$ ), and the recombination of photoinduced electrons and holes will release energy in the form of photoluminescence. Hence, a lower PL intensity indicates less charge recombination. The TiO<sub>2</sub> showed a broad and high PL intensity at around 580 nm due to the high photoinduced charge carrier recombination, whereas the PL intensity was minimized upon the addition of Ag on the TiO<sub>2</sub> surface (**Figure 4.3(A)**). This was mainly attributed to the formation of the Schottky barrier at the Ag/TiO<sub>2</sub> interface, which could act as an electron sink to efficiently prevent the electron–hole recombination process (Du et al.,

2006). The Ag@TiO<sub>2</sub> with 2.5 wt. % Ag showed the lowest PL emission intensity, which indicated the least electron–hole recombination compared to Ag contents of 1, 10, and 20 wt. % on the TiO<sub>2</sub> (**Figure 4.3(B)**).

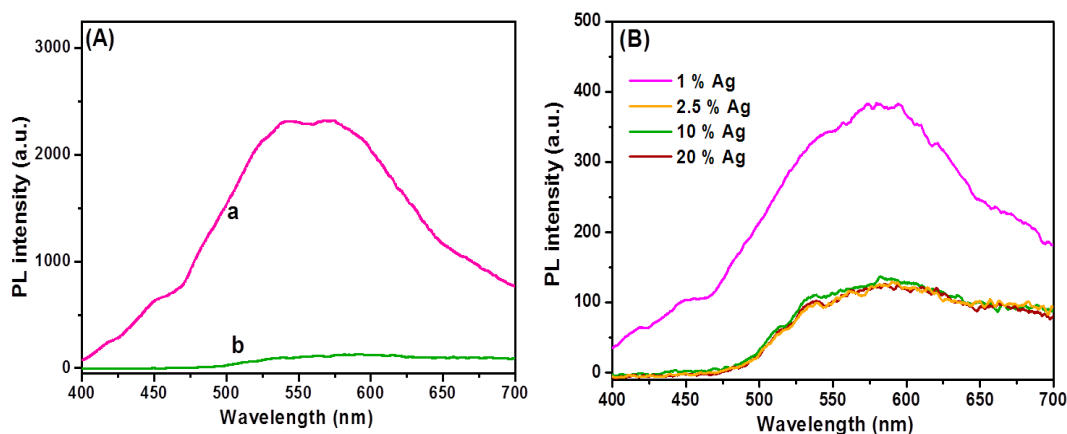


**Figure 4.3** (A) Photoluminescence spectra of (a) TiO<sub>2</sub> and (b) Ag@TiO<sub>2</sub> nanocomposites under 325-nm laser excitation. (B) Photoluminescence spectra of Ag@TiO<sub>2</sub> nanocomposites with different Ag contents under 325-nm laser excitation.

#### 4.2.2 Crystalline Properties of Ag@TiO<sub>2</sub> Nanocomposite Materials

The X-ray diffraction patterns indicated that the TiO<sub>2</sub> and Ag@TiO<sub>2</sub> were composed of mixed anatase and rutile phases (**Figure 4.4**), which was in good agreement with the reference patterns of JCPDS card Nos. 83-2243 and 21-1276, respectively. The diffraction peaks observed at the 2 $\theta$  values of 25.42°, 38.68°, 48.15°, and 74.4° corresponded to the anatase phase of TiO<sub>2</sub> and were assigned to the (101), (004), (200), and (215) crystallographic planes, respectively. In contrast, the peaks at the 2 $\theta$  values of 54.08° and 63.81° agreed well with the rutile phase of TiO<sub>2</sub> and were assigned to the (220) and (002) crystallographic planes, respectively. The crystallographic peaks due to the Ag overlapped with those for the rutile phase of the TiO<sub>2</sub>. Hence, the peaks were indistinguishable in Ag@TiO<sub>2</sub>.

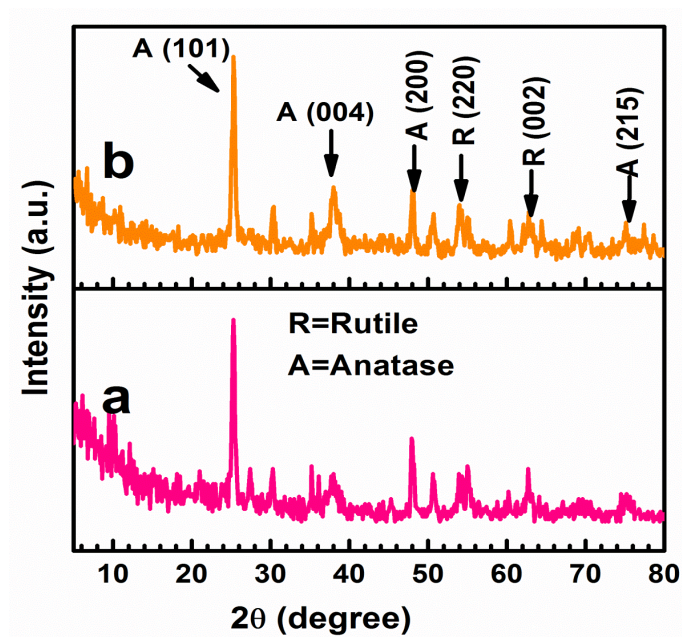


**Figure 4.4** X-ray diffraction patterns of (a) TiO<sub>2</sub> and (b) Ag@TiO<sub>2</sub> nanocomposites.

To further evaluate the phase identification of the TiO<sub>2</sub> and Ag@TiO<sub>2</sub>, Raman spectroscopy was performed in the range of 100–1000 cm<sup>-1</sup>, and the results are shown in **Figure 4.5**. The anatase TiO<sub>2</sub> phase was observed at 153, 198, 396, 516, and 637 cm<sup>-1</sup>, whereas the rutile TiO<sub>2</sub> phase was detected at 443 cm<sup>-1</sup> (Chandrasekharan et al., 2000; Chiarello et al., 2010; Sivaranjani et al., 2011). This clearly indicated that the TiO<sub>2</sub> and Ag@TiO<sub>2</sub> nanoparticles contained a mixture of anatase and rutile phases. No signals related to Ag particles were identified for the samples because of the relatively low concentration of Ag loaded onto the TiO<sub>2</sub> and its weak Raman scattering. An interesting observation is that the peak intensities were reduced by the presence of Ag, but the position of the Raman signal remained the same and was broadened. This indicated that the interaction between the Ag and TiO<sub>2</sub> affected the Raman resonance of the TiO<sub>2</sub> (Su et al., 2012). This observation showed the successful deposition of Ag on the TiO<sub>2</sub> surface without any phase transition (Pandikumar et al., 2013; Sivaranjani et al., 2011).

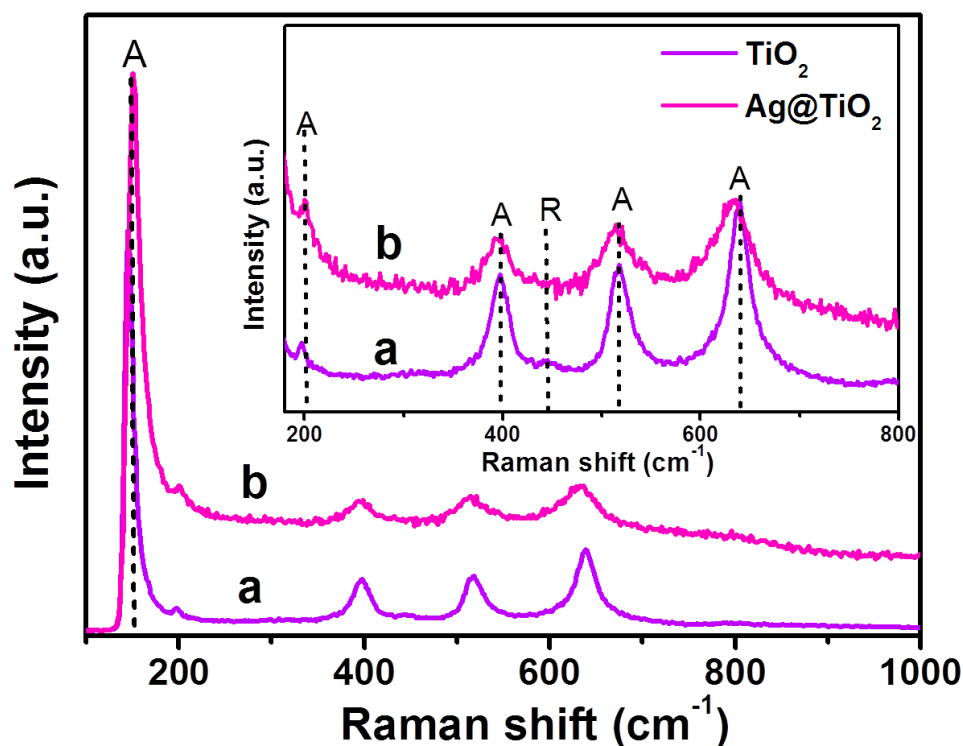


**Figure 4.5** Raman spectra of (a)  $\text{TiO}_2$  and (b)  $\text{Ag@TiO}_2$  nanocomposites with inset showing the anatase and rutile features of  $\text{TiO}_2$ .

#### 4.2.3 XPS Analysis of $\text{Ag@TiO}_2$ Nanocomposite Materials

The XPS spectra of the  $\text{TiO}_2$  and  $\text{Ag@TiO}_2$  were recorded to understand their chemical nature and are shown in **Figure 4.6**. **Figure 4.6(a)** shows the Ti 2p core level spectra for both samples, in which two peaks are observed at 454.1 and 459.9 eV corresponding to the binding energies of the Ti 2p<sub>3/2</sub> and Ti 2p<sub>1/2</sub> core levels due to the presence of the Ti(IV) state (Briggs, 1981). After the deposition of the Ag nanoparticles, it is obviously observed that the Ti 2p peak was shifted to lower binding energies due to its surrounding chemical environment (Wang et al., 2014). **Figure 4.6(b)** shows the O 1s spectra of the  $\text{TiO}_2$  and  $\text{Ag@TiO}_2$ , and the binding energy of the O 1s state of the samples is located at 530.9 eV, which is assigned to the bulk oxides ( $\text{O}^{2-}$ ) in the P25 lattice. The O 1s is slightly shifted to higher binding energies which indicate the increase in electron density around O atoms due to the interaction of residue precursor with  $\text{TiO}_2$  (Tian et al., 2013). The binding energy found for the Ag 3d<sub>5/2</sub> and Ag 3d<sub>3/2</sub>

levels are 367.5 and 373.5 eV, respectively (**Figure 4.6(C)**), with a peak separation of 6 eV due to the metallic silver(Tian et al., 2013). The XPS analysis provided support for the existence of elements such as Ti, O, and Ag in the nanocomposite materials.

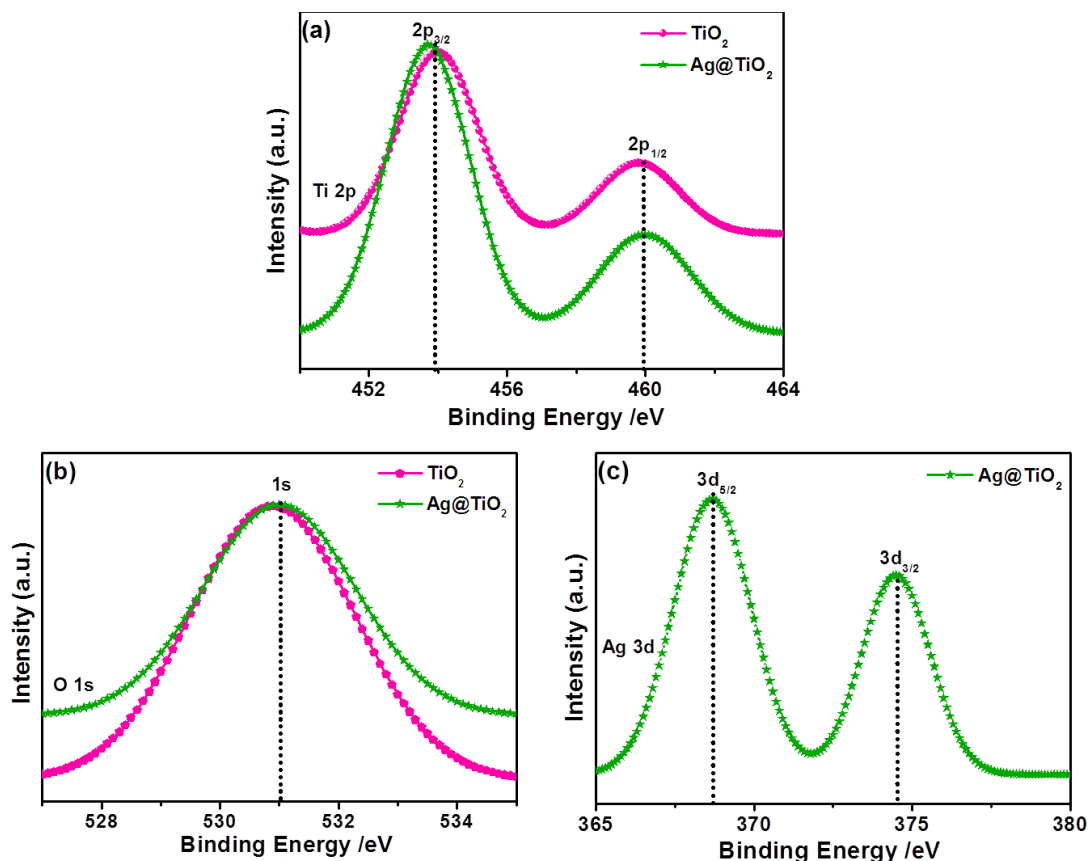


**Figure 4.6** XPS spectra of TiO<sub>2</sub> and Ag@TiO<sub>2</sub> and their corresponding (a) Ti 2p (b) O 1s, and (c) Ag 3d core-level spectra.

#### 4.2.4 Morphological Studies of Ag@TiO<sub>2</sub> Nanocomposite Materials

The microscopic morphologies of the as-prepared samples were studied using FESEM, TEM, and HRTEM. **Figure 4.7** shows the FESEM results for TiO<sub>2</sub>, which appear to be spherical with a uniform size. Upon the addition of Ag, no significant change in morphology was observed for the film (**Figure 4.7(b)**). The EDX analysis results are shown in **Figure 4.8 (c)**, which shows Ti, O, C, and Ag. The C peak found in the EDAX spectrum is a result of carbon tape. Further, TEM images of TiO<sub>2</sub> and

Ag@TiO<sub>2</sub> (2.5 wt% Ag) were also recorded and are shown in **Figure 4.8 (a and b)**, respectively. The TEM image shows that the Ag@TiO<sub>2</sub> nanoparticles are spherical in shape, with the TiO<sub>2</sub> particles having a size range of 20–25 nm. **Figure 4.8 (b)** clearly shows the deposition of distributed spherical and smaller Ag nanoparticles (2–4 nm) on the surface of TiO<sub>2</sub>. **Figure 4.8 (c)** depicts the selected area electron diffraction (SAED) pattern of the nanocrystalline TiO<sub>2</sub> particles. This pattern clearly reveals bright concentric rings, which are due to the diffraction from the (211), (200), (004), and (101) planes of anatase TiO<sub>2</sub>. The lattice resolved HRTEM image of the Ag@TiO<sub>2</sub> (**Figure 4.8 (d)**) shows d-spacing values for the lattice fringes of 2.28 Å and 2.50 Å, which correspond to the (200) and (101) rutile planes of TiO<sub>2</sub>, respectively; whereas the interplanar spacing of 1.89 Å was assigned to the (200) plane of anatase TiO<sub>2</sub>. In **Figure 4.8 (e)**, the areas of bright contrast on the element maps correlate with the Ti, O, and Ag signal maps.

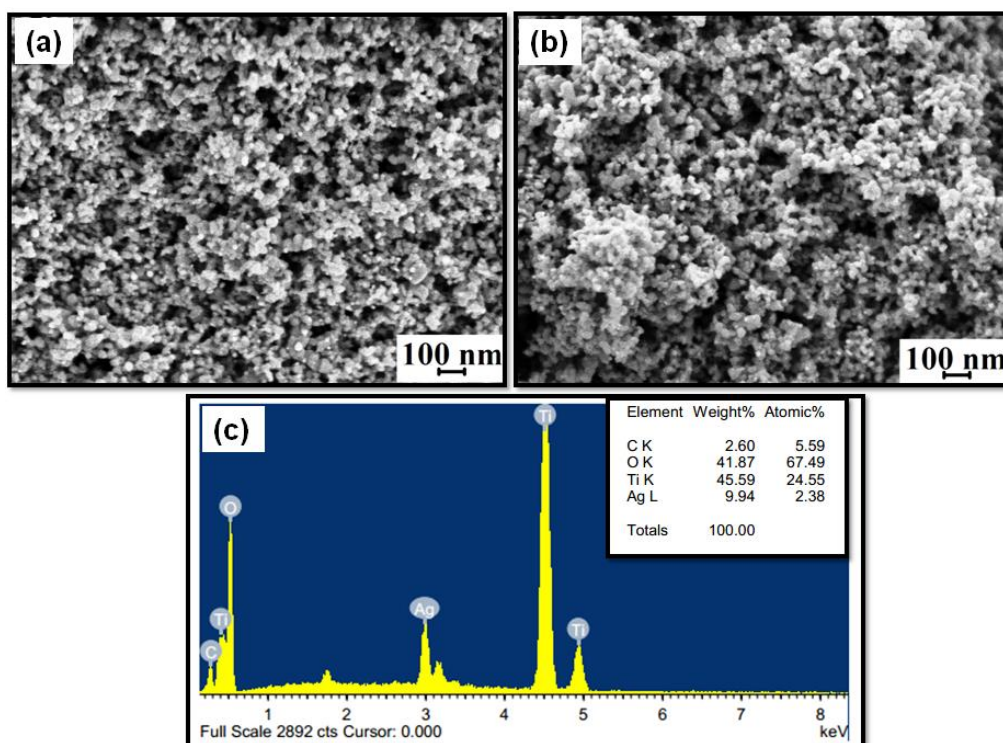


**Figure 4.7** FESEM images of (a) TiO<sub>2</sub>, (b) Ag@TiO<sub>2</sub> and (c) EDX analysis of Ag@TiO<sub>2</sub> nanocomposite.

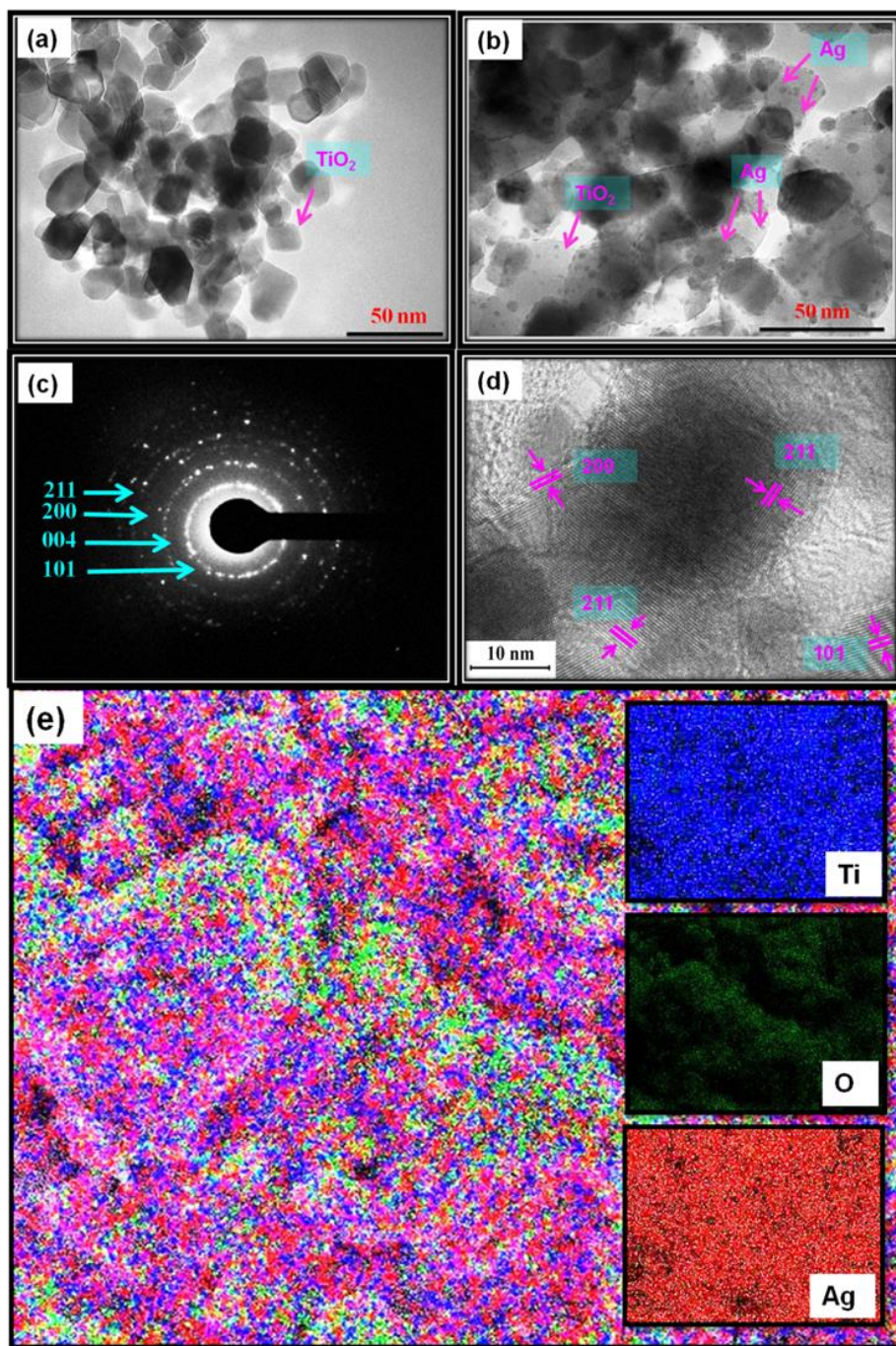


**Figure 4.8** TEM image of (a) TiO<sub>2</sub> and (b) Ag@TiO<sub>2</sub> nanocomposites, (c) SAED pattern, (d) lattice-resolved TEM image, and (e) elemental mapping of Ag@TiO<sub>2</sub> nanocomposite.

#### 4.2.5 Photovoltaic Performances of Ag@TiO<sub>2</sub> Plasmonic Nanocomposite-Modified Photoanode-Based DSSCs

The photovoltaic performances of the Ag@TiO<sub>2</sub> plasmonic nanocomposite-modified photoanode-based DSSCs with different Ag contents were evaluated under simulated solar AM 1.5G irradiation. Their obtained photocurrent density and

photovoltage (J–V) curves are shown in **Figure 4.9**, and their evaluated photovoltaic parameters are listed in **Table 1**. The Ag@TiO<sub>2</sub> plasmonic photoanode (2.5 wt.% of Ag) showed a higher efficiency (4.86 %) than the unmodified TiO<sub>2</sub> (2.57 %). The enhanced photovoltaic performance may have been due to the plasmonic effect and rapid interfacial charge transfer that arose from the Ag nanoparticles on the TiO<sub>2</sub>. The optimization of Ag on TiO<sub>2</sub> is essential from the economic and high-performance perspectives for a DSSC. Although increasing the Ag content on the TiO<sub>2</sub> surface beyond 2.5 wt.% showed a decrease in the conversion efficiency to 3.59 %, the observed results clearly revealed that the conversion efficiency of a DSSC was increased with an increase in the Ag content of the photoanode until it reached a maximum of 2.5 %. Then, a further increase in the Ag content eventually led to the decrease in conversion efficiency (**Figure 4.9 and Table 4.1**). The decrease in the efficiency at high Ag loading is due to the free standing/excess Ag in the composite may oxidized to Ag(I) (Guo et al., 2013; Zhao et al., 1997) and eroded by the electrolyte (Zhao et al., 1997). The oxidation of the Ag will act as new recombination centre, thus reducing the number of the charge carrier led to decrease in the  $J_{sc}$  and  $V_{oc}$ . Consequently, the overall conversion efficiency of the DSSC would have deteriorated. Moreover, the addition of Ag more than 2.5 wt. % might result in decrease of the active surface area of TiO<sub>2</sub> interacted with the dye molecules. Hence, the recombination between the electrons and holes will increase leads to decrease of  $J_{sc}$  value. The relationships between the photovoltaic parameters and Ag content on the TiO<sub>2</sub> surface are represented in **Figure 4.10(a-c)** for better understanding.

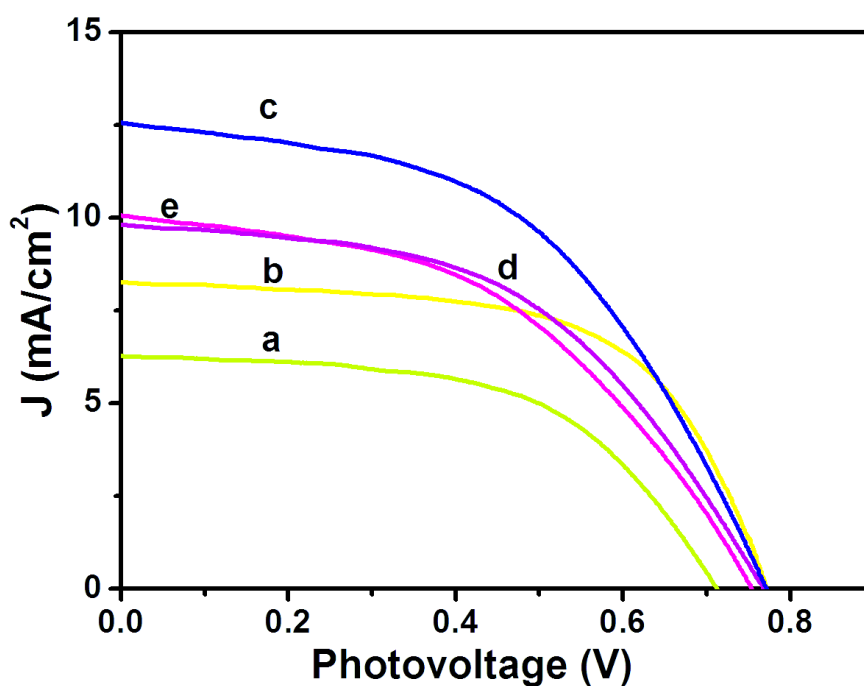


**Figure 4.9** Photocurrent density–photovoltage ( $J$ – $V$ ) curves obtained for Ag@TiO<sub>2</sub> nanocomposite thin films with (a) 0, (b) 1, (c) 2.5, (d) 10, and (e) 20 wt% of Ag content under 100 mW cm<sup>−2</sup> simulated AM 1.5G solar light irradiation.

**Table 4.1** Photovoltaic parameters of Ag@TiO<sub>2</sub> nanocomposite-modified photoanode-based DSSCs with different Ag contents.

Ag (wt.%)	$J_{sc}$ (mA/cm <sup>2</sup> )	$V_{oc}$ (V)	$J_{max}$ (mA/cm <sup>2</sup> )	$V_{max}$ (V)	$FF$	$\eta$ (%)
0	6.71	0.71	5.24	0.49	0.54	2.57
1	8.17	0.77	6.63	0.60	0.63	3.98
2.5	12.19	0.77	9.34	0.52	0.52	4.86
10	9.93	0.77	7.65	0.49	0.49	3.75
20	9.96	0.75	7.68	0.45	0.48	3.59

**Footnote:** The DSSC performance was evaluated under 100 mW cm<sup>−2</sup> simulated AM 1.5G solar light irradiation.  $J_{sc}$ : Short-circuit current density;  $V_{oc}$ : Open-circuit voltage;  $J_{max}$ : Maximum photocurrent density;  $V_{max}$ : Maximum photovoltage;  $FF$ : Fill factor;  $\eta$ : Power conversion efficiency. Area of the cell electrode was 0.5 cm<sup>2</sup>.

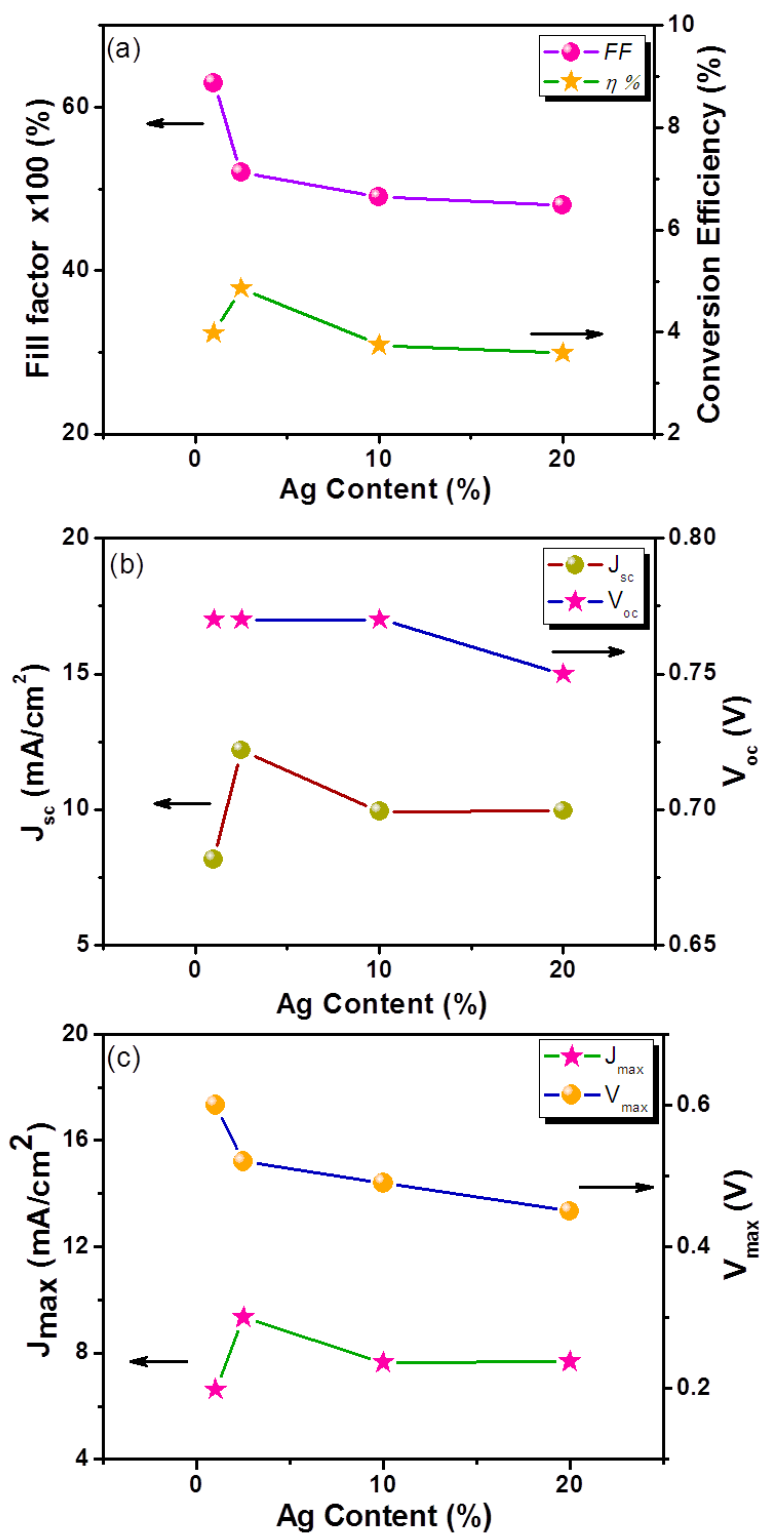


**Figure 4.10** Plots of (a) Fill factor (FF) and power conversion efficiency ( $\eta$ ), (b) short-circuit current density ( $J_{sc}$ ) and open-circuit voltage ( $V_{oc}$ ) and (c) maximum photocurrent density ( $J_{max}$ ) and maximum photovoltage ( $V_{max}$ ) with different Ag content for the Ag@TiO<sub>2</sub> nanocomposites based DSSCs.

#### 4.2.6 Electrochemical Behaviour of Ag@TiO<sub>2</sub> Plasmonic Photoanode-Based DSSCs

In order to gain deeper insight into the interfacial charge transfer process within the fabricated DSSC, the electrochemical impedance spectra (EIS) were recorded in a frequency range between 0.01 Hz and 100 KHz, and are shown in **Figure 4.11**. A well-defined semicircle in the middle-frequency region can be observed for the TiO<sub>2</sub> and Ag@TiO<sub>2</sub> based DSSCs. The intersection of a high-frequency semicircle at the real axis represents the equivalent series resistance of the device ( $R_s$ ); the arc in the middle-frequency range between 1 and 1000 Hz represents the charge transfer resistance ( $R_{ct}$ ) between the dye-adsorbed photoanode and the electrolyte interface (Binyu et al., 2011; Qi et al., 2011). From the Nyquist plot (**Figure 4.11(A)**), the  $R_s$  values for the TiO<sub>2</sub> and Ag@TiO<sub>2</sub> nanocomposite-based DSSCs are 21.03  $\Omega$  and 23.96  $\Omega$ , respectively. The  $R_{ct}$  value increased from 8.77  $\Omega$  to 9.01  $\Omega$ , after the addition of the Ag. This increase in the  $R_{ct}$  value could affect the open-circuit voltage ( $V_{oc}$ ) and fill factor (FF) of the DSSC device. Therefore, the origin of the higher  $J_{sc}$  in the Ag@TiO<sub>2</sub> is expected to arise from the device resistance ( $R_s$ ) and charge transport dynamics determined by the electron lifetime ( $\tau_n$ ) and  $R_{ct}$ . Based on the Bode phase plots in **Figure 4.12 (B)**, the frequency was apparently shifted to a lower frequency region with the addition of Ag. The maximum frequencies ( $\omega_{max}$ ) in the middle-frequency region of the Bode plots for TiO<sub>2</sub> and Ag@TiO<sub>2</sub> were 2511.89 Hz and 1995.26 Hz, respectively. Because  $\omega_{max}$  is inversely associated with the electron lifetime  $\tau_n = 1/(2\pi f)$  (Archana et al., 2014; Kim et al., 2013), a decrease in  $\omega_{max}$  indicates a reduced rate for the charge-recombination process in the DSSC. Electrons with longer  $\tau_n$  values will survive from the recombination. Therefore, it will be characterized by a larger  $R_{ct}$ .

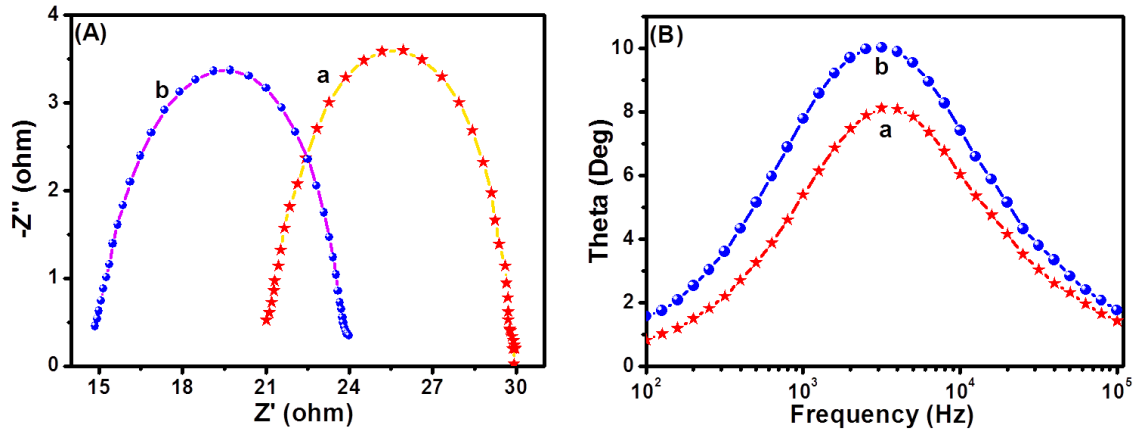


**Figure 4.11** (A) Nyquist plots and (B) Bode angle phase plots for (a)  $\text{TiO}_2$  and (b)  $\text{Ag@TiO}_2$  nanocomposite (2.5 wt% of Ag content)-based DSSCs.

Furthermore, **Table 2** and **Figure 4.11** summarize the results of the Nyquist plot. The  $\text{Ag@TiO}_2$  exhibited a faster electron transport time ( $\tau_s = R_s * C_\mu$ ) (Kim et al., 2013; Nissfolk et al., 2006; Wang et al., 2008) than the  $\text{TiO}_2$ . Hence its electron lifetime ( $\tau_n = R_{ct} * C_\mu$ ) (Kim et al., 2013; Nissfolk et al., 2006; Wang et al., 2008) was significantly increased and survived from the recombination. The photovoltaic performance of the DSSC is clearly reflected by the charge collection efficiency ( $\eta_c$ ) (Kim et al., 2013; Nissfolk et al., 2006; Wang et al., 2008) derived from  $\eta_c = (1 + R_s/R_{ct})^{-1}$ . Eventually, the charge collection efficiency was significantly increased with the addition of Ag. We can conclude that because of the longer  $\tau_n$  and larger  $R_{ct}$ , the devices fabricated using  $\text{Ag@TiO}_2$  showed improved  $J_{sc}$  values compared to  $\text{TiO}_2$ .

**Table 4.2** Electrochemical parameters of TiO<sub>2</sub> and Ag@TiO<sub>2</sub> nanocomposite-based DSSCs.

Photoanode	$R_s (\Omega)$	$R_{ct} (\Omega)$	$C_\mu (\mu F)$	$\tau_s (ms)$	$\tau_n (ms)$	$\eta_c (\%)$
TiO <sub>2</sub>	21.13	8.77	7.22	0.15	0.06	29
Ag@TiO <sub>2</sub>	23.93	9.01	8.85	0.13	0.08	38

**Footnote:** The electrochemical impedance spectra (EIS) were recorded at an applied bias of -0.7 V in the frequency range of 0.01 Hz to 100 KHz.  $R_s$ : Device resistance;  $R_{ct}$ : Charge transfer resistance;  $C_\mu$ : Chemical capacitance;  $\tau_s$ : Electron transport time;  $\tau_n$ : Electron lifetime;  $\eta_c$ : Charge collection efficiency.

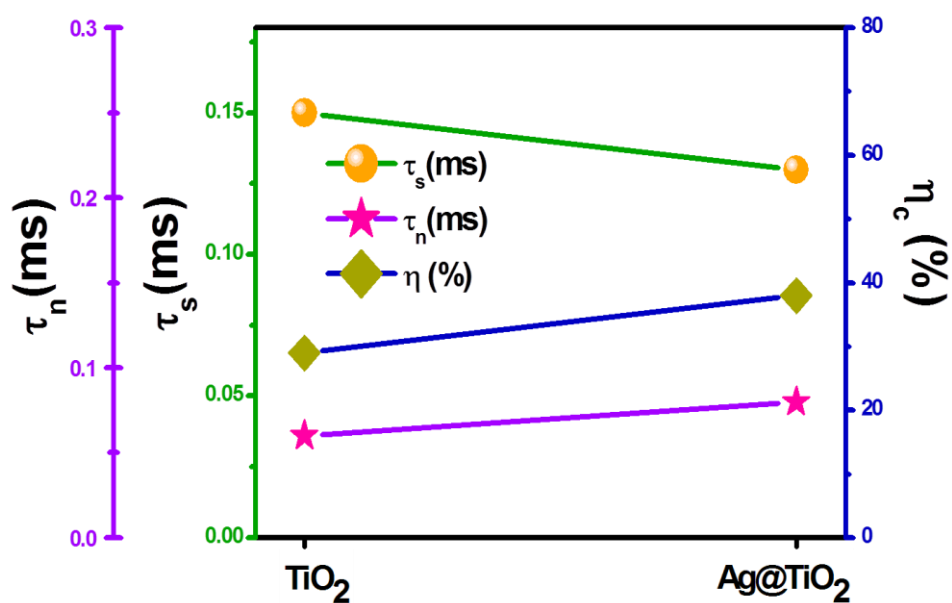


**Figure 4.12** Electron lifetime, electron transport time and charge collection efficiency of the TiO<sub>2</sub> and Ag@TiO<sub>2</sub> nanocomposite modified photoanode based DSSCs.

#### 4.2.7 Operation Principle of Ag@TiO<sub>2</sub> Plasmonic Photoanode-Based DSSC

The operation principle of the DSSC based on the Ag@TiO<sub>2</sub>-modified photoelectrode under illumination is shown in **(Figure 4.13)**. During light irradiation, the dye absorbs incident light and promotes electrons to the excited state. An excited electron is injected into the conduction band of the TiO<sub>2</sub> nanoparticles. The dye is then oxidized by receiving the electron from the electrolyte through the redox system, and is ready to be used again. The electrolyte itself will regenerate via the platinum counter-electrode by an electron passing through the external circuit. In our study, the Ag deposited onto the TiO<sub>2</sub> surface not only acted as an electron sink for the photoinduced charge carriers but could also be used as a scattering element for plasmonic scattering to trap the light and near field coupled with the dye molecules (Lin et al., 2012). This will eventually improve the optical absorption of the dye, resulting in a significant enhancement of the photocurrent **(Figure 4.13)**. Whenever the TiO<sub>2</sub> comes to contact with Ag, both will undergoes Fermi level equilibration to each other, resulted in the formation of Schottky barrier and thus led to large numbers of electron are accumulated at the surface of the metal (Ag) nanoparticles. This accumulation of electrons on the Ag nanoparticles shifted the position of the Fermi level closer to the conduction band of TiO<sub>2</sub> (Ni et al., 2007). The Schottky barrier formed between the Ag and TiO<sub>2</sub> helps to flow the electrons from the Ag to TiO<sub>2</sub> conduction band *via* rapid interfacial charge transfer process and were collected by the current collector (ITO), thus improve the photocurrent generation under irradiation (Christopher et al., 2010). Once the electrons being transfer to the conduction band of TiO<sub>2</sub>, the photo-excited electrons from the dye, N719, will start to accumulate on Ag surface again. Furthermore, the formation of Schottky barrier at the Ag/TiO<sub>2</sub> interface, which could act as an electron sink, also will help to prevent the electron–hole recombination process (Du et al., 2006). The similar

report also available for the metal-semiconductor (Ag-TiO<sub>2</sub>) photoanode sensitized with N719 based DSSC (Tian et al., 2013).

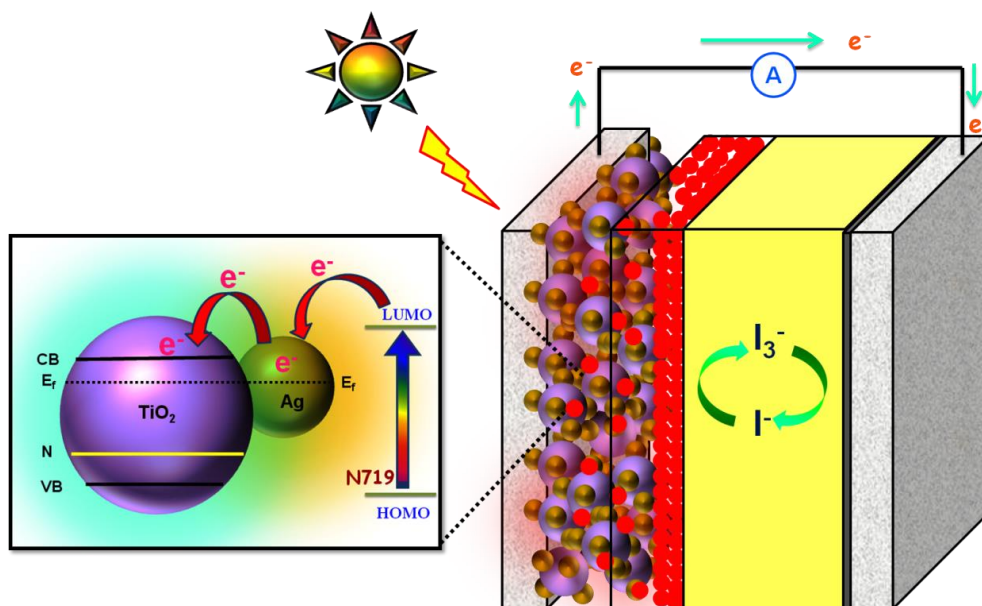


**Figure 4.13** Schematic functions of Ag@TiO<sub>2</sub> nanocomposite-modified photoanode-based dye-sensitized solar cells.

### 4.3 Conclusion

In conclusion, plasmonic silver nanoparticles modified titania (Ag@TiO<sub>2</sub>) nanocomposite materials with various Ag contents were synthesized by simple chemical reduction method without using any stabilizer and surfactants. The as-prepared Ag@TiO<sub>2</sub> plasmonic nanocomposite materials were used as photoanode in the dye-sensitized solar cells to investigate the solar to electrical energy conversion ability. The incorporation of Ag on the TiO<sub>2</sub> surface significantly influenced the optical properties in the region of 400–500 nm because of the surface plasmon resonance effect and the formation of 2–4 nm sized Ag nanoparticles on the TiO<sub>2</sub> was confirmed through the HRTEM. The DSSC assembled with the Ag@TiO<sub>2</sub>-plasmonic photoanode demonstrated an enhanced solar-to-electrical energy conversion efficiency (4.86 %) than that of bare TiO<sub>2</sub> (2.57 %) under an AM 1.5 G simulated solar irradiation of 100 mW cm<sup>-2</sup>, due the surface plasmon resonance effect of Ag nanoparticles present in the

nanocomposites. The influence of the Ag content on the overall efficiency was also investigated, and the optimized Ag content with  $\text{TiO}_2$  was found to be 2.5 wt.%. The enhanced solar energy conversion efficiency of the  $\text{Ag@TiO}_2$  plasmonic nanocomposite makes it a promising alternative to conventional photoanode-based DSSCs.

## CHAPTER 5

### Promotional Effect of Silver Nanoparticles on the Photovoltaic Performance of N-doped TiO<sub>2</sub> Photoanode-Dye-Sensitized Solar Cells

#### 5.1 Introduction

Out of consideration for natural resource depletion and environmental issues, dye-sensitized solar cells (DSSCs) have emerged as promising candidates for harvesting solar power, because of their low cost, flexibility, ease of production, relatively high energy conversion efficiency, and low toxicity to the environment (O'Regan et al., 1991). Encouragingly, significant progress has been achieved for DSSCs by introducing novel components such as electrolytes and dyes, along with various morphologies for the semiconductor materials. It is apparent that the further improvement of DSSCs is a key factor to accelerating their industrialization. Materials based on semiconductor oxides, especially titanium dioxide (TiO<sub>2</sub>), have potential for DSSC applications. The major drawback associated with the use of TiO<sub>2</sub> is the random manner of its electron transport, which will cause the electron–hole recombination process and hence affect the cell performance (Kopidakis et al., 2005; van de Lagemaat et al., 2000). In order to overcome this problem, designing a photoanode with an efficient transport pathway from the photoinjected charge carriers to the current collector seems to be a possible alternative to enhance the performance of DSSCs. With this aim, methods such as surface modification with metal, doping, semiconductor coupling, and hybridizing with carbon materials have been attempted (Lai et al., 2010; Macak et al., 2007; Yang et al., 2007; Zhao et al., 2007).

Nitrogen-doped TiO<sub>2</sub> possesses good photovoltaic properties. Hence, it has received much attention due to the narrowing of the band gap and shift to the visible region. The major limitation of the N-doping is the low concentration of N dopants that

can be doped in the  $\text{TiO}_2$  lattice, because the unstable N dopants in the  $\text{TiO}_2$  lattice may escape to become  $\text{N}_2$  or oxynitrides (Batzill et al., 2006; Graciani et al., 2008; Nambu et al., 2006). Meanwhile, the photogenerated electrons tend to recombine at the mono-doping type of dopant sites, which is another limitation of N-doped  $\text{TiO}_2$ -based DSSCs (Gai et al., 2009; Zhang et al., 2011). In order to overcome these limitations, N-doped  $\text{TiO}_2$  has been modified with a noble metal such as Au (Pandikumar et al., 2013), Ag (Gao et al., 2013), and Pt (Gao et al., 2013; Huang et al., 2007) to prevent the recombination of the photogenerated electron-hole pairs and improve the charge transfer efficiency. In addition, studies have reported that the introduction of metal nanoparticles to the N-doped  $\text{TiO}_2$  surface could enhance the amount of N that could be stabilized in  $\text{TiO}_2$ .  $\text{TiO}_2$ -Ag nanocomposites have shown improved DSSC performances, since the Ag nanoparticles act as an electron sink for the photoinjected charge carriers and also show the plasmonic absorption effect, which maximizes the DSSC efficiency (Lim et al., 2014b; Su et al., 2012). The co-deposition of Ag on the N-doped  $\text{TiO}_2$  is more beneficial and has shown enhanced photocatalytic properties due to the synergistic effect that arises between the Ag and N-doped  $\text{TiO}_2$  (Gao et al., 2013; Zhang et al., 2011).

Based on the above literature, so far the N- $\text{TiO}_2$  and  $\text{TiO}_2$ -Ag have been used separately as photoanodes in DSSCs. In this study, we explored the co-deposition of Ag nanoparticles on N-doped  $\text{TiO}_2$  as a photoanode for a DSSC. We successfully developed a facile synthetic route to deposit Ag nanoparticles on N- $\text{TiO}_2$  using a simple chemical reduction method and characterized it using various analytical techniques. The DSSC assembled with the N- $\text{TiO}_2$ -Ag-modified photoanode showed an enhanced conversion efficiency of 8.15% compared to the unmodified  $\text{TiO}_2$  (2.19%). This enhanced efficiency due to the reduced band gap energy and retarded charge

recombination resulted from the introduction of plasmonic Ag nanoparticles on the surface of N-TiO<sub>2</sub>. The influence of the Ag content on the overall efficiency was also explored, and the optimum content was 10 wt%. This novel N-TiO<sub>2</sub>-Ag nanocomposite could be a potential candidate for solar energy conversion.

## 5.2 Results and Discussion

### 5.2.1 Morphological Studies of N-TiO<sub>2</sub>-Ag Nanocomposite

The microscopic morphologies of the as-prepared N-TiO<sub>2</sub>-Ag nanocomposite (detailed preparation procedure is given in Chapter: 3; Section: 3.2.4) were studied using FESEM, TEM, and HRTEM. **Figure 5.1(a)** shows the FESEM results for N-TiO<sub>2</sub>, which appears to be spherical in shape with a uniform size. Upon the addition of Ag, no significant change in the morphology was observed for the film (**Figure. 5.1(b)**). The presence of Ag and N on the TiO<sub>2</sub> was confirmed by element mapping, as shown in **Figure 5.1(c)** and the N-TiO<sub>2</sub>-Ag thin film contained Ti, O, N, and Ag. Further, TEM images of the N-TiO<sub>2</sub>-Ag were recorded and are shown in **Figure 5.1(d)**. The TEM images show that the N-TiO<sub>2</sub> nanoparticles are spherical in shape, with a particle size range of 20–25 nm. **Figure 5.1(e)** clearly shows that the small spherical Ag nanoparticles with a particle size range of 2–4 nm are well distributed and decorated on the surface of the N-TiO<sub>2</sub>. **Figure 5.1(f)** depicted the selected area electron diffraction (SAED) pattern of the nanocrystalline particles. The pattern clearly reveals bright concentric rings, which are due to the diffraction from the (211), (111), (004), and (101) planes of the anatase TiO<sub>2</sub>. The lattice resolved HRTEM image of the N-TiO<sub>2</sub>-Ag (**Figure 5.1(g)**) shows d-spacing values for the lattice fringes of 2.18 Å, 1.68 Å, 2.49 Å, and 1.89 Å, which correspond to the (111), (211), (101), and (200) planes of TiO<sub>2</sub>.

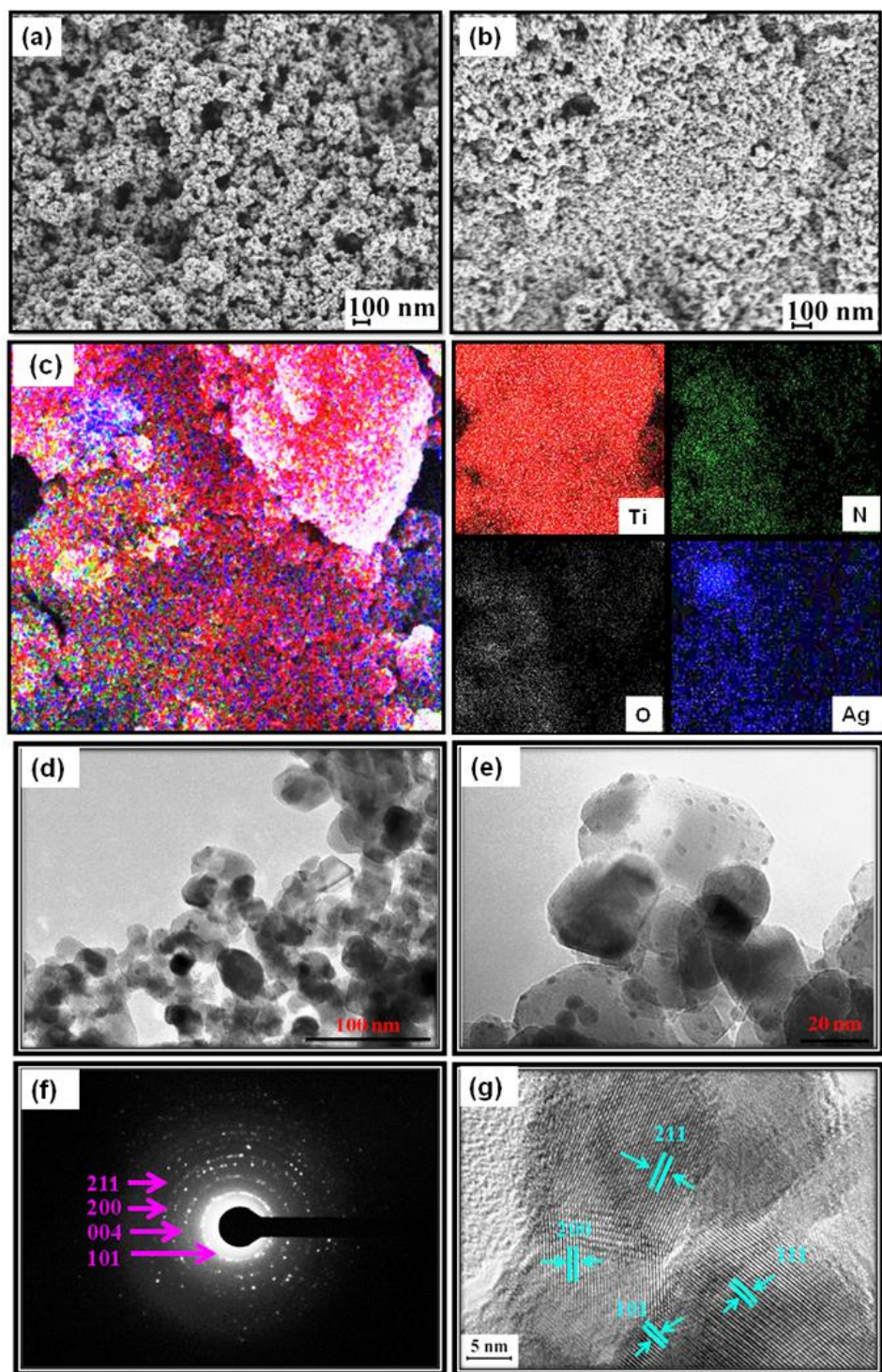


**Figure 5.1** FESEM images of (a) N-TiO<sub>2</sub> and (b) N-TiO<sub>2</sub>-Ag. (c) EDAX element mapping, (d and e) TEM images, (f) SAED pattern, and (h) lattice resolved TEM image of N-TiO<sub>2</sub>-Ag.

### 5.2.2 XPS Analysis of N-TiO<sub>2</sub>-Ag Nanocomposite

The XPS spectra of the TiO<sub>2</sub>, N-TiO<sub>2</sub>, and N-TiO<sub>2</sub>-Ag were recorded to understand their chemical natures and are shown in **Figure 5.2**. **Figure 5.2(a)** shows the Ti 2p core-level spectra for the samples, in which two prominent peaks are observed at 454.1 and 459.9 eV corresponding to the binding energies of the Ti 2p<sub>3/2</sub> and Ti 2p<sub>1/2</sub> core levels due to the presence of the Ti(IV) state. **Figure 5.2(b)** shows the O 1s spectra of the TiO<sub>2</sub>, N-TiO<sub>2</sub> and N-TiO<sub>2</sub>-Ag, and the binding energy of the O 1s state of the samples is located at 530.9 eV, which is assigned to the bulk oxides (O<sup>2-</sup>) in the P25 lattice. The binding energy of the N 1s atom is observed at 399.5 eV (**Figure 5.2(c)**). The binding energies found for the Ag 3d<sub>5/2</sub> and Ag 3d<sub>3/2</sub> levels are observed at 367.5 and 373.5 eV, respectively (**Figure 5.2(d)**), with a peak separation of 6 eV due to the metallic silver. The XPS analysis results provide support for the existence of elements such as Ti, O, N, and Ag in the nanocomposite materials.

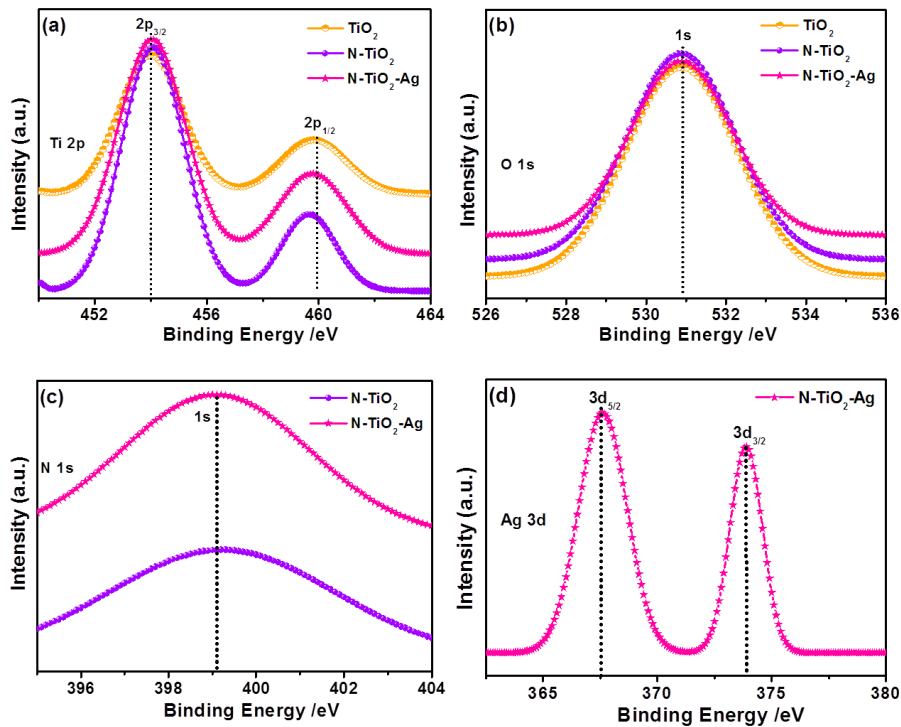


**Figure 5.2** XPS spectra of TiO<sub>2</sub>, N-TiO<sub>2</sub>, and N-TiO<sub>2</sub>-Ag and their corresponding (a) Ti 2p (b) O 1s (c) N 1s, and (d) Ag 3d core-level spectra.

### 5.2.3 Crystalline Nature of N-TiO<sub>2</sub>-Ag Nanocomposite

The XRD obtained pattern obtained for the N-TiO<sub>2</sub>-Ag nanocomposite is shown in **Figure 5.3**, together with those for the TiO<sub>2</sub> and N-TiO<sub>2</sub>. The TiO<sub>2</sub>, N-TiO<sub>2</sub>, and N-TiO<sub>2</sub>-Ag films are composed of mixed anatase and rutile phases, which agree with reference patterns JCPDS 83-2243 and 21-1276, respectively. The diffraction peaks at 25.3 °, 38.8 °, 48.35 °, and 74.5 ° correspond to the anatase phase of TiO<sub>2</sub> and are assigned to the (101), (004), (200), and (215) crystallographic planes, respectively. In contrast, the peaks at 54.08 ° and 63.21 ° agree well with the rutile phase of TiO<sub>2</sub> and are assigned to the (220) and (002) crystallographic planes, respectively. The diffraction peaks related to the metallic Ag are located at 38.2 °, 44.4 °, and 64.6 °, and they overlap each other. Thus, it is difficult to differentiate the Ag signals from the TiO<sub>2</sub> signals.

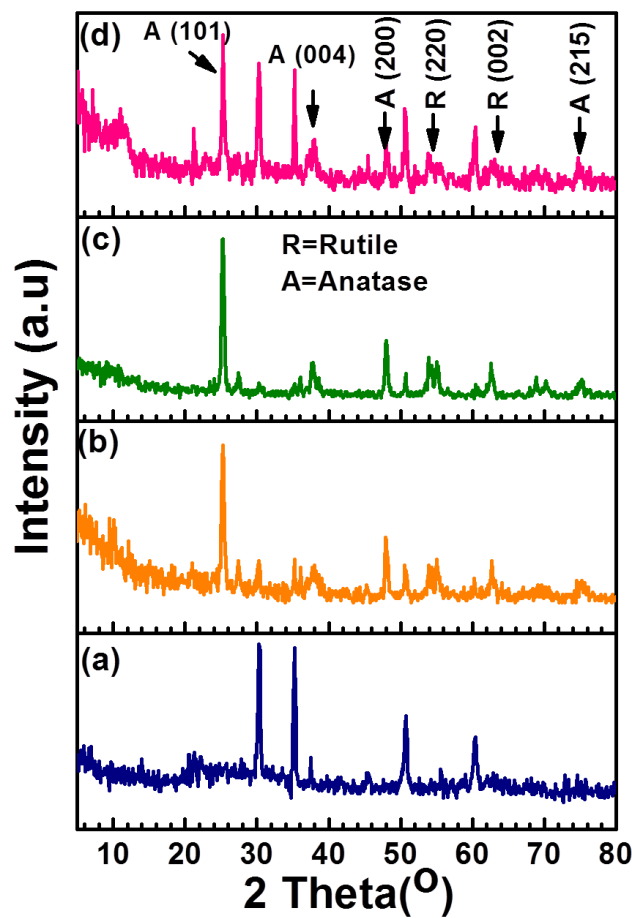


**Figure 5.3** X-ray diffraction patterns of (a) ITO, (b) TiO<sub>2</sub>, (c) N-TiO<sub>2</sub>, and (d) N-TiO<sub>2</sub>-Ag.

To further evaluate the phases in the prepared films, Raman studies were performed in the range of 100–1000  $\text{cm}^{-1}$ , and the results are shown in **Figure 5.4(a)**. The observed Raman peaks at 144, 199, 397, 516, and 635  $\text{cm}^{-1}$  are due to the anatase phase  $\text{TiO}_2$ . The rutile  $\text{TiO}_2$  phase was observed at 445  $\text{cm}^{-1}$  (Chiarello et al., 2010; Lim et al., 2014b; Sivaranjani et al., 2011). This clearly indicates that the  $\text{TiO}_2$  and N- $\text{TiO}_2$  nanoparticles contain a mixture of the anatase and rutile phases. The Raman signals of  $\text{TiO}_2$  did not change after doping with nitrogen, which indicated that no phase transition occurred. However, no signals related to Ag particles were identified for the samples because of the relatively low concentration of Ag loaded onto the  $\text{TiO}_2$  and its weak Raman scattering power. An interesting observation is that the peak intensities decreased with the deposition of Ag, although the position of the Raman signal remained the same but broadened. This indicates that there was an interaction between the Ag and  $\text{TiO}_2$  that affected the Raman resonance of  $\text{TiO}_2$  (Su et al., 2012). This observation shows that the deposition of Ag on  $\text{TiO}_2$  and N- $\text{TiO}_2$  does not cause any phase transition, but may bring about an electronic environment change in the surroundings (Chiarello et al., 2010; Ohsaka et al., 1978; Pandikumar et al., 2013; Sivaranjani et al., 2011).

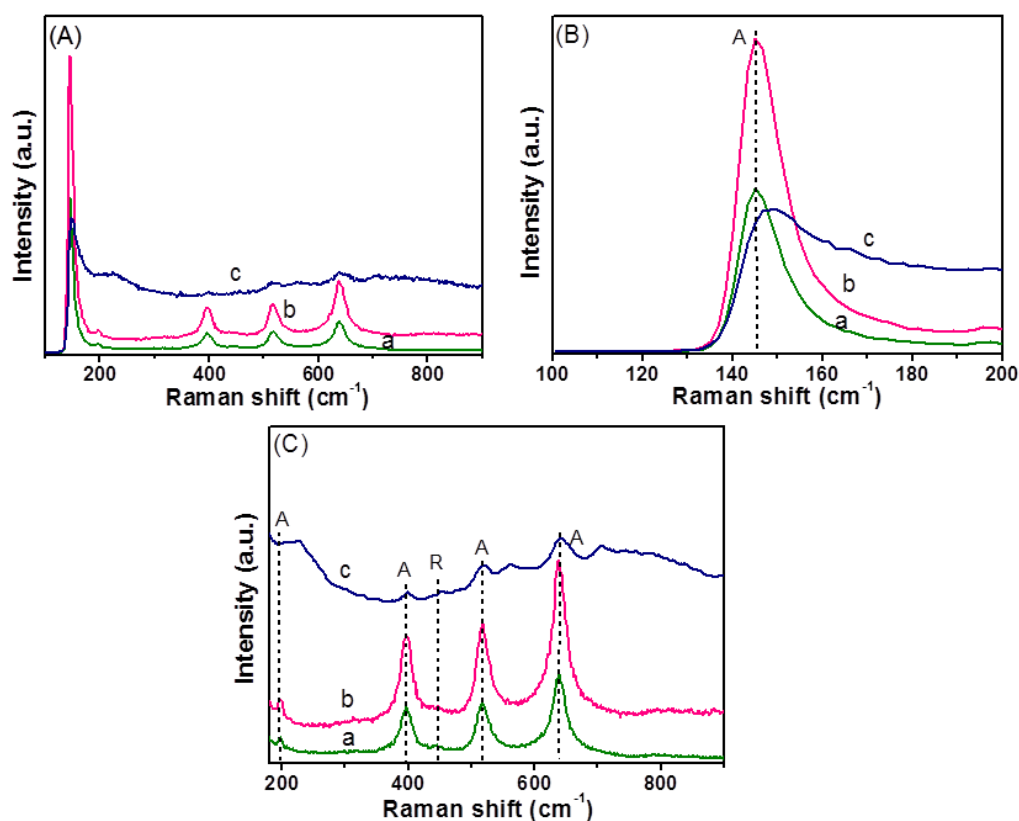


**Figure 5.4** Raman spectra of (a)  $\text{TiO}_2$ , (b)  $\text{N-TiO}_2$ , and (c)  $\text{N-TiO}_2\text{-Ag}$  in different frequency regions: (A)  $100\text{--}900\text{ cm}^{-1}$ , (B)  $100\text{--}200\text{ cm}^{-1}$ , and (C)  $180\text{--}900\text{ cm}^{-1}$ , which are provided separately for better clarity of the anatase and rutile phase  $\text{TiO}_2$ .

#### 5.2.4 Optical Properties of $\text{N-TiO}_2\text{-Ag}$ Nanocomposite

The UV-vis absorption spectra of the  $\text{TiO}_2$ ,  $\text{N-TiO}_2$ , and  $\text{N-TiO}_2\text{-Ag}$  were recorded and are shown in **Figure 5.5 (a)**. It can be seen that the prepared samples showed an intense absorption in the UV region. The bare  $\text{TiO}_2$  could not absorb the visible light, and the onset absorption started to drop at 380 nm. This revealed that the prepared  $\text{N-TiO}_2$  and  $\text{N-TiO}_2\text{-Ag}$  exhibited a wider and stronger absorption of visible light than the  $\text{TiO}_2$ . In addition, all of the  $\text{N-TiO}_2\text{-Ag}$  exhibited a significant absorption of both ultraviolet and visible light, along with an absorption band observed at  $\sim 500\text{ nm}$  due the Ag nanoparticles' characteristic surface plasmon resonance (SPR) band. The SPR effect of the Ag nanoparticles could extend the light absorption to longer wavelength, increasing the light scattering and rousing the photogenerated carriers in

the semiconductor by transferring the plasmonic energy from the Ag to the N-TiO<sub>2</sub> and N-TiO<sub>2</sub> semiconductor (Linic et al., 2011). Upon the deposition of Ag on the TiO<sub>2</sub> and N-TiO<sub>2</sub> surfaces, the Schottky barrier was formed between the Ag and the TiO<sub>2</sub> and N-TiO<sub>2</sub>, which acted as an electron sink, thus enhancing the separation of electron–hole pairs (Lu et al., 2013). Further, it was found that simultaneously doping TiO<sub>2</sub> with N and modifying it with Ag made its band gap narrow, which is beneficial for improving the solar energy conversion efficiency. The band-gap energies ( $E_{bg}$ ) of the TiO<sub>2</sub>, N-TiO<sub>2</sub>, and N-TiO<sub>2</sub>-Ag were calculated using the well-known Tauc's plot method (**Figure 5.5(b-d)**) (Lim et al., 2014b). The calculated  $E_{bg}$  values for TiO<sub>2</sub>, N-TiO<sub>2</sub>, and N-TiO<sub>2</sub>-Ag were 3.31, 3.23, and 3.04 eV, respectively. A remarkable reduction in the  $E_{bg}$  value for N-TiO<sub>2</sub> was observed due to the substitution of oxygen by nitrogen in the TiO<sub>2</sub> lattice. Mixing the N 2p states with the O 2p states resulted in a narrowing of the  $E_{bg}$  of TiO<sub>2</sub>. When Ag nanoparticles were added to N-TiO<sub>2</sub>, the  $E_{bg}$  was further decreased. This was because the free electron properties were exhibited with a downward shift in the conduction band and an upward shift in the valence band, which led to a decrease in the band-gap value.

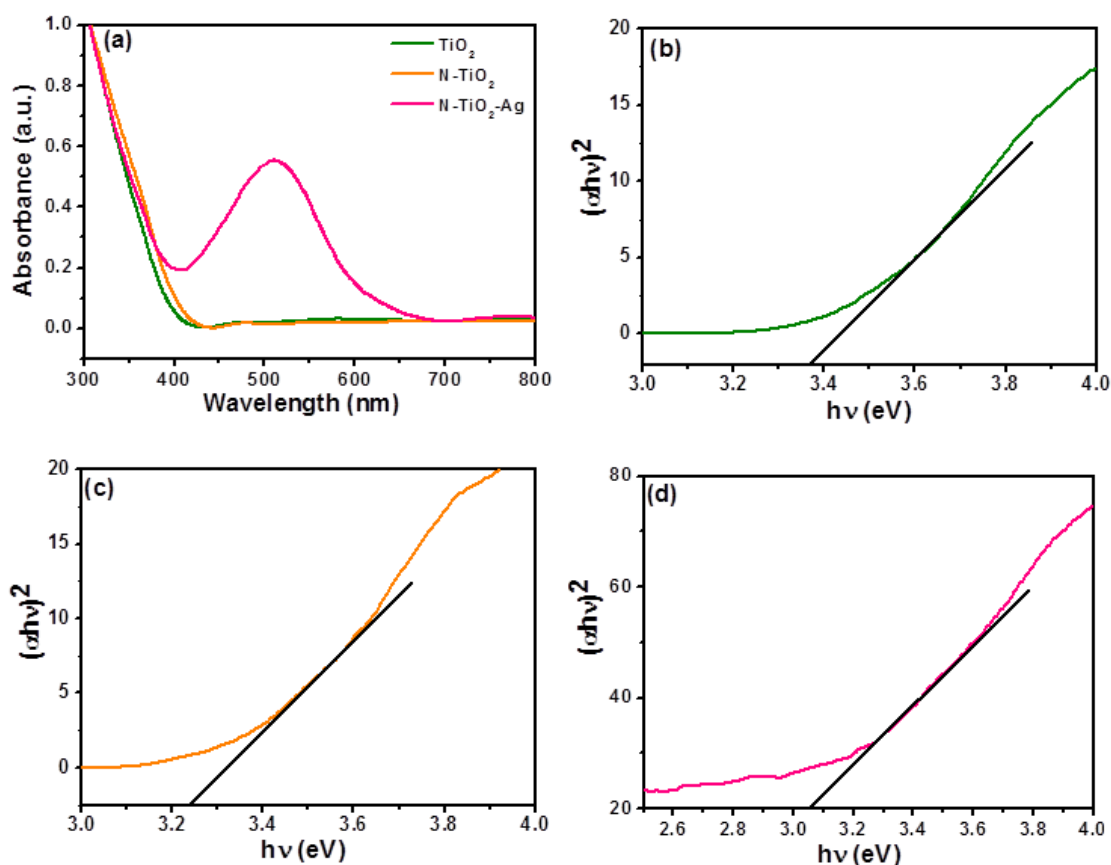


**Figure 5.5** (a) UV–visible absorption spectra of TiO<sub>2</sub>, N-TiO<sub>2</sub>, and N-TiO<sub>2</sub>-Ag. Plots of  $(\alpha h\nu)^2$  versus  $h\nu$  obtained for (b) TiO<sub>2</sub>, (c) N-TiO<sub>2</sub>, and (d) N-TiO<sub>2</sub>-Ag

Understanding the charge recombination process for a semiconductor is crucial because it would significantly influence the photoelectrochemical properties and DSSC performance. The TiO<sub>2</sub> absorbs incident photons with sufficient energy equal to or higher than the band-gap energy, and it produces photoinduced charge carriers ( $h^+ \dots e^-$ ). The recombination of photoinduced electrons and holes releases energy in the form of photoluminescence. Hence, a lower PL intensity indicates less charge recombination. The observed PL spectra for the TiO<sub>2</sub>, N-TiO<sub>2</sub>, and N-TiO<sub>2</sub>-Ag are shown in **Figure 5.6(a)**. A broad peak with a maximum emission at around 580 nm can be observed for the TiO<sub>2</sub>, N-TiO<sub>2</sub>, and N-TiO<sub>2</sub>-Ag. The TiO<sub>2</sub> and N-TiO<sub>2</sub> showed higher PL intensities due to the rapid recombination of photoinduced charge carriers. The PL intensity decreased when Ag was introduced to the N-TiO<sub>2</sub>. This is mainly attributed to the

formation of a Schottky barrier at the Ag and N-TiO<sub>2</sub> interface, which could act as an electron sink to efficiently prevent the electron–hole recombination process (Du et al., 2006). N-TiO<sub>2</sub>-Ag with 10% Ag showed the lowest PL emission intensity, which indicated the least electron–hole recombination compared to 2.5, 5, and 20% Ag content on the TiO<sub>2</sub> surface, as seen in **Figure 5.5(b)**.

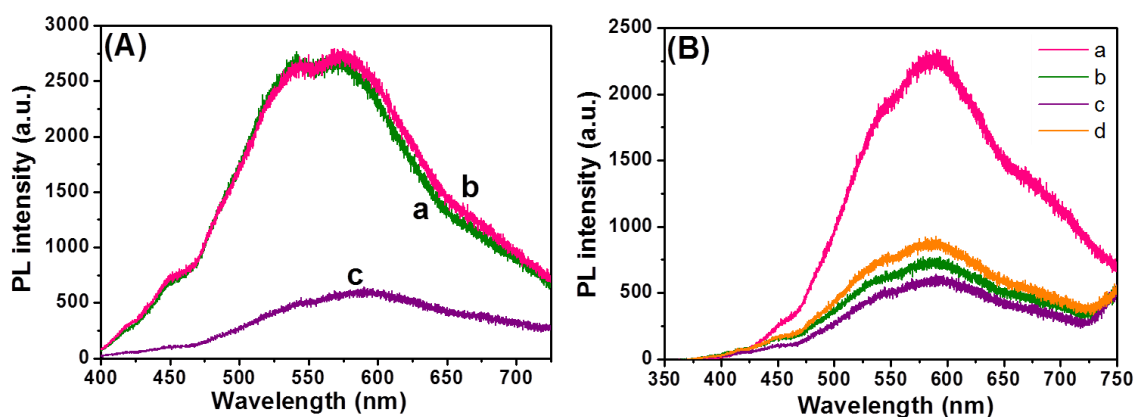


**Figure 5.6** (A) Photoluminescence spectra of (A) TiO<sub>2</sub>, (b) N-TiO<sub>2</sub>, and (c) N-TiO<sub>2</sub>-Ag. (B) N-TiO<sub>2</sub>-Ag nanocomposite thin films with (a) 2.5, (b) 5, (c) 10, and (d) 20 wt% of Ag content.

### 5.2.5 Photovoltaic Performance of N-TiO<sub>2</sub>-Ag-Modified Photoanode-Based DSSCs

The photovoltaic performances of the TiO<sub>2</sub>, N-TiO<sub>2</sub>, and N-TiO<sub>2</sub>-Ag photoanode-based DSSCs were investigated under simulated solar AM 1.5G irradiation, and the results are shown in **Figure 5.7**. The parameters are summarized in **Table 5.1**. The photocurrent density–photovoltage (J–V) curve of the N-TiO<sub>2</sub>-Ag photoanode-based DSSC shows a very high short-circuit current density of up to 21.51 mA/cm<sup>2</sup>. The N-TiO<sub>2</sub>-Ag photoanode showed an enhanced solar energy conversion ( $\eta$ ) of 8.15%, which was higher than those of the N-TiO<sub>2</sub> (2.93%) and pure TiO<sub>2</sub> (2.19%) photoanode-based DSSCs. The Ag nanoparticles showed a promotional effect on the overall energy conversion due to the surface plasmon resonance and synergetic effect between the Ag

and N-TiO<sub>2</sub>. The presence of N could extend the absorption of TiO<sub>2</sub> into the visible region. Moreover, the deposition of Ag onto the N-TiO<sub>2</sub> resulted in a change in the Fermi energy level. The electrons in the conduction band of the TiO<sub>2</sub> could be effectively captured by the Ag until the Fermi level equilibrium was obtained, which minimized the charge recombination process and thus improved the DSSC performance.

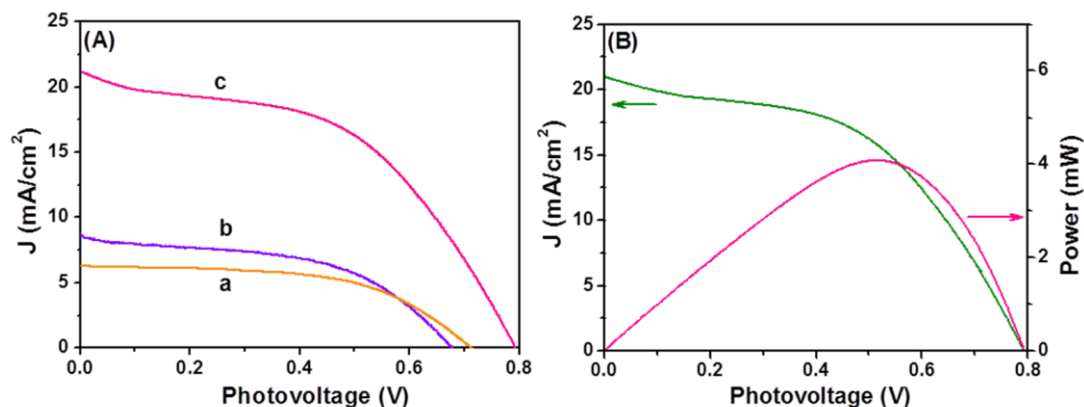


**Figure 5.7** (A) Photocurrent density–photovoltage curves obtained for (a) TiO<sub>2</sub>, (b) N-TiO<sub>2</sub>, and (c) N-TiO<sub>2</sub>-Ag photoanode-modified DSSCs. (B) Power output–photovoltage curves obtained for N-TiO<sub>2</sub>-Ag photoanode-modified DSSC.

**Table 5.1** Photovoltaic parameters of fabricated DSSCs with controlled configurations.

Photoanode	$J_{sc}$ (mA/cm <sup>2</sup> )	$V_{oc}$ (V)	$J_{max}$ (mA/cm <sup>2</sup> )	$V_{max}$ (V)	FF	$\eta$ (%)
TiO <sub>2</sub>	6.27	0.70	5.25	0.49	0.59	2.57
TiO <sub>2</sub> -Ag	12.19	0.77	9.34	0.52	0.52	4.86
N-TiO <sub>2</sub>	8.77	0.68	6.10	0.48	0.49	2.93
N-TiO <sub>2</sub> -Ag	21.51	0.79	15.99	0.51	0.48	8.15

**Footnote:** The DSSC performance was evaluated under 100 mW cm<sup>-2</sup> of simulated AM 1.5G solar light irradiation.  $J_{sc}$ : Short-circuit current density;  $V_{oc}$ : Open-circuit voltage;  $J_{max}$ : Maximum photocurrent density;  $V_{max}$ : Maximum photovoltage; FF: Fill factor;  $\eta$ : Power conversion efficiency. Area of the cell electrode was 0.5 cm<sup>2</sup>

In order to achieve a higher performance for the DSSC, it is very important to optimize the Ag content in the photoanode. In this regard, the loading of the Ag content in the photoanode was varied to enhance the DSSC performance. Photocurrent density–

photovoltage voltage (J–V) curves were recorded for the N-TiO<sub>2</sub>-Ag nanocomposite-modified photoanodes with different Ag contents and are shown in **Figure 5.8**. Their corresponding photovoltaic parameters are given in **Table 2**. The obtained conversion efficiencies for pristine N-TiO<sub>2</sub> and N-TiO<sub>2</sub> with 10 wt% Ag were 2.93% and 8.15%, respectively. In contrast, for 2.5, 5, and 20 wt% of Ag, the conversion efficiencies were 2.47, 7.44, and 1.63%, respectively. The observed results clearly revealed that the conversion efficiency of a DSSC was increased with an increase in the Ag content in the photoanode until it reached a maximum of 10 wt%. A further increase in the Ag content eventually led to a decrease in the conversion efficiency (**Figure 5.8 (a) and Table 5.2**). This decrease in the efficiency at a high Ag loading could be attributed to the following reasons: (i) the absorption and scattering of incident photons (Subramanian et al., 2003; Yu et al., 2006), (ii) the shielding of the TiO<sub>2</sub>/electrolyte interface from irradiation (Chandrasekharan et al., 2000), and (iii) the excess Ag may have undergone photooxidation by the photogenerated holes and/or surface hydroxyl radicals present in the TiO<sub>2</sub> particles (Subramanian et al., 2003). Consequently, the overall conversion efficiency of the DSSC deteriorated. The  $J_{sc}$  was increased with the increasing Ag content and attained a maximum of 22.51 mA/cm<sup>2</sup> at Ag loading of 5% (**Figure 5.9**). Further,  $J_{sc}$  decreased to 20.18 mA/cm<sup>2</sup> with 20% Ag loading in the photo anode of the DSSC. It can also be seen that the  $V_{oc}$  trends were almost the same, within the range of ~0.68–0.80 V. The  $J_{max}$  and  $V_{max}$  values of the device also followed trends similar to  $J_{sc}$  and  $V_{oc}$  (**Figure 5.9**).

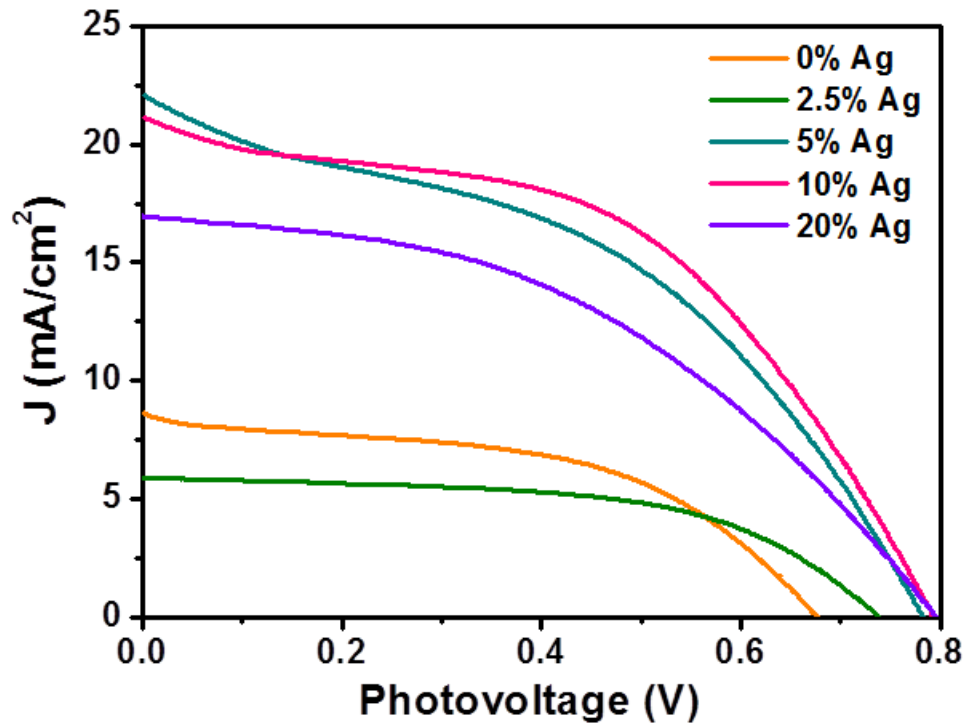


**Figure 5.8** Photocurrent density–photovoltage (J–V) curves obtained for N-TiO<sub>2</sub>-Ag nanocomposite photoanode-modified DSSCs with different Ag content.

**Table 5.2** Photovoltaic parameters of N-TiO<sub>2</sub>-Ag nanocomposite photoanode-modified DSSCs with different Ag content..

Ag (%)	$J_{sc}$ (mA/cm <sup>2</sup> )	$V_{oc}$ (V)	$J_{max}$ (mA/cm <sup>2</sup> )	$V_{max}$ (V)	FF	$\eta$ (%)
0	8.77	0.68	6.10	0.48	0.49	2.93
2.5	5.90	0.74	4.66	0.53	0.57	2.47
5	22.51	0.78	14.87	0.50	0.42	7.44
10	21.51	0.79	15.99	0.51	0.48	8.15
20	20.18	0.80	12.45	0.58	0.37	5.98

**Footnote:** The DSSC performance was evaluated under 100 mW cm<sup>-2</sup> of simulated AM 1.5G solar light irradiation.  $J_{sc}$ : Short-circuit current density;  $V_{oc}$ : Open-circuit voltage;  $J_{max}$ : Maximum photocurrent density;  $V_{max}$ : Maximum photovoltage; FF: Fill factor;  $\eta$ : Power conversion efficiency. Area of the cell electrode was 0.5 cm<sup>2</sup>.

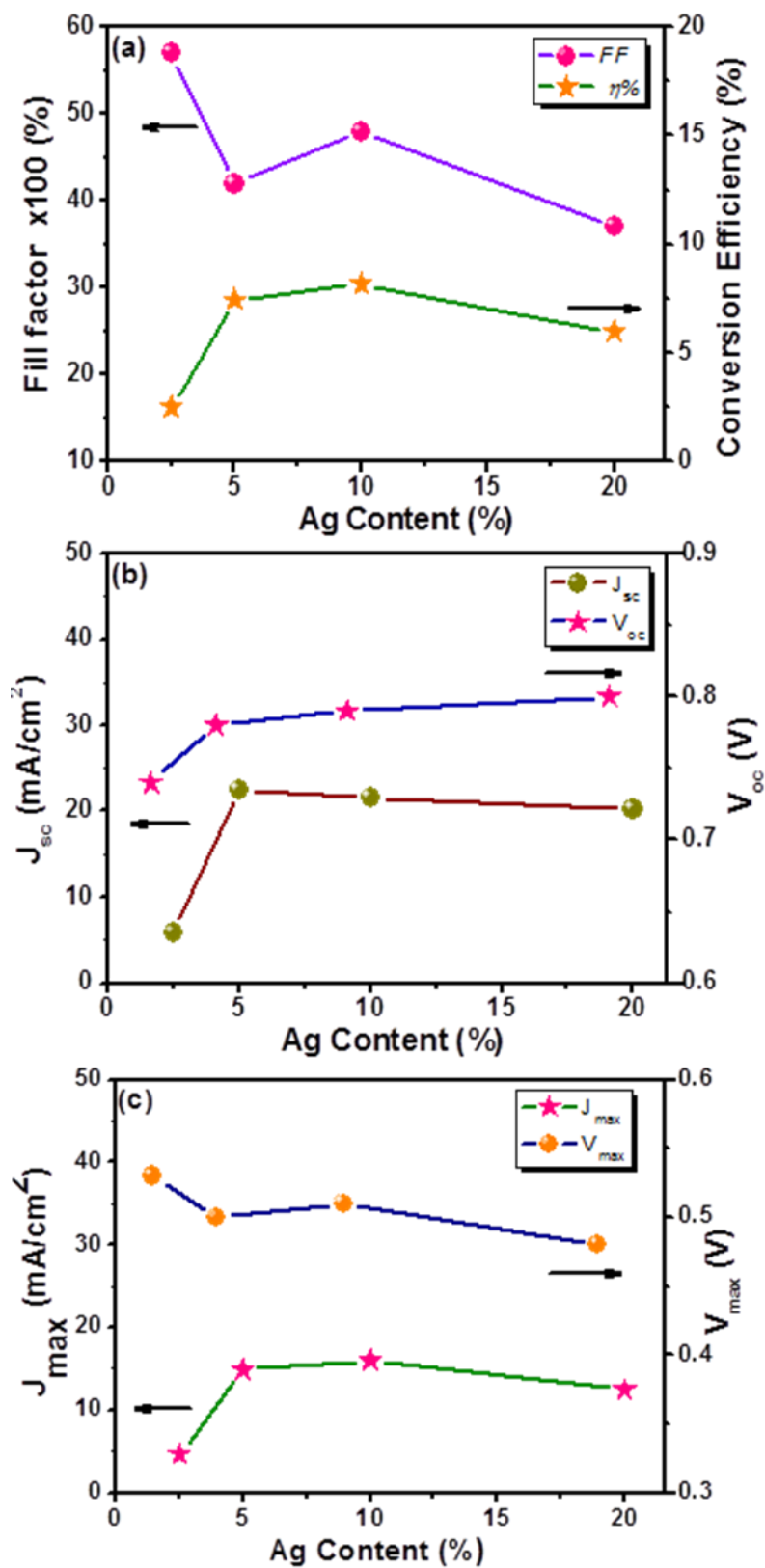


**Figure 5.9** Plots of (a) fill factor (FF) and power conversion efficiency ( $\eta$ ), (b) short-circuit current density ( $J_{sc}$ ) and open-circuit voltage ( $V_{oc}$ ), and (c) maximum photocurrent density ( $J_{max}$ ) and maximum photovoltage ( $V_{max}$ ) obtained for N-TiO<sub>2</sub>-Ag-based DSSC with different Ag contents.

### 5.2.6 Electrochemical Behavior of N-TiO<sub>2</sub>-Ag-Modified Photoanode

In order to obtain deep insights into the interfacial charge transfer process within the fabricated DSSC, the electrochemical impedance spectra (EIS) were recorded in the frequency range of 0.01 Hz to 100 KHz and are shown in **Figure 5.10**. A well-defined semicircle in the middle frequency region can be observed for the N-TiO<sub>2</sub>-Ag nanocomposite-modified photoanode-based DSSC. The intersection of the high frequency semicircle at the real axis represents the equivalent series resistance of the device ( $R_s$ ). The arc in the middle frequency range between 1 and 1000 Hz represents the charge transfer resistance ( $R_{ct}$ ) between the dye-adsorbed photoanode and the electrolyte interface (van de Lagemaat et al., 2000; Wang et al., 2012). **Figure 5.10(A)** shows the Nyquist plot of N-TiO<sub>2</sub> with different contents of Ag. Here, the  $R_s$  value can be ignored since it remains fairly consistent (15  $\Omega$ ), and the DSSC components are the same, except for the different concentrations of Ag in the photoanode. The changes in  $R_{ct}$  can mainly be attributed to the changes in the Ag content in the photoanode, which contributed the most to the internal impedance. An increase in the  $R_{ct}$  value of the N-TiO<sub>2</sub>-Ag-based photoanode was observed with the increasing Ag content. Thus, a photoanode that contained less Ag had a lower  $R_{ct}$  value, which corresponded to the efficient electron transfer process between the photoanode and electrolyte interface. The Nyquist plot of the different photoanodes is shown in **Figure 5.10 (B)**. As demonstrated by the Nyquist plot, both the real ( $Z'$ ) and imaginary ( $Z''$ ) parts of the total impedance, as well as  $R_{ct}$ , increased in the order TiO<sub>2</sub> < N-TiO<sub>2</sub> < N-TiO<sub>2</sub>-Ag, which showed the crucial dependence of the N and Ag incorporation on the charge transport. The increase in the  $R_{ct}$  value is more beneficial to suppress the charge recombination and could influence the short circuit current ( $J_{sc}$ ) of the DSSC. The  $R_s$  value also decreases with the addition of N and Ag. Therefore, the origin of the higher  $J_{sc}$  in N-TiO<sub>2</sub>-Ag is expected to arise from the  $R_s$ ,  $R_{ct}$ , and charge transport dynamics determined by the

electron lifetime ( $\tau_n$ ). From the Bode phase plots (**Figure 5.10(C) and (D)**), the frequency was apparently shifted to the lower frequency region with the addition of N and Ag. The maximum frequencies ( $\omega_{\max}$ ) in the middle frequency region of the Bode plots of TiO<sub>2</sub> and N-TiO<sub>2</sub>-Ag were 3162.27 Hz and 1995.26 Hz, respectively. Since  $\omega_{\max}$  is inversely associated with the electron lifetime,  $\tau_n = 1/(2\pi f)$  (Archana et al., 2014; Kim et al., 2013), a decrease in  $\omega_{\max}$  indicates a reduced rate for the charge-recombination process in a DSSC. Electrons with longer  $\tau_n$  will survive recombination, as characterized by a larger  $R_{ct}$ .

Furthermore, **Table 5.3** summarizes the results of the Nyquist plot. The N-TiO<sub>2</sub>-Ag exhibited a faster electron transport time ( $\tau_s = R_s * C\mu$ ) (Kim et al., 2013; Nissfolk et al., 2006; Wang et al., 2008) than TiO<sub>2</sub> and N-TiO<sub>2</sub>. Hence, its electron lifetime ( $\tau_n = R_{ct} * C\mu$ ) (Kim et al., 2013; Nissfolk et al., 2006; Wang et al., 2008) was significantly increased, and electrons survived the recombination. The photovoltaic performance of a DSSC is clearly reflected by the charge collection efficiency ( $\eta_c$ ) derived from  $\eta_c = (1 + R_s/R_{ct})^{-1}$ . (Kim et al., 2013; Kroon et al., 2007; Nissfolk et al., 2006) Eventually, the charge collection efficiency was significantly increased with the addition of N and Ag. We can conclude that, as a result of the longer  $\tau_n$  and larger  $R_{ct}$ , the devices fabricated using N-TiO<sub>2</sub>-Ag showed improved  $J_{sc}$  values compared to TiO<sub>2</sub> and N-TiO<sub>2</sub>.

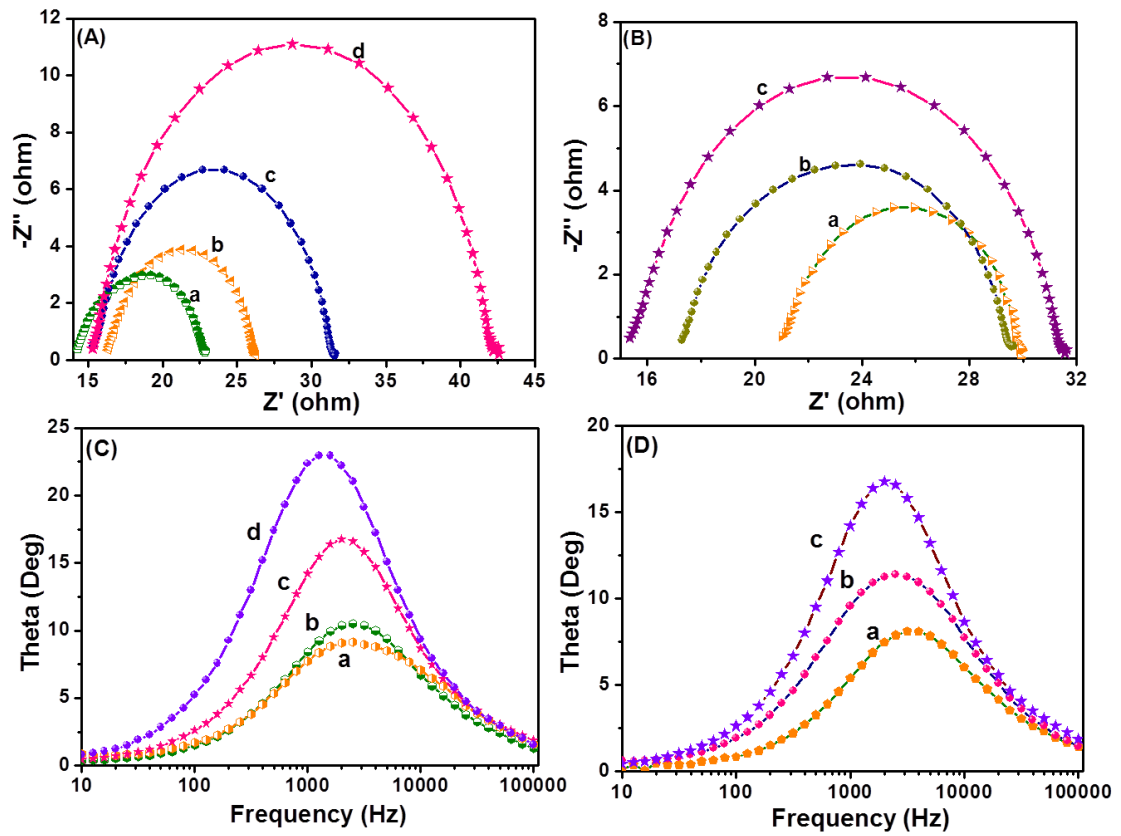


**Figure 5.10** (A) Nyquist plot and (C) Bode phase plots obtained for N-TiO<sub>2</sub>-Ag nanocomposite-modified photoanodes with (a) 2.5, (b) 5, (c) 10, and (d) 20 wt% of Ag content. (B) Nyquist plot and (D) Bode phase plots of (a) TiO<sub>2</sub>, (b) N-TiO<sub>2</sub>, and (c) N-TiO<sub>2</sub>-Ag (10 wt% Ag).

**Table 5.3** EIS analysis results for fabricated DSSC with controlled configurations.

Photoanode	$R_s (\Omega)$	$R_{ct} (\Omega)$	$C_\mu (\mu F)$	$\tau_s (ms)$	$\tau_n (ms)$	$\eta_c (\%)$
TiO <sub>2</sub>	21.01	8.91	7.10	0.14	0.06	29
N-TiO <sub>2</sub>	17.21	12.36	8.12	0.13	0.10	41
N-TiO <sub>2</sub> -Ag	15.34	20.28	6.23	0.09	0.12	57

**Footnote:** The electrochemical impedance spectra (EIS) were recorded at an applied bias of -0.7 V in the frequency range of 0.01 Hz to 100 KHz.  $R_s$ : Device resistance;  $R_{ct}$ : Charge transfer resistance;  $C_\mu$ : Chemical capacitance;  $\tau_s$ : Electron transport time;  $\tau_n$ : Electron lifetime;  $\eta_c$ : Charge collection efficiency.

### 5.2.7 Operation Principle of N-TiO<sub>2</sub>-Ag-Modified Photoanode-Based DSSC

The operation principle of the DSSC based on the N-TiO<sub>2</sub>-Ag-modified photoelectrode under illumination is shown in **Figure 5.11a**. The DSSC is based on the photo-excitation of the dye, followed by electron injection into the conduction band of the TiO<sub>2</sub> nanoparticle. During light irradiation, the dye absorbs incident light and promotes electrons to the excited state. The excited electrons are injected into Ag nanoparticles and then transferred to the conduction bands of TiO<sub>2</sub> nanoparticles. The dye is then oxidized by receiving electrons from the electrolyte through the redox system, and is ready to be used again. The electrolyte itself will be regenerated via the platinum counter electrode, by electrons passing through the external circuit. In our study, the Ag deposited onto the N-TiO<sub>2</sub> not only acted as an electron sink for an efficient charge transfer but could also be used as a scattering element for plasmonic scattering to trap the light and near-field coupled with the dye molecules (Lin et al., 2012). This will eventually improve the optical absorption of dye, resulting in a significant photocurrent enhancement (**Figure 5.12b**). Additionally, the incorporation of Ag also resulted in a change in the Fermi energy level. A large number of electrons accumulated on the surfaces of Ag nanoparticles due to the surface plasmon resonance effect. The accumulation of electrons on Ag nanoparticles shifted the position of the Fermi level closer to the conduction band of TiO<sub>2</sub> (Ni et al., 2007). The excited electrons in the Ag nanoparticles transferred to the conduction band of TiO<sub>2</sub> and were collected by the current collector (ITO). Thus, the photocurrent was improved under irradiation in the visible region (Christopher et al., 2010). In this way, the photovoltaic performance significantly improved with the enhancement of absorption in the visible region due to the surface plasmon resonance of the Ag nanoparticles. In addition to the ideal property of Ag nanoparticles, the presence of the N also successfully reduced the band-gap and helped to shift the optical absorbance toward the visible region. The

incorporation of N in  $\text{TiO}_2$  that existed in the form of N-Ti-O would partially convert the system from  $\text{Ti}^{4+}$  to  $\text{Ti}^{3+}$  and effectively contributed toward visible light absorption (Naik et al., 2010; Pany et al., 2013).

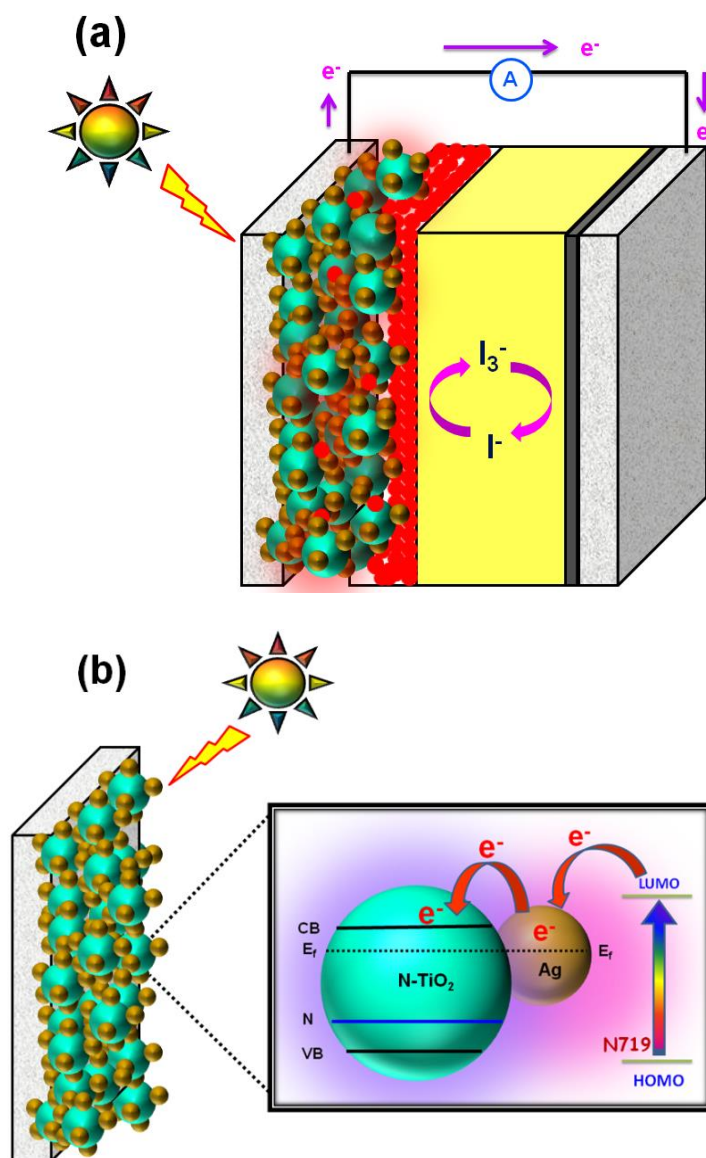


**Figure 5.11** (a) Schematic diagram and (b) charge transfer mechanism for N-TiO<sub>2</sub>-Ag photoanode-modified DSSC.

### 5.3 Conclusion

In summary, a facile route to prepare Ag nanoparticles deposited on N-TiO<sub>2</sub> via a simple chemical reduction method was demonstrated in this report. The DSSC fabricated with N-TiO<sub>2</sub>-Ag showed an enhanced solar-to-electrical energy conversion efficiency of 8.15% compared to the photoanode of a DSSC composed of unmodified TiO<sub>2</sub> (2.19%) under simulated solar irradiation of 100 mW cm<sup>-2</sup> with AM 1.5 G. The improvement was mainly attributed to the Ag nanoparticles, which enhanced the visible light adsorption due to a light harvesting property in the visible range as a result of the surface plasmon resonance effect. In addition, the promotion of the interfacial charge transfer effectively minimized the charge recombination process. The optimum Ag content in the N-TiO<sub>2</sub>-Ag for an efficient photoanode was found to be 10 wt%. In addition, the presence of N was also successfully reduced the band gap and helped to shift the optical absorbance toward the visible region. The conversion efficiency was nearly threefold that of unmodified TiO<sub>2</sub>. The synergetic effects of the Ag nanoparticles, surface plasmon resonance effect, reduction in the band gap, and effective charge transfer ameliorated the photocurrent generation and conversion efficiency of DSSCs.

## CHAPTER 6

### **Boosting Photovoltaic Performance of N, S-Co-Doped-TiO<sub>2</sub> Photoanode Based Dye-Sensitized Solar Cells With Silver Nanoparticles**

#### **6.1 Introduction**

Renewable energy sources have become important approaches for gaining independence from fossil fuels. Utilizing solar energy is certainly one of the most viable ways to solve the world's energy crisis. Dye-sensitized solar cells (DSSCs) have emerged as promising candidates for harnessing solar power because of their low cost, flexibility, ease of production, relatively high energy conversion efficiency, and low toxicity to the environment (O'Regan et al., 1991). Several efforts have been made to fabricate highly efficient DSSCs by the introduction of novel components such as electrolytes, dyes, counter electrodes, and semiconductor photoanodes. Among these DSSC components, the photoanode plays a vital role in determining the DSSC performance. So far, a titanium dioxide (TiO<sub>2</sub>) is one of the most commonly used photoanode materials, and it is promising material for a DSSC because of its low cost, ease of fabrication, relatively high energy conversion efficiency, high specific surface area, and non-toxicity. However, the major limitation associated with using TiO<sub>2</sub> as a photoanode is its random electron transport, which will cause the electron-hole recombination process and hence hinder the cell performance (Kopidakis et al., 2005; van de Lagemaat et al., 2000). In order to solve this serious issue, designing a photoanode with an efficient charge transport pathway from the photoinjected carriers to the current collector seems to be a possible alternative to enhance the performance of DSSCs. With this aim, surface modifications of TiO<sub>2</sub> with metal doping, semiconductor coupling, and hybridization with a carbon material has have been attempted and shown better results (Lai et al., 2010; Macak et al., 2007; Yang et al., 2007; Zhao et al., 2007).

The modification of  $\text{TiO}_2$  with a noble metal such as gold (Au) (Muduli et al., 2012), silver (Ag) (Gao et al., 2013) , or platinum (Pt) (Huang et al., 2007) has been actively reported for the photoanodes in DSSC applications to prevent the recombination of the photogenerated electron–hole pairs and improve the charge transfer efficiency. In the present decade, Ag nanoparticle-modified  $\text{TiO}_2$  has been applied as a photoanode with the aim of improving the efficiency of a DSSC. The Ag nanoparticles play dual roles in the DSSC performance, including the enhancement of the absorption coefficient of the dye and optical absorption due to surface plasmonic resonance (Eagen, 1981; Mock et al., 2002; Schaadt et al., 2005). Moreover, they act as an electron sink for photoinduced charge carriers, improve the interfacial charge transfer process, and minimize the charge recombination, thereby enhancing the electron transfer process in a DSSC (Lee et al., 2008; Wen et al., 2000; Zhao et al., 1997). Hence, the performance of a DSSC with  $\text{Ag@TiO}_2$  plasmonic nanocomposite material-modified photoanodes has been actively investigated (Lee et al., 2008; Wen et al., 2000; Zhao et al., 1997). On the other hand, to improve the light absorption of a  $\text{TiO}_2$  material in the visible region, non-metals such as nitrogen (N), carbon (C), sulfur (S), and phosphorus (P) have been widely studied as dopants for  $\text{TiO}_2$  (Zhang et al., 2010). Among these, nitrogen doped  $\text{TiO}_2$  possesses good photovoltaic properties and hence has received much attention due to the narrowing of the band gap and shift to the visible region (Kang et al., 2010). Hence, the co-deposition of Ag on doped  $\text{TiO}_2$  showed enhanced photovoltaic properties due to the synergistic effect between the Ag and doped  $\text{TiO}_2$  (Pany et al., 2013; Zhang et al., 2011).

In the present investigation, we successfully developed a facile route to synthesize N,S- $\text{TiO}_2$ @Ag nanocomposite materials as a photoanode for high-performance dye-sensitized solar cells. The influence of the Ag content in the N,S- $\text{TiO}_2$ @Ag on the DSSC performance was also investigated. The introduction of

plasmonic Ag nanoparticles on the N,S-TiO<sub>2</sub> surface showed multifunctional properties, including a surface plasmon resonance effect, a reduction in the band-gap, an improved interfacial charge transfer, and the minimization of the charge recombination process as a result of the synergistic photovoltaic performance.

## 6.2 Results and Discussion

### 6.2.1 Morphological Studies of N,S-TiO<sub>2</sub>@Ag Nanocomposite

**Figure 6.1** shows the FESEM microscopic morphology of the as-prepared N,S-TiO<sub>2</sub>@Ag nanocomposite (detailed preparation procedure is given in Chapter: 3; Section: 3.2.5), and **Figure 6.1(a)** shows an FESEM image of N,S-TiO<sub>2</sub>, which appeared to be spherical, with a uniform size. Upon the addition of Ag nanoparticles, no significant change in the morphology was observed for the N,S-TiO<sub>2</sub>@Ag film (**Figure 6.1(b)**). An energy dispersive X-ray spectrometry (EDS) mapping analysis of the N,S-TiO<sub>2</sub>@Ag thin film also confirmed that the N,S-TiO<sub>2</sub>@Ag nanocomposite, composed of Ag, N, and S elements, was dispersed on the surface of the TiO<sub>2</sub> nanoparticles with Ti and O signals (**Figure 6.1(c)**). Further, TEM images of the N,S-TiO<sub>2</sub> were also recorded and are shown in **Figure 6.2(a)**. The TEM images show that the N,S-TiO<sub>2</sub> nanoparticles are spherical in shape, with a TiO<sub>2</sub> particle size range of 20–25 nm. **Figure 6.2(b)** clearly shows that small spherical Ag nanoparticles with a particle size range of 2–5 nm were well distributed and decorated on the surface of the N,S-TiO<sub>2</sub> nanoparticles. **Figure 6.2(c)** depicts the selected area electron diffraction (SAED) pattern of the N,S-TiO<sub>2</sub>@Ag nanocomposite. The pattern clearly reveals bright concentric rings, which were due to the diffraction from the (211), (200), (004), and (101) planes of the anatase TiO<sub>2</sub>. In the HRTEM image of the N,S-TiO<sub>2</sub>@Ag (**Figure 6.2(d)**), lattice fringes with d-spacing values of 3.51 Å, 1.34 Å, and 1.89 Å were observed, which corresponds to

the (101), (220), and (200) planes of the anatase  $\text{TiO}_2$ , respectively; while the interplanar d-spacing value of  $2.05 \text{ \AA}$  was assigned to the (210) plane of rutile  $\text{TiO}_2$ .

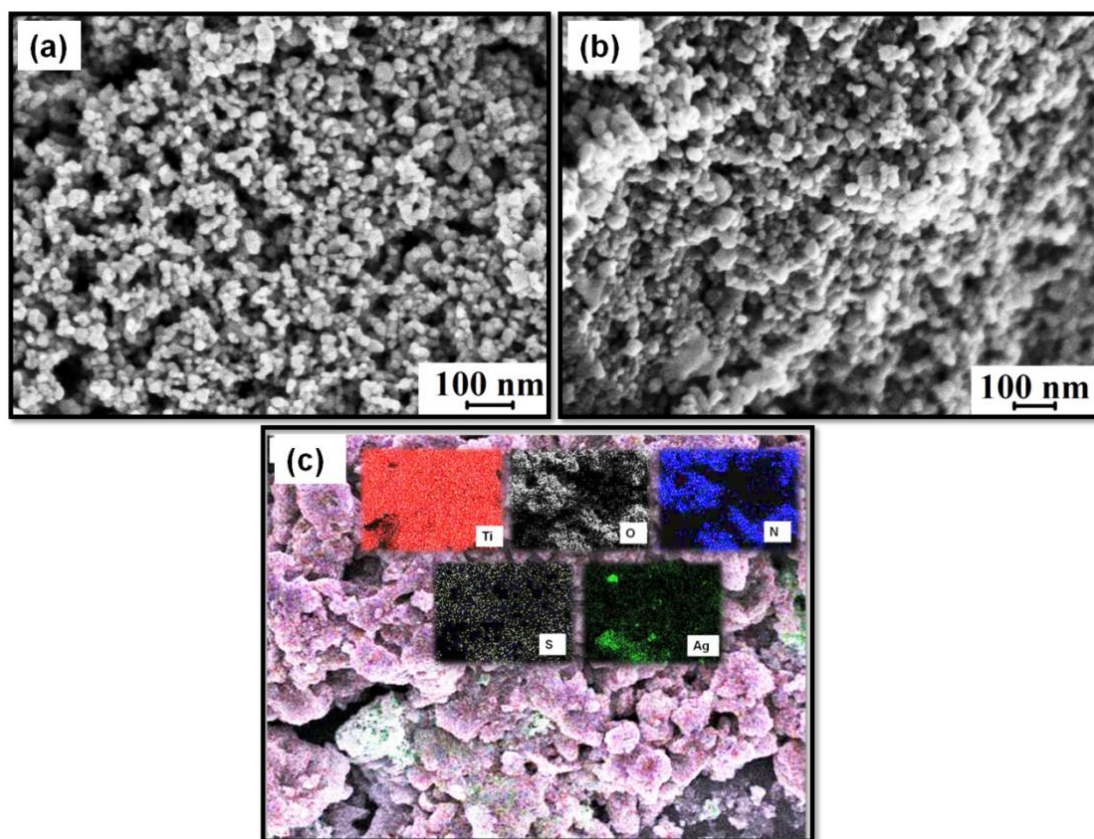


**Figure 6.1** FESEM images of (a) N,S-TiO<sub>2</sub>, (b) N,S-TiO<sub>2</sub>@Ag and (c) element mapping of N,S-TiO<sub>2</sub>@Ag nanocomposite.

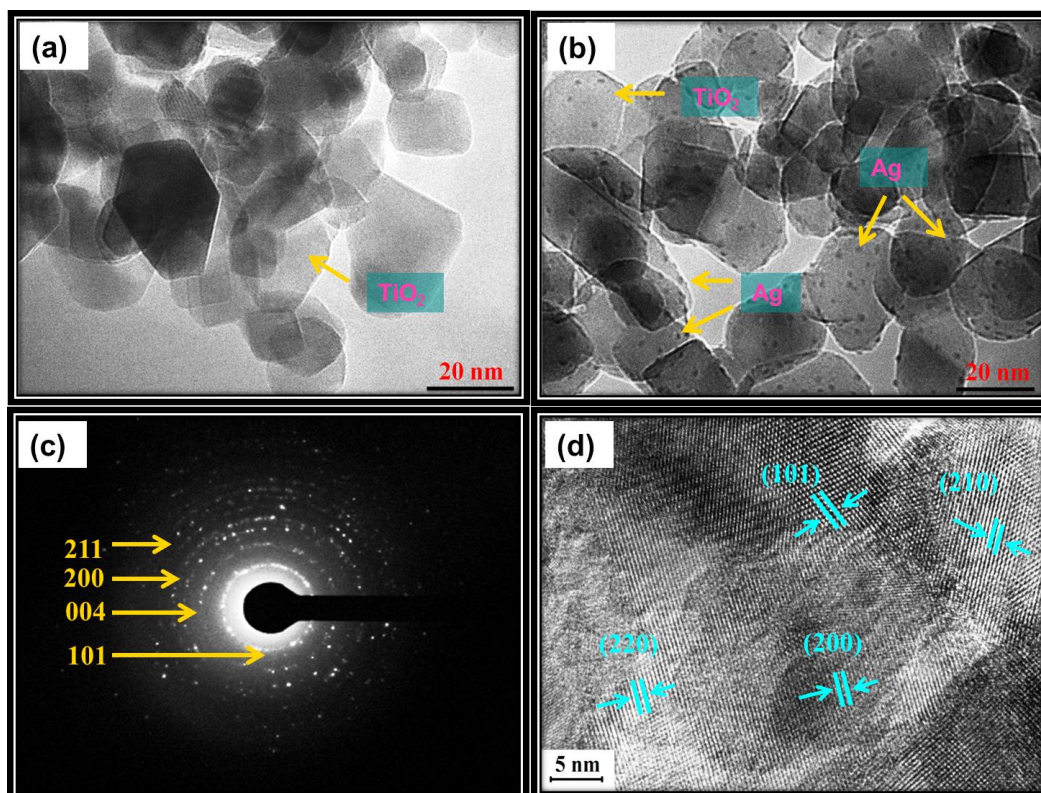


**Figure 6.2** TEM images of (a) N,S-TiO<sub>2</sub>, (b) N,S-TiO<sub>2</sub>@Ag, (c) SAED pattern and (d) HRTEM image of N,S-TiO<sub>2</sub>@Ag.

### 6.2.2 Crystalline Studies of N,S-TiO<sub>2</sub>@Ag Nanocomposite

The XRD pattern obtained for the N,S-TiO<sub>2</sub>@Ag is shown in **Figure 6.3**, along with those of TiO<sub>2</sub> and N,S-TiO<sub>2</sub> for comparison. The TiO<sub>2</sub>, N,S-TiO<sub>2</sub>, and N,S-TiO<sub>2</sub>@Ag films were composed of mixed anatase and rutile phases, which agreed with reference patterns JCPDS 83-2243 and 21-1276, respectively. The diffraction peaks observed at 25.4 °, 38.4 °, 48.2 °, and 74.5 ° corresponded to the anatase phase of TiO<sub>2</sub> and were assigned to the (101), (004), (200), and (215) crystallographic planes. In contrast, the peaks at 54.09 °, 63.2 °, and 64.9 ° agreed well with the rutile phase of TiO<sub>2</sub> and were assigned to the (220), (002), and (310) crystallographic planes. It was difficult to differentiate the Ag from the TiO<sub>2</sub> signals because of the overlapping of the Ag signal with the rutile plane in the N,S-TiO<sub>2</sub> nanocomposite. The XRD patterns clearly confirmed the anatase and rutile phases were retained without a phase change after the nitrogen and sulfur doping and the deposition of Ag nanoparticles. The additional peaks were due to the ITO substrate.

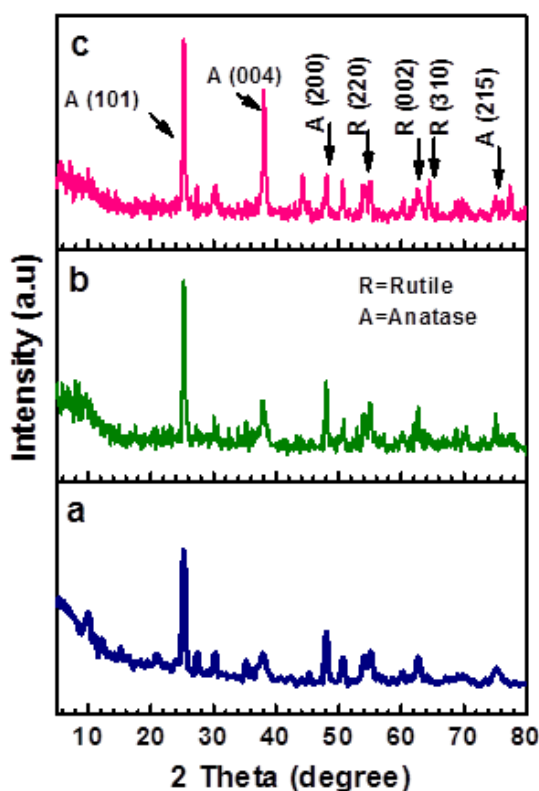


**Figure 6.3** XRD patterns of (a) TiO<sub>2</sub>, (b) N,S-TiO<sub>2</sub> and (c) N,S-TiO<sub>2</sub>@Ag

To further evaluate the phases in the prepared films, Raman studies were performed in the range of 100–1000  $\text{cm}^{-1}$ , and the results are shown in **Figure 6.4(A)**. The values of 147.48, 199, 395.28, 515.74, 639.25, and 710.18  $\text{cm}^{-1}$  were due to the anatase phase  $\text{TiO}_2$  (Chiarello et al., 2010; Sivaranjani et al., 2011). The rutile  $\text{TiO}_2$  phase was observed at 444  $\text{cm}^{-1}$  (Chiarello et al., 2010; Sivaranjani et al., 2011). This clearly indicated that the  $\text{TiO}_2$  and N,S- $\text{TiO}_2$  nanoparticles contained a mixture of the anatase and rutile phases. The Raman signals of  $\text{TiO}_2$  did not change after adding nitrogen and sulfur, which indicated that no phase transition occurred. However, no signals related to Ag particles were identified for the samples because of the relatively low concentration of Ag loaded onto the  $\text{TiO}_2$  and its weak Raman scattering power. An interesting observation was that the peak intensities increased with the deposition of Ag, while the position of the Raman signal remained the same. This indicates that there was an interaction between the Ag and  $\text{TiO}_2$  that affected the Raman resonance of  $\text{TiO}_2$  (Lim et al., 2014a; Su et al., 2012). This observation shows that the deposition of Ag on  $\text{TiO}_2$  and N,S- $\text{TiO}_2$  does not cause any phase transition, but may bring about an electronic environment change in the surroundings (Chiarello et al., 2010; Sivaranjani et al., 2011).

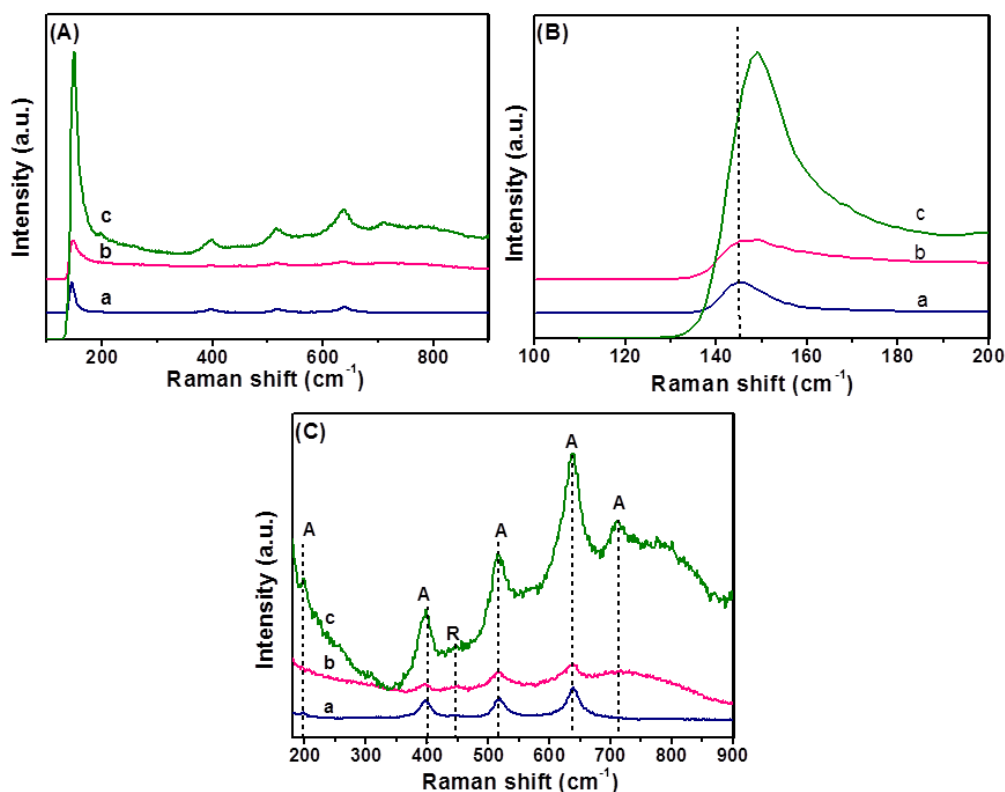


**Figure 6.4** Raman spectra of (a) TiO<sub>2</sub>, (b) N,S-TiO<sub>2</sub> and (c) N,S-TiO<sub>2</sub>@Ag in different frequency regions. **A:** 100-900 cm<sup>-1</sup>, **B:** 100-200 cm<sup>-1</sup> and **C:** 180-900 cm<sup>-1</sup> separately given for better clarity of the anatase and rutile phase TiO<sub>2</sub>.

### 6.2.3 XPS Analysis of N,S-TiO<sub>2</sub>@Ag Nanocomposite

The XPS spectra of the TiO<sub>2</sub>, N,S-TiO<sub>2</sub>, and N,S-TiO<sub>2</sub>@Ag were recorded in order to analyze and determine the chemical composition and identify the chemical states of the N, S, Ti, O, and Ag elements, and are shown in **Figure 6.5**. **Figure 6.5(A)** shows the Ti 2p spectra for the samples, in which two peaks are observed at 454.1 and 460 eV, corresponding to the binding energies of Ti 2p<sub>3/2</sub> and Ti 2p<sub>1/2</sub> core levels due to the presence of the Ti(IV) state. **Figure 6.5(b)** shows the O 1s spectra of TiO<sub>2</sub> and Ag@TiO<sub>2</sub>, and the binding energy of the O 1s state of the samples was located at 531.1 eV, which was assigned to the bulk oxides (O<sup>2-</sup>) in the P25 lattice. The N 1s peak at 399.2 eV was assigned to the anionic N-doping, where O was replaced by N atoms involving substitutional N-doping, and the peak at 398.4 eV was also due to anionic N-

doping but incorporated in the  $\text{TiO}_2$  as an N–Ti–O structural feature (Chen et al., 2005; Saha et al., 1992; Sathish et al., 2006) (**Figure 6.5(c)**). **Figure 6.5(d)** shows the corresponding high-resolution XPS spectrum of the S 2p region, and the binding energy peak that appeared at around 164.1 eV corresponds to the Ti–S bond due to the fact that sulfur atoms replaced some of the oxygen atoms on the  $\text{TiO}_2$  surface (Yu et al., 2005; Zhou et al., 2008). The binding energies found for the Ag 3d<sub>5/2</sub> and Ag 3d<sub>3/2</sub> levels were 368.4 and 374.5 eV, respectively (**Figure 6.5(e)**), with a peak separation of 6 eV due to the metallic silver. The XPS analysis provided support for the existence of elements such as Ti, O, N, S, and Ag in the nanocomposite materials.

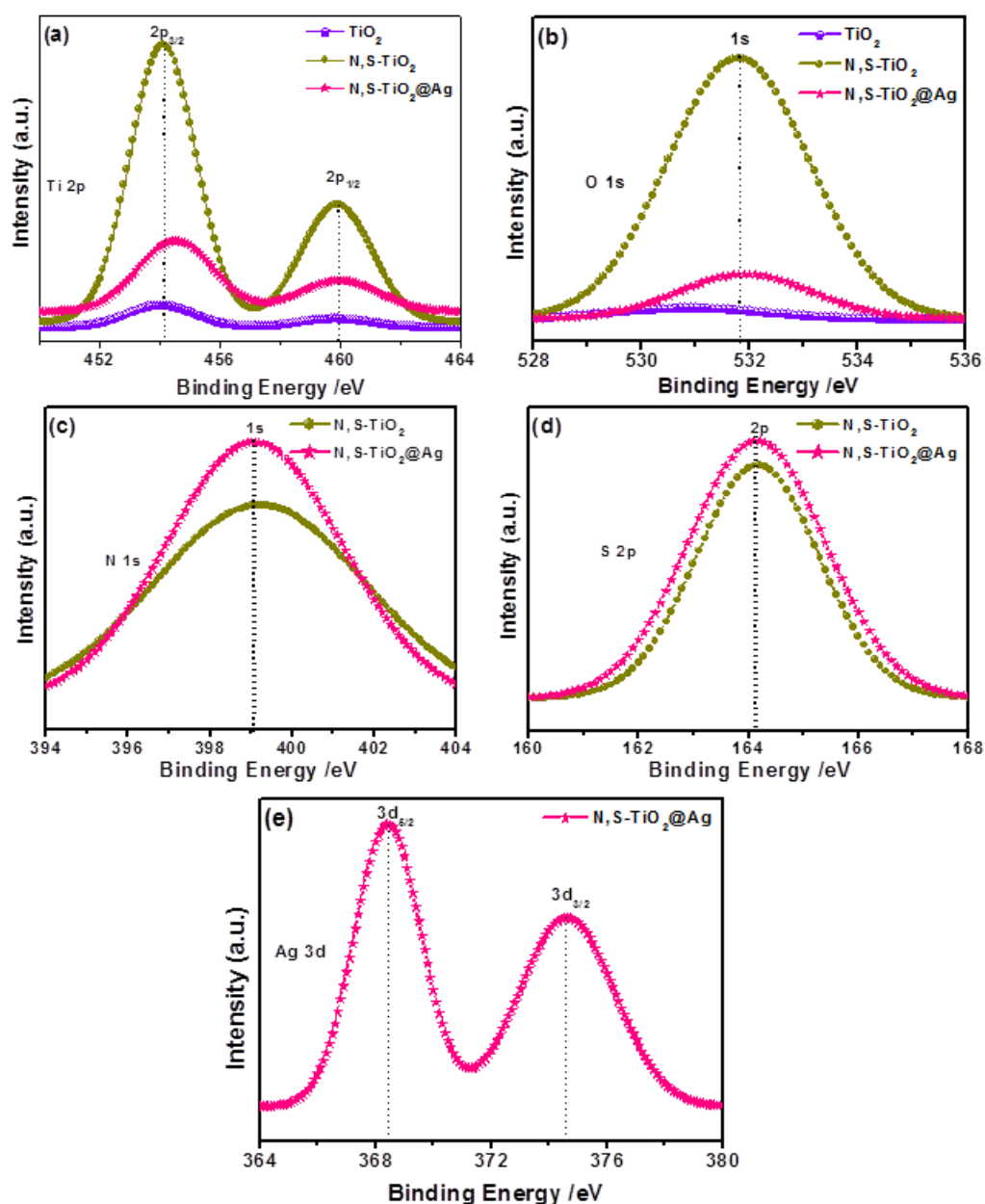


**Figure 6.5** XPS spectra of  $\text{TiO}_2$ ,  $\text{N,S-TiO}_2$  and  $\text{N,S-TiO}_2@\text{Ag}$  and their corresponding (a) Ti 2p (b) O 1s (c) N 1s (d) S 2p and (e) Ag 3d core-level spectra.

#### 6.2.4 Optical properties of $\text{N,S-TiO}_2@\text{Ag}$ nanocomposite

The optical absorption properties of the  $\text{TiO}_2$ ,  $\text{N,S-TiO}_2$ , and  $\text{N,S-TiO}_2@\text{Ag}$  were studied by recording the UV–visible absorption spectra, which are shown in **Figure 6.6(A)**. It can be seen that the absorption edge of  $\text{TiO}_2$  was red shifted after the doping with N and S. The further deposition of Ag nanoparticles on the surface of the  $\text{N,S-TiO}_2$

significantly influenced the visible light absorption, and an additional peak was also observed at 517 nm. The enhanced absorption in the visible region was due to the surface plasmon resonance (SPR), which was aroused by the collective oscillation of electrons in the Ag nanoparticles stimulated by optical excitation (Subramanian et al., 2004). The band-gap energy ( $E_{bg}$ ) values of the  $TiO_2$ , N,S- $TiO_2$ , and N,S- $TiO_2$ -Ag were calculated using the well-known Tauc's plot method (Lim et al., 2014b). The calculated  $E_{bg}$  values of  $TiO_2$ , N,S- $TiO_2$ , and N,S- $TiO_2$ @Ag were 3.36, 3.20, and 2.90 eV, respectively (**Figure 6.6(B-D)**). A remarkable reduction in the  $E_{bg}$  value of N,S- $TiO_2$  was observed due to the substitution of oxygen by nitrogen and sulfur in the  $TiO_2$  lattice. The mixing of the N 2p and S 2p states with O 2p states resulted in a band gap narrowing of  $TiO_2$  (Zhang et al., 2010). When Ag nanoparticles were added to the N,S- $TiO_2$ , the  $E_{bg}$  value was further decreased. This was due to the free electron properties being exhibited with a downward shift in the conduction band and upward shift in the valence band, which then led to a decrease in the  $E_{bg}$  value (Lim et al., 2014b).

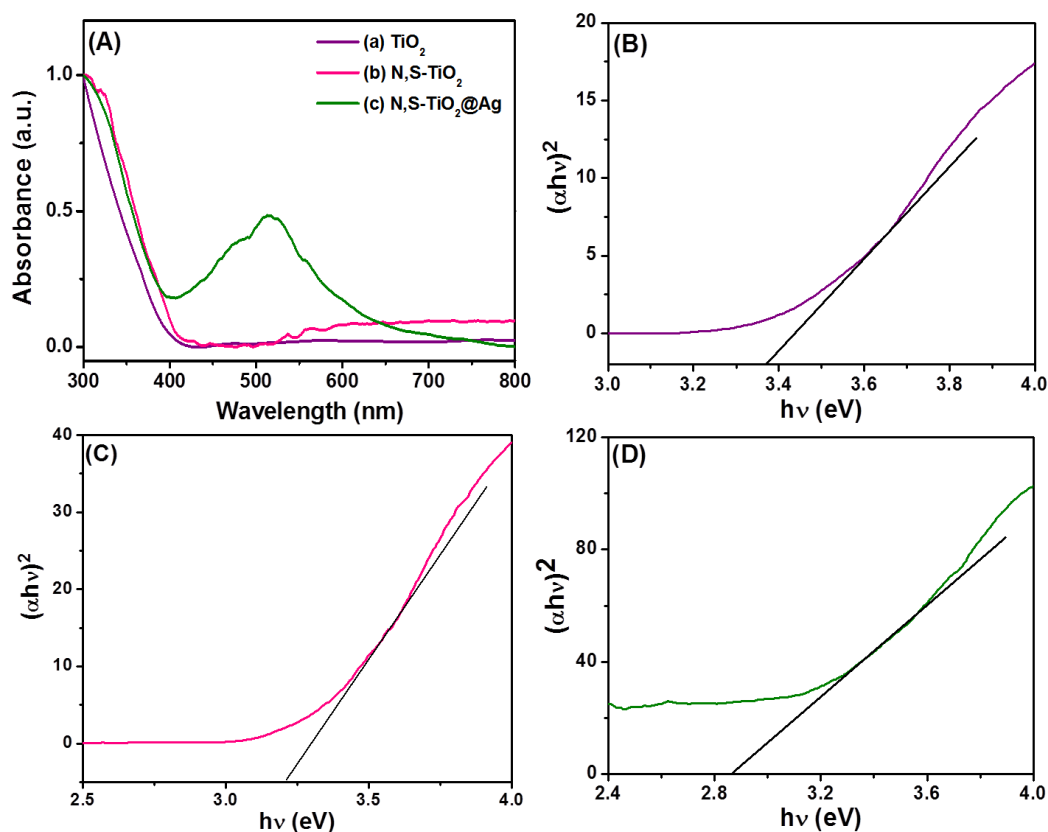


**Figure 6.6** (A) UV-Visible absorption spectra of the (a)  $\text{TiO}_2$ , (b)  $\text{N,S-TiO}_2$  and (c)  $\text{N,S-TiO}_2@\text{Ag}$ . Plots of  $(\alpha h\nu)^2$  versus  $h\nu$  obtained for (B)  $\text{TiO}_2$ , (C)  $\text{N,S-TiO}_2$  and (D)  $\text{N,S-TiO}_2@\text{Ag}$ .

Understanding the charge recombination process of a semiconductor is crucial because it significantly influences the photoelectrochemical properties and DSSC performance. Photoluminescence (PL) is a suitable tool to study the efficiency of charge carrier trapping, migration, and transfer, and to understand the fate of electron-hole pairs in semiconductor particles because PL emissions result from the recombination of free carriers. The  $\text{TiO}_2$  will absorb the incident photons with sufficient energy equal to or higher than the band-gap energy, which will produce photoinduced charge carriers ( $\text{h}^+ \dots \text{e}^-$ ). In addition, the recombination of photoinduced electrons and holes releases energy in the form of PL emission spectra. Hence, a lower PL intensity indicates less charge recombination. The observed PL spectra of  $\text{TiO}_2$ ,  $\text{N,S-TiO}_2$ , and  $\text{N,S-TiO}_2-\text{Ag}$  are shown in **Figure 6.7**. A broad peak with a maximum emission at around 580 nm can be observed for  $\text{TiO}_2$ ,  $\text{N,S-TiO}_2$ , and  $\text{N,S-TiO}_2-\text{Ag}$ . The  $\text{TiO}_2$  showed a higher PL

intensity due to the rapid recombination of photoinduced charge carriers. The PL intensity decreased when N, S, and Ag were introduced to TiO<sub>2</sub>. This can mainly be attributed to the formation of a Schottky barrier at the Ag and TiO<sub>2</sub> interface, which could act as an electron sink to efficiently prevent the electron hole recombination process (Du et al., 2006).

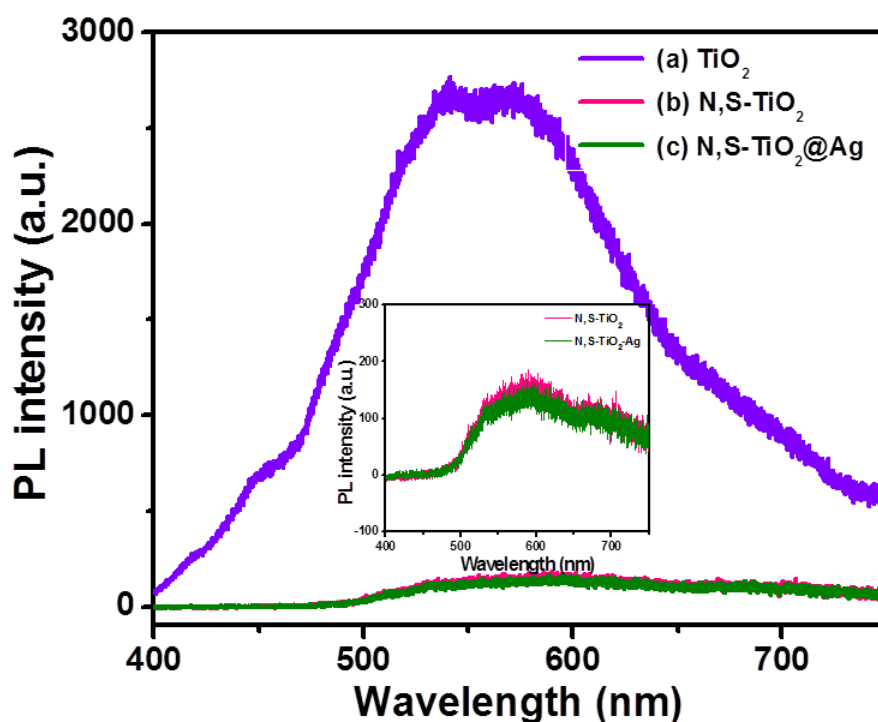


**Figure 6.7** Photoluminescence spectra of (a) TiO<sub>2</sub>, (b) N,S-TiO<sub>2</sub> and (c) N,S-TiO<sub>2</sub>@Ag.

### 6.2.5 Photovoltaic performance of N,S-TiO<sub>2</sub>@Ag photoanode-modified DSSCs

The photovoltaic performances of TiO<sub>2</sub>, N,S-TiO<sub>2</sub>, and N,S-TiO<sub>2</sub>@Ag photoanode-modified DSSCs under simulated solar irradiation of AM 1.5 G were studied by recording the J-V profiles, which are shown in **Figure 6.8**. The corresponding photovoltaic parameters are summarized in **Table 6.1**. A significant boost in the short-circuit current up to 29.05 mA/cm<sup>2</sup> can be observed from the J-V curve of N,S-TiO<sub>2</sub>@Ag compared to those of the DSSCs based on TiO<sub>2</sub> (6.27 mA/cm<sup>2</sup>) and N,S-TiO<sub>2</sub> (9.78 mA/cm<sup>2</sup>). The N,S-TiO<sub>2</sub>@Ag-based DSSC showed a conversion

efficiency ( $\eta = 8.22\%$ ) that was 145% and 231% higher than those of the DSSCs based on N, S-TiO<sub>2</sub> ( $\eta = 3.35\%$ ) and pure TiO<sub>2</sub> ( $\eta = 2.57\%$ ). This significant improvement in the photovoltaic performance was due to the synergetic effect of the N, S, and Ag. The presence of N in the TiO<sub>2</sub> successfully reduced the band gap and extended the absorption of TiO<sub>2</sub> into the visible region. The existence of S facilitated the electron transfer process and consequently increased the forward reduction reaction. The electrons from the conduction band could transfer to the more electropositive S atoms, which were reduced from S<sup>6+</sup> to S<sup>4+</sup>. The electrons were then transferred to the Ag to retain the system at S<sup>6+</sup> (Pany et al., 2013; Zhang et al., 2011). Moreover, the deposition of Ag onto the N,S-TiO<sub>2</sub> resulted in a change in the Fermi energy level. A large number of the electrons accumulated on the surfaces of the Ag nanoparticles due to the surface plasmon resonance effect. The accumulation of these electrons on the Ag nanoparticles shifted the position of the Fermi level closer to the conduction band of TiO<sub>2</sub> (Ni et al., 2007). The electrons in the Ag nanoparticles that were excited due to the SPR effect were transferred to the conduction band of the TiO<sub>2</sub> and collected by the current collector (ITO), which improved the photocurrent under irradiation in the visible region (Christopher et al., 2010). In this way, the photovoltaic performance significantly improved with the enhancement of absorption in the visible region. The synergetic effect of Ag and S as a redox couple played a potential role in the enhanced DSSC performance.

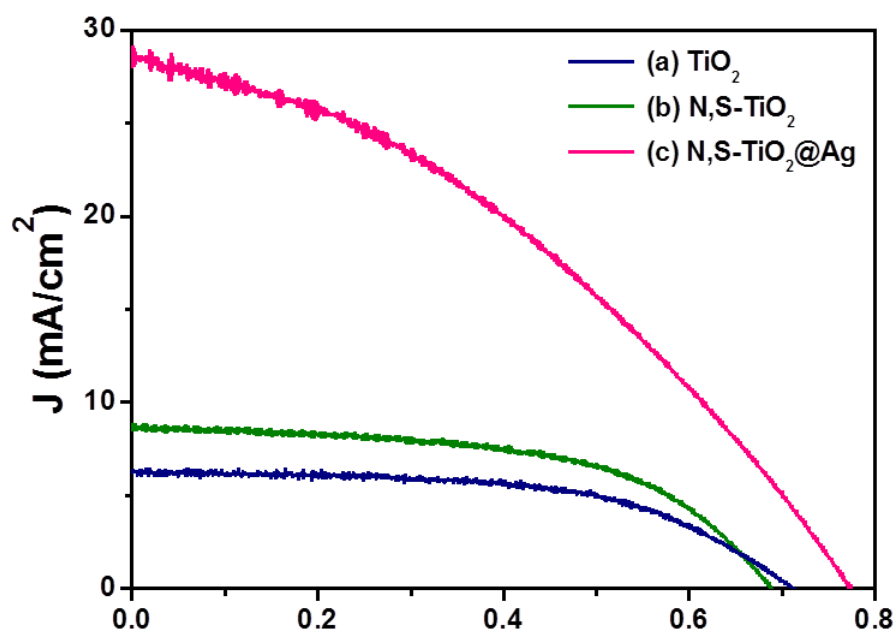


**Figure 6.8** Photocurrent density-photovoltage (J-V) curves obtained for the (a)  $\text{TiO}_2$ , (b)  $\text{N,S-TiO}_2$  and (c)  $\text{N,S-TiO}_2@\text{Ag}$  photoanode modified DSSCs.

**Table 6.1** Photovoltaic parameters of the fabricated DSSCs with controlled configurations

Photoanode	$J_{sc}$ ( $\text{mA}/\text{cm}^2$ )	$V_{oc}$ (V)	$J_{max}$ ( $\text{mA}/\text{cm}^2$ )	$V_{max}$ (V)	FF	$\eta$ (%)
$\text{TiO}_2$	6.27	0.70	5.25	0.49	0.59	2.57
$\text{N,S-TiO}_2$	9.78	0.69	6.69	0.50	0.50	3.35
$\text{N,S-TiO}_2@\text{Ag}$	29.05	0.77	17.88	0.46	0.37	8.22

**Foot note:** The DSSCs performance was evaluated under  $100 \text{ mW cm}^{-2}$  simulated AM 1.5G solar light irradiation.  $J_{sc}$ : Short-circuit current density;  $V_{oc}$ : Open-circuit voltage;  $J_{max}$ : Maximum photocurrent density;  $V_{max}$ : Maximum photovoltage; FF: Fill factor;  $\eta$ : Power conversion efficiency. Area of the cell electrode was  $0.5 \text{ cm}^2$

### 6.2.6 Influence of Ag content on photovoltaic performance of N,S-TiO<sub>2</sub>@Ag photoanode-modified DSSCs

The loading of the Ag content in the N,S-TiO<sub>2</sub>@Ag photoanode was varied to obtain a high-performance DSSC. The photocurrent density–photovoltage (J-V) curves were recorded for the N,S-TiO<sub>2</sub>@Ag nanocomposite-modified photoanodes with different Ag contents and are shown in **Figure 6.9**. Their corresponding photovoltaic parameters were also evaluated and are listed in **Table 6.2**. The obtained conversion efficiency for the N,S-TiO<sub>2</sub> photoanode without Ag showed a value of 3.39%, whereas N,S-TiO<sub>2</sub> with 20% Ag showed an efficiency of 8.22%. Those with 5, 10, and 40 % Ag showed conversion efficiencies of 5.42, 5.90, and 4.40 %, respectively. The observed results clearly revealed that the conversion efficiency of the DSSC was increased with an increase in the Ag content in the photoanode until it reached a maximum of 20%, and a further increase in the Ag content eventually led to a decrease in the conversion efficiency (**Figure 6.10 and Table 6.2**). The decrease in efficiency at a high Ag loading was due to the free standing/excess Ag in the composite, which could oxidize to Ag(I) (Guo et al., 2000; Zhao et al., 1997) and erode to the redox electrolyte (Zhao et al., 1997). The oxidation of the Ag would have acted as a new recombination center, thus reducing the number of charge carriers, which led to a decrease in the  $J_{sc}$  and  $V_{oc}$ . Consequently, the overall conversion efficiency of the DSSC deteriorated. The  $J_{sc}$  was increased by an increase in the Ag content and attained a maximum of 29.05 mA/cm<sup>2</sup> with 20% (**Figure 6.10(b)**). Then,  $J_{sc}$  decreased to 16.65 mA/cm<sup>2</sup> with 40% Ag loading in the photoanode of the DSSC. It could also be seen that the  $V_{oc}$  trend was almost the same, within the range of ~0.69–0.75 V. The  $J_{max}$  and  $V_{max}$  values of the device also followed trends similar to those of  $J_{sc}$  and  $V_{oc}$  (**Figure 6.10(c)**).

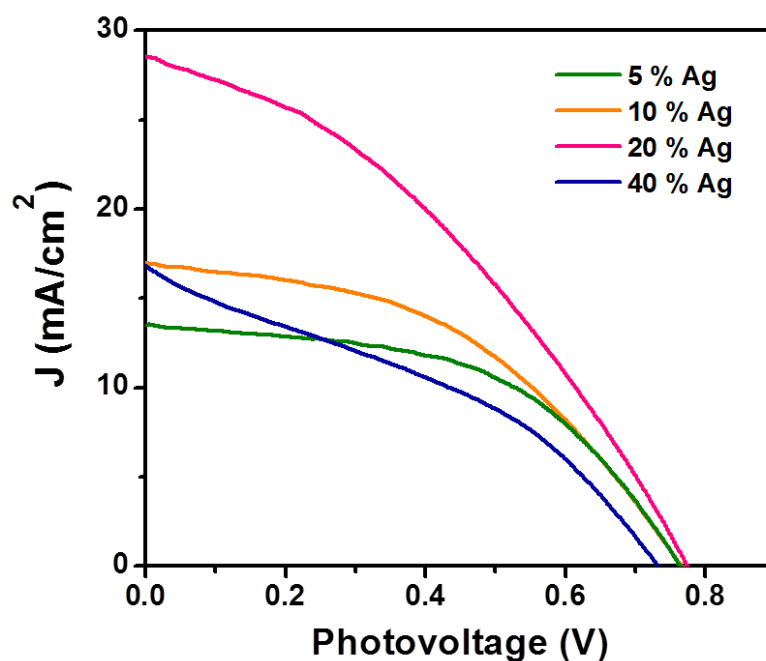


**Figure 6.9** Photocurrent density-photovoltage (J-V) curves obtained for the N,S-TiO<sub>2</sub>@Ag nanocomposite modified photoanodes with different Ag content.

**Table 6.2** Photovoltaic parameters of the N,S-TiO<sub>2</sub>@Ag photoanode with various Ag content.

Ag (%)	$J_{sc}$ (mA/cm <sup>2</sup> )	$V_{oc}$ (V)	$J_{max}$ (mA/cm <sup>2</sup> )	$V_{max}$ (V)	FF	$\eta$ (%)
0	9.78	0.69	6.69	0.50	0.50	3.35
5	13.33	0.76	10.42	0.52	0.53	5.42
10	17.04	0.76	12.29	0.48	0.49	5.90
20	29.05	0.77	17.88	0.46	0.37	8.22
40	16.65	0.73	9.37	0.47	0.36	4.40

**Foot note:** The DSSCs performance was evaluated under 100 mW cm<sup>-2</sup> simulated AM 1.5G solar light irradiation.  $J_{sc}$ : Short-circuit current density;  $V_{oc}$ : Open-circuit voltage;  $J_{max}$ : Maximum photocurrent density;  $V_{max}$ : Maximum photovoltage; FF: Fill factor;  $\eta$ : Power conversion efficiency. Area of the cell electrode was 0.5 cm<sup>2</sup>.

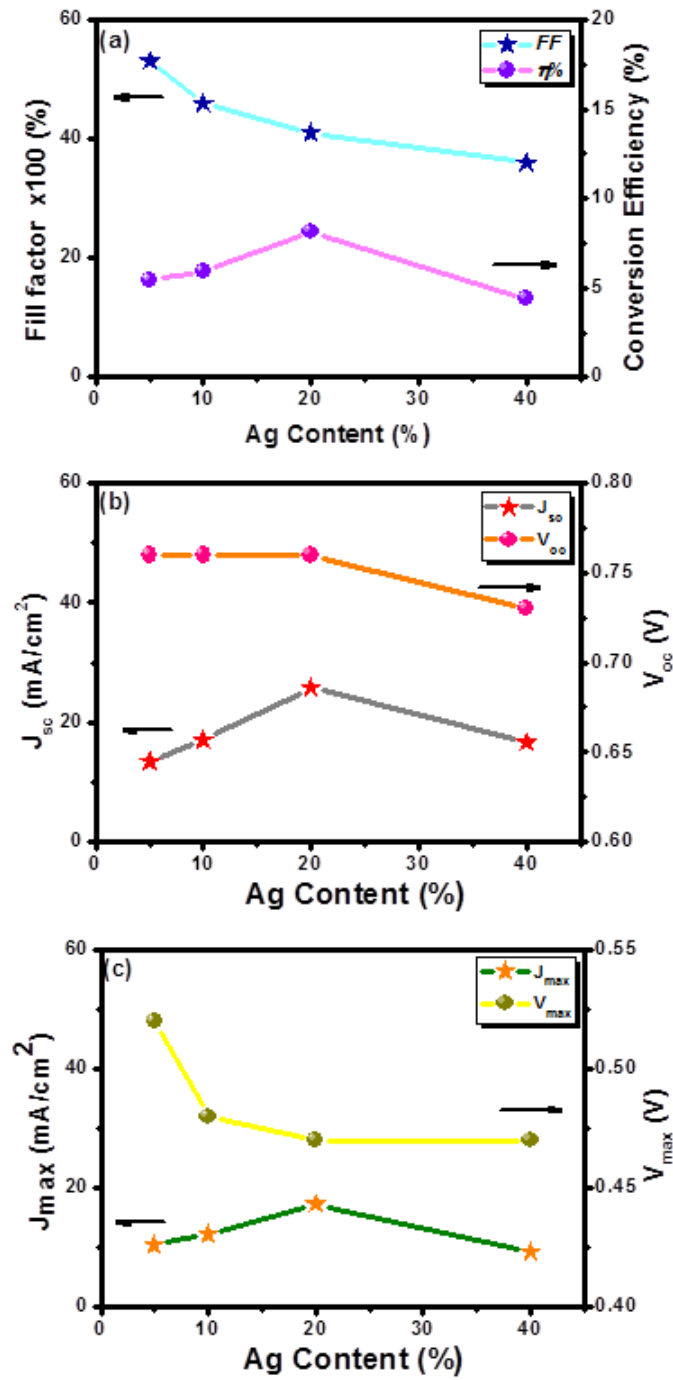


**Figure 6.10** Plots of (a) Fill factor (FF) and power conversion efficiency ( $\eta$ ), (b) short-circuit current density ( $J_{sc}$ ) and open-circuit voltage ( $V_{oc}$ ) and (c) maximum photocurrent density ( $J_{max}$ ) and maximum photovoltage ( $V_{max}$ ) with different Ag content.

### 6.2.7 Electrochemical Behavior of N,S-TiO<sub>2</sub>@Ag Photoanode-Modified DSSCs

For the interfacial charge transfer process within the fabricated DSSC with the N,S-TiO<sub>2</sub>@Ag photoanode, the electrochemical impedance spectra (EIS) were recorded in the frequency range between 0.01 Hz and 100 KHz, and are shown in **Figure 6.11**. Well-defined semicircles in the middle frequency region for the DSSCs with N,S-TiO<sub>2</sub>@Ag nanocomposite-modified photoanodes with different Ag contents were observed in the Nyquist plots (**Figure 6.11(A)**). The intersection of the high-frequency semicircle at the real axis represents the equivalent series resistance of the device ( $R_s$ ); the arc in the middle frequency range between 1 and 1000 Hz represents the charge transfer resistance ( $R_{ct}$ ) between the dye-adsorbed photoanode and electrolyte interface (van de Lagemaat et al., 2000; Wang et al., 2012). The  $R_s$  values varied because different concentrations of Ag used in the photoanode. An increase in the  $R_{ct}$  value of the N,S-TiO<sub>2</sub>@Ag-based photoanode was observed with the increasing Ag content. Thus, a photoanode that contained a high amount of Ag with a higher  $R_{ct}$  value corresponded to an ineffective electron transfer process between the photoanode and electrolyte interface. The changes in  $R_s$  and  $R_{ct}$  could mainly be attributed to the changes in the Ag content of the photoanode, which contributed the most to the internal impedance. The Nyquist plot for different types of photoanodes is shown in **Figure 6.11(B)**. As demonstrated in the Nyquist plot, both the real ( $Z'$ ) and imaginary ( $Z''$ ) parts of the total impedance, as well as the  $R_{ct}$  value, increased in the order N,S-TiO<sub>2</sub> < TiO<sub>2</sub> < N,S-TiO<sub>2</sub>@Ag, which showed the crucial dependence of the charge transport on the dopants (N and S) and Ag incorporation. The  $R_s$  value also increased with the addition of N, S, and Ag. Therefore, the origin of the higher  $J_{sc}$  in N,S-TiO<sub>2</sub>@Ag is expected to have arisen from the device resistance ( $R_s$ ),  $R_{ct}$ , and charge transport dynamics determined by the electron lifetime ( $\tau_n$ ). Based on the Bode phase plots (**Figure 6.11(C and D)**), the frequency was apparently shifted to the lower frequency

region with the addition of N, S, and Ag. The maximum frequencies ( $\omega_{\max}$ ) in the middle frequency region of the Bode plots for  $\text{TiO}_2$  and  $\text{N,S-TiO}_2\text{@Ag}$  were 792.44 Hz and 316.23 Hz, respectively. Since  $\omega_{\max}$  is inversely associated with the electron lifetime  $\tau_n = 1/(2\pi f)$  (Archana et al., 2014; Kim et al., 2013), the decrease in  $\omega_{\max}$  indicated a reduced rate for the charge-recombination process in the DSSC. Hence, electrons with longer  $\tau_n$  values were prevented from recombining, characterized by a larger  $R_{\text{ct}}$ .

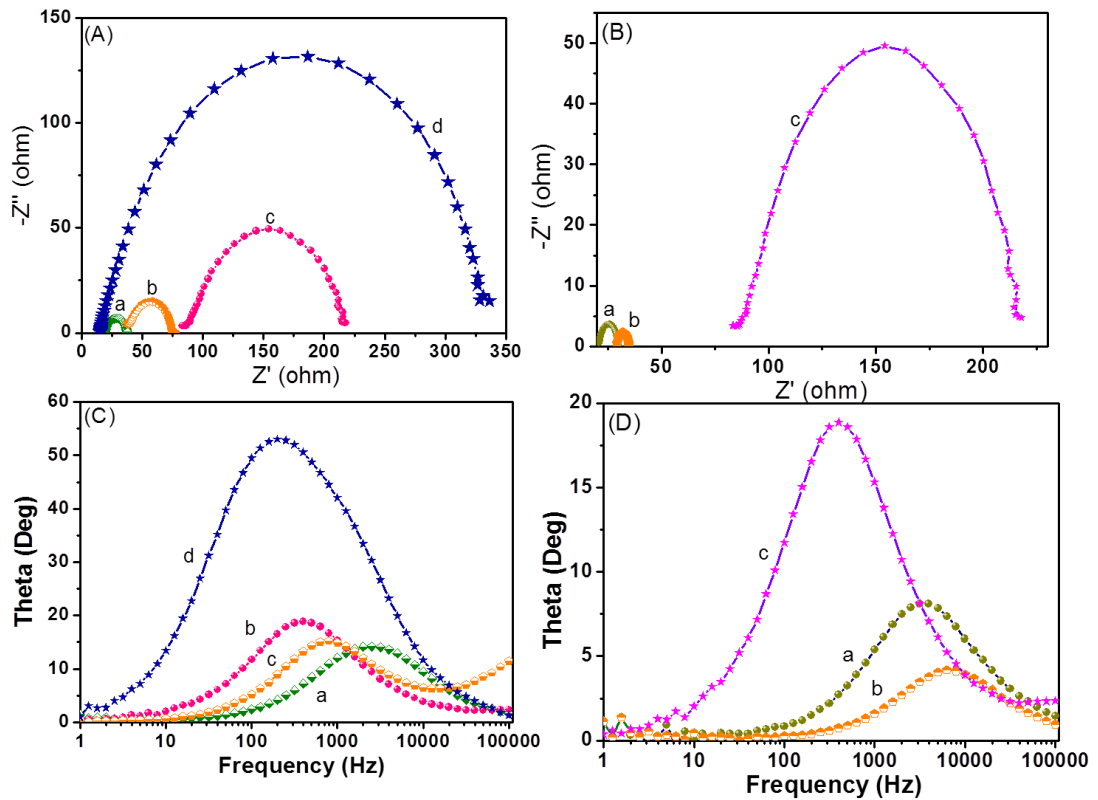


**Figure 6.11**(A) Nyquist plot and (C) Bode phase plots obtained for  $\text{N,S-TiO}_2\text{@Ag}$  nanocomposite modified photoanodes with (a) 5, (b) 10, (c) 20, and (d) 40 % of Ag content. (B) Nyquist plot and (D) Bode phase plots of (a)  $\text{TiO}_2$ , (b)  $\text{N/S-TiO}_2$  and (c)  $\text{N,S-TiO}_2\text{@Ag}$ .

Furthermore, **Table 6.3** and **Figure 6.12** summarize the results obtained from the Nyquist plot. The N,S-TiO<sub>2</sub>@Ag photoanode exhibited a faster electron transport time ( $\tau_s = R_s * C_\mu$ ) (Kim et al., 2013; Nissfolk et al., 2006; Wang et al., 2008) than TiO<sub>2</sub>. Hence, its electron lifetime ( $\tau_n = R_{ct} * C_\mu$ ) (Kim et al., 2013; Nissfolk et al., 2006; Wang et al., 2008) was significantly increased, and they were prevented from recombining. The photovoltaic performance of the DSSC was clearly reflected by the charge collection efficiency ( $\eta_c$ ) derived from  $\eta_c = (1 + R_s/R_{ct})^{-1}$  (Kim et al., 2013; Nissfolk et al., 2006; Wang et al., 2008). Eventually, the charge collection efficiency was significantly increased upon the addition of N, S, and Ag. Therefore, we can conclude that as a result of the longer  $\tau_n$  and larger  $R_{ct}$ , the devices fabricated using N,S-TiO<sub>2</sub>@Ag showed improved  $J_{sc}$  values compared to the TiO<sub>2</sub> and N,S-TiO<sub>2</sub> photoanode-based DSSCs.

**Table 6.3** EIS analysis results of the fabricated DSSC.

Photoanode	$R_s(\Omega)$	$R_{ct}(\Omega)$	$C_\mu(\mu F)$	$\tau_s(ms)$	$\tau_n(ms)$	$\eta_c(\%)$
TiO <sub>2</sub>	21.01	8.91	7.10	0.48	0.20	29
N,S-TiO <sub>2</sub>	17.21	12.36	8.12	0.13	0.25	16
N,S-TiO <sub>2</sub> @Ag	15.34	20.28	6.23	0.32	0.50	60

**Foot note:** The electrochemical impedance spectra (EIS) were recorded at an applied bias of -0.7 V in the frequency range between 0.01 Hz and 100 KHz.  $R_s$ : Devise resistance;  $R_{ct}$ : Charge transfer resistance;  $C_\mu$ : chemical capacitance;  $\tau_s$ : Electron transport time;  $\tau_n$ : Electron lifetime;  $\eta_c$ : charge collection efficiency.

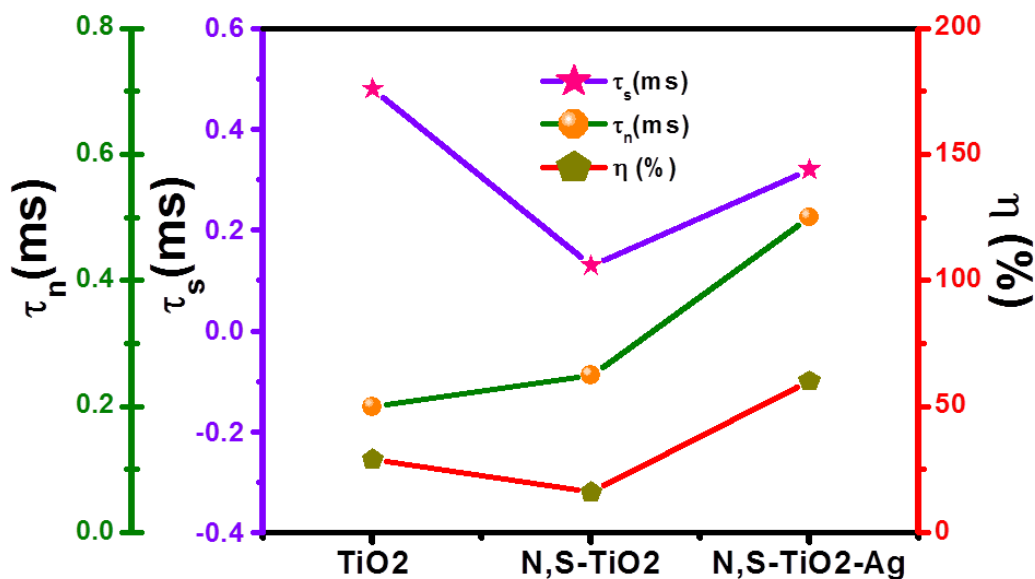


**Figure 6.12** Electron lifetime, electron transport time and charge collection efficiency of TiO<sub>2</sub>, N,S-TiO<sub>2</sub> and N,S-TiO<sub>2</sub>@Ag photoanode based DSSCs.

### 6.2.8 Operation Principle of N,S-TiO<sub>2</sub>@Ag Photoanode-Modified DSSCs

The operation principle of the N,S-TiO<sub>2</sub>@Ag nanocomposite photoanode-modified DSSC under illumination is shown in **Figure 6.13(a)**. Upon illumination, the adsorbed dye molecules (N719) underwent photo-excitation. The excited electrons were injected into the conduction band of the N,S-TiO<sub>2</sub> nanocomposite. The dye<sup>+</sup> became oxidized by receiving electrons from the electrolyte through the redox system, and was regenerated. The electrolyte itself was regenerated *via* the platinum counter electrode by electrons passing through the external circuit. In our study, the deposition of Ag onto the surface of N,S-TiO<sub>2</sub> not only acted as an electron sink for efficient charge transfer, but could also be used as a scattering element for plasmonic scattering to trap the light in the near field coupled with the dye molecules (Lin et al., 2012). This will eventually improve the optical absorption of the dye, resulting in a significant photocurrent enhancement (**Figure 6.13(b)**). In addition, the inclusion of Ag nanoparticles resulted in

a change in the Fermi energy level. The electrons in the conduction band of the  $\text{TiO}_2$  could be effectively captured by the Ag until a Fermi level equilibrium was obtained and the charge recombination process was minimized, which improved the DSSC performance. The ideal property of Ag nanoparticles and the presence of N and S also successfully reduced the band gap and helped to shift the optical absorbance toward the visible region. The incorporation of N in the  $\text{TiO}_2$  lattice in the form of N-Ti-O partially converted the system from  $\text{Ti}^{4+}$  to  $\text{Ti}^{3+}$  and effectively contributed to the visible light absorption (Naik et al., 2010; Pany et al., 2013). Furthermore, the existence of S also played a vital role in the photovoltaic performance, facilitated the electron transfer process, and consequently increased the forward reduction reaction. The Ag and S acted as co-catalysts and effectively minimized the electron recombination process. The attractiveness of the present photoanode is that it combines all of the photovoltaic fundamental criteria within its electronic environment.



### 6.3 Conclusion

A simple approach to prepare Ag nanoparticle-deposited N,S-TiO<sub>2</sub> nanocomposite *via* a chemical reduction method to fabricate a novel photoanode for a DSSC was demonstrated. The N,S-TiO<sub>2</sub>@Ag nanocomposite was characterized using UV–visible absorption, PL, Raman, XRD, XPS, SEM, EDAX, and TEM analyses. The DSSC fabricated with an N,S-TiO<sub>2</sub>@Ag-modified photoanode showed an enhanced solar-to-electrical energy conversion efficiency of 8.22% compared to the photoanode of a DSSC composed of unmodified TiO<sub>2</sub> (2.57%) under simulated solar irradiation of 100 mWcm<sup>-2</sup> with AM 1.5 G. The enhancement in the photovoltaic performance was mainly attributed to the plasmonic Ag nanoparticles, which enhanced the visible light adsorption as a result of their light harvesting property in the visible range due the surface plasmon effect. These Ag nanoparticles also significantly promoted interfacial charge transfer, which minimized the charge recombination process. The optimal Ag content in the N,S-TiO<sub>2</sub> to obtain an efficient photoanode was found to be 20 wt.% Ag. In addition, the presence of the N and S dopants also helped to reduce the band gap, shift the optical absorbance toward the visible region, and also suppress the charge recombination. The synergetic effect of the Ag nanoparticles, surface plasmon effect, reduction of the band gap, and effective charge transfer ameliorated the photocurrent generation and conversion efficiency of the DSSC.

## CHAPTER 7

### Gold and Silver Co-Deposited Titania Based Plasmonic Nanocomposite for Higher Efficiency Dye-Sensitized Solar Cells

#### 7.1 Introduction

Solar cells are attracting much attention for utilizing natural resources to produce electricity because of concerns over energy depletion and our high dependence on fossil fuels. Among the various types of solar cells, dye-sensitized solar cells (DSSCs) have emerged as promising candidates for harvesting solar power, because of their low cost, flexibility, ease of production, relatively high energy conversion efficiency, and low toxicity to the environment (O'Regan et al., 1991). However, the efficiency of the DSSC is still lower than that the conventional crystalline silicon based solar cells. The efficient operation of a DSSC greatly depends on the minimization of the charge recombination occurring at the  $\text{TiO}_2$ /dye/electrolyte interface. Therefore, designing a photoanode with an efficient transport pathway from the photo-injected charge carriers to the current collector seems to be a possible alternative to enhance the performance of DSSCs.

Many active studies being conducted to overcome the deficiency of  $\text{TiO}_2$ -based DSSCs, which can be divided into a few approaches such as efforts to increase the dye sensitization area through the control structure and morphology of the  $\text{TiO}_2$  to improve the monolayer dye absorption (Meng et al., 2008; Wu et al., 2013). Research has also been done on ways to improve the light absorption in the visible region. There are two solutions to this problem: (i) synthesizing a higher efficiency dye and (ii) improving the light absorption in the visible region by incorporating a noble metal into  $\text{TiO}_2$  (Eagen, 1981; Mock et al., 2002; Schaadt et al., 2005). In order to enhance the efficiency of DSSCs, it is essential to prevent the charge recombination process at the  $\text{TiO}_2$ /dye/electrolyte interfaces. The most common approach is surface modification

with metal nanoparticles, non-metals, coupling semiconductor, and hybridizing with carbon materials (Lai et al., 2010; Macak et al., 2007; Yang et al., 2007; Zhao et al., 2010).

Recently, the surface of  $\text{TiO}_2$  has been modified with noble metal nanoparticles such as silver (Ag) and gold (Au), with the aim of improving the efficiency of a DSSC. These noble metal nanoparticles play dual roles in the DSSC performance, including the enhancement of the absorption coefficient of the dye and the optical absorption due to surface plasmon resonance (Eagen, 1981; Mock et al., 2002; Schaadt et al., 2005). Moreover, they also play role in improving the interfacial charge transfer process, and minimizing the charge recombination, thereby enhancing the electron transfer process in a DSSC (Lee et al., 2008; Wen et al., 2000; Zhao et al., 1997). Hence, noble metals nanoparticles have been targeted for use in DSSCs with the goal of improving the interfacial charge transfer process and photon-to-electron conversion in the visible region. . Recently, the performance of a DSSC with  $\text{Au@TiO}_2$  and  $\text{Ag@TiO}_2$  plasmonic nanocomposite material-modified photoanodes has been actively investigated (Ghaffari et al., 2012; Li et al., 2011; Sahu et al., 2012; Tian et al., 2013; Xu et al., 2013).

Based on the above studies,  $\text{Au@TiO}_2$  and  $\text{Ag@TiO}_2$  have most commonly used separately as photoanodes in DSSCs. Till date, no study has yet explored the co-deposition of Au and Ag nanoparticles on  $\text{TiO}_2$  as a photoanode for a DSSC. In the present study, we successfully developed a facile synthetic method to co-deposit Au and Ag nanoparticles on a  $\text{TiO}_2$  surface using a simple chemical reduction, and characterized by various suitable analytical techniques. The DSSC assembled with the  $\text{Au-Ag@TiO}_2$ -modified photoanode showed an enhanced conversion efficiency of 9.54% compared to one with the unmodified  $\text{TiO}_2$  (2.22%). Thus, the introduction of plasmonic Au and Ag

nanoparticles on the  $\text{TiO}_2$  surface enhanced the efficiency due to the reduced band gap energy and retarded charge recombination. The influence of the Au-Ag ratio on the overall efficiency was also explored, and the optimum composition was found to be 75:25. This Au-Ag@ $\text{TiO}_2$  nanocomposite could be a potential candidate for solar energy conversion.

## 7.2 Results and Discussion

### 7.2.1 Formation of Au-Ag@ $\text{TiO}_2$ Nanocomposite

During the synthesis of the Au-Ag@ $\text{TiO}_2$  nanocomposite (Detailed synthetic procedure was given in Chapter: 3; Section: 3.2.6), it was observed that the color of the nanocomposite changed during the stirring process, and the extent of this change depended on the Au-Ag ratio on the  $\text{TiO}_2$ . The  $\text{TiO}_2$  nanocomposite without the Au and Ag was white. After adding the Au and Ag precursors, the initial color of the mixture was clear yellow. As the stirring process continued, the mixture with only Ag turned green and then greenish brown, whereas a purple color was observed when Au was added. The nanocomposite became darker in color as the Au content increased (**Figure 7.1**). The different color of the nanocomposite that was obtained after the incorporation of the metal indicated that a different visible light absorption was exhibited by the nanocomposite with the addition of the different metals.



**Figure 7.1** Physical appearance of as-prepared Au@Ag/ $\text{TiO}_2$  nanocomposites with different composition of Au:Ag ratio.

### 7.2.2 Morphological Characterization of Au-Ag@TiO<sub>2</sub> Nanocomposite

The back-scattered electrons (BSE) and FESEM images indicated the general structure and distribution of the Au and Ag within the synthesized Au-Ag@TiO<sub>2</sub> nanoparticles, as shown in **Figure 7.2**. **Figure 7.2(a)** shows the FESEM image of the TiO<sub>2</sub> nanoparticles, which appeared to be spherical and uniform in size. Upon the addition of Au and Ag nanoparticles, no significant change in morphology was observed for the Au-Ag@TiO<sub>2</sub> nanocomposite (**Figure 7.2(b)**). Since the distribution of Au and Ag cannot be clearly shown by the FESEM image, hence BSE image is taken for the Au-Ag@TiO<sub>2</sub> nanocomposite. The quantity of the back-scattered electrons is highly dependent on the atomic number of sample. Material with a higher atomic number will have more back-scattered electrons (Enzhou et al., 2014). Since the Au and Ag have greater atomic numbers than titanium and oxygen, Au and Ag nanoparticles will be brighter than titanium dioxide. From the BSE image, it can be observed that the Au and Ag nanoparticles were homogenously distributed on the TiO<sub>2</sub> nanoparticles. There are two particle size ranges observed on the TiO<sub>2</sub> surface. It was believed that the Au and Ag had different particle sizes. The energy dispersive X-ray spectrometry (EDS) mapping analysis of the Au-Ag@TiO<sub>2</sub> thin film also confirmed that the Au-Ag@TiO<sub>2</sub> nanocomposite, composed of Au and Ag elements, dispersed on the surface of the TiO<sub>2</sub> nanoparticles with Ti and O signals (**Figure 7.2(c)**).

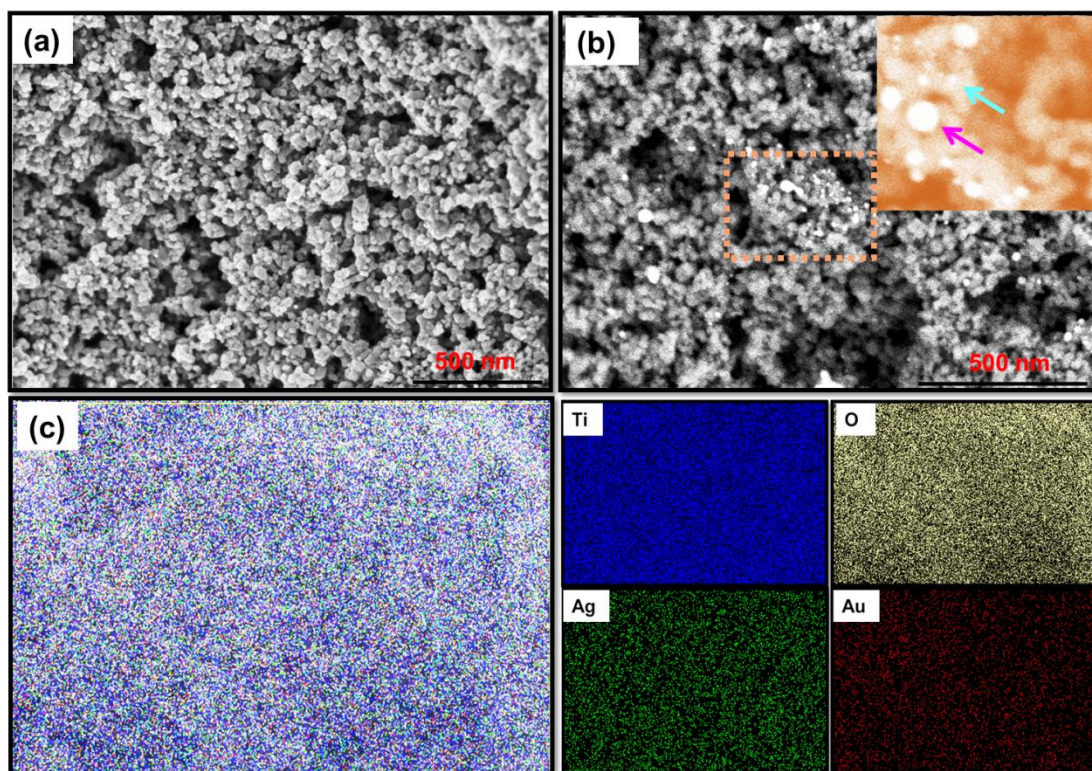


**Figure 7.2** FESEM image of TiO<sub>2</sub>, (b) Back-scattered electron image of Au@Ag/TiO<sub>2</sub> and (c) element mapping of Au@Ag/TiO<sub>2</sub> nanocomposite.

Further, TEM images for Au-Ag@TiO<sub>2</sub> were also recorded, and are shown in **Figure 7.3(a-c)**. The **Figure 7.3(a)** shows Ag@TiO<sub>2</sub> nanoparticles, and it can be observed that the TiO<sub>2</sub> nanoparticles are spherical in shape, with a particle size range of 20–25 nm. Further, the TEM image clearly shows that the small spherical Ag nanoparticles with a particle size range of 2–5 nm are well distributed and decorated on the surfaces of the TiO<sub>2</sub> nanoparticles. The TEM image of the Au@TiO<sub>2</sub> nanoparticles is presented in **Figure 7.3(b)** and the Au particle size range is 8–20 nm. Thus, we can observe that the particle size of the Au decoration is larger than the Ag particle size, which explains the BSE image of the Au-Ag@TiO<sub>2</sub> nanocomposite. **Figure 7.3(c)** depicts the TEM image of the Au-Ag@TiO<sub>2</sub> (Au<sub>75</sub>-Ag<sub>25</sub>). It is also observed that the Au and Ag nanoparticles interact with the TiO<sub>2</sub>, with most of the Au and Ag nanoparticles actually embedded within the TiO<sub>2</sub> and a few of them surrounding the TiO<sub>2</sub>. The selected area electron diffraction (SAED) pattern of the Au-Ag@TiO<sub>2</sub> nanocomposite is

shown in **Figure 7.3(d)**. The pattern clearly reveals that the bright concentric rings from the center outward belong to the diffraction from (111), (310), (312), and (421) rutile  $\text{TiO}_2$  and Au (222).

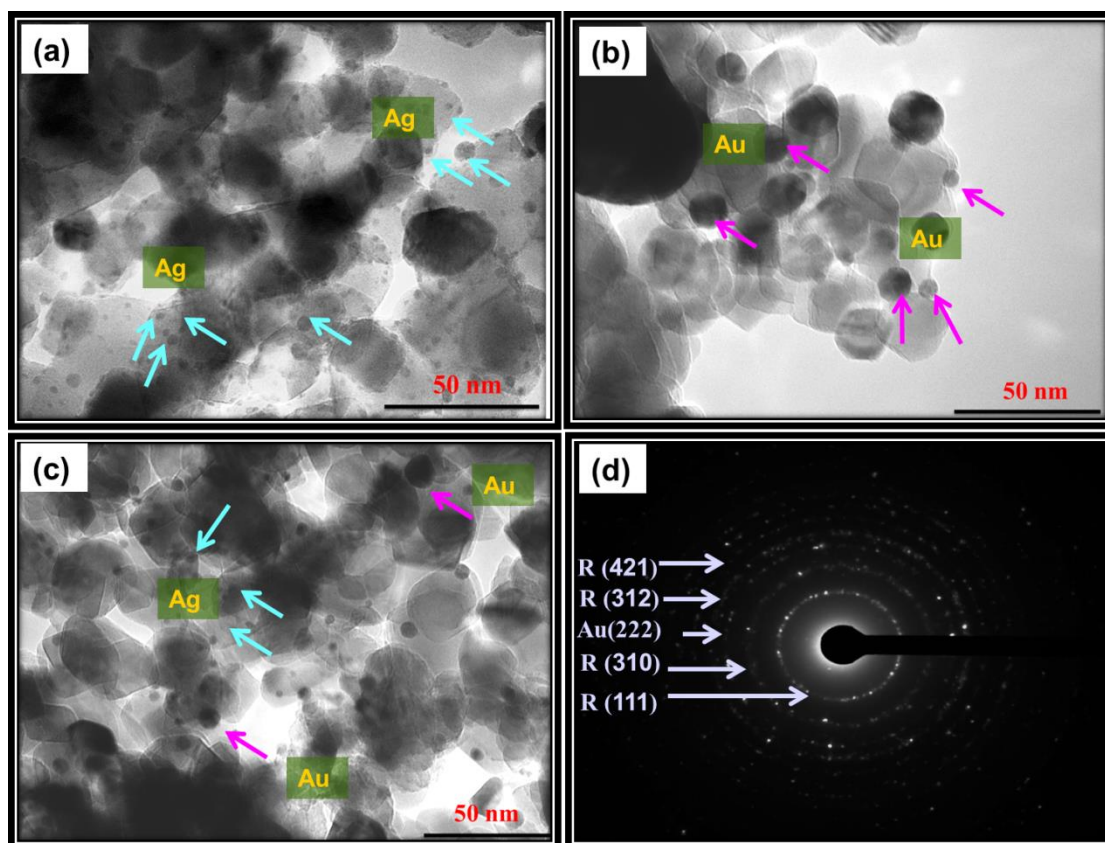


**Figure 7.3** TEM images of (a)  $\text{Ag@TiO}_2$ , (b)  $\text{Au@TiO}_2$ , (c)  $\text{Au@Ag/TiO}_2$  ( $\text{Au}_{75}\text{:Ag}_{25}$ ) and (d) SAED pattern of  $\text{Au@Ag/TiO}_2$ .

### 7.2.3 Crystalline Studies of $\text{Au-Ag@TiO}_2$ Nanocomposite

The XRD pattern obtained for  $\text{Au-Ag@TiO}_2$  is shown in **Figure 7.4**, along with those for the  $\text{TiO}_2$ ,  $\text{Au/TiO}_2$ , and  $\text{Ag/TiO}_2$  for comparison. The  $\text{TiO}_2$ ,  $\text{Ag@TiO}_2$ ,  $\text{Au@TiO}_2$ , and  $\text{Au-Ag@TiO}_2$  films were composed of mixed anatase and rutile phases, which agreed with reference patterns JCPDS 83-2243 and 21-1276, respectively. The diffraction peaks observed at  $25.5^\circ$ ,  $38.4^\circ$ ,  $48.2^\circ$ , and  $75^\circ$  correspond to the anatase phase of  $\text{TiO}_2$  and are assigned to the (101), (004), (200), and (215) crystallographic planes, respectively. In contrast, the peaks at  $54.9^\circ$  and  $63^\circ$  are in good agreement with

the rutile phase of  $\text{TiO}_2$  and are assigned to the (220) and (002) crystallographic planes, respectively. No XRD peak could be discerned because of the low content of Ag in the nanocomposite. However, for the 100% Au composition, a peak at  $44^\circ$  could be identified as belonging to the (200) plane of a face-centered cubic gold phase (JCPDS 04-0784). It was difficult to differentiate the Ag from the  $\text{TiO}_2$  signals even at a 100% Ag composition due to the overlapping of the Ag signal with rutile plane in  $\text{TiO}_2$ . The XRD patterns clearly confirmed that the anatase and rutile phases were retained without a phase change after the deposition of Au and Ag nanoparticles. The additional peaks were due to the ITO substrate.

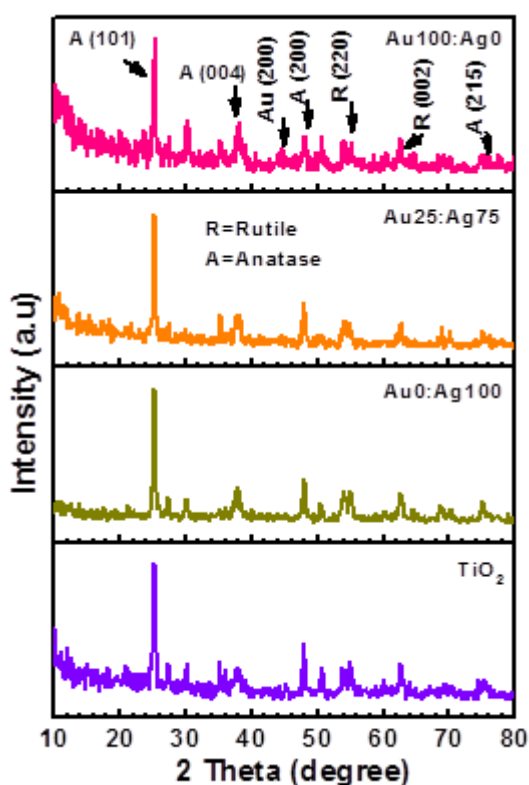


**Figure 7.4** XRD patterns of Au-Ag@ $\text{TiO}_2$  nanocomposite with different composition of Au-Ag.

An alternative method to explore the crystalline property is Raman scattering, it is a local probe and very sensitive to the crystalline structure and nanostructure of a material. Raman studies were performed in the range of  $100\text{--}1000\text{ cm}^{-1}$ , and the results are shown in **Figure 7.5**. The peaks at  $143.32$ ,  $202.61$ ,  $397.92$ ,  $514.89$ , and  $635.22\text{ cm}^{-1}$  were due to the anatase phase  $\text{TiO}_2$  (Chiarello et al., 2010; Sivaranjani et al., 2011). It

can be observed that the peaks became weak and broad with the addition of Au and Ag when the samples had a local lattice defect (Zhang et al., 2000). The Raman peaks also showed a red-shift toward a lower frequency.

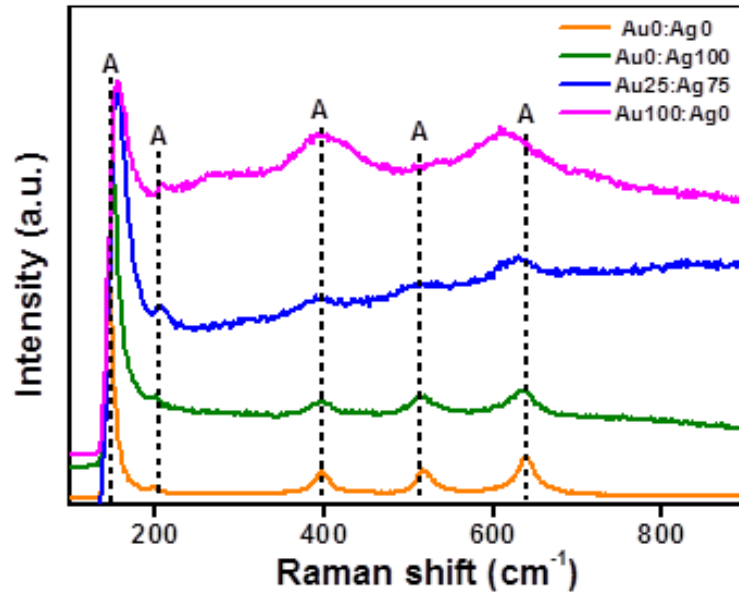


**Figure 7.5** Raman spectra of Au-Ag@TiO<sub>2</sub> nanocomposite with different composition of Au-Ag.

This can be attributed to the strain induced by the Au and Ag loading and may have been due to the changes in the crystalline size (Xiang et al., 2010). However, no signals related to metal particles were identified for the samples because of the relatively low concentration of Au or Ag loaded onto the TiO<sub>2</sub> and its weak Raman scattering power. An interesting observation is that the peak intensities increased with the deposition of Ag, and the position of the Raman signal remained the same. This indicates that there was an interaction between the Ag and TiO<sub>2</sub> that affected the Raman resonance of TiO<sub>2</sub> (Lim et al., 2014b; Su et al., 2012). This observation shows that the deposition of Ag on TiO<sub>2</sub> does not cause any phase transition, but may bring about an electronic environment change in the surrounding (Chiarello et al., 2010; Sivaranjani et al., 2011).

#### 7.2.4 XPS Analysis of Au-Ag@TiO<sub>2</sub> Nanocomposite

The XPS spectra of the TiO<sub>2</sub>, Ag@TiO<sub>2</sub>, Au@TiO<sub>2</sub> and Au-Ag@TiO<sub>2</sub> were recorded in order to identify the chemical state of Ti, O, Au and Ag elements and are shown in **Figure 7.6**. **Figure 7.6(a)** shows the Ti 2p spectra for the samples in which two peaks are observed at 458 and 463.8 eV corresponding to the binding energies of Ti 2p<sub>3/2</sub> and Ti 2p<sub>1/2</sub> core levels, respectively, due to the presence of the Ti(IV) state (Briggs, 1981). After the deposition of the Au and Ag nanoparticles, it is observed that the Ti 2p peak was slightly shifted to lower binding energies due to its surrounding chemical environment (Wang et al., 2014). **Figure 7.6(b)** shows the O 1s spectra of the TiO<sub>2</sub>, Ag@TiO<sub>2</sub>, Au@TiO<sub>2</sub>, and Au-Ag@TiO<sub>2</sub>. The binding energy of the O 1s state of the samples was located at 531 eV, which was assigned to the bulk oxides (O<sup>2-</sup>) in the P25 lattice. The O 1s is slightly shifted to higher binding energies with the addition of Au or Ag, indicating an increase in electron density around the O atoms due to the interaction of the residue precursor with TiO<sub>2</sub> (Tian et al., 2013). The Au 4f spectra of Au@TiO<sub>2</sub> and Au-Ag@TiO<sub>2</sub> samples are shown in **Figure 7.6(c)**. The binding energies are 83.8 and 87.7 eV, respectively which suggests that the Au is in the metallic state. The binding energies found for Ag 3d<sub>5/2</sub> and Ag 3d<sub>3/2</sub> levels are 368.5 and 374.5 eV, respectively (**Figure 7.6(d)**), with a peak separation of 6 eV due to the metallic silver. Hence, the XPS analysis provides the support for the existence of elements such as, Ti, O, Au and Ag in the nanocomposite materials.

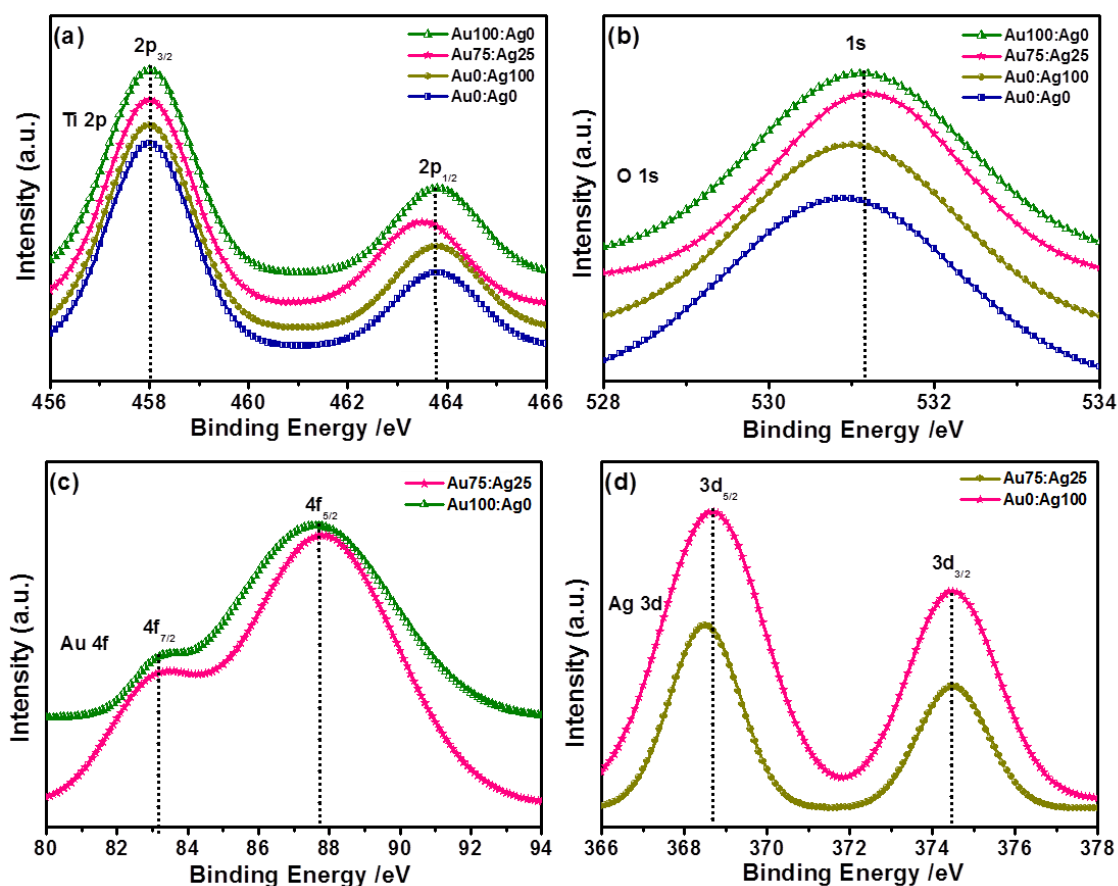


**Figure 7.6** XPS spectra of Au-Ag@TiO<sub>2</sub> nanocomposite with Au<sub>75</sub>-Ag<sub>25</sub> and their corresponding core-level spectra of (a) Ti 2p (b) O 1s (c) Au 4s and (d) Ag 3d.

### 7.2.5 Optical Properties of Au-Ag@TiO<sub>2</sub> Nanocomposite

The optical absorption properties of the TiO<sub>2</sub>, Ag/TiO<sub>2</sub>, Au/TiO<sub>2</sub>, and Au-Ag@TiO<sub>2</sub> were studied by recording the UV–visible absorption spectra, which shown in **Figure 7.7 (a and b)**. The bare TiO<sub>2</sub> nanoparticles did not show any absorption in the visible light region (**Figure 7.7(b)**). The deposition of the Au and Ag nanoparticles on the TiO<sub>2</sub> surface leads to a prominent increase in the absorbance in the visible region. An additional peak due to the surface plasmon resonance (SPR) was also observed with the incorporation of Au and Ag. The maximum absorption values for Ag@TiO<sub>2</sub> and Au@TiO<sub>2</sub> were observed at 444 and 523 nm, respectively, due to the characteristic surface plasmon resonance (SPR) of the Au and Ag nanoparticles. For the various composition of the Au-Ag in TiO<sub>2</sub>, Au<sub>25</sub>:Ag<sub>75</sub>, Au<sub>50</sub>:Ag<sub>50</sub> and Au<sub>75</sub>:Ag<sub>25</sub>, the SPR band

was observed between the 477 and 524 nm region (**Figure 7.7(a)**). When the Au content was increased in the nanocomposite, it can be seen that there was a red-shift in the visible absorption edge of the nanocomposite. The deposition of Au and Ag nanoparticles on the TiO<sub>2</sub> surface significantly influenced the visible light absorption. The enhancement of absorption in the visible region was due to the SPR, which was aroused by the collective oscillation of electrons in the Ag and Au nanoparticles stimulated by optical excitation (Subramanian et al., 2004). It was reported that the interfacial chemical interaction and charge transfer between the noble metal nanoparticles and the matrix will influence the free electron density and consequently affect the SPR frequency (Chen et al., 2001; Hövel et al., 1993).

One of the main objectives of incorporating Au and Ag nanoparticles into the TiO<sub>2</sub> was to reduce the band gap energy ( $E_{bg}$ ) of the TiO<sub>2</sub>, with the aim of increasing the absorption in the visible region. Hence, the determination of the  $E_{bg}$  values of the Au/TiO<sub>2</sub>, Ag/TiO<sub>2</sub>, and Au-Ag@TiO<sub>2</sub> nanocomposites were very important. The  $E_{bg}$  values were calculated using the well-known Tauc's plot method (Lim et al., 2014b). The  $E_{bg}$  values of the nanocomposites with various Au or Ag contents were calculated, and the corresponding plots are shown in (**Figure 7.7(c and d)**). It is observed that the  $E_{bg}$  of the TiO<sub>2</sub> (3.27 eV) showed a gradual decrease with the addition of Au and Ag, with values of 3.23, 3.19, 3.17, 3.11, and 3.21 eV for the Au-Ag nanoparticles at Au<sub>0</sub>:Ag<sub>100</sub>, Au<sub>25</sub>:Ag<sub>75</sub>, Au<sub>50</sub>:Ag<sub>50</sub>, Au<sub>75</sub>:Ag<sub>25</sub>, and Au<sub>100</sub>:Ag<sub>0</sub>, respectively. Remarkable reductions in the  $E_{bg}$  value were observed when Au and Ag nanoparticles were added to TiO<sub>2</sub>. This was because the free electron properties were exhibited with a downward shift in the conduction band and upward shift in the valence band, which then led to a decrease in the  $E_{bg}$  value (Lim et al., 2014a; Pandikumar et al., 2012).

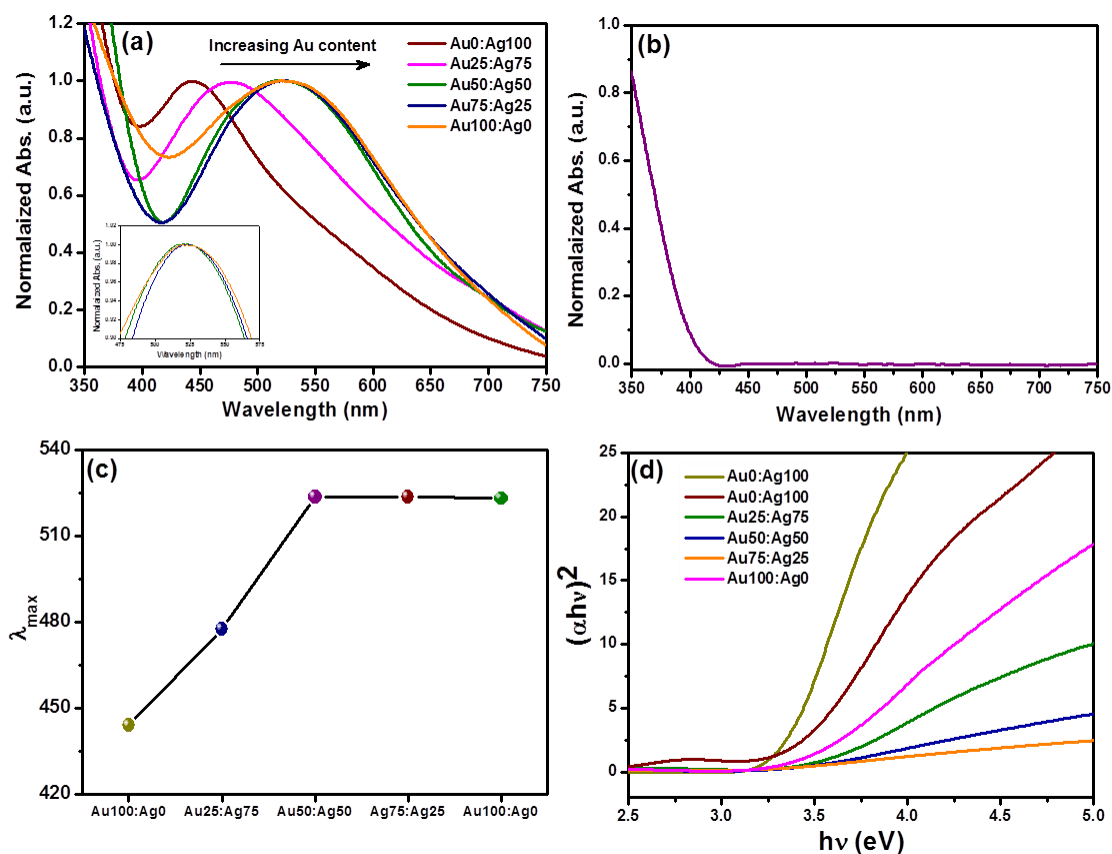


**Figure 7.7** (a) UV-Visible absorption spectra of the Au-Ag@TiO<sub>2</sub> nanocomposite with different composition of Au-Ag and (b) the corresponding plot of SPR band ( $\lambda_{\max}$ ) vs. Au-Ag composition present in the nanocomposite. (c) Plots of  $(\alpha h\nu)^2$  vs.  $h\nu$  obtained for Au-Ag@TiO<sub>2</sub> nanocomposite with different composition of Au-Ag.

Understanding the charge recombination process of a photoanode material is crucial because it can significantly influence the photovoltaic performance of a DSSC. The TiO<sub>2</sub> will absorb incident photons with sufficient energy equal to or higher than the band-gap energy. This will produce photo-induced charge carriers ( $h^+ \dots e^-$ ), and the recombination of photo-induced electrons and holes will release energy in the form of photoluminescence. Hence, a lower PL intensity indicates less charge recombination. The TiO<sub>2</sub> showed a broad and high PL intensity at around 580 nm due to the high photo-induced charge carrier recombination; whereas the PL intensity was minimized upon the addition of Au and Ag on the TiO<sub>2</sub> surface (**Figure 7.8**). This was mainly attributed to the formation of the Schottky barrier at the Ag/TiO<sub>2</sub> interface, which acted as an electron sink to efficiently prevent the electron-hole recombination process (Du et

al., 2006). The Au-Ag@TiO<sub>2</sub> with an Au-Ag composition of 75:25 showed the lowest PL emission intensity, which indicated the least electron–hole recombination compared to the other Au-Ag ratios.

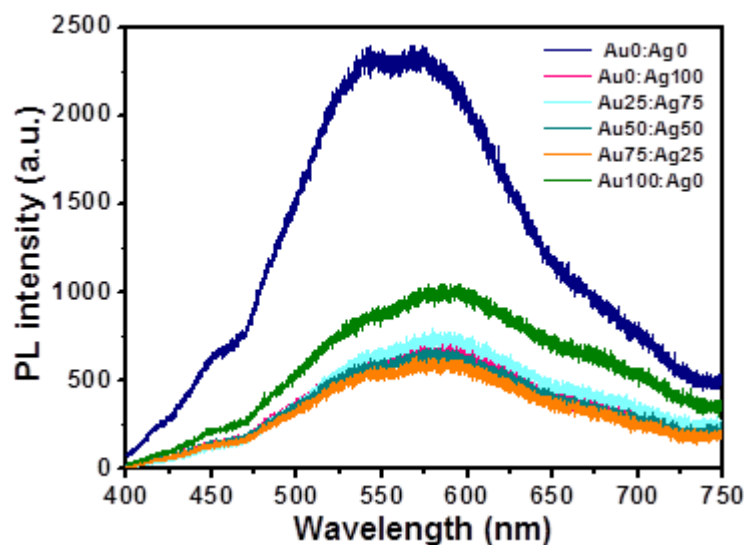


**Figure 7.8** Photoluminescence spectra of Au-Ag@TiO<sub>2</sub> nanocomposite with different composition of Au-Ag.

#### 7.2.6 Photovoltaic Performance of Au-Ag@TiO<sub>2</sub> Nanocomposite Photoanode Based DSSCs

The photovoltaic performances of the Au-Ag@TiO<sub>2</sub> plasmonic nanocomposite-modified photoanode-based DSSCs with different Au-Ag compositions were evaluated under simulated solar AM 1.5G irradiation. Their obtained photocurrent densities and photovoltage (J–V) curves are shown in **Figure 7.9**, and their evaluated photovoltaic parameters are listed in **Table 7.1**. It can be observed from the J–V curve of Au-Ag@TiO<sub>2</sub> that there was a significant boost in the short-circuit current up to 30.54 mA/cm<sup>2</sup> compared to the TiO<sub>2</sub> (5.83 mA/cm<sup>2</sup>), Ag/TiO<sub>2</sub> (7.07 mA/cm<sup>2</sup>), and Au/TiO<sub>2</sub> (14.11 mA/cm<sup>2</sup>)-based DSSCs. The value of the DSSC with Au-Ag@TiO<sub>2</sub> ( $\eta = 9.54\%$ ) was 423%, 331%, and 116% higher than those of the DSSCs based on pure TiO<sub>2</sub> ( $\eta = 2.22\%$ ), Ag/TiO<sub>2</sub> ( $\eta = 2.81\%$ ), and Au/TiO<sub>2</sub> ( $\eta = 4.26\%$ ), respectively. The metal-modified photoanode displayed a higher efficiency than the unmodified TiO<sub>2</sub>, indicating

enhanced photovoltaic performance due to the presence of the plasmonic metal nanoparticles. The low efficiency of the  $\text{TiO}_2$ -based DSSC was due to its insufficient absorption of visible light. The significant improvement in the photovoltaic performance of the Au-Ag@ $\text{TiO}_2$  nanocomposite-modified photoanode-based DSSC is was due to the synergetic effect and surface plasmon resonance effect of the Au and Ag nanoparticles. The deposition of Au and Ag onto the  $\text{TiO}_2$  resulted in a change in the Fermi energy level. A large number of electrons accumulated over on the surface of the Ag nanoparticles due to the surface plasmon resonance effect. The accumulation of these electrons on the Au and Ag nanoparticles shifted the position of the Fermi level closer to the conduction band of  $\text{TiO}_2$  (Asim et al., 2012). The excited electrons in the Ag nanoparticles due to the SPR effect transferred to the conduction band of the  $\text{TiO}_2$  and were collected by the current collector (ITO), thus improving the photocurrent under irradiation in the visible (Christopher et al., 2010). In addition, the significant improvement in absorption in the visible region would also enhance the photovoltaic performance. The improved photovoltaic performance is mainly attributed to the synergistic effect exhibited by the bimetallic nanoparticles with  $\text{TiO}_2$ , the effective interfacial charge transfer between the bimetallic nanoparticles and  $\text{TiO}_2$ , and hence the minimized photo-generated electron–hole recombination process.

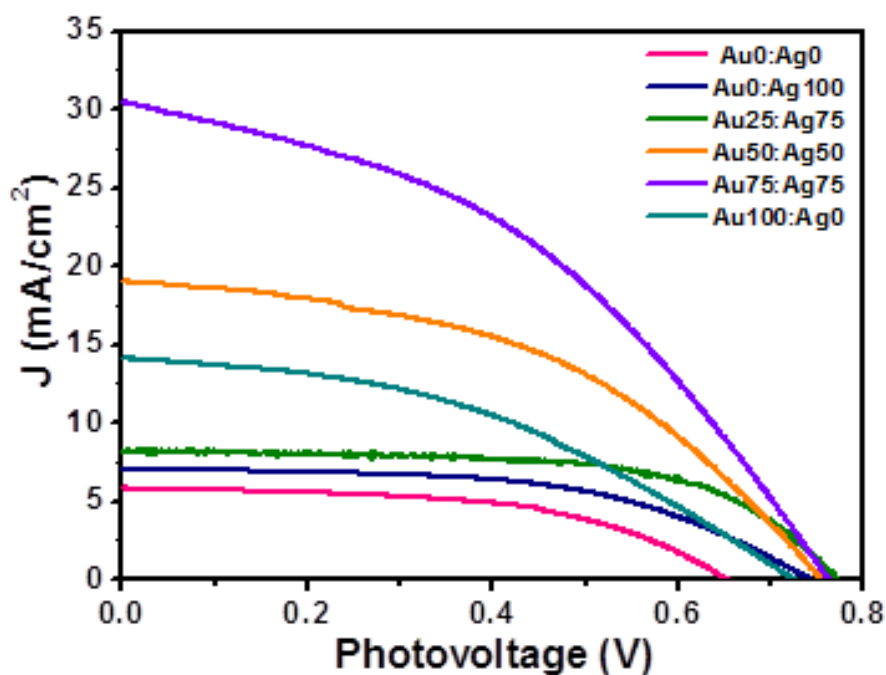


**Figure 7.9** Photocurrent density-photovoltage (J-V) curves obtained for the Au-Ag@TiO<sub>2</sub> nanocomposite modified photoanode contains different composition of Au-Ag based DSSCs sensitized with N719 dye under simulated AM 1.5 G solar irradiation of 100 mW/cm<sup>2</sup>.

The optimization of the Au-Ag composition on the TiO<sub>2</sub> surface is essential from the economic and high-performance perspectives for a DSSC. From the J–V curves, it was observed that the optimum ratio for Au-Ag is 75:25, as compared to 25:75 and 50:50. The enhanced photovoltaic performance may have been due to the synergistic effect and rapid interfacial charge transfer that arose from the Au and Ag nanoparticles on the TiO<sub>2</sub>. When the Au-Ag ratio on the TiO<sub>2</sub> surface was increased beyond 75:25, it showed a decrease in the conversion efficiency to 4.26 %%. The observed results clearly revealed that the conversion efficiency of a DSSC was increased with an increase in the Au content of the photoanode until it reached a maximum of 75. Then, a further increase in the Au content in the nanocomposite eventually led to a decrease in the conversion efficiency (**Figure 7.10 and Table 7.1**). This was mainly due decrease in the adsorption edge and increase in the band gap after reaching a value of Au<sub>75</sub> in the nanocomposite.

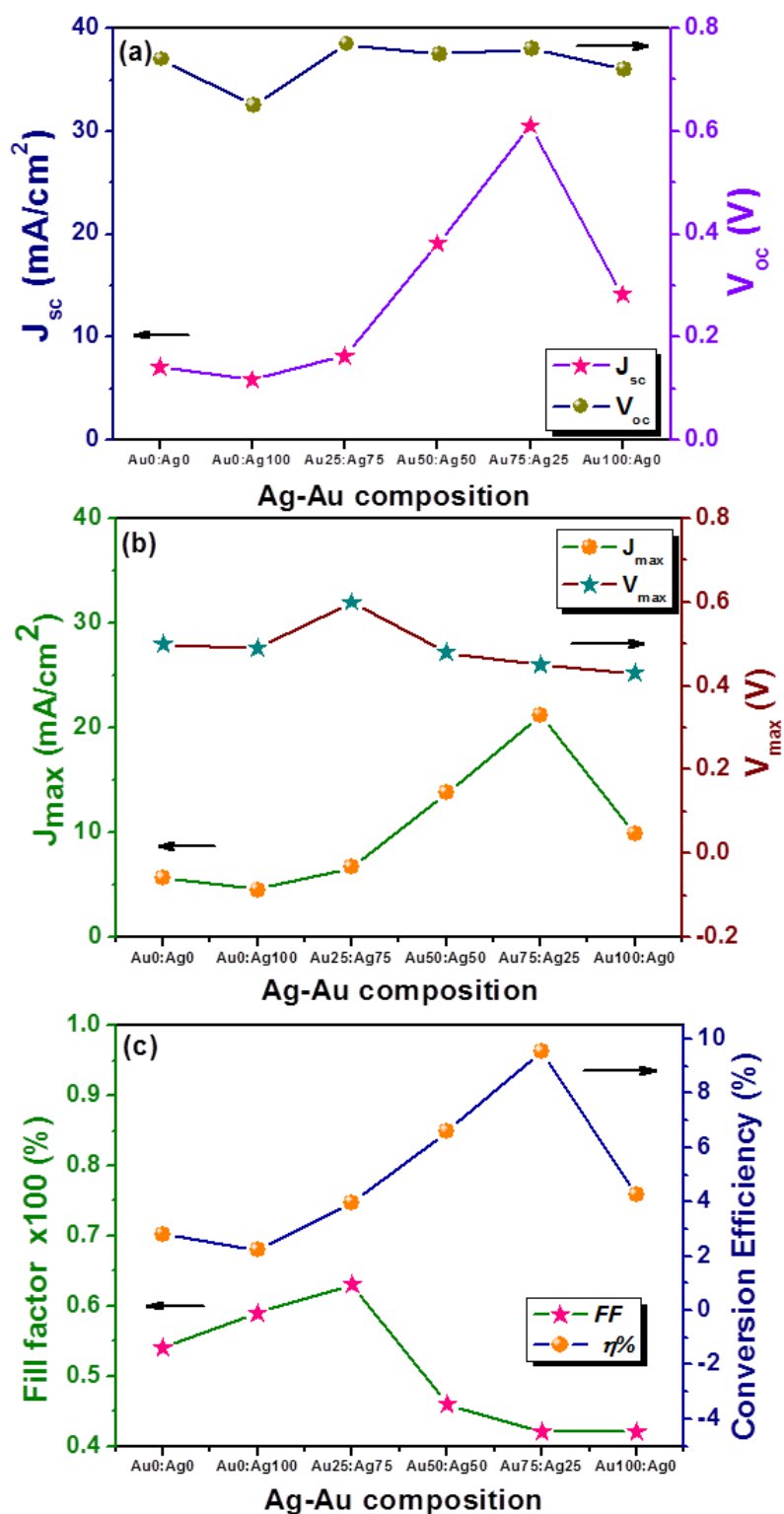


**Figure 7.10** Plots of (a) Fill factor (FF) and power conversion efficiency ( $\eta$ ), (b) short-circuit current density ( $J_{sc}$ ) and open-circuit voltage ( $V_{oc}$ ) and (c) maximum photocurrent density ( $J_{max}$ ) and maximum photovoltage ( $V_{max}$ ) obtained for the Au-Ag/TiO<sub>2</sub> nanocomposite modified photoanode with different composition of Au-Ag.

**Table 7.1** Photovoltaic parameters of the fabricated DSSCs with Au-Ag@TiO<sub>2</sub> nanocomposite modified photoanodes.

Photoanode	J <sub>sc</sub> (mA/cm <sup>2</sup> )	V <sub>oc</sub> (V)	J <sub>max</sub> (mA/cm <sup>2</sup> )	V <sub>max</sub> (V)	FF	η (%)
TiO <sub>2</sub>	5.83	0.65	4.53	0.49	0.59	2.22
Au <sub>0</sub> -Ag <sub>100</sub>	7.07	0.74	5.62	0.50	0.54	2.81
Au <sub>25</sub> -Ag <sub>75</sub>	8.17	0.77	6.63	0.6	0.63	3.98
Au <sub>50</sub> -Ag <sub>50</sub>	19.04	0.75	13.75	0.48	0.46	6.60
Au <sub>75</sub> -Ag <sub>25</sub>	30.54	0.76	21.2	0.45	0.42	9.54
Au <sub>100</sub> -Ag <sub>0</sub>	14.11	0.72	9.9	0.43	0.42	4.26

**Foot note:** The DSSCs performance was evaluated under 100 mW cm<sup>-2</sup> simulated AM 1.5G solar light irradiation. J<sub>sc</sub>: Short-circuit current density; V<sub>oc</sub>: Open-circuit voltage; J<sub>max</sub>: Maximum photocurrent density; V<sub>max</sub>: Maximum photovoltage; FF: Fill factor; η: Power conversion efficiency. Area of the cell electrode was 0.5 cm<sup>2</sup>

### 7.2.7 Electrochemical Properties of Au-Ag@TiO<sub>2</sub> Photoanode-Based DSSCs

The interfacial charge transfer process within the fabricated DSSC with the Au-Ag@TiO<sub>2</sub> photoanode studied by recording the the electrochemical impedance spectra (EIS) in the frequency range between 0.01 Hz and 100 KHz, and are shown in **Figure 7.11**. Well-defined semicircles in the middle frequency region for the Au-Ag@TiO<sub>2</sub> nanocomposite-modified photoanodes with the different Au-Ag ratios for DSSCs were observed from the Nyquist plots (**Figure 7.11(a)**). The intersection of the high-frequency semicircle at the real axis represents the equivalent series resistance of the device (R<sub>s</sub>); the semicircle in the middle frequency region between 1 and 1000 Hz represents the charge transfer resistance (R<sub>ct</sub>) throughout the semiconductor and at the semiconductor/dye/electrolyte interfaces (van de Lagemaat et al., 2000; Wang et al., 2012). The R<sub>s</sub> values are varied since different ratio of Au and Ag are used in the photoanode. The calculated R<sub>s</sub> values for Au<sub>0</sub>:Ag<sub>100</sub>, Au<sub>25</sub>:Ag<sub>75</sub>, Au<sub>50</sub>:Ag<sub>50</sub>, Au<sub>75</sub>:Ag<sub>25</sub>, and Au<sub>0</sub>:Ag<sub>100</sub> were 38.16, 37.44, 27.68, 21.98, and 23.17 Ω, respectively; and the R<sub>ct</sub>

values were 16.11, 12.7, 7.93, 5.61, and 3.18, respectively. An increase in the  $R_{ct}$  value of the Au-Ag@TiO<sub>2</sub>-based photoanode was observed with a decrease in the Ag content. Thus, the photoanode that contained a high amount of Ag had a higher  $R_{ct}$  value, which corresponded to an ineffective electron transfer process between the photoanode and electrolyte interface. The changes in  $R_s$  and  $R_{ct}$  can mainly be attributed to the changes in the Au-Ag content in the photoanode, which contributed the most to the internal impedance. The increases in  $R_s$  and  $R_{ct}$  with an increase in Au were due to the high conductivity and catalytic activity of the Au in the nanocomposite. As demonstrated in the Nyquist plot, both the real ( $Z'$ ) and imaginary ( $Z''$ ) parts of the total impedance, as well as the  $R_{ct}$  value, increased in the order Au/TiO<sub>2</sub> < TiO<sub>2</sub> < Au-Ag@TiO<sub>2</sub> < Ag/TiO<sub>2</sub>, which showed the crucial effect of the Au and Ag incorporation on the charge transport. The  $R_s$  value also decreased with the increasing amount of Ag. Therefore, the origin of the higher  $J_{sc}$  in the Au-Ag@TiO<sub>2</sub> is expected to have arisen from  $R_s$ ,  $R_{ct}$ , and the charge transport dynamics determined by the electron lifetime ( $\tau_n$ ). From the Bode phase plots (**Figure 7.11(b)**), the frequency was apparently shifted to the lower frequency region with an increase in the amount of Ag. The maximum frequencies ( $\omega_{max}$ ) in the middle frequency regions of the Bode plots for TiO<sub>2</sub> and Ag/TiO<sub>2</sub> were 3162.27 Hz and 1995.26 Hz, respectively. Since  $\omega_{max}$  is inversely associated with the electron lifetime  $\tau_n = 1/(2\pi f)$  (Lim et al., 2014b; Lim et al., 2014), a decrease in  $\omega_{max}$  indicates a reduced rate for the charge-recombination process in the DSSC. Hence, electrons with longer  $\tau_n$  values will survive the recombination, and are therefore characterized by the larger  $R_{ct}$ . However, the frequency was shifted to the higher frequency region with an increase in the amount of Au, which indicated that a higher charge-recombination occurred in the nanocomposite. The higher charge-recombination rate had a negative effect on the overall charge collection efficiency. However, this effect was offset by the significant enhancement in  $J_{sc}$  with the increasing amount of Au in the bimetallic nanocomposite.

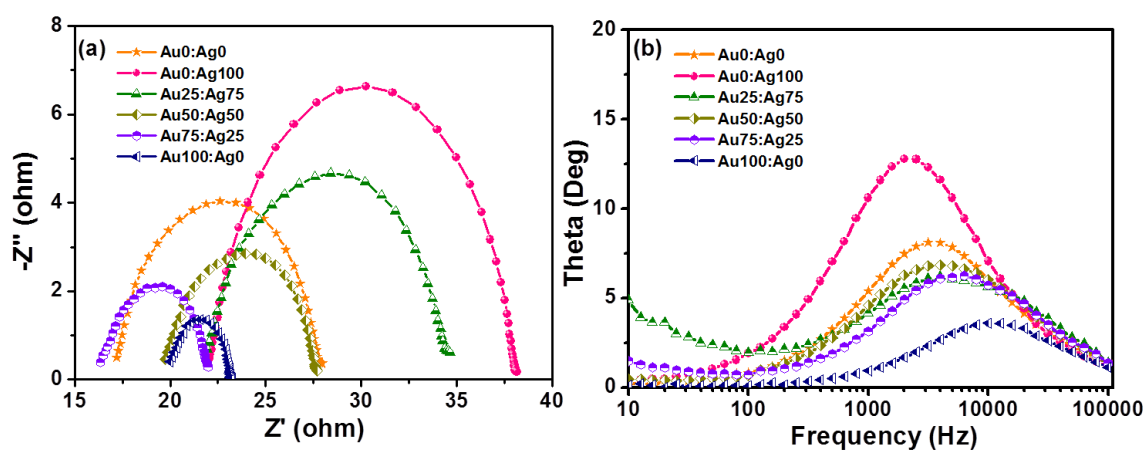


**Figure 7.11** Nyquist plot and (b) Bode phase plots obtained for Au-Ag/TiO<sub>2</sub> nanocomposite modified photoanodes with different composition of Au-Ag.

### 7.2.8 Operation Principle of Au-Ag@TiO<sub>2</sub> Modified Photoanode-Based DSSCs

The operation principle of the DSSC based on the Ag@TiO<sub>2</sub>-modified photoelectrode under illumination is shown in **Figure 7.12**. During light irradiation, the dye absorbs incident light and promotes electrons to the excited state. An excited electron is injected into the conduction band of the TiO<sub>2</sub> nanoparticles. The dye is then oxidized by receiving an electron from the electrolyte through the redox system, and is ready to be used again. The electrolyte itself will regenerate via the platinum counter-electrode by an electron passing through the external circuit. In our study, the metal deposited onto the TiO<sub>2</sub> surface could be used as a scattering element for plasmonic scattering to trap the light and was near-field coupled with the dye molecules (Lin et al., 2012). This will eventually improve the optical absorption of the dye, resulting in a significant enhancement of the photocurrent (**Figure 7.12**). Whenever the TiO<sub>2</sub> comes into contact with the metal, both will undergo a Fermi level equilibration to each other, resulting in the formation of a Schottky barrier and thus leading to large numbers of electrons being accumulated at the metal nanoparticles surface. This accumulation of electrons on the Ag nanoparticles will shift the position of the Fermi level closer to the conduction band of TiO<sub>2</sub> (Ni et al., 2007). The Schottky barrier formed between the metal nanoparticles and TiO<sub>2</sub> helps the electrons to flow from the metal to the TiO<sub>2</sub>

conduction band *via* a rapid interfacial charge transfer process, where they are collected by the current collector (ITO), thus which improves the photocurrent generation under irradiation (Christopher et al., 2010). Once the electrons are transferred to the conduction band of the  $\text{TiO}_2$ , the photo-excited electrons from the dye, N719, will start to accumulate on the metal surface again. Furthermore, the formation of the Schottky barrier at the metal/ $\text{TiO}_2$  interface, which can act as an electron sink, will also help to prevent the electron–hole recombination process (Du et al., 2006).

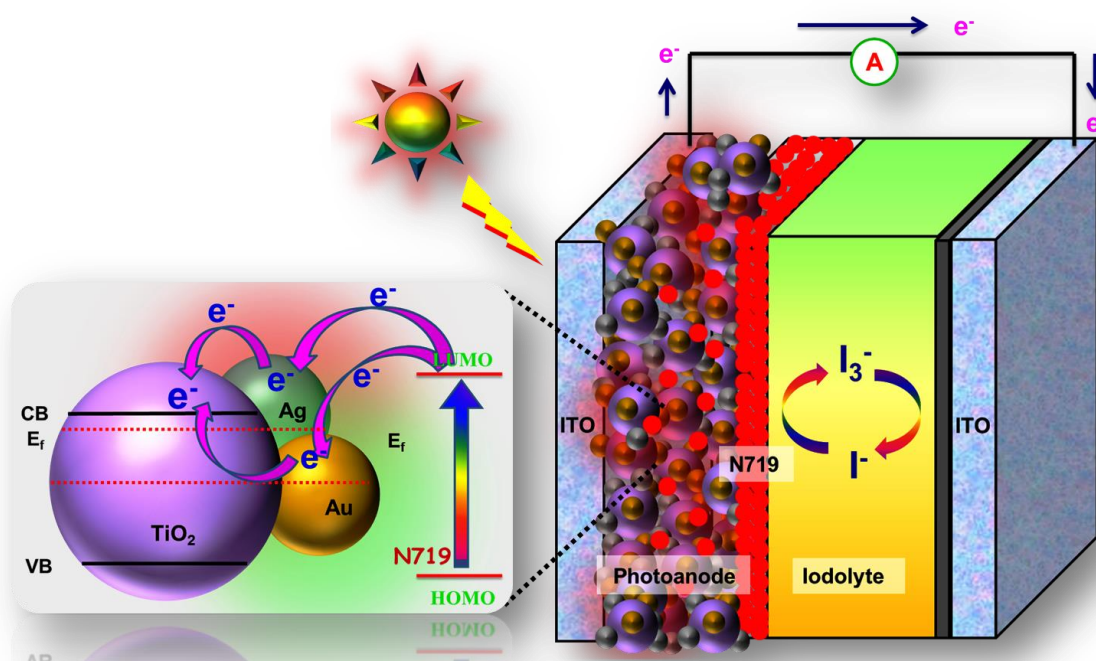


**Figure 7.12** Schematic functions of Au-Ag/ $\text{TiO}_2$  nanocomposite-modified photoanode-based dye-sensitized solar cells.

## 7.2.9 Conclusion

In conclusion, a simple approach was shown to co-deposit Au and Ag nanoparticles in the preparation of  $\text{TiO}_2$  plasmonic nanocomposites *via* a chemical reduction method to fabricate novel photoanodes for DSSCs. The Au-Ag@ $\text{TiO}_2$  nanocomposite was characterized by UV–visible absorption, PL, Raman, XRD, XPS, SEM, and TEM analyses. In the presence of Au and Ag nanoparticles, the Au-

Ag@TiO<sub>2</sub> could effectively absorb visible light as a result of the SPR effect. The DSSC fabricated with the Au-Ag@TiO<sub>2</sub>-modified photoanode showed an enhanced solar-to-electrical energy conversion efficiency of 9.54% and a 328% improvement compared to the photoanode of a DSSC composed of unmodified TiO<sub>2</sub> (2.22%) under simulated solar irradiation of 100 mWcm<sup>-2</sup> with AM 1.5G. The Ag/TiO<sub>2</sub> and Au/TiO<sub>2</sub>-modified photoanodes showed 26% and 92% efficiency enhancements compared to that of the TiO<sub>2</sub> unmodified photoanode. These significant improvements were mainly due to the synergistic effect shown by the co-deposition of plasmonic Au and Ag nanoparticles on the TiO<sub>2</sub> surface. The metal nanoparticles could enhance the visible light adsorption due to the light harvesting property in the visible region as a result of the surface plasmon effect. Moreover, these metal nanoparticles also significantly promoted an interfacial charge transfer, which minimized the charge recombination process. The improved solar energy conversion efficiency of the Au-Ag@TiO<sub>2</sub> nanocomposite makes it as a promising alternative to conventional photoanode-based DSSCs.

## CHAPTER 8

### Summary and Future Work

#### 8.1 Summary

The first chapter of this thesis describes the importance of renewable energy, development of solar cells, scope of thesis, research objective and thesis outline. Chapter two provides the historical development of photoelectrochemical cells and dye-sensitized solar cells. It also provides details about the components and operation principle of the dye-sensitized solar cells. Furthermore, a detailed literature survey was provided on the recent development in the plasmonic photoanode based dye-sensitized solar cells. Chapter 3 summarizes the materials and chemicals used for this investigation, synthetic methods used for the preparation of plasmonic nanocomposites and details about the analytical techniques and instruments used for the characterization of nanocomposites.

The principle goal of this research is to develop an efficient DSSC with  $\text{TiO}_2$  based photoanode. The primary approach to improve the DSSC's efficiency in this work is through the modification of the  $\text{TiO}_2$  with noble metal (Au and Ag) and non-metal (N and S) element. This work is divided into four parts and summarized in the following.

In Chapter 4, it was demonstrated that the addition of Ag can improve the conversion efficiency of the DSSC. The  $\text{TiO}_2$  modified with various Ag nanoparticles content ( $\text{Ag@TiO}_2$ ) were prepared through a chemical reduction method. This method did not require a stabilizer or surfactant and it was carried out at room temperature. The influence of the Ag content on the overall efficiency was also investigated, and the optimized Ag content with  $\text{TiO}_2$  was found to be 2.5 wt.%. The DSSC assembled with

the Ag@TiO<sub>2</sub>-plasmonic photoanode demonstrated an enhanced solar-to-electrical energy conversion efficiency (4.86%) than that of bare TiO<sub>2</sub> (2.57%) under an AM 1.5 G simulated solar irradiation of 100 mW cm<sup>-2</sup>, due the surface plasmon resonance effect of Ag nanoparticles present in the nanocomposites. There are many positive aspects of the Ag-modified TiO<sub>2</sub>, including the synergetic interaction of the Ag nanoparticles on the TiO<sub>2</sub> surface, surface plasmon resonance effect, reduction of the band gap, and enhancement of the charge transfer process. These multifunctional properties of the prepared Ag@TiO<sub>2</sub> plasmonic nanocomposite led to superior performance in the DSSC.

In chapter 5, the TiO<sub>2</sub> was first modified with nitrogen (N) before deposited with Ag to form a tertiary nanocomposite (N-TiO<sub>2</sub>-Ag) and used as photoanode. The N modified TiO<sub>2</sub> possesses good photovoltaic properties. Hence, the presence of N in the nanocomposite served an important role to reduce the band gap and helped to shift the optical absorbance towards the visible region. The synergetic effect of the Ag nanoparticles and N with TiO<sub>2</sub> successfully boost the conversion efficiency to nearly 3-fold than that of unmodified TiO<sub>2</sub> from 2.19% to 8.15%. Till date, N-TiO<sub>2</sub>-Ag is used for the first time as photoanode in DSSC and achieved high conversion efficiency.

In Chapter 6, the work was to investigate the effect of co-deposition of sulphur (S) and N on TiO<sub>2</sub> and Ag@TiO<sub>2</sub> for the photovoltaic properties enhancement. The existence of S played a vital role in the photovoltaic performance because it facilitated the electron transfer process and consequently increased the forward reduction reaction. Both Ag and S acted as co-catalyst and effectively minimize the electron recombination process. Apart from the ideal property of Ag nanoparticles, the presence of N and S also successfully reduced the band gap and helped to shift the optical absorbance towards visible region. Hence, the attractiveness of this photoanode (N,S-TiO<sub>2</sub>@Ag) was that it

combined the entire photovoltaic fundamental criteria of DSSC within its electronic environment. The DSSC fabricated with N,S-TiO<sub>2</sub>@Ag showed an enhanced  $\eta$  of 8.22 % when compared to the photoanode of DSSC composed with unmodified TiO<sub>2</sub>. The nearly 3-fold enhancement than that of unmodified TiO<sub>2</sub> was due to synergetic effects of Ag nanoparticles, surface plasmon effect, reduction of band gap and effective charge transfer, which ameliorated the photocurrent generation and conversion efficiency of DSSC.

Finally in Chapter 7, the studies sought to focus on the gold (Au) and Ag nanoparticles modified TiO<sub>2</sub>, which aimed to further enhance the overall conversion efficiency by utilizing the plasmon resonance effect of Ag and Au. The Au@Ag/TiO<sub>2</sub> plasmonic nanocomposite materials with different Au-Ag composition were prepared using a simple one-step chemical reduction method to be used as a photoanode. The incorporation of Ag on the TiO<sub>2</sub> surface influenced the optical properties in the region of 400–500 nm, while after the addition of Au, the optical properties was significantly improved in the region of 500–600 nm due to the surface plasmon resonance effect. Finally, the greatly improved conversion efficiency (9.54%) was attributed to optimum of Ag-Au composition and well dispersion of Ag-Au nanoparticles on the TiO<sub>2</sub> surface.

The systematic enhancement achieved in the present investigation on the overall energy conversion efficiency of DSSC with different plasmonic nanocomposite modified photoanodes are summarized in **Table 8.1**.

**Table 8.1** Summary of the DSSC performance and the optimization techniques carried in this research work.

Photoanode	Before modification ( $\eta$ %)	After modification ( $\eta$ %)	Optimization technique
<b>Ag@TiO<sub>2</sub></b>	2.57	4.86	Using Ag to enhance the visible light absorption and improve charge transfer process with varying amount of AgNO <sub>3</sub>
<b>N-TiO<sub>2</sub>@Ag</b>	2.19	8.15	Using Ag and N to improve the efficiency. Further optimization through Ag loading.
<b>N,S-TiO<sub>2</sub>@Ag</b>	2.57	8.22	Using Ag, S and N to improve the efficiency. Further optimization by controlling the Ag content.
<b>Au-Ag@TiO<sub>2</sub></b>	2.22	9.54	Co-deposition Au and Ag with TiO <sub>2</sub> and optimisation of Au-Ag composition.

## 8.2 Recommendations for Future Works

Based on the understanding acquired in these studies, the suggestions are worth investigating in the future for DSSC development:

1. In this research, the liquid electrolyte iodide/triiodide was used for the fabrication of the DSSC. However, the major drawbacks in the practical operation of the employment of the electrolyte in the liquid state DSSC are related to the leakage, volatilization of the solvents, possible desorption of the attached dyes and corrosion towards the counter electrode that restricts the long term performance and stability of the DSSC (Chan et al., 2013). Hence, replacements for iodine-based liquid electrolytes have been extensively studied. Many substitutions have thus emerged, such as ionic liquids, p-type semiconductor (CuI, CuBr, CuSCN, NiO), solid-state electrolyte and quasi solid-state electrolyte (Bach et al., 1998;

Burschka et al., 2011; Chung et al., 2012; Wu et al., 2007). Future efforts should focused on searching or synthesizing new electrolytes for replacing the liquid electrolyte iodide/triiodide to enhance the DSSC's stability.

2. The porous  $\text{TiO}_2$  layer, which is essential to serves the purpose of collecting and transporting photoelectrons, could leave a portion of transparent conductive substrate (TCO) surface uncovered. This will cause the percolation of redox electrolyte on the TCO surface that permits direct electrochemical reduction of  $\text{I}_3^-$  ( $\text{I}_3^- + 2\text{e}^- \rightarrow 3\text{I}^-$ ), leading to the consumption of the photogenerated electron (Xia et al., 2006). This combination will affect the overall device performance (Peng et al., 2004). Hence, the introduction of a blocking layer (compact layer between TCO and photoanode) is important to prevent electron leakage to increase the overall efficiency of the device (Haque et al., 2005). The use of a blocking layer has been shown to increase the solar cell's efficiency (Li et al., 2013). Future works can include introducing the blocking layer to improve DSSC performance.
3. Counter electrode plays a crucial role in increasing the conversion efficiency of the DSSC as it serves as a mediator for collecting electrons from the external circuit, reduces  $\text{I}_3^-$  into  $\text{I}^-$  and regenerates the oxidized dye after electron injection (Thomas et al., 2014). The efficient counter electrodes can reduce internal energy loss in DSSCs and thus produces higher current densities and fill factors (Thomas et al., 2014). So far, the most preferred material for counter electrode in DSSC is platinum (Pt), due to its excellent electrocatalytic activity towards  $\text{I}_3^-$  reduction (Thomas et al., 2014). However, the high-cost and the rarity of Pt significantly hinder its practical application in DSSCs, including mass production and commercialization (Thomas et al., 2014). This has promoted large research

interest in exploring alternative counter electrode materials for Pt-free DSSCs. In the past decades, carbon-based materials (Balamurugan et al., 2012; Dong et al., 2011; Han et al., 2010; Joshi et al., 2010; Kang et al., 2012; Sun et al., 2010; Veerappan et al., 2011), conducting polymers (Li et al., 2009; Sun et al., 2010) and transition metal based inorganic materials (Gong et al., 2012; Stoller et al., 2008; Wu et al., 2008) have been used as counter electrode materials and they showed reliable conversion efficiencies in DSSCs comparable to Pt-based counter electrode. Hence, future works could be done by using other potential materials to replace the Pt counter electrode with the aim to reduce the cost and improve the conversion efficiency of the DSSC.

4. For photoanode, nanoparticles with large specific surface areas are useful in DSSC application because they can uptake large amount of dye. On the other hand, one-dimensional (1D) TiO<sub>2</sub> nanomaterials (such as nanowires, nanofibers, and nanorods) can potentially improve electron transfer due to the small grain interfaces and light scattering properties, which can eventually enhance the efficiency of the DSSC (Kang et al., 2008; Park et al., 2013; Yang et al., 2013). Hence, controlled synthesis of TiO<sub>2</sub> with different structure can be prepared and used as efficient photoanode for the enhancement of DSSC efficiency.

## REFERENCES

- Agarwala, S., & Ho, G. (2012). Self-ordering anodized nanotubes: Enhancing the performance by surface plasmon for dye-sensitized solar cell. *J. Solid State Chem.*, 189, 101-107.
- Archana, P. S., Gupta, A., Yusoff, M. M., & Jose, R. (2014). Tungsten doped titanium dioxide nanowires for high efficiency dye-sensitized solar cells. *Phys. Chem. Chem. Phys.*, 16(16), 7448-7454.
- Asim, N., Sopian, K., Ahmadi, S., Saeedfar, K., Alghoul, M., Saadatian, O., & Zaidi, S. H. (2012). A review on the role of materials science in solar cells. *Renew Sust Energ Rev* 16(8), 5834-5847.
- Bach, U., Lupo, D., Comte, P., Moser, J. E., Weissortel, F., Salbeck, J., . . . Gratzel, M. (1998). Solid-state dye-sensitized mesoporous TiO<sub>2</sub> solar cells with high photon-to-electron conversion efficiencies. *Nature*, 395(6702), 583-585.
- Bai, X., Zhai, Y., & Zhang, Y. (2011). Green approach to prepare graphene-based composites with high microwave absorption capacity. *J. Phys. Chem. C*, 115(23), 11673-11677.
- Balamurugan, J., Pandurangan, A., Thangamuthu, R., & Senthilkumar, S. M. (2012). Effective synthesis of well-graphitized carbon nanotubes on bimetallic SBA-15 template for use as counter electrode in dye-sensitized solar cells. *Ind. Eng. Chem. Res.*, 52(1), 384-393.
- Balasingam, S. K., Kang, M. G., & Jun, Y. (2013). Metal substrate based electrodes for flexible dye-sensitized solar cells: fabrication methods, progress and challenges. *Chem. Commun.*, 49(98), 11457-11475.
- Batzill, M., Morales, E. H., & Diebold, U. (2006). Influence of Nitrogen doping on the defect formation and surface properties of TiO<sub>2</sub> rutile and anatase. *Phys. Rev. Lett.*, 96(2), 026103.
- Becquerel, A. (1839). On electric effects under the influence of solar radiation. *CR Acad. Sci*, 9, 711-714.
- Benanti, T. L., & Venkataraman, D. (2006). Organic solar cells: An overview focusing on active layer morphology. *Photosynth. Res.*, 87(1), 73-81.
- Berginc, M., Opara Krašovec, U., & Topič, M. (2014). Solution processed silver nanoparticles in dye-sensitized solar sells. *J.Nano Mat.*, 2014, 11.
- Binyu, Y., Kar Man, L., Qiuquan, G., Woon Ming, L., & Jun, Y. (2011). Synthesis of Ag-TiO<sub>2</sub> composite nano thin film for antimicrobial application. *Nanotechnology*, 22(11), 115603.
- Birkmire, R. W., & Eser, E. (1997). Polycrystalline thin film solar cells: Present status and future potential. *Annu. Rev. Mater. Sci.*, 27(1), 625-653.
- Birol, F. (2013). *World Energy Outlook: The role of nuclear & renewables*. Paper presented at the Nucl éaire et renouvelables dans la transition énerg éique.
- Briggs, D. (1981). Handbook of X-ray Photoelectron Spectroscopy *Surf. Interface Anal.*, 3(4), v.
- Burschka, J., Dualeh, A., Kessler, F., Baranoff, E., Cevey-Ha, N.-L., Yi, C., . . . Grätzel, M. (2011). Tris (2-(1 H-pyrazol-1-yl) pyridine) cobalt (III) as p-type dopant for organic semiconductors and its application in highly efficient solid-state dye-sensitized solar cells. *J. Am. Chem. Soc.*, 133(45), 18042-18045.
- Byun, H.Y., Vittal, R., Kim, D. Y., & Kim, K.J. (2004). Beneficial role of cetyltrimethylammonium bromide in the enhancement of photovoltaic properties of dye-sensitized rutile TiO<sub>2</sub> solar cells. *Langmuir*, 20(16), 6853-6857.
- Calogero, G., Di Marco, G., Cazzanti, S., Caramori, S., Argazzi, R., Di Carlo, A., & Bignozzi, C. A. (2010). Efficient dye-sensitized solar cells using red turnip and purple wild sicilian prickly pear fruits. *Int. J. Mol. Sci.*, 11(1), 254-267.

- Calogero, G., & Marco, G. D. (2008). Red Sicilian orange and purple eggplant fruits as natural sensitizers for dye-sensitized solar cells. *Sol. Energy Mater. Sol. Cells*, 92(11), 1341-1346.
- Cameron, P. J., Peter, L. M., & Hore, S. (2004). How Important is the Back Reaction of Electrons via the Substrate in Dye-Sensitized Nanocrystalline Solar Cells? *J. Phys. Chem. B*, 109(2), 930-936.
- Chan, Y.F., Wang, C.C., & Chen, C.Y. (2013). Quasi-solid DSSC based on a gel-state electrolyte of PAN with 2-D graphenes incorporated. *J. Mater. Chem.A*, 1(18), 5479-5486.
- Chandiran, A. K., Abdi-Jalebi, M., Nazeeruddin, M. K., & Grätzel, M. (2014). Analysis of electron transfer properties of ZnO and TiO<sub>2</sub> photoanodes for dye-sensitized solar cells. *ACS Nano*, 8(3), 2261-2268.
- Chandrasekharan, N., & Kamat, P. V. (2000). Improving the photoelectrochemical performance of nanostructured TiO<sub>2</sub> films by adsorption of gold nanoparticles. *J. Phys. Chem. B*, 104(46), 10851-10857.
- Chapin, D. M., Fuller, C. S., & Pearson, G. L. (1954). A new silicon p-n junction photocell for converting solar radiation into electrical power. *J. Appl. Phys.*, 25(5), 676-677.
- Chen, H.Y., Kuang, D.B., & Su, C.-Y. (2012). Hierarchically micro/nanostructured photoanode materials for dye-sensitized solar cells. *J. Mater. Chem.*, 22(31), 15475-15489.
- Chen, J., Li, B., Zheng, J., Zhao, J., Jing, H., & Zhu, Z. (2011). Polyaniline nanofiber/carbon film as flexible counter electrodes in platinum-free dye-sensitized solar cells. *Electrochim. Acta*, 56(12), 4624-4630.
- Chen, K.F., Liu, C.-H., Huang, H.K., Tsai, C.H., & Chen, F.R. (2013). Polyvinyl butyral-based thin film polymeric electrolyte for dye-sensitized solar cell with long-term stability. *Int. J. Electrochem. Sci*, 8, 3524-3539.
- Chen, L.C., Chen, C.C., & Tseng, B.-S. (2010). Improvement of short-circuit current density in dye-sensitized solar cells using sputtered nanocolumnar TiO<sub>2</sub> compact layer. *J.Nano Mat.*, 2010, 61.
- Chen, S., Li, J., Qian, K., Xu, W., Lu, Y., Huang, W., & Yu, S. (2010). Large scale photochemical synthesis of M@TiO<sub>2</sub> nanocomposites (M = Ag, Pd, Au, Pt) and their optical properties, CO oxidation performance, and antibacterial effect. *Nano Res.*, 3(4), 244-255.
- Chen, W., Cai, W., Wang, G., & Zhang, L. (2001). Effects of interface interaction on the Mie resonance absorption of gold nanoparticles dispersed within pores of mesoporous silica. *Appl. Surf. Sci.*, 174(1), 51-54.
- Chen, X., Lou, Y. B., Samia, A. C. S., Burda, C., & Gole, J. L. (2005). Formation of oxynitride as the photocatalytic enhancing site in nitrogen-doped titania nanocatalysts: comparison to a commercial nanopowder. *Adv. Funct. Mater.*, 15(1), 41-49.
- Chiarello, G. L., Aguirre, M. H., & Selli, E. (2010). Hydrogen production by photocatalytic steam reforming of methanol on noble metal-modified TiO<sub>2</sub>. *J. Catal.*, 273(2), 182-190.
- Chou, C.S., Yang, R.Y., Yeh, C.K., & Lin, Y.J. (2009). Preparation of TiO<sub>2</sub>/Nano-metal composite particles and their applications in dye-sensitized solar cells. *Powder Technol.*, 194(1-2), 95-105.
- Chou, C., Wu, K., Chi, Y., Hu, W., Yu, S. J., Lee, G., . . . Chou, P. (2011). Ruthenium (II) sensitizers with heteroleptic tridentate chelates for dye-sensitized solar cells. *Angew. Chem. Int. Edn*, 50(9), 2054-2058.
- Christopher, P., Ingram, D. B., & Linic, S. (2010). Enhancing Photochemical Activity of Semiconductor Nanoparticles with Optically Active Ag Nanostructures:

- Photochemistry Mediated by Ag Surface Plasmons. *J. Phys. Chem. C*, 114(19), 9173-9177.
- Chung, I., Lee, B., He, J., Chang, R. P., & Kanatzidis, M. G. (2012). All-solid-state dye-sensitized solar cells with high efficiency. *Nature*, 485(7399), 486-489.
- Cusano, D. (1963). CdTe solar cells and photovoltaic heterojunctions in II-VI compounds. *Solid-State Electron.*, 6(3), 217-218.
- Daeneke, T., Kwon, T.-H., Holmes, A. B., Duffy, N. W., Bach, U., & Spiccia, L. (2011). High-efficiency dye-sensitized solar cells with ferrocene-based electrolytes. *Nat Chem*, 3(3), 211-215.
- Daeneke, T., Uemura, Y., Duffy, N. W., Mozer, A. J., Koumura, N., Bach, U., & Spiccia, L. (2012). Aqueous dye-sensitized solar cell electrolytes based on the ferricyanide-ferrocyanide redox couple. *Adv. Mater.*, 24(9), 1222-1225.
- Desai, U. V., Xu, C., Wu, J., & Gao, D. (2013). Hybrid TiO<sub>2</sub>-SnO<sub>2</sub> nanotube arrays for dye-sensitized solar cells. *J. Phys. Chem. C*, 117(7), 3232-3239.
- Desilvestro, J., Graetzel, M., Kavan, L., Moser, J., & Augustynski, J. (1985). Highly efficient sensitization of titanium dioxide. *J. Am. Chem. Soc.*, 107(10), 2988-2990.
- Dong, P., Pint, C. L., Hainey, M., Mirri, F., Zhan, Y., Zhang, J., . . . Lou, J. (2011). Vertically aligned single-walled carbon nanotubes as low-cost and high electrocatalytic counter electrode for dye-sensitized solar cells. *ACS Appl. Mater. Interfaces*, 3(8), 3157-3161.
- Du, J., Qi, J., Wang, D., & Tang, Z. (2012). Facile synthesis of Au@TiO<sub>2</sub> core-shell hollow spheres for dye-sensitized solar cells with remarkably improved efficiency. *Energy Environ. Sci*, 5(5), 6914-6918.
- Du, J., Zhang, J., Liu, Z., Han, B., Jiang, T., & Huang, Y. (2006). Controlled synthesis of Ag/TiO<sub>2</sub> core-shell nanowires with smooth and bristled surfaces via a one-step solution route. *Langmuir* 22, 1307-1312.
- Duonghond, D., Serpone, N., & Grätzel, M. (1984). Integrated systems for water cleavage by visible light; Sensitization of TiO<sub>2</sub> particles by surface derivatization with ruthenium complexes. *Helv. Chim. Acta*, 67(4), 1012-1018.
- Dye-sensitized Solar Cells by G24 Power. Retrieved 1/9, 2013, from <http://gcell.com/>
- Eagen, C. F. (1981). Nature of the enhanced optical absorption of dye-coated Ag island films. *Appl. Opt.*, 20(17), 3035-3042.
- Enomoto, M., Taniguchi, K., & Ihara, M. (2010). Dye-sensitized solar cells using localized surface plasmon of gold and silver nanoparticles with comb-shaped block copolymer. *ECS Trans.*, 25(42), 37-48.
- Enzhou, L., Limin, K., Yuhao, Y., Tao, S., Xiaoyun, H., Changjun, Z., . . . Jun, F. (2014). Plasmonic Ag deposited TiO<sub>2</sub> nano-sheet film for enhanced photocatalytic hydrogen production by water splitting. *Nanotech.*, 25(16), 165401.
- Fujishima, A. (1972). Electrochemical photolysis of water at a semiconductor electrode. *Nature*, 238, 37-38.
- Gai, Y., Li, J., Li, S.S., Xia, J.B., & Wei, S.H. (2009). Design of narrow-gap TiO<sub>2</sub>: a passivated codoping approach for enhanced photoelectrochemical activity. *Phys. Rev. Lett.*, 102(3), 036402.
- Gao, Y., Fang, P., Chen, F., Liu, Y., Liu, Z., Wang, D., & Dai, Y. (2013). Enhancement of stability of N-doped TiO<sub>2</sub> photocatalysts with Ag loading. *Appl Surf Sci*, 265(0), 796-801.
- Gerischer, H. (1969). Charge transfer processes at semiconductor-electrolyte interfaces in connection with problems of catalysis. *Surf. Sci.*, 18(1), 97-122.

- Ghaffari, M., Cosar, M. B., Yavuz, H. I., Ozenbas, M., & Okyay, A. K. (2012). Effect of Au nano-particles on TiO<sub>2</sub> nanorod electrode in dye-sensitized solar cells. *Electrochim. Acta*, 76(0), 446-452.
- Gong, F., Wang, H., Xu, X., Zhou, G., & Wang, Z.-S. (2012). In situ growth of Co<sub>0.85</sub>Se and Ni<sub>0.85</sub>Se on conductive substrates as high-performance counter electrodes for dye-sensitized solar cells. *J. Am. Chem. Soc.*, 134(26), 10953-10958.
- Graciani, J., Álvarez, L. J., Rodriguez, J. A., & Sanz, J. F. (2008). N doping of rutile TiO<sub>2</sub> (110) surface. A theoretical DFT study. *J. Phys. Chem. C*, 112(7), 2624-2631.
- Grätzel, M. (2009). Recent advances in sensitized mesoscopic solar cells. *Acc. Chem. Res.*, 42(11), 1788-1798.
- Grätzel, M., & Moser, J.-E. (2001). Solar energy conversion (Vol. 5, pp. 589-644): Wiley-VCH: Weinheim.
- Guo, K., Li, M., Fang, X., Liu, X., Sebo, B., Zhu, Y., . . . Zhao, X. (2013). Preparation and enhanced properties of dye-sensitized solar cells by surface plasmon resonance of Ag nanoparticles in nanocomposite photoanode. *J. Power Sources*, 230(0), 155-160.
- Guo, K., Li, M., Fang, X., Liu, X., Zhu, Y., Hu, Z., & Zhao, X. (2013). Enhancement of properties of dye-sensitized solar cells by surface plasmon resonance of Ag nanowire core-shell structure in TiO<sub>2</sub> films. *J. Mater. Chem.A*, 1(24), 7229-7234.
- Guo, L., Yang, S., Yang, C., Yu, P., Wang, J., Ge, W., & Wong, G. K. L. (2000). Highly monodisperse polymer-capped ZnO nanoparticles: Preparation and optical properties. *Appl. Phys. Lett.*, 76(20), 2901-2903.
- Hagfeldt, A., & Graetzel, M. (1995). Light-induced redox reactions in nanocrystalline systems. *Chem. Rev.*, 95(1), 49-68.
- Hagfeldt, A., & Grätzel, M. (2000). Molecular photovoltaics. *Acc. Chem. Res.*, 33(5), 269-277.
- Hagfeldt, A., Lindström, H., Södergren, S., & Lindquist, S.E. (1995). Photoelectrochemical studies of colloidal TiO<sub>2</sub> films: The effect of oxygen studied by photocurrent transients. *J. Electroanal. Chem.*, 381(1-2), 39-46.
- Hamnett, A., Dare-Edwards, M., Wright, R., Seddon, K., & Goodenough, J. (1979). Photosensitization of titanium (IV) oxide with tris (2, 2'-bipyridine) ruthenium (II) chloride. Surface states of titanium (IV) oxide. *J. Phys. Chem.*, 83(25), 3280-3290.
- Han, J., Kim, H., Kim, D. Y., Jo, S. M., & Jang, S. Y. (2010). Water-soluble polyelectrolyte-grafted multiwalled carbon nanotube thin films for efficient counter electrode of dye-sensitized solar cells. *ACS Nano*, 4(6), 3503-3509.
- Haque, S. A., Palomares, E., Cho, B. M., Green, A. N., Hirata, N., Klug, D. R., & Durrant, J. R. (2005). Charge separation versus recombination in dye-sensitized nanocrystalline solar cells: the minimization of kinetic redundancy. *J. Am. Chem. Soc.*, 127(10), 3456-3462.
- Haque, S. A., Palomares, E., Cho, B. M., Green, A. N. M., Hirata, N., Klug, D. R., & Durrant, J. R. (2005). Charge separation versus recombination in dye-sensitized nanocrystalline solar cells: the minimization of kinetic redundancy. *JACS*, 127(10), 3456-3462.
- Ho Lee, J. (2007). A highly efficient organic sensitizer for dye-sensitized solar cells. *Chem. Commun.*(46), 4887-4889.
- Hong, W., Xu, Y., Lu, G., Li, C., & Shi, G. (2008). Transparent graphene/PEDOT-PSS composite films as counter electrodes of dye-sensitized solar cells. *Electrochem. Commun.*, 10(10), 1555-1558.

- Hoshikawa, T., Ikebe, T., Yamada, M., Kikuchi, R., & Eguchi, K. (2006). Preparation of silica-modified TiO<sub>2</sub> and application to dye-sensitized solar cells. *J. Photochem. Photobiol., A*, 184(1), 78-85.
- Hoshikawa, T., Yamada, M., Kikuchi, R., & Eguchi, K. (2005). Impedance analysis for dye-sensitized solar cells with a three-electrode system. *J. Electroanal. Chem.*, 577(2), 339-348.
- Hövel, H., Fritz, S., Hilger, A., Kreibig, U., & Vollmer, M. (1993). Width of cluster plasmon resonances: Bulk dielectric functions and chemical interface damping. *Phys. Rev. B*, 48(24), 18178-18188.
- Huang, L. H., Sun, C., & Liu, Y. L. (2007). Pt/N-codoped TiO<sub>2</sub> nanotubes and its photocatalytic activity under visible light. *Appl. Surf. Sci.*, 253(17), 7029-7035.
- Ito, S., Miura, H., Uchida, S., Takata, M., Sumioka, K., Liska, P., . . . Grätzel, M. (2008). High-conversion-efficiency organic dye-sensitized solar cells with a novel indoline dye. *Chem. Commun.*(41), 5194-5196.
- Ito, S., Murakami, T. N., Comte, P., Liska, P., Grätzel, C., Nazeeruddin, M. K., & Grätzel, M. (2008). Fabrication of thin film dye sensitized solar cells with solar to electric power conversion efficiency over 10%. *Thin Solid Films*, 516(14), 4613-4619.
- Jang, Y. H., Jang, Y. J., Kochuveedu, S. T., Byun, M., Lin, Z., & Kim, D. H. (2014). Plasmonic dye-sensitized solar cells incorporated with Au-TiO<sub>2</sub> nanostructures with tailored configurations. *Nanoscale*, 6(3), 1823-1832.
- Jayaweera, P., Perera, A., & Tennakone, K. (2008). Why Gratzel's cell works so well. *Inorg. Chim. Acta*, 361(3), 707-711.
- Jeong, H., Pak, Y., Hwang, Y., Song, H., Lee, K. H., Ko, H. C., & Jung, G. Y. (2012). Enhancing the charge transfer of the counter electrode in dye-sensitized solar cells using periodically aligned platinum nanocups. *Small*, 8(24), 3757-3761.
- Jiang, W., Liu, H., Yin, L., & Ding, Y. (2013). Fabrication of well-arrayed plasmonic mesoporous TiO<sub>2</sub>/Ag films for dye-sensitized solar cells by multiple-step nanoimprint lithography. *J. Mater. Chem. A*, 1(21), 6433-6440.
- Jin, E., Zhao, X., Park, J.-Y., & Gu, H.-B. (2012). Enhancement of the photoelectric performance of dye-sensitized solar cells using Ag-doped TiO<sub>2</sub> nanofibers in a TiO<sub>2</sub> film as electrode. *Nanoscale Res. Lett.*, 7(1), 1-5.
- Joshi, P., Zhang, L., Chen, Q., Galipeau, D., Fong, H., & Qiao, Q. (2010). Electrospun carbon nanofibers as low-cost counter electrode for dye-sensitized solar cells. *ACS Appl. Mater. Interfaces*, 2(12), 3572-3577.
- Kalyanasundaram, K. (2010). *Dye-sensitized solar cells*: EPFL press.
- Kang, D.-Y., Lee, Y., Cho, C.-Y., & Moon, J. H. (2012). Inverse opal carbons for counter electrode of dye-sensitized solar cells. *Langmuir*, 28(17), 7033-7038.
- Kang, S. H., Choi, S., Kang, M., Kim, J., Kim, H., Hyeon, T., & Sung, Y. (2008). Nanorod-based dye-sensitized solar cells with Improved charge collection efficiency. *Adv. Mater.*, 20(1), 54-58.
- Kang, S. H., Kim, H. S., Kim, J.-Y., & Sung, Y.-E. (2010). Enhanced photocurrent of nitrogen-doped TiO<sub>2</sub> film for dye-sensitized solar cells. *Mater. Chem. Phys.*, 124(1), 422-426.
- Kay, A., & Grätzel, M. (1996). Low cost photovoltaic modules based on dye sensitized nanocrystalline titanium dioxide and carbon powder. *Sol. Energy Mater. Sol. Cells*, 44(1), 99-117.
- Kazmerski, L., White, F., & Morgan, G. (1976). Thin-film CuInSe<sub>2</sub>/CdS heterojunction solar cells. *Appl. Phys. Lett.*, 29(4), 268-270.
- Kelly, C. A., & Meyer, G. J. (2001). Excited state processes at sensitized nanocrystalline thin film semiconductor interfaces. *Coord. Chem. Rev.*, 211(1), 295-315.

- Kern, R., Sastrawan, R., Ferber, J., Stangl, R., & Luther, J. (2002). Modeling and interpretation of electrical impedance spectra of dye solar cells operated under open-circuit conditions. *Electrochim. Acta*, 47(26), 4213-4225.
- Kim, J.Y., Kang, S. H., Kim, H. S., & Sung, Y.E. (2009). Preparation of highly ordered mesoporous Al<sub>2</sub>O<sub>3</sub>/TiO<sub>2</sub> and its application in dye-sensitized solar cells. *Langmuir*, 26(4), 2864-2870.
- Kim, S. G., Ju, M. J., Choi, I. T., Choi, W. S., Choi, H.-J., Baek, J.-B., & Kim, H. K. (2013). Nb-doped TiO<sub>2</sub> nanoparticles for organic dye-sensitized solar cells. *RSC Adv.*, 3(37), 16380-16386.
- King, R. R., Law, D. C., Edmondson, K. M., Fetzer, C. M., Kinsey, G. S., Yoon, H., . . . Karam, N. H. (2007). 40% efficient metamorphic GaInP/GaInAs/Ge multijunction solar cells. *Appl. Phys. Lett.*, 90(18), 183516-183516-3.
- Kong, F.-T., Dai, S.-Y., & Wang, K.-J. (2007). Review of recent progress in dye-sensitized solar cells. *Adv. Optoelectron.*, 2007.
- Kopidakis, N., Neale, N. R., Zhu, K., van de Lagemaat, J., & Frank, A. J. (2005). Spatial location of transport-limiting traps in TiO<sub>2</sub> nanoparticle films in dye-sensitized solar cells. *Appl. Phys. Lett.*, 87(20), 202106.
- Kroon, J. M., Bakker, N. J., Smit, H. J. P., Liska, P., Thampi, K. R., Wang, P., . . . Tulloch, G. E. (2007). Nanocrystalline dye-sensitized solar cells having maximum performance. *Prog. Photovoltaics Res. Appl.*, 15(1), 1-18.
- Kumara, G., Kaneko, S., Okuya, M., Onwona-Agyeman, B., Konno, A., & Tennakone, K. (2006). Shiso leaf pigments for dye-sensitized solid-state solar cell. *Sol. Energy Mater. Sol. Cells*, 90(9), 1220-1226.
- Lai, W. H., Su, Y. H., Teoh, L. G., & Hon, M. H. (2008). Commercial and natural dyes as photosensitizers for a water-based dye-sensitized solar cell loaded with gold nanoparticles. *J. Photochem. Photobiol., A*, 195(2), 307-313.
- Lai, Y., H. Zhuang, Xie, K., Gong, D., Tang, Y., L. Sun, C. L., & Chen, Z. (2010). Fabrication of uniform Ag/TiO<sub>2</sub> nanotube array structures with enhanced photoelectrochemical performance. *New J. Chem.*(34), 1335-1340.
- Lan, Z., Wu, J., Lin, J., & Huang, M. (2012). Bi-functional TiO<sub>2</sub> cemented Ag grid under layer for enhancing the photovoltaic performance of a large-area dye-sensitized solar cell. *Electrochim. Acta*, 62(0), 313-318.
- Langhals, H. (2004). Color Chemistry. Synthesis, properties and applications of organic dyes and pigments. 3rd revised edition. By Heinrich Zollinger. *Angew. Chem. Int. Ed.*, 43(40), 5291-5292.
- Lantratov, V. M., Kalyuzhnyi, N. A., Mintairov, S. A., Timoshina, N. K., Shvarts, M. Z., & Andreev, V. M. (2007). High-efficiency dual-junction GaInP/GaAs tandem solar cells obtained by the method of MOCVD. *Semicond.*, 41(6), 727-731.
- Lee, K.C., Lin, S.-J., Lin, C.-H., Tsai, C.-S., & Lu, Y.J. (2008). Size effect of Ag nanoparticles on surface plasmon resonance. *Surf. Coat. Technol.*, 202(22-23), 5339-5342.
- Lee, K.M., Chiu, W.H., Lu, M.-D., & Hsieh, W.F. (2011). Improvement on the long-term stability of flexible plastic dye-sensitized solar cells. *J. Power Sources*, 196(20), 8897-8903.
- Lenzmann, F., & Kroon, J. (2007). Recent advances in dye-sensitized solar cells. *Adv. Optoelectron.*, 2007.
- Li, B., Lü G., Luo, L., & Tang, Y. (2010). TiO<sub>2</sub>@MgO core-shell film: Fabrication and application to dye-sensitized solar cells. *Wuhan University Journal of Natural Sciences*, 15(4), 325-329.

- Li, J., Chen, X., Ai, N., Hao, J., Chen, Q., Strauf, S., & Shi, Y. (2011). Silver nanoparticle doped TiO<sub>2</sub> nanofiber dye sensitized solar cells. *Chem. Phys. Lett.*, 514(1–3), 141-145.
- Li, X., Qiu, Y., Wang, S., Lu, S., Gruar, R. I., Zhang, X., . . . He, T. (2013). Electrophoretically deposited TiO<sub>2</sub> compact layers using aqueous suspension for dye-sensitized solar cells. *Phys. Chem. Chem. Phys.*, 15(35), 14729-14735.
- Li, Z., Ye, B., Hu, X., Ma, X., Zhang, X., & Deng, Y. (2009). Facile electropolymerized-PANI as counter electrode for low cost dye-sensitized solar cell. *Electrochem. Commun.*, 11(9), 1768-1771.
- Lim, S. P., Huang, N. M., Lim, H. N., & Mazhar, M. (2014a). Aerosol assisted chemical vapour deposited (AACVD) of TiO<sub>2</sub> thin film as compact layer for dye-sensitised solar cell. *Ceram. Int.*, 40(6), 8045-8052.
- Lim, S. P., Huang, N. M., Lim, H. N., & Mazhar, M. (2014b). Surface modification of aerosol-assisted CVD produced TiO<sub>2</sub> thin film for dye sensitised solar cell. *Int. J. Photoenergy* 2014, 12.
- Lim, S. P., Pandikumar, A., Huang, N. M., & Lim, H. N. (2014a). Enhanced photovoltaic performance of silver@titania plasmonic photoanode in dye-sensitized solar cells. *RSC Adv.*, 4(72), 38111-38118.
- Lim, S. P., Pandikumar, A., Huang, N. M., & Lim, H. N. (2014b). Silver/titania nanocomposite-modified photoelectrodes for photoelectrocatalytic methanol oxidation. *Int. J. Hydrogen Energy*, 39(27), 14720-14729.
- Lim, S. P., Pandikumar, A., Huang, N. M., Lim, H. N., Gu, G., & Ma, T. (2014). Promotional effect of silver nanoparticles on performance of N-doped TiO<sub>2</sub> photoanode-based dye-sensitized solar cells. *RSC Adv.*
- Lim, S. P., Pandikumar, A., Lim, Y. S., Huang, N. M., & Lim, H. N. (2014). In-situ electrochemically deposited polypyrrole nanoparticles incorporated reduced graphene oxide as an efficient counter electrode for platinum-free dye-sensitized solar cells. *Sci. Rep.*, 4, 5305.
- Lin, S., Lee, K., Wu, J., & Wu, J. (2012). Plasmon-enhanced photocurrent in dye-sensitized solar cells. *Solar Energy*, 86(9), 2600-2605.
- Linic, S., Christopher, P., & Ingram, D. B. (2011). Plasmonic-metal nanostructures for efficient conversion of solar to chemical energy. *Nat Mater*, 10(12), 911-921.
- Liu, W.L., Lin, F.C., Yang, Y.C., Huang, C.-H., Gwo, S., Huang, M. H., & Huang, J.-S. (2013). The influence of shell thickness of Au@TiO<sub>2</sub> core-shell nanoparticles on the plasmonic enhancement effect in dye-sensitized solar cells. *Nanoscale*, 5(17), 7953-7962.
- Liu, Y., Xu, H., Wang, H., Zhao, W., Liang, C., Zhong, M., & Shen, H. (2011). Flexible TiO<sub>2</sub> nanotube-based dye-sensitized solar cells using laser-drilled microhole array electrodes. *Appl. Phys. A*, 102(1), 127-130.
- Longo, C., Nogueira, A., De Paoli, M.-A., & Cachet, H. (2002). Solid-state and flexible dye-sensitized TiO<sub>2</sub> solar cells: A study by electrochemical impedance spectroscopy. *J. Phys. Chem. B*, 106(23), 5925-5930.
- Lu, J., Su, F., Huang, Z., Zhang, C., Liu, Y., Ma, X., & Gong, J. (2013). N-doped Ag/TiO<sub>2</sub> hollow spheres for highly efficient photocatalysis under visible-light irradiation. *RSC Adv.*, 3(3), 720-724.
- Luan, X., & Wang, Y. (2014). Plasmon-enhanced performance of dye-sensitized solar cells based on wlectrodeposited Ag nanoparticles. *J. Mater. Sci. Technol.*, 30(1), 1-7.
- Luque, A., Martí A., & Nozik, A. J. (2007). Solar cells based on quantum dots: multiple exciton generation and intermediate bands. *MRS Bull.*, 32(03), 236-241.

- Macak, J. M., Schmidt-Stein, F., & Schmuki, P. (2007). Efficient oxygen reduction on layers of ordered TiO<sub>2</sub> nanotubes loaded with Au nanoparticles. *Electrochem. Commun.*, 9(7), 1783-1787.
- Mathew, S., Yella, A., Gao, P., Humphry-Baker, R., Curchod Basile, F. E., Ashari-Astani, N., . . . Grätzel, M. (2014). Dye-sensitized solar cells with 13% efficiency achieved through the molecular engineering of porphyrin sensitizers. [Article]. *Nat Chem*, 6(3), 242-247.
- Matthews, D., Infelta, P., & Grätzel, M. (1996). Calculation of the photocurrent-potential characteristic for regenerative, sensitized semiconductor electrodes. *Sol. Energy Mater. Sol. Cells*, 44(2), 119-155.
- McEvoy, A. J., & Grätzel, M. (1994). Sensitisation in photochemistry and photovoltaics. *Sol. Energy Mater. Sol. Cells*, 32(3), 221-227.
- Meng, S., Ren, J., & Kaxiras, E. (2008). Natural dyes adsorbed on TiO<sub>2</sub> nanowire for photovoltaic applications: enhanced light absorption and ultrafast electron injection. *Nano Lett.*, 8(10), 3266-3272.
- Mock, J. J., Barbic, M., Smith, D. R., Schultz, D. A., & Schultz, S. (2002). Shape effects in plasmon resonance of individual colloidal silver nanoparticles. *J. Chem. Phys.*, 116(15), 6755-6759.
- Muduli, S., Game, O., Dhas, V., Vijayamohanan, K., Bogle, K. A., Valanoor, N., & Ogale, S. B. (2012). TiO<sub>2</sub>-Au plasmonic nanocomposite for enhanced dye-sensitized solar cell (DSSC) performance. *Sol. Energy*, 86(5), 1428-1434.
- Murakami, T. N., & Grätzel, M. (2008). Counter electrodes for DSC: Application of functional materials as catalysts. *Inorg. Chim. Acta*, 361(3), 572-580.
- Murakami, T. N., Ito, S., Wang, Q., Nazeeruddin, M. K., Bessho, T., Cesar, I., . . . Pálchy, P. (2006). Highly efficient dye-sensitized solar cells based on carbon black counter electrodes. *J. Electrochem. Soc.*, 153(12), A2255-A2261.
- Nahm, C., Choi, H., Kim, J., Jung, D.-R., Kim, C., Moon, J., . . . Park, B. (2011). The effects of 100 nm-diameter Au nanoparticles on dye-sensitized solar cells. *Appl. Phys. Lett.*, 99(25), 253107.
- Naik, B., Parida, K. M., & Gopinath, C. S. (2010). Facile synthesis of N- and S-incorporated nanocrystalline TiO<sub>2</sub> and direct solar-light-driven photocatalytic activity. *J. Phys. Chem. C*, 114(45), 19473-19482.
- Nambu, A., Graciani, J., Rodriguez, J. A., Wu, Q., Fujita, E., & Fdez Sanz, J. (2006). N doping of TiO<sub>2</sub>(110): Photoemission and density-functional studies. *J. Phys. Chem.*, 125(9), 094706.
- Nazeeruddin, M. K., Bessho, T., Cevey, L., Ito, S., Klein, C., De Angelis, F., . . . Imai, H. (2007). A high molar extinction coefficient charge transfer sensitizer and its application in dye-sensitized solar cell. *J. Photochem. Photobiol., A*, 185(2), 331-337.
- Nazeeruddin, M. K., Kay, A., Rodicio, I., Humphry-Baker, R., Müller, E., Liska, P., . . . Grätzel, M. (1993). Conversion of light to electricity by cis-X<sub>2</sub>bis (2, 2'-bipyridyl-4, 4'-dicarboxylate) ruthenium (II) charge-transfer sensitizers (X= Cl-, Br-, I-, CN-, and SCN-) on nanocrystalline titanium dioxide electrodes. *J. Am. Chem. Soc.*, 115(14), 6382-6390.
- Ng, S.P., Lu, X., Ding, N., Wu, C.M. L., & Lee, C.S. (2014). Plasmonic enhanced dye-sensitized solar cells with self-assembly gold-TiO<sub>2</sub>@core-shell nanoislands. *Sol. Energy*, 99(0), 115-125.
- Ni, M., Leung, M. K. H., Leung, D. Y. C., & Sumathy, K. (2007). A review and recent developments in photocatalytic water-splitting using for hydrogen production. *Renew. Sust. Energ. Rev.*, 11(3), 401-425.

- Nissfolk, J., Fredin, K., Hagfeldt, A., & Boschloo, G. (2006). Recombination and transport processes in dye-sensitized solar cells investigated under working conditions. *J. Phys. Chem. B*, 110(36), 17715-17718.
- O'Regan, B., & Gratzel, M. (1991). A low-cost, high-efficiency solar cell based on dye-sensitized colloidal TiO<sub>2</sub> films. *Nature*, 353(6346), 737-740.
- Ohsaka, T., Izumi, F., & Fujiki, Y. (1978). Raman spectrum of anatase, TiO<sub>2</sub>. *J. Raman Spectrosc.*, 7(6), 321-324.
- Pandikumar, A., Manonmani, S., & Ramaraj, R. (2012). TiO<sub>2</sub>-Au nanocomposite materials embedded in polymer matrices and their application in the photocatalytic reduction of nitrite to ammonia. *Catal. Sci. Technol.*, 2(2), 345-353.
- Pandikumar, A., Sivaranjani, K., Gopinath, C. S., & Ramaraj, R. (2013). Aminosilicate sol-gel stabilized N-doped TiO<sub>2</sub>-Au nanocomposite materials and their potential environmental remediation applications. *RSC Adv.*, 3, 13390-13398.
- Pang, A., Sun, X., Ruan, H., Li, Y., Dai, S., & Wei, M. (2014). Highly efficient dye-sensitized solar cells composed of TiO<sub>2</sub>@SnO<sub>2</sub> core-shell microspheres. *Nano Energy*, 5(0), 82-90.
- Pany, S., Naik, B., Martha, S., & Parida, K. (2013). Plasmon induced nano Au particle decorated over S,N-modified TiO<sub>2</sub> for exceptional photocatalytic hydrogen evolution under visible light. *ACS Appl. Mater. Interfaces* 6(2), 839-846.
- Pany, S., Parida, K. M., & Naik, B. (2013). Facile fabrication of mesoporosity driven N-TiO<sub>2</sub>@CS nanocomposites with enhanced visible light photocatalytic activity. *RSC Adv.*, 3(15), 4976-4984.
- Papageorgiou, N. (2004). Counter-electrode function in nanocrystalline photoelectrochemical cell configurations. *Coord. Chem. Rev.*, 248(13), 1421-1446.
- Park, J.O., Lee, J.H., Kim, J.J., Cho, S.H., & Cho, Y. K. (2005). Crystallization of indium tin oxide thin films prepared by RF-magnetron sputtering without external heating. *Thin Solid Films*, 474(1), 127-132.
- Park, J. T., Chi, W. S., Jeon, H., & Kim, J. H. (2014). Improved electron transfer and plasmonic effect in dye-sensitized solar cells with bi-functional Nb-doped TiO<sub>2</sub>/Ag ternary nanostructures. *Nanoscale*, 6(5), 2718-2729.
- Park, N.G., Schlichthörl, G., Van de Lagemaat, J., Cheong, H., Mascarenhas, A., & Frank, A. (1999). Dye-sensitized TiO<sub>2</sub> solar cells: structural and photoelectrochemical characterization of nanocrystalline electrodes formed from the hydrolysis of TiCl<sub>4</sub>. *J. Phys. Chem. B*, 103(17), 3308-3314.
- Park, Y. D., Anabuki, K., Kim, S., Park, K.W., Lee, D. H., Um, S. H., . . . Cho, J. H. (2013). Fabrication of stable electrospun TiO<sub>2</sub> nanorods for high-performance dye-sensitized solar cells. *Macromol. Res.*, 21(6), 636-640.
- Peng, B., Jungmann, G., Jäger, C., Haarer, D., Schmidt, H.W., & Thelakkat, M. (2004). Systematic investigation of the role of compact TiO<sub>2</sub> layer in solid state dye-sensitized TiO<sub>2</sub> solar cells. *Coord. Chem. Rev.*, 248(13-14), 1479-1489.
- Peng, S., Wu, Y., Zhu, P., Thavasi, V., Mhaisalkar, S. G., & Ramakrishna, S. (2011). Facile fabrication of polypyrrole/functionalized multiwalled carbon nanotubes composite as counter electrodes in low-cost dye-sensitized solar cells. *J. Photochem. Photobiol., A*, 223(2), 97-102.
- Photiphat, C., Rakkwamsuk, P., Muthitamongkol, P., Sae-Kung, C., & Thanachayanont, C. (2011). Effect of silver nanoparticle size on efficiency enhancement of dye-sensitized solar cells. *Int. J. Photoenergy*, 2011.
- Plonska-Brzezinska, M. E., Lapinski, A., Wilczewska, A. Z., Dubis, A. T., Villalta-Cerdas, A., Winkler, K., & Echegoyen, L. (2011). The synthesis and

- characterization of carbon nano-onions produced by solution ozonolysis. *Carbon*, 49(15), 5079-5089.
- Qi, J., Dang, X., Hammond, P. T., & Belcher, A. M. (2011). Highly efficient plasmon-enhanced dye-sensitized solar cells through metal@oxide core-shell nanostructure. *ACS Nano*, 5(9), 7108-7116.
- Ramasamy, E., Lee, W. J., Lee, D. Y., & Song, J. S. (2007). Nanocarbon counterelectrode for dye sensitized solar cells. *Appl. Phys. Lett.*, 90(17), 173103.
- Rokesh, K., Pandikumar, A., & Jothivenkatachalam, K. (2014). *Dye sensitized solar cell: A summary*. Paper presented at the Materials Science Forum.
- Saha, N. C., & Tompkins, H. G. (1992). Titanium nitride oxidation chemistry: An X-ray photoelectron spectroscopy study. *J. Appl. Phys.*, 72(7), 3072-3079.
- Sahu, G., Gordon, S. W., & Tarr, M. A. (2012). Synthesis and application of core-shell Au-TiO<sub>2</sub> nanowire photoanode materials for dye sensitized solar cells. *RSC Adv.*, 2(2), 573-582.
- Sahu, G., Wang, K., Gordon, S. W., Zhou, W., & Tarr, M. A. (2012). Core-shell Au-TiO<sub>2</sub> nanoarchitectures formed by pulsed laser deposition for enhanced efficiency in dye sensitized solar cells. *RSC Adv.*, 2(9), 3791-3800.
- Sathish, M., Viswanathan, B., & Viswanath, R. P. (2006). Alternate synthetic strategy for the preparation of CdS nanoparticles and its exploitation for water splitting. *Int. J. Hydrogen Energy*, 31(7), 891-898.
- Schaadt, D. M., Feng, B., & Yu, E. T. (2005). Enhanced semiconductor optical absorption via surface plasmon excitation in metal nanoparticles. *Appl. Phys. Lett.*, 86(6), 063106.
- Sebo, B., Huang, N., Liu, Y., Tai, Q., Liang, L., Hu, H., . . . Zhao, X.-Z. (2013). Dye-sensitized solar cells enhanced by optical absorption, mediated by TiO<sub>2</sub> nanofibers and plasmonics Ag nanoparticles. *Electrochim. Acta*, 112, 458-464.
- Seo, H.K., Fisher, E. R., Elliott, C. M., & Shin, H.S. (2012). Fast one-step method to synthesize TiO<sub>2</sub> nanoparticle clusters for dye sensitized solar cells. *J. Nanosci. Nanotechnol.*, 12(8), 6276-6282.
- Sheehan, S. W., Noh, H., Brudvig, G. W., Cao, H., & Schmittenmaer, C. A. (2012). Plasmonic enhancement of dye-sensitized solar cells using core-shell-shell nanostructures. *J. Phys. Chem. C*, 117(2), 927-934.
- Sivaranjani, K., & Gopinath, C. S. (2011). Porosity driven photocatalytic activity of wormhole mesoporous TiO<sub>2-x</sub>N<sub>x</sub> in direct sunlight. [10.1039/C0JM03825C]. *J. Mater. Chem.*, 21(8), 2639-2647.
- Smestad, G., Bignozzi, C., & Argazzi, R. (1994). Testing of dye sensitized TiO<sub>2</sub> solar cells I: Experimental photocurrent output and conversion efficiencies. *Sol. Energy Mater. Sol. Cells*, 32(3), 259-272.
- Song, M.-k., Rai, P., Ko, K.-J., Jeon, S.-H., Chon, B.-S., Lee, C.-H., & Yu, Y.-T. (2014). Synthesis of TiO<sub>2</sub> hollow spheres by selective etching of Au@TiO<sub>2</sub> core-shell nanoparticles for dye sensitized solar cell applications. *RSC Adv.*, 4(7), 3529-3535.
- Sony Design. Retrieved 15/9, 2014, from <http://www.sony.net/>
- Stoller, M. D., Park, S., Zhu, Y., An, J., & Ruoff, R. S. (2008). Graphene-based ultracapacitors. *Nano Lett.*, 8(10), 3498-3502.
- Su, C., Liu, L., Zhang, M., Zhang, Y., & Shao, C. (2012). Fabrication of Ag/TiO<sub>2</sub> nanoheterostructures with visible light photocatalytic function via a solvothermal approach. *CrystEngComm*, 14(11), 3989-3999.
- Su, H., Zhang, M., Chang, Y.-H., Zhai, P., Hau, N. Y., Huang, Y.-T., . . . Feng, S.-P. (2014). Highly conductive and low cost Ni-PET flexible substrate for efficient dye-sensitized solar cells. *ACS Appl. Mater. Interfaces*, 6(8), 5577-5584.

- Subramanian, V., Wolf, E. E., & Kamat, P. V. (2003). Green emission to probe photoinduced charging events in ZnO-Au nanoparticles. Charge distribution and fermi-level equilibration. *J. Phys. Chem. B*, 107, 7479-7485.
- Subramanian, V., Wolf, E. E., & Kamat, P. V. (2003). Influence of metal/metal-ion concentration on the photocatalytic activity of TiO<sub>2</sub>-Au composite nanoparticles. *Langmuir*, 19, 469-474.
- Subramanian, V., Wolf, E. E., & Kamat, P. V. (2004). Catalysis with TiO<sub>2</sub>/gold nanocomposites. Effect of metal particle size on the fermi level equilibration. *J. Am. Chem. Soc.*, 126(15), 4943-4950.
- Suk Jang, J., & Jin Ham, D. (2010). Platinum-free tungsten carbides as an efficient counter electrode for dye sensitized solar cells. *Chem. Commun.*, 46(45), 8600-8602.
- Sun, H., Luo, Y., Zhang, Y., Li, D., Yu, Z., Li, K., & Meng, Q. (2010). In situ preparation of a flexible polyaniline/carbon composite counter electrode and its application in dye-sensitized solar cells. *J. Phys. Chem. C*, 114(26), 11673-11679.
- Sun, M., Fu, W., Yang, H., Sui, Y., Zhao, B., Yin, G., . . . Zou, G. (2011). One-step synthesis of coaxial Ag/TiO<sub>2</sub> nanowire arrays on transparent conducting substrates: Enhanced electron collection in dye-sensitized solar cells. *Electrochem. Commun.*, 13(12), 1324-1327.
- Tao, Q., Zhao, X., Chen, Y., Li, J., Li, Q., Ma, Y., . . . Wang, X. (2013). Enhanced Vickers hardness by quasi-3D boron network in MoB<sub>2</sub>. *RSC Adv.*, 3(40), 18317-18322.
- Tepavcevic, S., Darling, S. B., Dimitrijevic, N. M., Rajh, T., & Sibener, S. J. (2009). Improved hybrid solar cells via in situ UV polymerization. *Small*, 5(15), 1776-1783.
- Thomas, S., Deepak, T. G., Anjusree, G. S., Arun, T. A., Nair, S. V., & Nair, A. S. (2014). A review on counter electrode materials in dye-sensitized solar cells. [10.1039/C3TA13374E]. *J. Mater. Chem.*, 2(13), 4474-4490.
- Tian, Y., & Tatsuma, T. (2005). Mechanisms and applications of plasmon-induced charge separation at TiO<sub>2</sub> films loaded with gold nanoparticles. *J. Am. Chem. Soc.*, 127(20), 7632-7637.
- Tian, Z., Wang, L., Jia, L., Li, Q., Song, Q., Su, S., & Yang, H. (2013). A novel biomass coated Ag-TiO<sub>2</sub> composite as a photoanode for enhanced photocurrent in dye-sensitized solar cells. *RSC Adv.*, 3(18), 6369-6376.
- Tripathi, B., Yadav, P., & Kumar, M. (2013). Plasmon-enhanced light trapping to improve efficiency of TiO<sub>2</sub> nanorod-based dye-sensitized solar cell. *Plasmonics*, 8(3), 1501-1507.
- Tsubomura, H., Matsumura, M., Nomura, Y., & Amamiya, T. (1976). Dye sensitised zinc oxide: aqueous electrolyte: platinum photocell. *Nature*, 261, 402-403.
- van de Lagemaat, J., Park, N. G., & Frank, A. J. (2000). Influence of electrical potential distribution, charge transport, and recombination on the photopotential and photocurrent conversion efficiency of dye-sensitized nanocrystalline TiO<sub>2</sub> solar cells: A study by electrical impedance and optical modulation techniques. *J. Phys. Chem.B*, 104(9), 2044-2052.
- Veerappan, G., Bojan, K., & Rhee, S.-W. (2011). Sub-micrometer-sized graphite as a conducting and catalytic counter electrode for dye-sensitized solar cells. *J. Am. Chem. Soc.*, 3(3), 857-862.
- Wang, H., Leonard, S. L., & Hu, Y. H. (2012). Promoting effect of graphene on dye-sensitized solar cells. *Ind. Eng. Chem. Res.*, 51(32), 10613-10620.
- Wang, L., Jia, L., & Li, Q. (2014). A novel sulfur source for biosynthesis of (Ag, S)-modified TiO<sub>2</sub> photoanodes in DSSC. *Mater. Lett.*, 123(0), 83-86.

- Wang, M., Chamberland, N., Breau, L., Moser, J.-E., Humphry-Baker, R., Marsan, B., . . . Grätzel, M. (2010). An organic redox electrolyte to rival triiodide/iodide in dye-sensitized solar cells. *Nat. Chem.*, 2(5), 385-389.
- Wang, P., Klein, C., Humphry-Baker, R., Zakeeruddin, S. M., & Grätzel, M. (2005). Stable  $\geq 8\%$  efficient nanocrystalline dye-sensitized solar cell based on an electrolyte of low volatility. *Appl. Phys. Lett.*, 86(12), 123508.
- Wang, P., Zakeeruddin, S. M., Moser, J.-E., Humphry-Baker, R., & Grätzel, M. (2004). A solvent-free,  $\text{SeCN}/(\text{SeCN})_3^-$  based ionic liquid electrolyte for high-efficiency dye-sensitized nanocrystalline solar cells. *J. Am. Chem. Soc.*, 126(23), 7164-7165.
- Wang, Q., Zhang, Z., Zakeeruddin, S. M., & Grätzel, M. (2008). Enhancement of the performance of dye-sensitized solar cell by formation of shallow transport levels under visible light illumination. *J. Phys. Chem. C*, 112(17), 7084-7092.
- Wang, Z.S., Sayama, K., & Sugihara, H. (2005). Efficient eosin Y dye-sensitized solar cell containing  $\text{Br}^-/\text{Br}_3^-$  electrolyte. *J. Phys. Chem. B*, 109(47), 22449-22455.
- Wang, Z.S., Yamaguchi, T., Sugihara, H., & Arakawa, H. (2005). Significant efficiency improvement of the black dye-sensitized solar cell through protonation of  $\text{TiO}_2$  films. *Langmuir*, 21(10), 4272-4276.
- Wen, C., Ishikawa, K., Kishima, M., & Yamada, K. (2000). Effects of silver particles on the photovoltaic properties of dye-sensitized  $\text{TiO}_2$  thin films. *Sol. Energy Mater. Sol. Cells*, 61(4), 339-351.
- Wolfbauer, G., Bond, A. M., Eklund, J. C., & MacFarlane, D. R. (2001). A channel flow cell system specifically designed to test the efficiency of redox shuttles in dye sensitized solar cells. *Sol. Energy Mater. Sol. Cells*, 70(1), 85-101.
- Wu, J., Hao, S., Lan, Z., Lin, J., Huang, M., Huang, Y., . . . Sato, T. (2007). A thermoplastic gel electrolyte for stable quasi-solid-state dye-sensitized solar cells. *Adv. Funct. Mater.*, 17(15), 2645-2652.
- Wu, J., Hao, S., Lan, Z., Lin, J., Huang, M., Huang, Y., . . . Sato, T. (2008). An all-solid-state dye-sensitized solar cell-based poly(N-alkyl-4-vinyl-pyridine iodide) electrolyte with efficiency of 5.64%. *J. Am. Chem. Soc.*, 130(35), 11568-11569.
- Wu, W.-Q., Lei, B.-X., Rao, H.-S., Xu, Y.-F., Wang, Y.-F., Su, C.-Y., & Kuang, D.-B. (2013). Hydrothermal fabrication of hierarchically anatase  $\text{TiO}_2$  nanowire arrays on FTO glass for dye-sensitized solar cells. *Sci. Rep.*, 3.
- Xia, J., Masaki, N., Jiang, K., & Yanagida, S. (2006). Deposition of a Thin Film of  $\text{TiO}_x$  from a Titanium Metal Target as Novel Blocking Layers at Conducting Glass/ $\text{TiO}_2$  Interfaces in Ionic Liquid Mesoscopic  $\text{TiO}_2$  Dye-Sensitized Solar Cells. *The Journal of Physical Chemistry B*, 110(50), 25222-25228.
- Xiang, P., Li, X., Wang, H., Liu, G., Shu, T., Zhou, Z., . . . Liu, L. (2011). Mesoporous nitrogen-doped  $\text{TiO}_2$  sphere applied for quasi-solid-state dye-sensitized solar cell. *Nanoscale Res. Lett.*, 6(1), 1-5.
- Xiang, Q., Yu, J., Cheng, B., & Ong, H. (2010). Microwave-hydrothermal preparation and visible-light photoactivity of plasmonic photocatalyst Ag- $\text{TiO}_2$  nanocomposite hollow spheres. *Chemistry, an Asian journal*, 5(6), 1466.
- Xu, C., Wu, J., Desai, U. V., & Gao, D. (2012). High-efficiency solid-state dye-sensitized solar cells based on  $\text{TiO}_2$ -coated ZnO nanowire arrays. *Nano Lett.*, 12(5), 2420-2424.
- Xu, M., Zhou, D., Cai, N., Liu, J., Li, R., & Wang, P. (2011). Electrical and photophysical analyses on the impacts of arylamine electron donors in cyclopentadithiophene dye-sensitized solar cells. *Energy Environ. Sci.*, 4(11), 4735-4742.

- Xu, Q., Liu, F., Liu, Y., Cui, K., Feng, X., Zhang, W., & Huang, Y. (2013). Broadband light absorption enhancement in dye-sensitized solar cells with Au-Ag alloy popcorn nanoparticles. *Sci. Rep.*, 3, 2112.
- Xu, X., Huang, D., Cao, K., Wang, M., Zakeeruddin, S. M., & Grätzel, M. (2013). Electrochemically reduced graphene oxide multilayer films as efficient counter electrode for dye-sensitized solar cells. *Sci. Rep.*, 3, 1489.
- Xuhui, S., Xinglan, C., Wanquan, T., Dong, W., & Kefei, L. (2014). Performance comparison of dye-sensitized solar cells by using different metal oxide-coated TiO<sub>2</sub> as the photoanode. *AIP Adv.*, 4(3), 1304.
- Yamaguchi, T., Tobe, N., Matsumoto, D., Nagai, T., & Arakawa, H. (2010). Highly efficient plastic-substrate dye-sensitized solar cells with validated conversion efficiency of 7.6%. *Sol. Energy Mater. Sol. Cells*, 94(5), 812-816.
- Yang, L., He, D., Cai, Q., & Grimes, C. A. (2007). Fabrication and Catalytic Properties of Co-Ag-Pt Nanoparticle-Decorated Titania Nanotube Arrays. *J. Phys. Chem. C*, 111(23), 8214-8217.
- Yang, L., & Leung, W. W. F. (2013). Electrospun TiO<sub>2</sub> nanorods with carbon nanotubes for efficient electron collection in dye-sensitized solar cells. *Adv. Mater.*, 25(12), 1792-1795.
- Yella, A., Lee, H.W., Tsao, H. N., Yi, C., Chandiran, A. K., Nazeeruddin, M. K., . . . Grätzel, M. (2011). Porphyrin-sensitized solar cells with cobalt (II/III)-based redox electrolyte exceed 12 percent efficiency. *Science*, 334(6056), 629-634.
- Yoshimura, M., Suchanek, W., & Han, K.-S. (1999). Recent developments in soft, solution processing: one step fabrication of functional double oxide films by hydrothermal-electrochemical methods. *J. Mater. Chem.*, 9(1), 77-82.
- Yu, J. C., Ho, W., Yu, J., Yip, H., Wong, P. K., & Zhao, J. (2005). Efficient Visible-Light-Induced photocatalytic dDisinfection on sulfur-doped nanocrystalline titania. *Environ. Sci. Technol.*, 39(4), 1175-1179.
- Yu, K., Tian, Y., & Tatsuma, T. (2006). Size effects of gold nanoparticles on plasmon-induced photocurrents of gold-TiO<sub>2</sub> nanocomposites. *Phys. Chem. Chem. Phys.*, 8, 5417-5420.
- Zaban, A., Ferrere, S., & Gregg, B. A. (1998). Relative energetics at the semiconductor/sensitizing dye/electrolyte interface. *J. Phys. Chem. B*, 102(2), 452-460.
- Zhang, J., Wu, Y., Xing, M., Leghari, S. A. K., & Sajjad, S. (2010). Development of modified N doped TiO<sub>2</sub> photocatalyst with metals, nonmetals and metal oxides. *Energy Environ. Sci.*, 3(6), 715-726.
- Zhang, J. C., Han, Z. Y., Li, Q. Y., Yang, X. Y., Yu, Y., & Cao, W. L. (2011). N, S-doped TiO<sub>2</sub> anode effect on performance of dye-sensitized solar cells. *J. Phys. Chem. Solids*, 72(11), 1239-1244.
- Zhang, S., Peng, F., Wang, H., Yu, H., Zhang, S., Yang, J., & Zhao, H. (2011). Electrodeposition preparation of Ag loaded N-doped TiO<sub>2</sub> nanotube arrays with enhanced visible light photocatalytic performance. *Catal. Commun.*, 12(8), 689-693.
- Zhang, W. F., He, Y. L., Zhang, M. S., Yin, Z., & Chen, Q. J. (2000). Raman scattering study on anatase TiO<sub>2</sub> nanocrystals. *J. Phys. D: Appl.*, 33.
- Zhang, X., Liu, J., Li, S., Tan, X., Yu, M., & Du, J. (2013). Bioinspired synthesis of Ag@TiO<sub>2</sub> plasmonic nanocomposites to enhance the light harvesting of dye-sensitized solar cells. *RSC Adv.*, 3(40), 18587-18595.
- Zhang, Z., Chen, P., Murakami, T. N., Zakeeruddin, S. M., & Grätzel, M. (2008). The 2, 2, 6, 6-tetramethyl-1-piperidinyloxy radical: An efficient, iodine-free redox mediator for dye-sensitized solar cells. *Adv. Funct. Mater.*, 18(2), 341-346.

- Zhao, B., Huang, H., Jiang, P., Zhao, H., Huang, X., Shen, P., . . . Tan, S. (2011). Flexible counter electrodes based on mesoporous carbon aerogel for high-performance dye-sensitized solar cells. *J. Phys. Chem. C*, 115(45), 22615-22621.
- Zhao, G., Kozuka, H., & Yoko, T. (1997). Effects of the incorporation of silver and gold nanoparticles on the photoanodic properties of rose bengal sensitized TiO<sub>2</sub> film electrodes prepared by sol-gel method. *Sol. Energy Mater. Sol. Cells*, 46(3), 219-231.
- Zhao, H., Chen, Y., Quan, X., & Ruan, X. (2007). Preparation of Zn-doped TiO<sub>2</sub> nanotubes electrode and its application in pentachlorophenol photoelectrocatalytic degradation. *Chin. Sci. Bull.*, 52(11), 1456-1461.
- Zhao, J., Wu, S., Liu, J., Liu, H., Gong, S., & Zhou, D. (2010). Tin oxide thin films prepared by aerosol-assisted chemical vapor deposition and the characteristics on gas detection. *Sens. Actuators, B*, 145(2), 788-793.
- Zheng, W., Cui, S., & Zhang, X. (2012). *The research of CaO/TiO<sub>2</sub> nanocrystalline film for dye-sensitized solar cell*. Paper presented at the Strategic Technology (IFOST), 2012 7th International Forum on.
- Zhou, H., Wu, L., Gao, Y., & Ma, T. (2011). Dye-sensitized solar cells using 20 natural dyes as sensitizers. *J. Photochem. Photobiol., A*, 219(2), 188-194.
- Zhou, M., & Yu, J. (2008). Preparation and enhanced daylight-induced photocatalytic activity of C,N,S-tridoped titanium dioxide powders. *J. Hazard. Mater.*, 152(3), 1229-1236.

## LIST OF PUBLICATIONS AND PAPERS PRESENTED

### Publications

- [1] **S. P. Lim**, A. Pandikumar, N. M. Huang and H. N. Lim, Reduced graphene oxide-titania nanocomposite-modified photoanode for efficient dye-sensitized solar cells, *Int. J. Energy Res.* (2015)
- [2] **S. P. Lim**, A. Pandikumar, N. M. Huang, H. N. Lim, G. Gu and T. Ma, Promotional effect of silver nanoparticles on performance of N-doped TiO<sub>2</sub> photoanode-based dye-sensitized solar cells, *RSC Adv.* (2014)
- [3] **S. P. Lim**, A. Pandikumar, N. M. Huang and H. N. Lim, Enhanced photovoltaic performance of silver@titania plasmonic photoanode in dye-sensitized solar cells, *RSC Adv.* 4 (2014) 38111-38118.
- [4] **S. P. Lim**, A. Pandikumar, Y. S. Lim, N. M. Huang and H. N. Lim, In-situ electrochemically deposited polypyrrole nanoparticles incorporated reduced graphene oxide as an efficient counter electrode for platinum-free dye-sensitized solar cells, *Sci. Rep.* 4 (2014)
- [5] **S. P. Lim**, N. M. Huang, H. N. Lim and M. Mazhar, Aerosol assisted chemical vapour deposited (AACVD) of TiO<sub>2</sub> thin film as compact layer for dye-sensitised solar cell, *Ceram. Int.* 40 (2014) 8045-8052.
- [6] **S. P. Lim**, A. Pandikumar, N. M. Huang and H. N. Lim, Silver/titania nanocomposite-modified photoelectrodes for photoelectrocatalytic methanol oxidation, *Int. J. Hydrogen Energy* 39 (2014) 14720-14729.
- [7] **S. P. Lim**, N. M. Huang, H. N. Lim and M. Mazhar, Surface modification of aerosol-assisted CVD produced TiO<sub>2</sub> thin film for dye sensitised solar cell, *Int. J. Photoenergy* 2014 (2014) 1-12.
- [8] **S. P. Lim**, N. M. Huang and H. N. Lim, Solvothermal synthesis of SnO<sub>2</sub>/graphene nanocomposites for supercapacitor application, *Ceram. Int.* 39 (2013) 6647-6655.
- [9] **S. P. Lim**, A. Pandikumar, N. M. Huang and H. N. Lim, Facile synthesis of Au@TiO<sub>2</sub> Nanocomposite and Its Application as Photoanode in Dye-Sensitized Solar Cells, *RSC Adv.* 5 (2015) 44398-44407.
- [10] **S. P. Lim**, A. Pandikumar, R. Ramaraj, N. M. Huang and H. N. Lim, Boosting Photovoltaic Performance of Dye-Sensitized Solar Cells Using Silver Nanoparticle-Decorated N,S-Co-Doped-TiO<sub>2</sub> Photoanode, *Sci. Rep.* (Article In Press)
- [11] F.A. Jumeri, H.N. Lim, Z. Zainal, N.M. Huang, A. Pandikumar, **S.P. Lim**, Dual Functional Reduced Graphene Oxide as Photoanode and Counter Electrode in Dye-

Sensitized Solar Cells and Its Exceptional Efficiency Enhancement. J. Power Sources, 2015, (Article in Press)

- [12] Y. S. Lim, H. N. Lim, **S. P. Lim** and N. M. Huang, Catalyst-assisted electrochemical deposition of graphene decorated polypyrrole nanoparticles film for high-performance supercapacitor, RSC Adv. 4 (2014) 56445-56454.

**Paper presented in international conference:**

1. **S. P. Lim**, N. M. Huang and H. N. Lim, “Solvothermal synthesis of SnO<sub>2</sub>/graphene nanocomposites for supercapacitor application” in 4<sup>th</sup> *International Conference on Solid State Science & Technology*, 18-20 December 2012, Holiday Inn Hotel, Malacca, Malaysia.
2. **S. P. Lim**, Y. S. Lim, A. Pandikumar, N. M. Huang and H. N. Lim, “Gold-Silver@TiO<sub>2</sub> Nanocomposite-Modified Plasmonic Photoanode for Higher Efficiency Dye-Sensitized Solar Cells” in *Future Energy*, 3-5 November 2014, UNSW, Sydney, Australia.